ASSESSMENT OF ANALYTICAL PROCEDURES FOR DESIGNING METAL BUILDINGS FOR WIND DRIFT SERVICEABILITY

Maninder Singh Bajwa

Thesis submitted to the Faculty of the

Virginia Polytechnic Institute and State University

in partial fulfillment of the requirements for the degree of

Master of Science

In

Civil Engineering

Finley A. Charney

Cristopher D. Moen

W. Samuel Easterling

August 3, 2010

Blacksburg, Virginia

Keywords: Metal Buildings, Wind Drift Serviceability, Column-Base Connection, Diaphragm Flexibility

ASSESSMENT OF ANALYTICAL PROCEDURES FOR DESIGNING METAL BUILDINGS FOR WIND DRIFT SERVICEABILITY

Maninder Singh Bajwa

ABSTRACT

While designing metal buildings for wind drift, for simplicity of analysis and design, connection at base of column is considered as pinned which provides no rotational restraint. The actual behavior of the connection however, is partially rigid, that provides some rotational stiffness even in case of single row of bolts. Moreover, using a two-dimensional (planar) structural model for analysis ignores any load distribution provided by roof and wall sheeting. Simulation of true behavior of base connection and diaphragm stiffness can substantially reduce drift caused due to lateral forces thereby lessening the conservatism in traditional design practices. This thesis provides results obtained from full-scale experimental testing and analytical study for a metal building.

A full scale load test was conducted to quantify the lateral stiffness of an existing metal building. A static lateral load, consistent in magnitude with the building's design wind pressure, was applied to the knee of a primary frame, and the resulting lateral displacements and column-base rotations for all primary frames were measured. The test procedure was repeated at several locations. The experimentally obtained results were then validated using two-dimensional and three-dimensional analytical models. The three-dimensional models explicitly simulated the primary and secondary framing, roof and wall diaphragms, and column-base stiffness. A couple of approaches have been proposed to model column-base plate connection varying in complexity and accuracy. Once validated, the FE model is utilized to quantify the relative stiffness contributions of the metal building system components to lateral drift.

While performing analysis some other parameters were also studied. These consisted of effect of base plate thickness and length of anchor bolts on column-base rigidity. Also, effect of including shear deformations and considering the haunch (column-rafter junction) as rigid were studied. Another small but important part of the paper is comparison of wind pressures obtained using different procedure of ASCE 7-05 with database assisted design pressures. Once these parameters are quantified practical engineering guidelines are developed to incorporate the influence of secondary framing, roof diaphragms, wall cladding, and column-base stiffness and wind loads in metal building design.

Acknowledgements

I would like to thank Dr. Finley A. Charney for serving as my primary advisor and committee chair. His endless patience and faith in me made me complete this research work successfully. I am really thankful to him for all I have learned from him as a Graduate student and Research Assistant. I would like to thank Dr. Cristopher D. Moen equally for always being there for his support all along the project, especially for the testing program. I would also like to thank Dr. W. Samuel Easterling for serving on my committee and providing valuable input to my thesis.

I would like to thank the Metal Building Manufacturer's Association for sponsoring the research described in this report. Special thanks are due to Dr. Lee Shoemaker, who has served as the main contact between MBMA and the research team.

Blue Ridge Timberwrights, of Christiansburg Virginia, made the Test Building available to the research team for several months. Sandy Bennett owner of the building provided full access to the building. Paula Davis, the contact person for any issues related to the building provided full support. Sandy's and Paula's enduring patience with the research team is greatly appreciated.

The loading frame was fabricated at the Thomas M. Murray Structures Research Lab. Laboratory instrument makers Dennis Huffman and Brett Farmer fabricated the frame and provided assistance in the in the laboratory and at the test building site.

All photographs that have been included in this thesis were made by either the author or Dr. Finley A. Charney in year 2009.

The testing of the building in Christainsburg could not have been completed without the help from Ms. Fae Garstang, Mr. Amey Bapat, Mr. Adam Bowland, Mr. William Collins, Mr. Bernie Kassner, Mr. Joseph Dulka, Mr. Gokul Kamath, Mr. Andrew Nguyen, Mr. Behrooz Sororri-Rad, Mr. Rohan Girish Talwalkar, Mr. Karthik Ganesan, Mr. Yash Gajbhiye, Mr. Dhawal Ashar, Ms Anumeha and Mr. Prashant Sharma. I would especially like to thank Ms. Kalyani Tipnis for her untiring support and presence for most of the testing program. These individuals, undergraduate and graduate students at Virginia Tech, volunteered their time to the project. Special thanks are due to all.

Lastly, and most importantly, I would like to thank my family for supporting me and showing confidence in my abilities. Without their help, sacrifices, love and nice words I would not have been able to accomplish the goals that I have.

TABLE OF CONTENTS

LIST OF FIGURES

LIST OF TABLES

Chapter 1 Introduction

1.1 Introduction

When designing metal buildings for wind drift, it is traditional to use a simple two-dimensional (planar) structural analysis model. The wind loads on these models are based on tributary area; ignoring the load redistribution provided by the metal roofing, and hence considering fully flexible diaphragms. The connecting points between the main wind-load resisting frames and the supporting foundation are modeled as pinned, rather than partially rigid. These and other simplifications that are inherent in the analysis tend to produce conservative estimates of drift, possibly resulting in unnecessary costs.

The purpose of the research reported herein is to identify those aspects of the current analytical approach that lead to overestimates of computed drift, and to provide recommendations for improving the analysis. To achieve these objectives an existing metal building was identified, and analyzed both experimentally and computationally. The experimental work consisted of applying static lateral loads to both ends of several of the interior gable frames of the building, and measuring the response in terms of displacements, strains, and rotations. The analytical work included a literature review, an evaluation of existing analytical models, and the creation and analysis of a variety of finite element models of two-dimensional sub-systems of the Test Building. As explained later in this thesis a complete three-dimensional analysis of the entire Test Building was performed because experimental results indicated that such detailed modeling was necessary.

Also at issue in wind drift serviceability design are the magnitude and spatial distribution of wind pressures used in the analysis. It is expected that these pressures are conservative, but the source of and degree of conservatism are not known. For this reason, a secondary part of the project was to review the methods available in ASCE 7-05 (ASCE, 2006) for computing wind loads. No effort was made to determine the accuracy of the ASCE 7 loads with respect to actual loads determined from field tests or from wind tunnel or other studies.

It is important to note, however, that structural analysis and wind load determination are only two components of wind drift serviceability design. Additional considerations include the basic definition of the "drift" measure that is to be controlled, setting the limiting values of drift, and determining how often drifts beyond the established limits may be tolerated. Each of these issues has its own set of complexities, some of which are discussed in Fisher and West (2004), Charney (1990), Griffis (1993), Newman (1997), and Berding (2006). A brief overview of these concepts is provided in the following sections.

1.2 Overview of Conceptual Basis of Wind Drift Serviceability Design

1.2.1 Drift Damage Measure and Drift Damage Index

For wind design, drift is a serviceability issue, and the motive for limiting drift is to avoid or limit damage to nonstructural components. For tier type building construction (e.g. multistory office buildings) the best measure of damage is shear strain in nonstructural components because damage thresholds for nonstructural components are usually determined from racking tests. Charney (1990) has recommended a comprehensive wind drift serviceability design procedure in which the computed shear strain in nonstructural components is termed the "Drift Damage Measure", and the limiting shear strain (acceptance criteria) is called the "Drift Damage Limit". The goal of the serviceability design is to limit the "Drift Damage Index" to a maximum value of 1.0 where

$$\text{Drift Damage Index} = \frac{\text{Drift Damage Measure}}{\text{Drift Damage Limit}} \qquad (1\text{-}1)$$

The Drift Damage Measure is computed from three dimensional finite element analyses, wherein the nonstructural components are modeled as membrane elements (three-dimensional elements with only in-plane stiffness properties). The stiffness of these elements is usually set to near zero because all that is needed from the elements is the in-plane shear strain. It is noted that only a few of the nonstructural components are modeled, with the elements placed at locations that are expected to produce the greatest deformation. These locations are referred to as Drift Damageable Zones.

The procedure used for tier buildings is applicable to low-rise metal buildings. Consider, for example, the building shown in Figure 1-1 where six different Drift Damageable Zones have been identified. A three dimensional finite element analysis would be used to compute the shear strains (Drift Damage Measure) in these elements, and these would be compared to the established limits.

1.2.2 Drift Damage Limits

The Drift Damage Limit is assigned for each Drift Damageable Zone on a material basis. For drywall, for example, the limiting strain might be 1/400 (Griffis, 1993). Limiting lateral drift indices as high as H/60 have been used for deflections at the ridge of gable frames (Fisher and West, 2004). Unfortunately, it is difficult to relate this to damage in the structure or in the nonstructural components. An alternate approach might be to limit the strain in the roof or wall

panels. For example, a damage based limiting strain of 1/60 might be used for the numbered panels in Figure 1-1.

In practice, these limits should be based on the intended use of the facility, and on economic considerations related to the costs of avoiding damage or the costs of repairing damage that may occur.

For metal buildings, there are other aspects of deformation that might need to be limited. Newman (1997), for example, indicates that it might be necessary to limit deformations at mid bay, or even a mid-height of the mid-bay location to prevent damage. As shown in Figure 1-2, this displacement consists of three components; the eave displacement, the roof diaphragm displacement, and the cladding displacement.

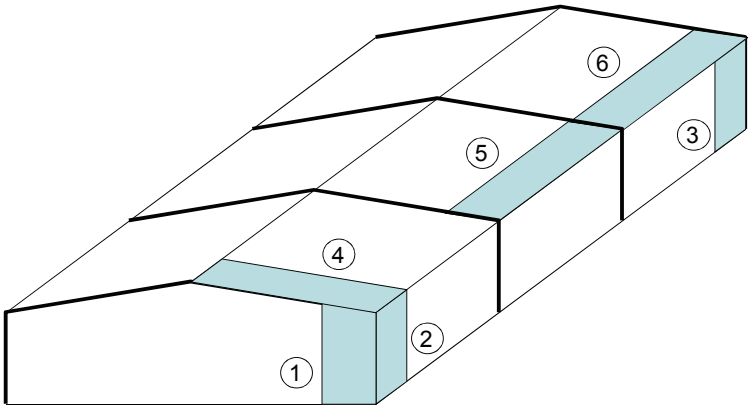

Figure 1-1: Potential Drift Damage Zones in a Typical Metal Building

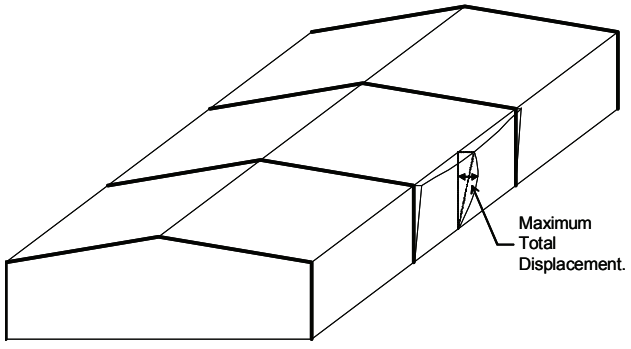

Figure 1-2: Combined Displacement at Mid-height of a Wall Panel

1.2.3 **Mean Recurrence Interval of Wind Loads Used in Serviceability Design**

Related to the Drift Damage Limit is the return period for the wind loads used in the analysis. For wind drift serviceability design it is now common practice to use a wind speed with a mean recurrence interval of ten years (Ellingwood, et al., 1980; Charney, 1990; Fisher and West, 2004). The use of a ten year MRI results in wind pressures (for non-hurricane regions) that are approximately 70 percent of the unfactored wind pressures used for strength based design (ASCE, 2006).

1.2.4 **Wind Pressure Distributions**

ASCE 7-05 (ASCE, 2006) provides guidelines for applying wind loads for strength design, and except for the mean recurrence interval used for strength (50 to 100 years) versus wind drift (10 years), these procedures should be equally applicable to analysis related to serviceability under wind.

The ASCE 7 wind loads provide a simple and convenient way to calculate wind loads for design. Due to the highly complex nature of wind loads, however, it is likely that the ASCE 7 pressure values and pressure distributions are conservative, and possibly highly conservative. This is similar to the situation for multi-story tier buildings, where it has become common practice to use wind tunnel tests to provide improved (almost always lower than code) estimates of the loads used for the design of the main wind force resisting system and the cladding of the structure. While it is not practical to test all metal buildings in such a manner, much can be learned from research-based wind tunnel tests that have been performed in the past (Case and Isyumov, 1998; Uematsu and Isyumov, 1999; Surry, et al. (2005).

The use of wind tunnels to determine wind pressures for drift design of metal buildings is not practical, but data collected from such tests would be useful in evaluating the degree of conservatism of the code loads. Similarly, computational fluid dynamics, while not practical for every day design, is a potentially viable alternate to wind tunnel testing (Murakami, 2002). Both wind tunnel and computational fluid dynamics studies would be useful in the development of a database assisted design approach for determining wind pressures (Simiu and Stathopoulos, 1997; Whalen, et. al., 1998). Database assisted design uses a database of the results of previously completed wind tunnel tests of buildings similar to the building being designed, in lieu of new tests on the building.

1.2.5 Structural Analysis Used for Computing the Drift Damage Measures

The analytical models used for the design of metal buildings usually represent the individual frames in two dimensions, and hence, the concept of a Drift Damage Index (which relies on shear strain) is not viable. When using such an analysis, therefore, one must go back to the traditional measure of drift which is generally taken as the displacement at the eave. The principal uncertainties associated with the planar models include the magnitude of load on an individual frame (which is dependent on the assumed in-plane diaphragm stiffness), the effective rotational stiffness at the column-to-base connection, and the stiffness of the panel zone region (the region where the columns rafters are connected.)

If three-dimensional (full building) models are used the diaphragms can be modeled explicitly. However, the diaphragm effectiveness is particularly difficult to quantify as the behavior depends on a variety of factors, including main and secondary structural framing, diaphragm slope, aspect ratio, metal roof orientation and its profile, and attachment, (through fastened versus standing seam). Uncertainties related to panel zone behavior and rigidity of the column-to-base connections is relevant to three dimensional models as well.

An additional set of uncertainties related to the analysis is the loading under which the analysis is to be performed. The direction of the loads is of concern because the in-plane stiffness of the portion of the diaphragm under positive (downward) pressure is likely to be different than the same diaphragm under negative (uplift) pressure. The stiffness of the column-to-base connection may also be dependent on loading direction and on load combination. Another consideration for analysis is the P-Delta effect. For light metal buildings such effects would seem to be negligible. However, if drift limits as high as H/60 are used, P-Delta effects might become an important factor in the analysis.

1.3 Objectives and Scope of Research

The basic objective of the research reported herein was to test an existing building, and to use information gained from the tests to determine if the current analytical methods are appropriate. A broader investigation, including a review of the current drift serviceability design philosophy and an assessment of the various components of the philosophy, while potentially important, was outside the scope of the work.

Thus the work presented in this thesis is limited to the following:

- A brief review of analysis methods for wind drift analysis of metal buildings (Chapter 2)
- A review of the wind loading provisions in ASCE 7 (Chapter 3)

- A description of the Test Building (Chapter 4)
- Development of wind loads for the Test Building (Chapter 5)
- Structural analysis of the Test Building (Chapter 6)
- Testing procedure and summary of results (Chapter 7)
- Three-Dimensional Modeling (Chapter 8)
- Correlation of analytical and experimental results (Chapter 9)
- Summary, conclusions, and recommendations (Chapter 10)

A variety of supporting appendices are provided at the end of the thesis.

It should be noted that the vast majority of the work reported herein is related to the analysis and testing of the Test Building and the correlation of the results obtain by analysis and testing. Two types of analyses of building have been presented in this thesis. Planar two-dimensional analysis has been presented in Chapter 6. A more refined and detailed analysis has been presented in Chapter 8.

Chapter 2 Overview of Analysis Methodologies

2.1 Overview of Structural Analysis Methodologies

The typical metal building is a highly complex three-dimensional system consisting of gable frames, end frames, metal roofing, and bracing. The simplest type of building is illustrated in Figure 2-1. In some buildings one or both of the end-frames may be gable frames, and some or all of the X-bracing may not be present. The load path from the metal roofing to the purlins to the gable frames and end-walls varies considerably, as does the method of connecting the diaphragm panels to the purlins and to each other (screw type or standing seam metal roofing and attachment).

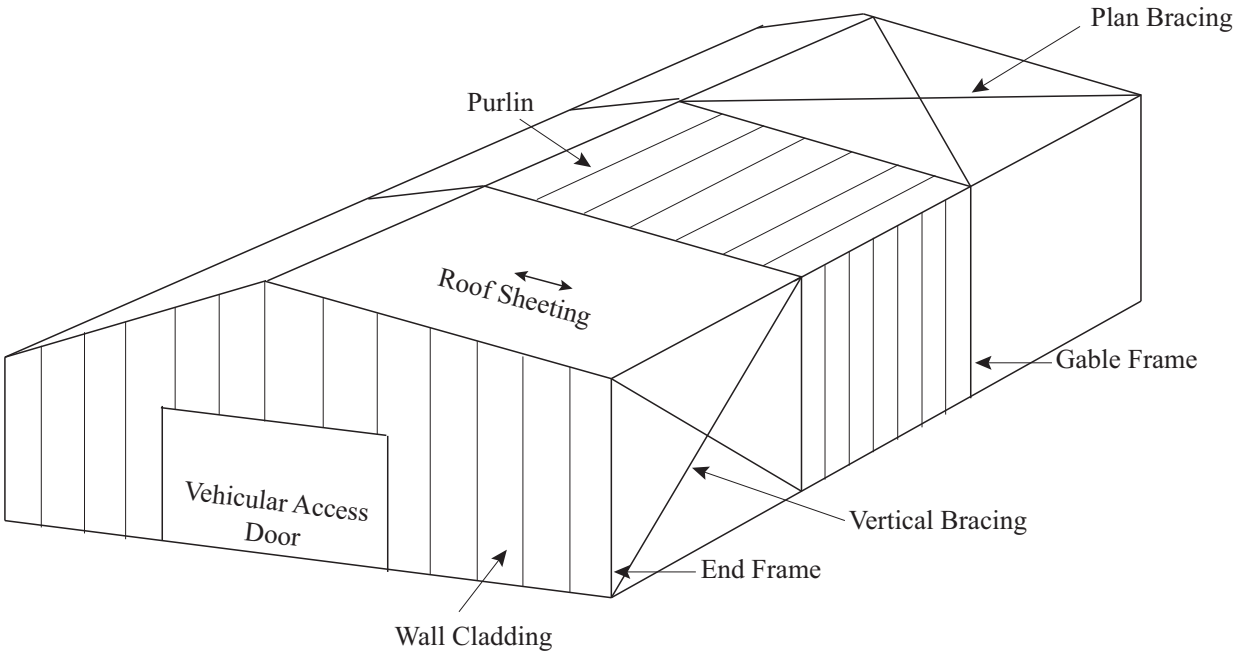

Figure 2-1: Schematic View of Typical Metal Building

The columns and rafters of the gable frames are typically constructed from custom-made tapered steel I-shape members. The base of the columns is usually welded to a base plate, and this plate is anchored into the concrete foundation using anchor bolts. Grout may or may not be present between the base plate and the foundation.

Although the interaction of the various structural components is three dimensional, it is generally not practical to perform a three dimensional analysis of the entire structure shown in Figure 2-1. The lack of practicality comes not from the three-dimensional character of the problem, but rather from a large assortment of difficulties associated with modeling and quantifying the behavior of the various components and particularly the connections between the components.

Thus, instead of three dimensional analysis, it is traditional to analyze the individual "frames" separately, wherein it is assumed that the only contribution of the metal roofing is to distribute gravity loads and wind loads to the main frames on a tributary basis. While this approach clearly simplifies the analysis, there are a host of questions that can be asked about the modeling of these frames. For example, for the frame shown in Figure 2-2, one could ask:

1. How should the gable frame be modeled? Among the possible choices are:
   Use of several prismatic 2-dimensional frame elements
   Use of several nonprismatic 2-dimensional frame elements
   Use of finite elements (e.g. shell elements).
2. When 2-Dimensional elements are used, should shear deformations be included?
3. When 2-Dimensional elements are used, how should the "Panel Zone" of the column-rafter connection be modeled?
4. Does the connection between the column and the foundation provide any rotational stiffness? If so, how is this connection modeled?
5. Does the roof sheeting act compositely with the columns and rafters?
6. Is it necessary to include P-Delta Effects?

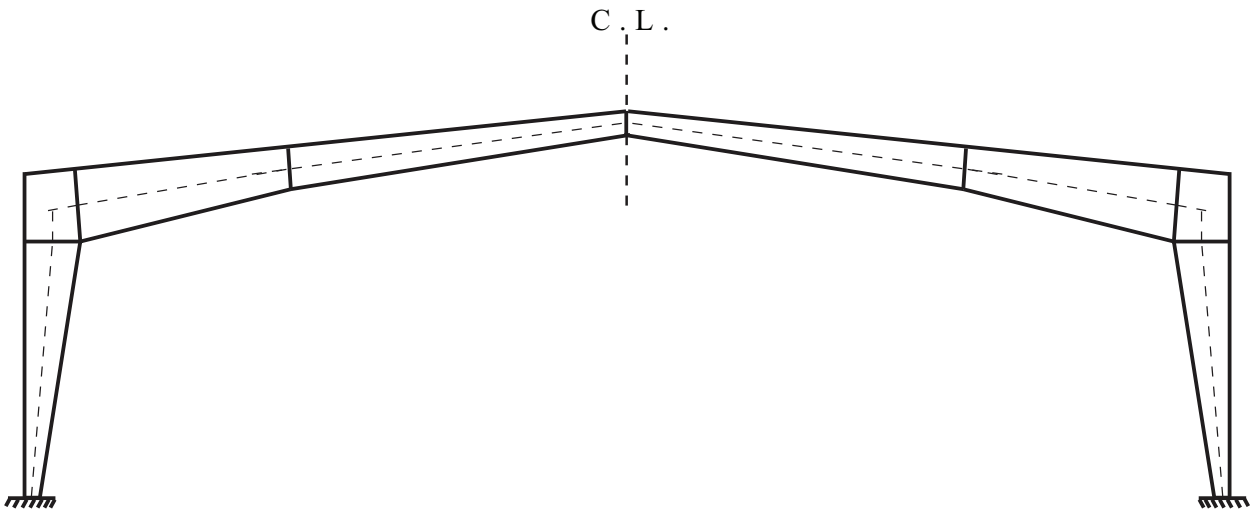

Figure 2-2: Typical Gable Frame

These issues are briefly discussed in the remainder of the chapter, with the goal of providing a methodology for the analysis of the test building (described in Chapter 6).

2.2 Modeling the Gable Frames

Due to the tapered cross sections, it is most appropriate to model the members of gable frames with nonprismatic elements. As long as it is possible to define precise functions for the

variations of geometry along the element length, it is straight forward to develop "mathematically exact" element stiffness and fixed end forces, and to automatically include the effect of axial, flexural, and shear deformations. A computer model for a typical web-tapered gable frame is shown in Figure 2-3. Note that nodes are needed only at abrupt discontinuities of section geometry. The modeling of the frame in the region of the column-rafter connection is described later.

Some commercial programs, such as SAP 2000 model nonprismatic members by specifying properties at each end of the member, and indicating whether the variation in moment of inertia varies in a linear, quadratic, or cubic manner along the length. For web-tapered I sections the quadratic variation is most accurate, but is not exact.

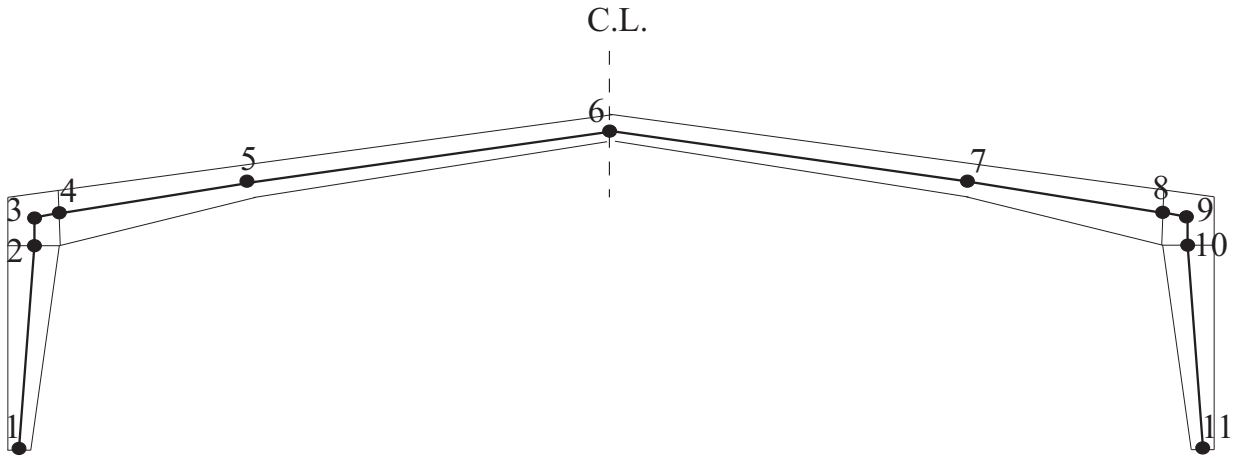

Figure 2-3: Computer Model for Gable Frame with Web Tapered Members

2.3 Including Shear Deformations

Shear deformations should always be included in analysis of steel buildings with I-shaped cross sections (Charney et al., 2005; Charney and Pathak, 2007a; Charney and Pathak, 2007b). For traditional steel moment frames such deformations can be responsible for as much as 15 percent of the total lateral drift (Charney, 1990). When shear deformations are included, it is recommended that the shear area be taken as the web thickness times the depth between flanges (Charney, et al., 2005).

2.4 Modeling the Column-Rafter Panel Zone Region

The region of the frame where the column and rafter are joined is referred to as the "panel zone" of the frame. It is well known that similar regions in tiered moment frames can be a very

significant source of deformation (Charney, 1990). Procedures for modeling panel zones have been developed for steel moment frame buildings. The two most common of these, the Krawinkler model and the Scissors model are described in Charney and Marshall (2006). The Krawinkler model attempts to model the panel zone explicitly through the use of an assemblage of rigid links and rotational springs. The Scissors model also uses rigid elements and springs, but is much simpler than the Krawinkler model. The Krawinkler model is preferred due to its kinematic accuracy.

When explicit panel zone modeling is not used it is recommended that centerline analysis be used. For the left end panel zone of the gable frame shown in Figure 2-3, for example, the elements between nodes 2 and 3 and 3 and 4 would be modeled as simple prismatic members. The elements between nodes 2 and 3 would have the same moment of inertia as the deepest portion of the column, and the element between nodes 3 and 4 would have a moment of inertia equal to that of the deepest portion of the rafter. In no circumstances should the elements between nodes 2 and 3 or nodes 3 and 4 be modeled as "rigid". Nor should the element between nodes 2 and 3 (or node 3 and 4) be considered as a "rigid end zone" extension of the column (or rafter).

2.5 Modeling the Base Connection

In the analysis of a metal building, the base plate connection between the column and the foundation may be assumed as rigid (allowing no rotation), pinned (free to rotate without restraint), or, more realistically, partially rigid (somewhere in between). The forces and deflections that develop in the frame can be significantly influenced by the stiffness of the base connection, and hence, it may be of value to include the base connection stiffness in the structural analysis.

For the purpose of strength design the connection is usually assumed as pinned, without any rotational resistance. Considering the connection as pinned will result in a conservative building frame design. For example, moments at the frame knee are maximized with a pinned connection, resulting in a heavier connection detail. Moreover, drifts are also maximized when the restraint offered by the base connection is neglected. The conservatism in strength design might be warranted, but may be unnecessary when computing drift, which is a serviceability issue.

In the following sections the various modeling procedures that are available for base connections are discussed. The information presented is based on a literature review, and on a variety of analytical procedures that have been developed at Virginia Tech. The methods reviewed and developed vary in complexity and accuracy, ranging from fully detailed models involving non-

linear springs to represent concrete and anchor bolts, to a simple model using just one rotational spring at the base of a column.

2.5.1 **Factors affecting the rotational stiffness of connection**

The rotational restraint provided by a column base connection is affected by a large number of factors, including the dimensions and thickness of the base plate; the column size and shape; the anchor bolt diameter, length, and location, the presence or absence of grout; the sign and magnitude of axial force in the column; and the behavior of the concrete-soil interface.

To obtain an understanding of the principal factors affecting the true behavior of the base connection, a series of tests were performed by Hon and Melchers (Hon and Melchers 1988). The main variables in the tests were column size, base plate thickness and bolt size. The tests were conducted on three different column sizes (460 UB, 310 UC, 310 UB), five different base plate thicknesses (12mm, 16mm, 20mm, 25mm and 30 mm) and two different bolt sizes (M20 and M24). The nomenclature of the sections used during testing refers to British standard sections which includes Universal Beams (UB) and Universal Columns (UC).

The assembly used for experiments is shown in Figure 2-4. The stub column was welded to a base plate with nominal weld (6mm fillet weld in all cases), and the base plate was anchored to a concrete foundation with two anchor bolts. A grout layer 20 mm thick was provided between base plate and concrete block. The stub column was loaded using a hydraulic jack through a loading arm so as to provide an eccentricity which would result in a moment acting at the base of column. It was desired to obtain the moment-rotation response of the connection. A load cell was used to measure the load which when multiplied by lever arm produces the moment at the base. In order to measure rotation at the base, two inclinometers were used, one on the web of the column near the base and the other on the concrete block. The relative rotation between two inclinometers gave true rotation which was used to plot moment rotation behavior.

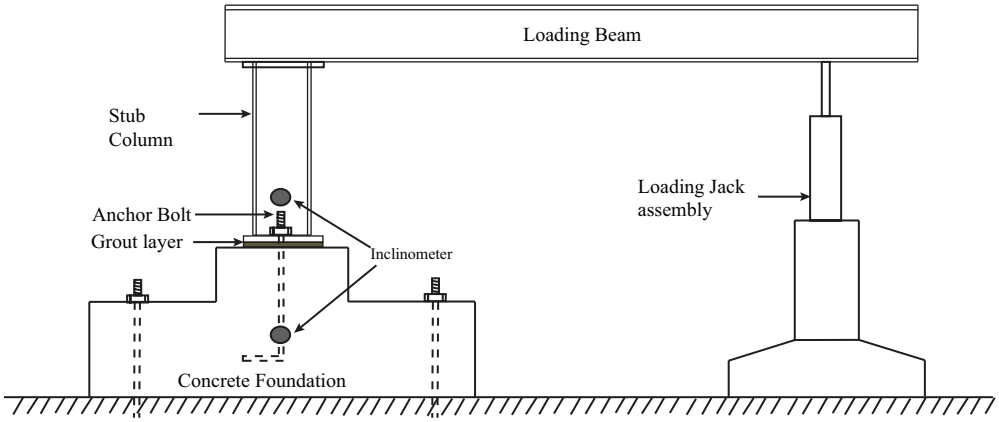

Figure 2-4: Testing apparatus (Hon and Melchers 1988)

From the test results as shown in the Hon and Melchers paper, it was suggested that the thickness of base plate was the most important variable which governed the behavior of the connection. Figure 2-5 shows the difference in resulting moment capacity for two thicknesses of base plates. Also it was noticed that for thin plates, behavior was inclined towards a ductile failure, resulting from bending of the base plate and the formation of yield-line mechanisms. For thicker base plates the behavior was a brittle failure governed primarily by the characteristics of the bolts. The weld between the column and the base plate did not fail in any of the tests. Note that the stiffness of the connection (the initial slope of the curve) is greatly affected by base plate thickness.

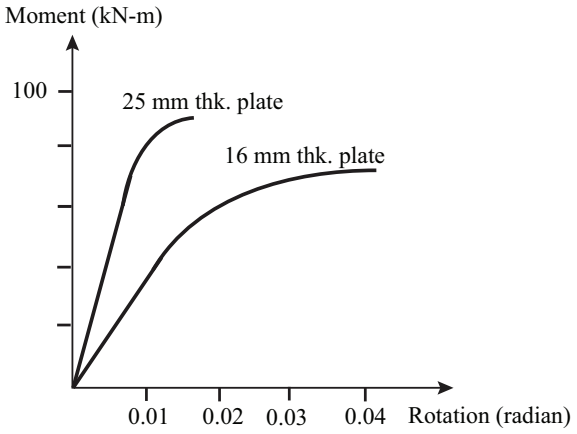

Figure 2-5: Moment-Rotation Response as a function of Base Plate Thickness (Hon and Melchers 1988)

For base plates governed by ductile behavior, base plate plan dimensions had some impact on the moment capacity as larger plan dimensions resulted in slight increase in the moment due to larger lever arm.

Larger bolt sizes caused considerable increase in the stiffness of the connection for the tests which were governed by bolt failure (thicker base plates) and slight increase for the tests which were governed by base plate failure (thinner base plates). Figure 2-6 shows a plot where results have been compared for two different bolt sizes used with the base plates of such thickness that behavior is governed by bolts rather than the base plate. Hence, the stiffness is affected by the size of the anchor bolt and not the base plate.

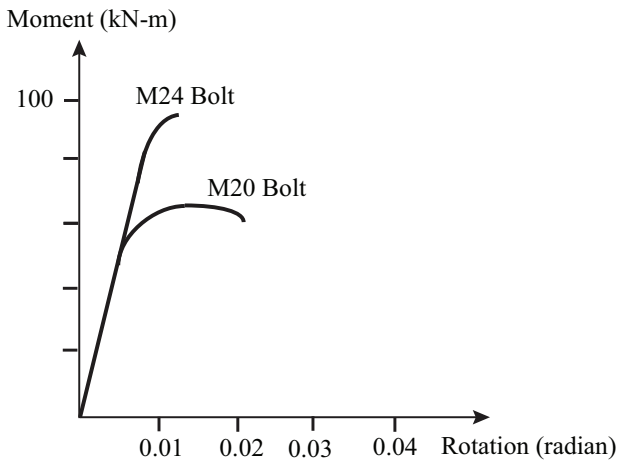

Figure 2-6: Moment Rotation Response as a function of Anchor Bolt Size (Hon and Melchers 1988)

Another variable considered during the tests was the size of the stub column. The column size was varied in two ways; keeping the weight of the column the same and increasing the dimensions, and keeping the dimensions of the column the same and increasing its weight. Increasing the weight of the column resulted in a higher stiffness of the section itself and hence the connection. Keeping the weight the same but increasing the plan dimensions of the section again results in a slight increase in rotational stiffness of the connection due to the larger lever arm resisting the moment. Figure 2-7 shows the comparison of results for a test where the weight of the column is increased.

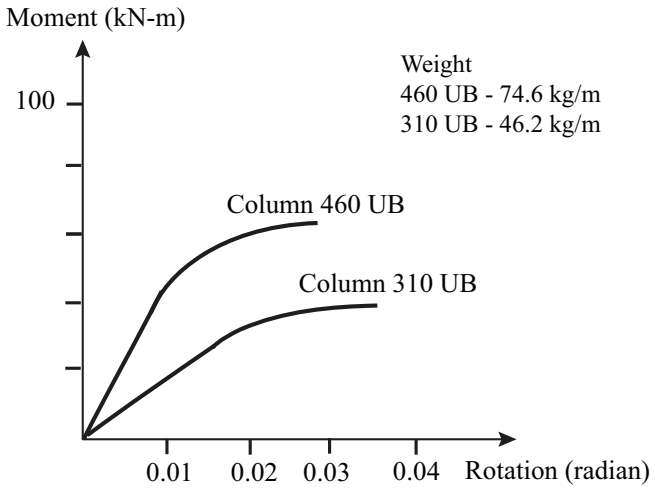

Figure 2-7: Moment-Rotation Response as a Function of Column Size (Hon and Melchers 1988)

Picard and Beaulieu (Picard and Beaulieu 1985) tested base connections for a simple cantilever column. The base plate was attached to the concrete foundation using two or four anchor bolts.

Testing was done on stub columns 1220 mm long. For two out of three tests an I-section was used. A hollow section was used for the third test. The yield strength of steel used was 250 MPa for base plates, 300 MPa for I-sections and 350 MPa for hollow steel sections. The anchor bolts were 19 mm in diameter and 450 mm length. For the first type of connection two bolts were used which were located at mid-depth of the section on either side of web. The second type of connection had four anchor bolts located outside the flanges on both sides of the column. The connection for the HSS section again used four bolts. Each of the connection types are shown in Figure 2-8.

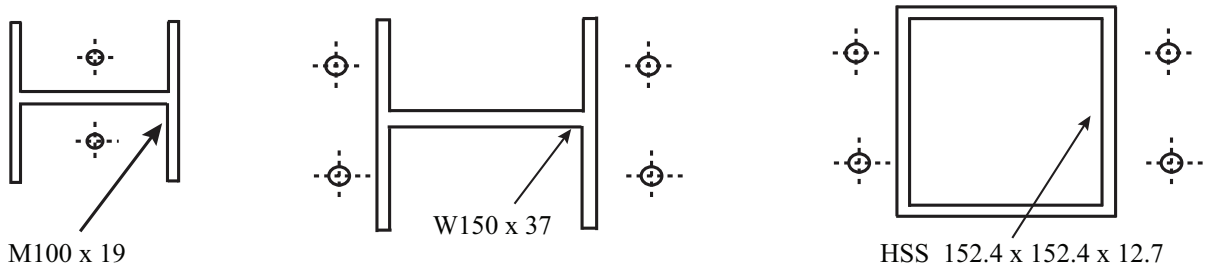

Figure 2-8: Base Plate Dimensions (Picard and Beaulieu 1985)

The concrete footing was 1270 x 610 mm in plan and had a compressive strength of 20 MPa. A 20 mm thick grout layer having a compressive strength of 25 MPa was used between the base plate and the concrete foundation. Figure 2-9 shows the general arrangement of the test specimen.

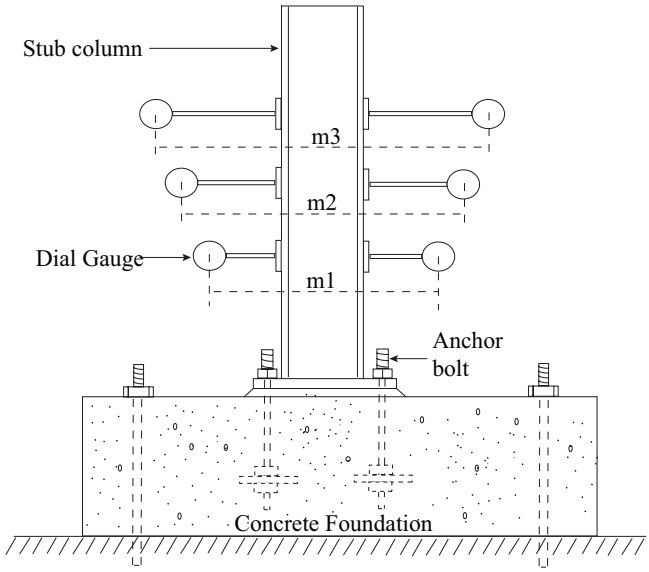

Figure 2-9: Test Specimen (Picard and Beaulieu 1985)

The tests were conducted for two different loading conditions; shear plus moment, and shear plus moment plus axial force. For the first type of loading condition, with shear force and bending moment on the stub column, a hydraulic jack was horizontally placed at the top of the column at distance *L* from the top of the base plate to apply a load *P*. This resulted in a lever arm which would cause a moment acting at the base of the column having a magnitude of *P* x *L* as shown in Figure 2-10.

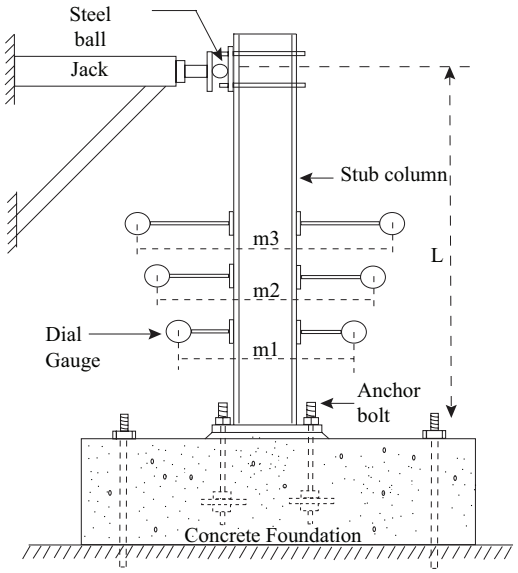

Figure 2-10: Test specimen subjected to shear and bending only (Picard and Beaulieu 1985)

For the second test specimen, where the stub column was subjected to axial force in addition to shear and bending moment, a vertical hydraulic jack at a distance *e* from the center of the column was used to apply vertical load P. This would result in bending moment of magnitude *P* x *e* acting at the base of column as shown in Figure 2-11.

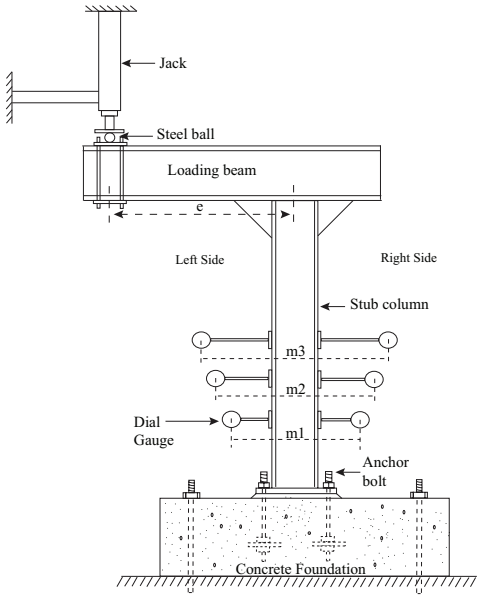

Figure 2-11: Test specimen subjected to shear, bending and axial force (Picard and Beaulieu 1985)

A series of dial gauges were mounted vertically on the steel column with their bases welded to column flanges to measure the rotation of the column. The rotation of the columns was calculated by dividing the absolute vertical distance between two adjacent dial gauges by the horizontal distance between the two as given by the Equation 2-1.

$$\theta = \frac{D_{iL} + D_{iR}}{m_i} \qquad 2\text{-}1$$

where D_{iL} and D_{iR} is the value of rotation at location i for left and right gauges respectively and m_i in the horizontal distance between two dial gauges at location i.

Moment-Rotation plots for I- sections are shown in Figures 2-12 and 2-13 for the two-bolt and four-bolt connections, respectively for both the test conditions where the specimens were subjected to shear plus flexure and compression plus flexure. Load was applied to the specimens in increments till failure point. The failure point was identified to be reached when either anchor bolts on tension side reached breaking load or grout was crushed. The tension side of base plate showed visible lift-off which supported the rotational restraint of the connection. The stiffness of the connection is calculated for the initial portion of the curve where it is assumed to behave elastically. The transition from linear to non-linear response is not very clear for the test involving two-bolted connection, so rotational stiffness as reported by the author has been marked on the plot. The results for HSS section are not presented because typical metal building column sections are primarily tapered I-sections.

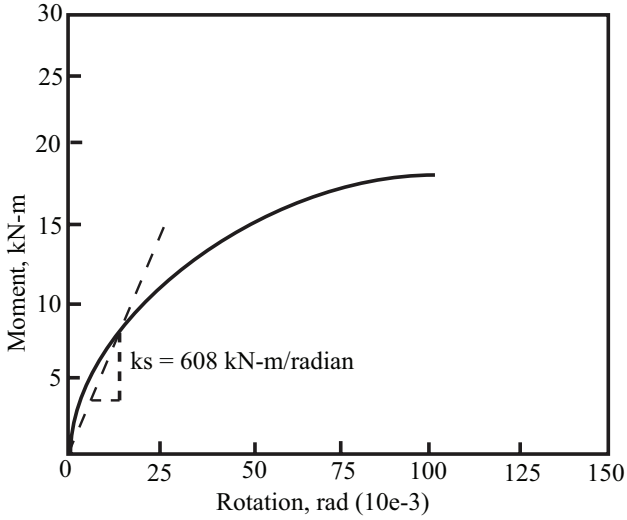

Specimen subjected to shear and flexure

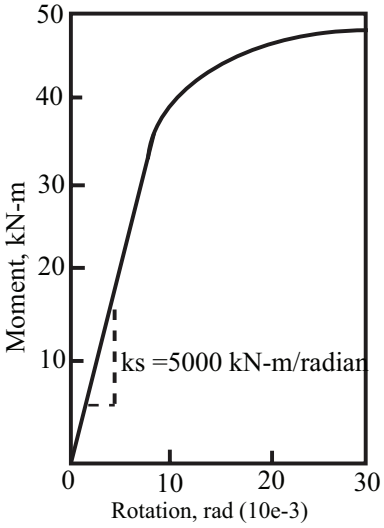

Specimen subjected to compression and flexure

Figure 2-12: Moment - rotation response for two bolted connection (Picard and Beaulieu 1985)

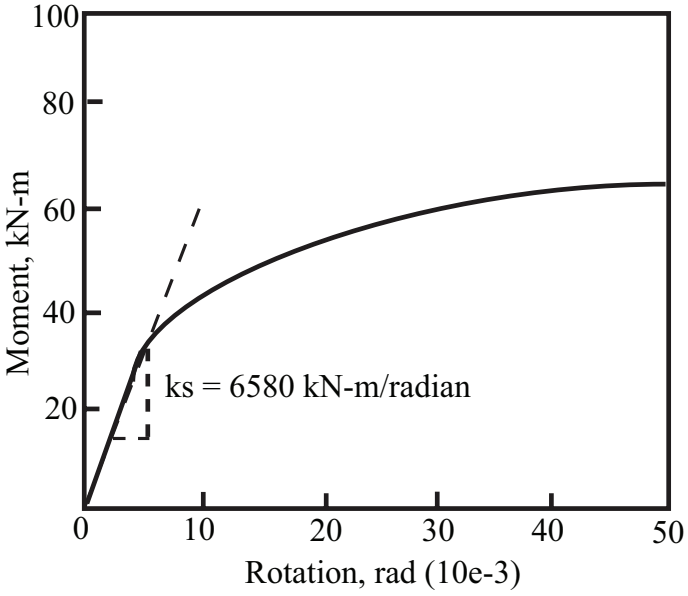

Specimen subjected to shear and flexure

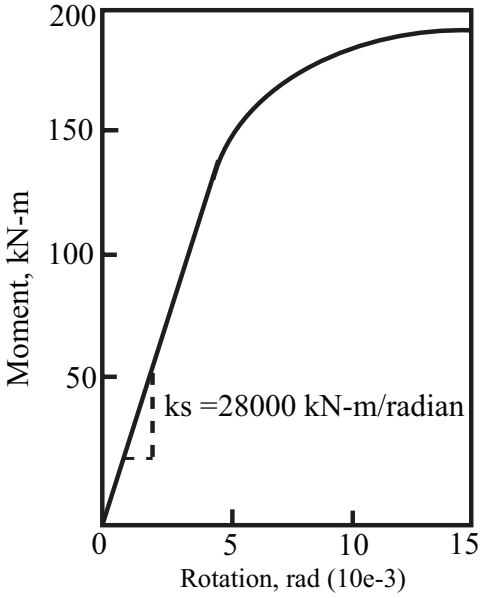

Specimen subjected to compression and flexure

Figure 2-13: Moment-rotation response for four bolted connection (Picard and Beaulieu 1985)

It was observed from test results that the presence of axial load significantly increased the rotational stiffness of the base connection. The two bolted connection specimen with axial load had almost ten times more stiffness than the specimen without axial load. The four bolted connection with axial load exhibited about five times more stiff behavior.

Based on the tests conducted on the column base connections it was substantiated that true behavior of connection is partially rigid. Keeping in view the previous studies and tests, Hamizi et al (Hamizi and Hannachi 2007) developed nonlinear finite element models. The models included nonlinear behavior of materials and the nonlinearity arising at the contact between the concrete and base plate. The models were created for the same arrangement of bolts (two bolts and four bolts) for which tests were conducted (Picard and Beaulieu 1985). The same two sets of loading conditions, one comprised of shear and bending, and the other comprising of shear, bending and axial force were used in the model. More details for the development of the model can be obtained from Hamizi et al (Hamizi and Hannachi 2007). Figure 2-14 shows the finite element model of the column base connection that was used for modeling.

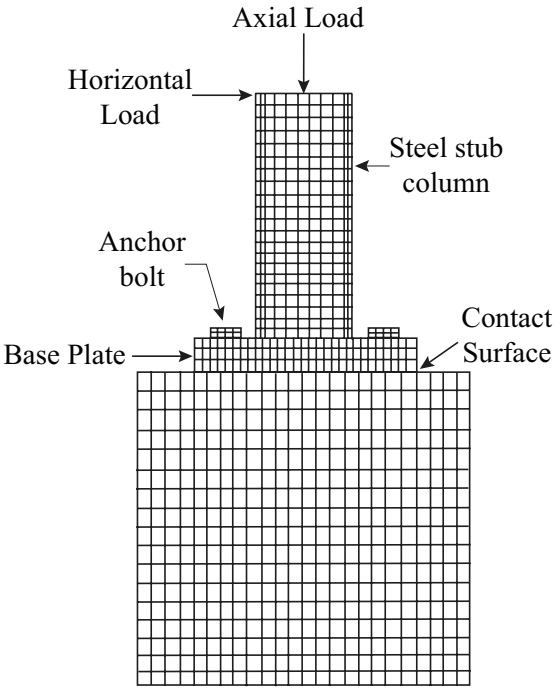

Figure 2-14: Finite element model of connection (Hamizi and Hannachi 2007)

Several assumptions were considered in the finite element analysis. To simplify modeling, anchors bolts were modeled as square cross sections of equivalent area instead of round cross-section. It was assumed that the soil beneath the concrete foundation does not undergo any deformation.

To apply the desired loads, the lateral force was applied at top of the column to induce shear and bending moment at the base of column. Load was applied in increments so that the response could be measured for different load values. For the second loading condition, concentrated load acting in the gravity direction was applied at the top of the column to induce axial force. For various increments of loads, the moment-deformation response was plotted to obtain rotational stiffness of connections having two bolts and four bolts. The results obtained from the finite element analysis are shown in Figures 2-15 and 2-16. The test specimens which were subjected to axial compression in addition to flexure showed considerable increase in moment capacity. This is due to the stability provided by compression which increases the rotational stiffness of the connection against lateral loads. Since the intent of presenting results from the literature review is only to substantiate the rotational stiffness of the connection, limited results are presented; only for the specimens which were subjected to flexure.

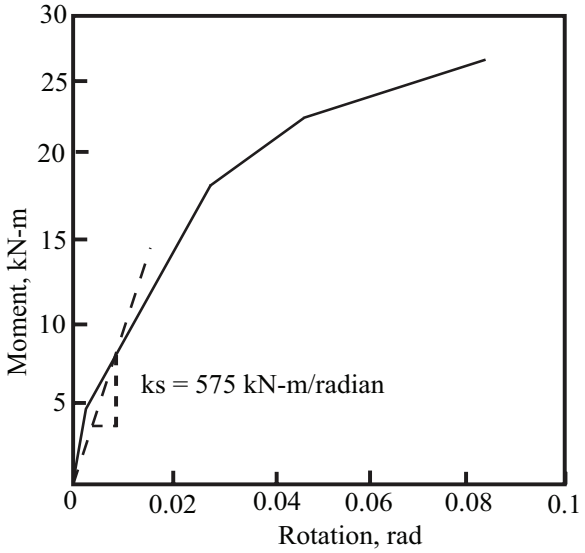

Figure 2-15: Moment-rotation plot for 2 bolted connection (Hamizi and Hannachi 2007)

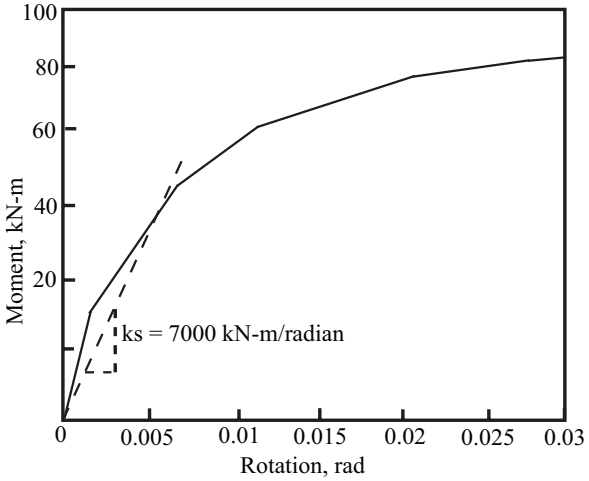

Figure 2-16: Moment rotation plot for four bolted connection (Hamizi and Hannachi 2007)

Table 2-1 presents the correlation of results obtained from testing and finite element analysis. As may be observed, the finite element analysis was able to provide a reasonable estimate of the rotational stiffness of the base connection.

Table 2-1: Correlation Between Experimental and Analytical Connection Stiffness

Connection Type	Stiffness (kN-m/radian)	
	Experiment: Picard et al (Picard and Beaulieu 1985)	Analysis: Hamizi et al (Hamizi and Hannachi 2007)
Two-bolted connection	608	575
Four-bolted connection	6580	7000

Based on the literature review done on experimental testing and finite element modeling for understanding the true behavior of the column to base connection, it can be concluded that even a two bolted column base connection has non-negligible rotational stiffness. Simulation of true behavior can reduce the drifts considerably and result in optimum use of connections.

2.5.2 Suggested Analytical Approaches for Modeling Column-to-Base Connections

Some methods for modeling the column to base connection are provided in the next section. The methods vary in complexity and accuracy, ranging from fully detailed models involving non-linear springs to represent concrete and anchor bolts, to a simple model using just one rotational spring at the base of a column.

2.5.2.1 Detailed Finite Element Model

As lateral load is applied to a metal building, a moment develops at the base of a column. The moment, shown at base of column in Figure 2-17, could result in three possible conditions. First, the moment can cause one flange of the column to go in compression and other into tension (Figure 2-17). Second, in case of total uplift there will be no compression acting on the base plate which might occur due to high lateral load. Third, if there is substantial axial load acting there might not be tension at all. For all these three possible cases tension and compression resisting components remain the same. The base plate resists uplift through tension in the anchor bolts. Compression is transferred through the base plate to grout layer and into the foundation (or directly into the foundation if there is no grout).

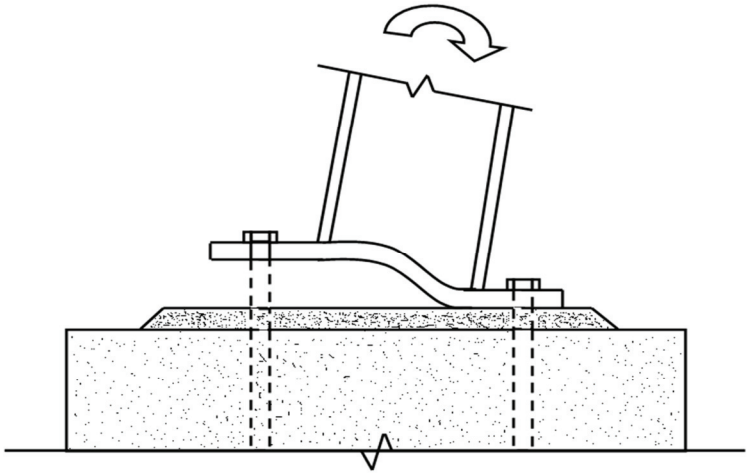

Figure 2-17: Base plate bending

The axial tensile stiffness of the anchor bolts can be simulated with an effective length of bolt anchored into concrete. The effective length depends upon the distribution of stress along the depth of embedment of anchor bolt. A uniformly varying stress distribution along the depth of embedment with no loss of bond is shown Figure 2-18. This stress distribution assumes that the tensile force is uniformly transferred to the concrete along the embedment depth.

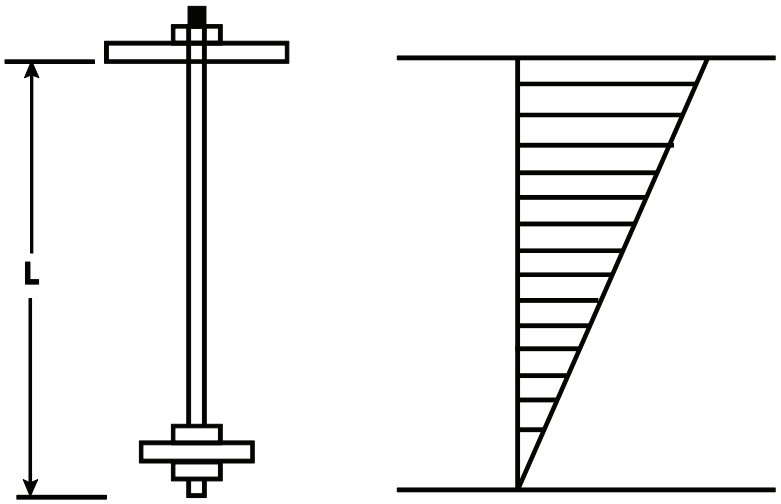

Figure 2-18: Anchor bolt stress distribution

The axial stiffness of an anchor bolt can be calculated given by Equation 2-2:

$$K_{eff} = \frac{A_{Rod} E}{L_{eff}} \qquad 2\text{-}2$$

where, A_{Rod} is the cross-sectional area of the bolt, E is the modulus of elasticity of the bolt and L_{eff} is the effective length of the bolt. With the stress distribution in Figure 2-18, the effective stiffness of bolt is:

$$K_{bolt} = \frac{A_{Rod} E}{L/2} \qquad 2\text{-}3$$

Nonlinear springs are placed at the locations of the anchor bolts and are given the axial tensile stiffness from Equation 2-2 and near-zero compressive stiffness as shown in Figure 2-19.

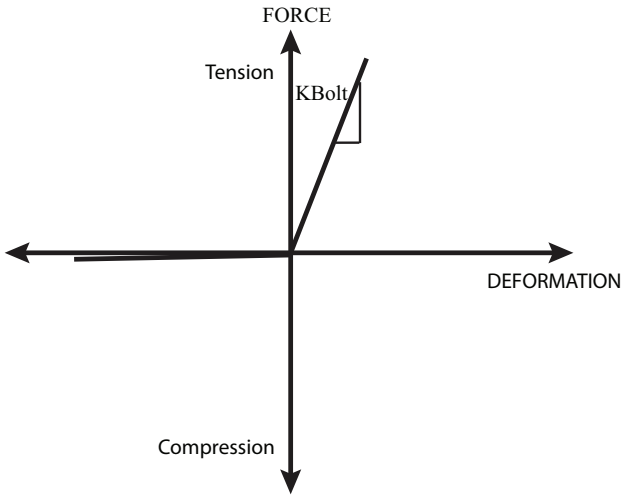

Figure 2-19: Force-Deformation relation for bolt spring

The stiffness on the compression side of a base plate resisted by concrete is simulated by representing the underlying concrete as a series of nonlinear springs which are active for compression only. It is assumed that the grout pad does not undergo any deformation so the springs have near infinite stiffness for compression and near-zero stiffness for tension (Figure 2-20). The size of compression block depends upon the magnitude of load applied.

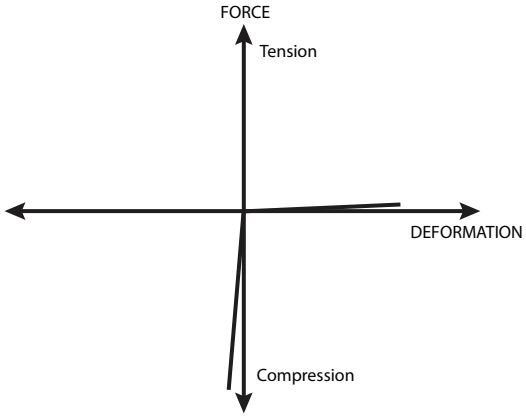

Figure 2-20: Force-Deformation relation for concrete spring

The nonlinear springs described in the previous sections are integrated into a model of a stub column (I-section) attached to a base plate (Figure 2-21). The height of the stub column is 12 in. The base plate is 0.5 in. thick with plan dimensions of 15 in. x 8 in. and bolts are located 3 in. from center of web on each side. The dimensions and material properties of members were selected so as to be consistent with that used in testing by Picard et al. (1985) and analysis by Hamizi et al. (2007).

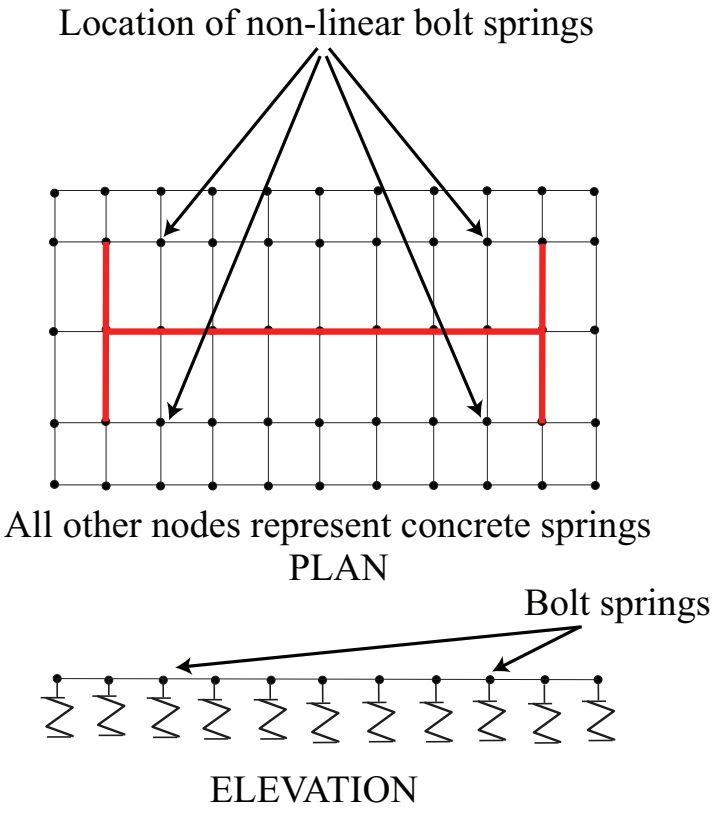

Figure 2-21: Plan and Elevation of base plate and nonlinear springs

The modeling of the column and the connection is performed in SAP 2000 (Computers and Structures (2008). The stub column and base plate have been modeled using shell elements with six degrees of freedom per node. The rendered view of the column and the connection are shown in Figure 2-22. Nonlinear springs are distributed in a grid pattern, as needed, (Figure 2-21) to represent the grout pad and anchor bolts.

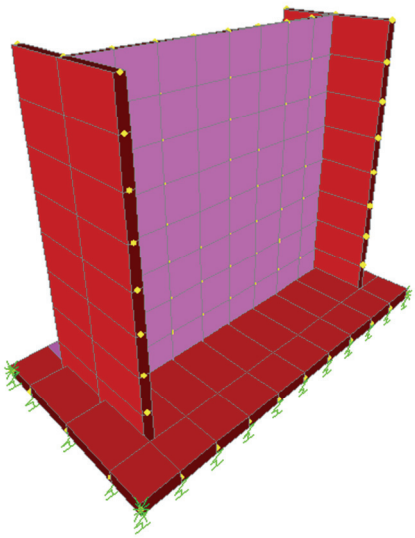

Figure 2-22: Stub column with nonlinear springs representing base connection

For calculating the stiffness of bolts, the diameter and length of bolts has been kept the same as that used by Picard et al. (1985) in their study for testing the base plate connection experimentally. The diameter and length of bolts is 1.0 in. and 13.5 in. respectively. With the stress distribution as shown in Figure 2-18, the effective length of the bolt is reduced to one-half and the stiffness of the bolt works out to be 3350 kip/in. using Equation 2-3. The concrete stiffness is evaluated iteratively, starting with a value of 100 kip/in. and increased until deformations are negligible on the compression side of base plate at 10000 kip/in.

The rotational stiffness from the model is evaluated as the stiffness provided by each bolt at center of base plate shown in Figure 2-23 and given by Equation 2-4.

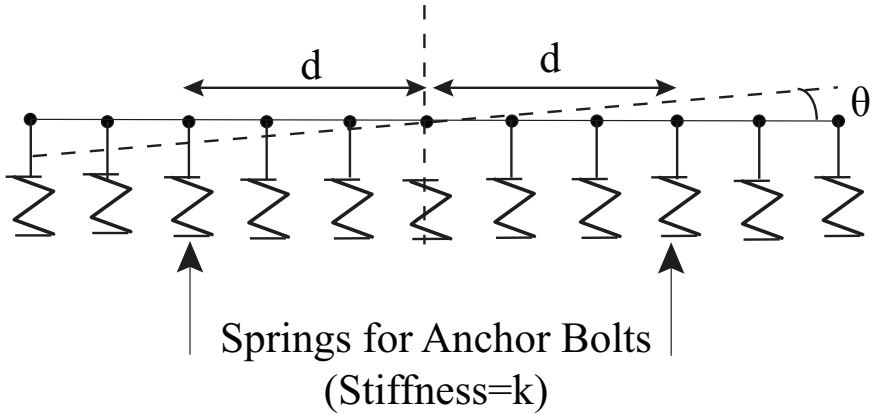

Figure 2-23: Rotational Stiffness Calculation

.

$$K_{\theta spring} = \frac{K(\theta d)d}{\theta} = Kd^2 \qquad 2\text{-}4$$

where,

K=Stiffness of bolt spring in vertical direction.

d=Distance of bolt to center of base plate.

This resulted in rotational stiffness of the connection of 126,000 kip-ft/radian demonstrating that the base plate connection can develop a moment, contrary to the common design assumption of a pinned base.

2.5.2.2 Simplified modeling approaches

Single Rotational Spring

This is the simplest approach where a rotational spring is provided at the base of a column. For this approach to be used it is required to have known the rotational stiffness of the connection beforehand. This stiffness of the connection can be obtained either by experimental testing or detailed finite element modeling as described in work by Hamizi et al (Hamizi and Hannachi 2007). Figure 2-24 represents the details of modeling.

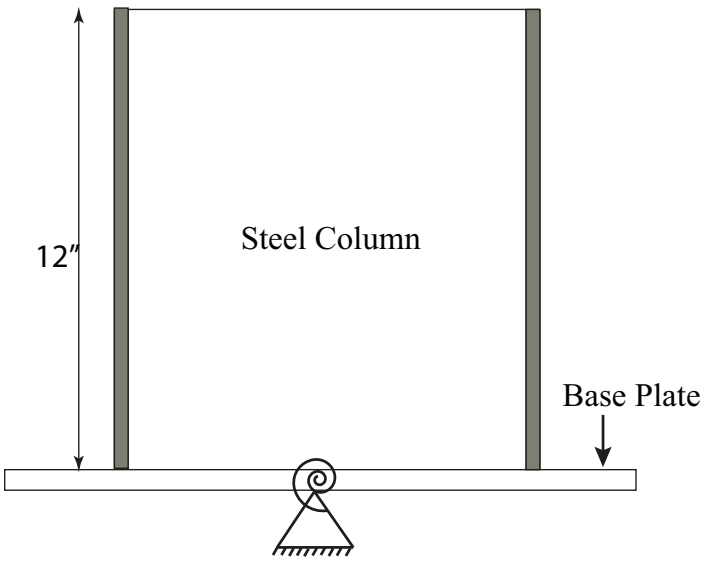

Figure 2-24: Base connection represented by pinned support and rotational spring

This method could not be used in for a loading condition on structure which results in total uplift. In this case the base connection will have no rotational restraint available. However, using a rotational spring will always be providing some restraint no matter what the loading condition is.

Model anchor bolts as vertical springs

Another simple approach is to model the connection by using linear springs at the location of anchor bolts as shown in Figure 2-25. The couple formed by the pair of tensile and compressive forces will provide rotational restraint of the true connection. Similar to the previous case it is required to know the true stiffness of the connection beforehand.

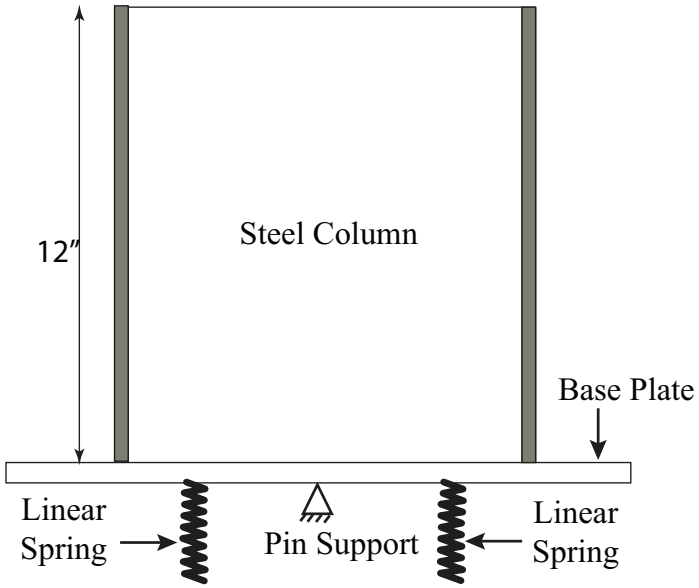

Figure 2-25: Base connection represented by linear vertical springs

Modeling the base connection using this approach is not completely reasonable due to two reasons. Firstly, the base plate deforms rigidly and thereby does not account for the flexibility of base plate. Secondly the compression side of base plate would deform below the slab line which is not true of a real column-base connection. Use of this approach to verify experimentally obtained results have been presented in Section 6.3 and Section 6.4.

Model anchor bolts as vertical springs with a pivot on compression end of base plate

For this method, the connection is modeled in a similar fashion to the previous method. However, one of the shortcomings of the previous method could be overcome by providing a pivot on the compression side of base plate (Figure 2-26). This would prevent the base plate from deforming below the slab line. Since the wind load is not direction dependent and can act from either side, so compression side of base plate is defined. Hence non-linear springs have to be used at location of pivot which only provides restraint against compression. The tension side of base plate would not be affected by the presence of this spring (support) and lift off when subjected to lateral load.

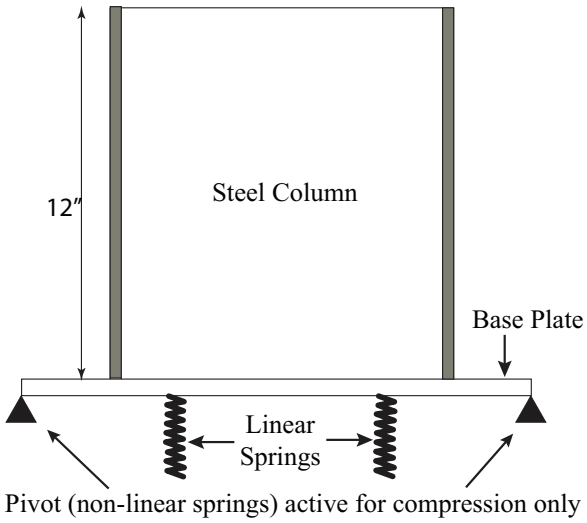

Figure 2-26: Base Connection represented by linear springs (anchor bolts) and pivot (compression end of base plate)

This approach is more realistic when compared to the approach with linear springs and no pivot at the ends (Figure 2-25). However, it still does not take into account flexibility of the base plate.

2.5.3 **Conclusion**

This chapter provides an overview of previous work preformed to evaluate the rotational stiffness of column-base connections in metal buildings. The connection is partially rigid, providing restraint against rotation when subjected to lateral forces. Stiffness of this connection is mainly affected by thickness and plan dimensions of the base plate, length and diameter of anchor bolts and thickness of grout. To incorporate partially rigid behavior of the connection, the detailed finite element method best represents the base condition, which takes into account stiffness of anchor rod and flexibility of base plate and loading condition (direction of loading). Chapter 6 presents further discussion on using these methods.

Chapter 3 Wind Loads

3.1 Introduction

For the design of metal buildings for wind loads, it is traditional practice to use simple two-dimensional planar frame models. The lateral wind load is applied to individual frames on the basis of the tributary area of each frame. This assumption ignores any load distribution among adjacent frames, hence, the roof diaphragm is considered as fully flexible. For metal buildings, the Main Wind Force Resisting System (MWFRS) may consist of interior gable frames, exterior gable frames, or exterior walls. The exterior walls typically consist of cold formed framing members, cladding, and possibly some tension-only X bracing.

ASCE 7-05 (ASCE 2006) provides three methods for the calculation of wind loads to be applied to the MWFRS. Method 1 is a simplified procedure which uses tabulated pressures that depend only on wind speed and roof slope. The applicability of this method is very limited as the building has to meet specific requirements, mentioned in the ASCE 7-05 guidelines (and explained in Section 3.2). Method 2 provides an analytical approach to calculate wind pressures and forces for the design of the MWFRS. This method is further categorized into two approaches, one of which is applicable for buildings of all heights and the other for low rise buildings (height less than 60 ft.). Certain requirements must be met for the building to be designed using the low rise approach (explained in Section 3.3). Method 3 is the Wind Tunnel procedure, which is generally used if the building is of unusual shape or is very flexible. The wind tunnel procedure is inappropriate for most metal buildings, but might be considered for very large or important buildings, such as hangars for airliner maintenance.

3.2 Method 1: Simplified Approach

A building must meet the following requirements to be designed using the method:

a) The building is a simple diaphragm building which as per ASCE is defined as a building in which both windward and leeward wind loads are transmitted by roof and vertically spanning wall assemblies, through continuous floor and roof diaphragms, to the MWFRS.
b) The building is a low rise building (height less than 60 ft).
c) The building is enclosed and conforms to the wind-borne debris provisions of ASCE.
d) The building is regular in shape.
e) The building is not classified as a flexible building. (Slender building and other structures that have a fundamental frequency less than 1 Hz).
f) The building does not have response characteristics making it subject to across wind loading, vortex shedding, instability due to galloping and flutter; and does not have a site

location for which channeling effects or buffeting in the wake of upwind obstructions warrant special consideration.

g) The building has an approximately symmetrical cross-section in each direction with either a flat roof or a gable or hip roof with $\theta \leq 45^{\circ}$.
h) The building is exempted from torsional load cases.

The basic equation for the calculation of wind pressure as per (ASCE 2006) is given by Equation 3-1 (Equation 6-1 of ASCE 7-05).

$$p_s = \lambda K_{zt} I p_{s30} \qquad 3\text{-}1$$

where,

λ Adjustment factor for building height and exposure
K_{zt} Topographic factor evaluated at mean roof height
I Importance factor
p_{s30} Simplified design pressure for Exposure B, height = 30 ft and I=1.0

For the design of MWFRS and components and cladding, design pressures are directly provided in ASCE 7-05, based on the wind speed and slope of roof. The pressure distribution for the design of the MWFRS is shown in Figure 3-1 (Figure 6-2 of ASCE 7-05).

Method 1 can be used without performing extensive calculations. For example, Table 3-1 shows the pressure distribution coefficients for any building with basic wind speed as 90 mph and roof slope of 10˚.

Cases of positive and negative internal pressure are considered automatically in the procedure. These pressure coefficients provided in Table 6-2 of ASCE 7-05 are for a building in exposure category B, at a height of 30 ft, and importance factor of 1. Coefficients for a building with different conditions can be obtained by using appropriate modification factors in ASCE 7 Eqn. 6-2. The method is easy to use, but is conservative when compared to Method 2.

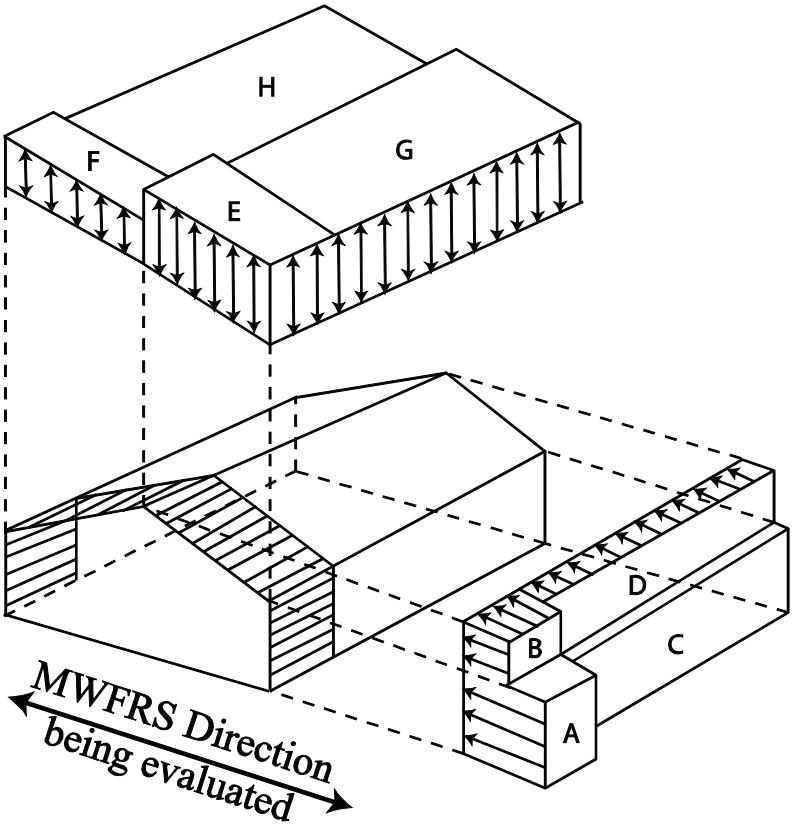

Figure 3-1: Wind Pressure Distribution

Table 3-1: Pressure Distribution Coefficients

Basic Wind Speed (mph)	Roof Angle (Degrees)	Load Case	Zones							
			Horizontal Pressures				Vertical Pressures			
			A	B	C	D	E	F	G	H
90	10	1	14.5	-6.0	9.6	-3.5	-15.4	-9.4	-10.7	-7.2

3.3 Method 2: Analytical Approach

The analytical method provides the wind pressures for the design of Main Wind Force Resisting System (MWFRS) and for components. This method requires a structure to be designed for winds coming from all directions. According to ASCE 7-05 the main points of this method are:

a) The procedure involves the determination of wind directionality and velocity pressure
b) It allows for determination or selection of an appropriate gust effect factor and selection of appropriate pressure or force coefficients.

c) The method considers the size and geometry of the building or structure to be designed and allows for modification that may need to be incorporated because of topographic features such as hills and escarpments.

Eight wind directions at an interval of 45˚ are considered. Four of these wind directions are along the primary axis of the building, as shown in Figure 3-2. For wind acting along a particular direction, the upwind exposure is determined for each of two sectors on either side of the direction. Wind load is evaluated on the basis of the sector which produces the larger exposure factor.

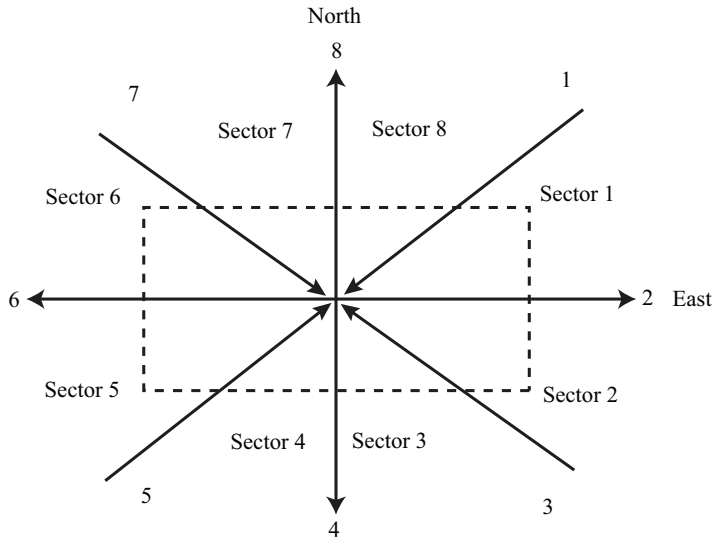

Figure 3-2: Determination of wind load from different directions

The analytical method has been further categorized into two approaches, as follows:

i. Buildings of all heights
ii. Low-rise buildings having a height less than or equal to 60 ft.

These approaches are briefly described below.

3.3.1 **Analytical Approach, Buildings of all Heights**

For buildings and structures of all heights, design wind pressures are based on ASCE 7-05 Eqn. 6-15. The approach mentioned above has been followed where wind loading on each surface of building is considered as a function of wind direction, i.e. wind acting parallel and perpendicular to the ridge line. The resulting pressure distribution is as shown in Figure 3-3.

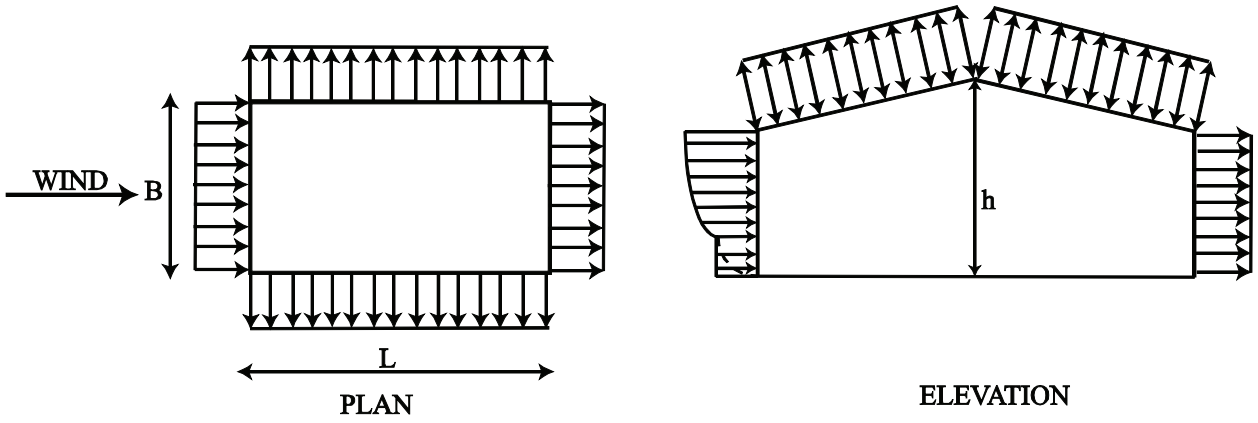

Figure 3-3: Wind pressure distribution as per ASCE 7-05 Method 2 (ASCE 2006)

The velocity pressure coefficient is evaluated using Equation 3-2(ASCE 7-05 Eqn. 6-15).

$$q_z = 0.00256 K_z K_{zt} K_d V^2 I \ (\text{lb/ft}^2) \qquad 3\text{-}2$$

where,

K_d = Wind directionality factor

K_z = Velocity pressure exposure coefficient

K_{zt} = Topographic factor

V = Basic wind velocity

I = Importance factor

q_h = velocity pressure coefficient evaluated at mean roof height h

Pressure distribution acting on the surface of building as shown in Figure 3-3 for designing MWFRSs is evaluated using Equation 3-3 (ASCE 7-05 Eqn. 6-17).

$$p = qGC_p - q_i(GC_{pi}) \ (\text{lb/ft}^2) \qquad 3\text{-}3$$

where,

q = q_z for windward walls evaluated at height z above ground

q = q_h for leeward walls, side walls and roofs, evaluated at height h above ground

q_i = q_h for windward walls, leeward walls, side walls and roofs, evaluated at height h above the ground

G = Gust effect factor

C_p = External pressure coefficient

GC_{pi} = Internal pressure coefficient

I = Importance factor

Calculation of wind pressure using this method for the test building has been provided in Appendix A.

3.3.2 **Method 2: Low-rise buildings having a height less than or equal to 60 ft**

"Pseudo" loading conditions are developed in this method which are independent of direction of wind. The loading conditions so developed should result in maximum structural actions. The primary structural actions of interest are

i. Total uplift
ii. Total horizontal shear
iii. Bending moment at knees (two-hinged frame)
iv. Bending moment at ridge (two-hinged frame)

The "pseudo" loading pressure coefficients are generated such as to obtain an envelope of forces induced. However, a loading which might produce maximum uplift may not result in maximum bending moment at same time. Hence the coefficients provided in ASCE 7-05 (ASCE 2006) are a result of fictitious loading condition which conservatively envelops the maximum of structural actions.

A structure shall be loaded with wind from all the directions by considering each corner of building as shown in Figure 3-4.

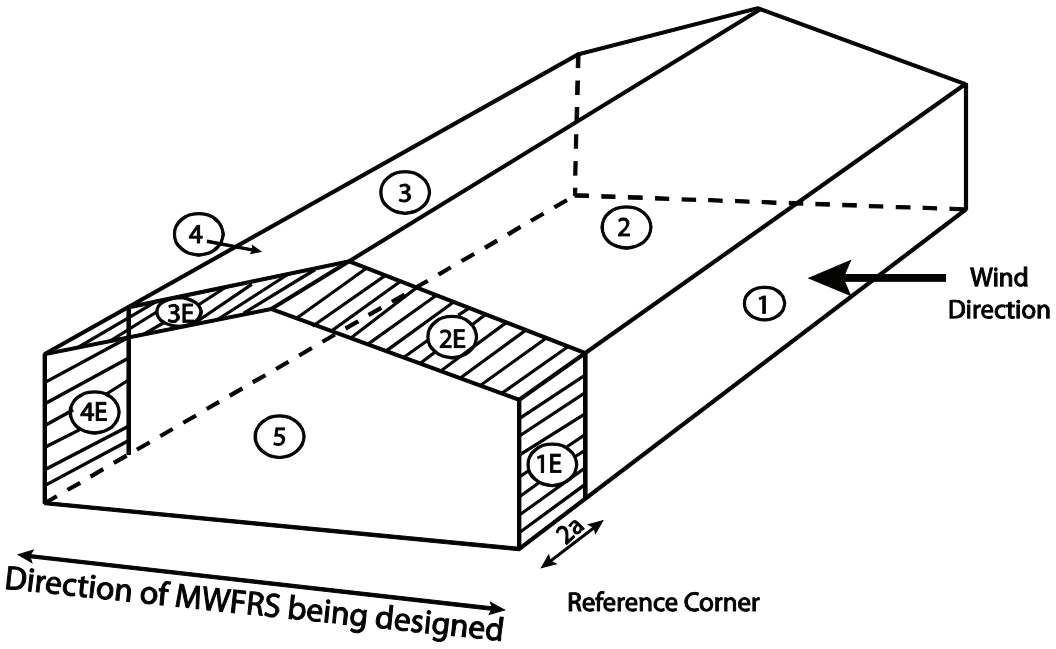

Figure 3-4: Pressure Distribution (ASCE 2006)

The velocity pressure coefficient is calculated using Equation 3-2. The design wind pressure acting on the surface of the MWFRSs of the low rise building is evaluated using Equation 3-4 (ASCE 7-05 Eqn. 6-18)

$$p = q_h[(GC_p) - (GC_{pi})] \text{ (lb/ft}^2\text{)} \qquad 3\text{-}4$$

where,
q_h = velocity pressure at mean roof height
GC_{pf} = external pressure coefficient
GC_{pi} = internal pressure coefficient

Calculation of wind pressure using this method for the test building has been provided in Appendix A.

3.4 Wind Tunnel Method

Wind tunnel testing is used where the intent is to determine the loads more accurately and reduce conservatism which comes into design of Methods I and II are used. Also for buildings and other structures for which Method I and II are not applicable, Wind tunnel testing is required. As per ASCE 7-05 (ASCE 2006) it is recommended to use the wind tunnel testing procedure when the structure satisfies one or more of the following conditions.

1. Building has a shape which differs significantly from a uniform rectangular prism or "box-like" shape.
2. Is flexible with natural frequencies below 1 Hz.
3. Is subjected to buffeting by the wake of upwind buildings or other structures.
4. Is subject to accelerated flow caused by channeling or local topographic features.
5. Curtain wall pressures resulting from irregular geometry.
6. Across wind and/or torsional loads.
7. Periodic loads caused by vortex shedding.
8. Load resulting from instabilities, such as flutter or galloping.

3.5 Wind pressures to be used for Wind Drift Serviceability Analysis and Design

The wind forces developed above are intended for use with the design level wind forces, which are based on a 50 year mean recurrence interval. As mentioned in Chapter 1, it is becoming more common to base serviceability analysis on a 10 year mean recurrence interval. Table C6-7 in ASCE 7-05 provides conversion factors for reducing the 50 year wind speed to the 10 year wind speed. These factors for *wind velocity* conversion are:

0.84 for wind velocities between 85 and 100 mph (non-hurricane regions)
0.74 for hurricane regions
0.87 for Alaska

Wind pressures are based on the wind speed squared. Thus the conversion factors for the 50 year to 10 year *wind pressure* are:

0.71 for wind velocities between 85 and 100 mph (non-hurricane regions)
0.55 for hurricane regions
0.76 for Alaska

These reductions are substantial, particularly for hurricane regions. However, AISC Design Guide 3 allows low-rise buildings to be designed for reduced pressures. Hence, further research was not done on the matter as it was beyond the scope of project.

3.6 Recent Developments: Database Assisted Design vs ASCE 7-05 Based Design

For design of low-rise buildings, wind pressures are generally calculated using the analytical method applicable for low rise buildings in ASCE 7-05. For such designs, wind tunnel tests are rarely used. The techniques used to calculate wind pressures are predominantly based on interpolation or extrapolation of wind pressure coefficients previously derived from wind tunnel experiments performed on full-scale buildings. These tests were conducted at University of Western Ontario (UWO) in the late 1970s. The tests were performed on a single building for nine different configurations, consisting of three roof slopes with three eave heights.

With limited instrumentation and data storage capabilities at that time, use of pressure coefficients developed for a particular building to design low-rise buildings of any plan dimensions could be justified. However, with advances in structural analysis, the concept of database-assisted design (DAD) provides an alternative for wind design of low-rise buildings.

In recent research it has been determined that wind pressures obtained by using ASCE 7-05 are underestimated when compared with pressures obtained using database-assisted design. Bradley et al. (2010) studied buildings with different plan dimensions and roof slope. The objective was to compare wind pressures and resulting bending moments in a steel portal frame (industrial building) at three locations, namely ridge, knee and rafter-rafter junction. In this study the ASCE generated wind pressures were obtained using analytical procedure for low rise buildings (Section 6.5 of ASCE 2005). The database-assisted wind pressures were calculated using wind-

PRESSURE software (Main 2006b). It was concluded that resulting bending moments from two different methods of analysis were always same and the difference in magnitude varied with building dimensions. Larger differences were found in buildings with higher eave heights and a steep roof slope. In some cases differences were as high as 60 percent for bending moments at the knee location.

The differences have been primarily related to the way pressure coefficients were determined in wind tunnel tests conducted at UWO. For evaluation of coefficients, eight directions of loading were considered at an increment of 45°. Due to the high complexity and uncertainty in wind direction, this could introduce large approximations. Moreover, as mentioned before in this section, these coefficients were developed for structural systems with specific building dimensions and structural properties. The current standard, however, allows the use of these coefficients for low-rise buildings of any dimensions.

3.7 Conclusion

It is not justifiable to conduct wind tunnel tests for each and every low-rise building, both practically and economically. The results obtained while comparing wind pressures (bending moment) show that ASCE 7-05 underestimates wind pressures. Hence, use of database-assisted design for design of such buildings could provide more realistic wind pressures. At the same time it was observed that greater differences were found for buildings with steeper slopes. The buildings with mild slopes yielded results close (if not same) to that obtained from database-assisted design. To conclude, the comparisons have been done on very limited testing but highlight an important aspect which needs to be explored more.

Chapter 4 Description of Test Building

4.1 Introduction

A metal building structure in Christiansburg, Virginia was selected for testing. This building, referred to as the "Test Building" herein, is owned by Blue Ridge Timber Wrights, a manufacturer of custom-made wood timber trusses. The building, shown in Figure 4-1, is of relatively new construction as it was erected in year 2007. The building is rectangular in plan with no major mezzanines or attached structures. The building floor plan is 150 ft. by 80 ft (Figure 4-2). The building is 18 ft. high at the eave and has a 1:12 roof slope. The roof and wall cladding consists of metal roofing which is attached to the main structure with metal screws. The building is used primarily as a storage warehouse, with no machines or overhead crane systems. There is a small office area in one corner of the building. This office area has a flat interior roof at the eave elevation. The building has two major vehicular access openings, each of width 14 ft.

The main wind load resisting system for loads parallel to the 80 ft. dimension consists of five gable frames and two end frames. The gable frames are constructed from web-tapered steel I sections. The end frames are cold-formed post and beam construction with screwed on metal wall sheeting.

The wind resisting system for loads parallel to the 150 ft. dimension consists of cold form studs and screwed-on metal sheeting. There is no X-Bracing in the structure.

4.2 Design Basis

The test building was designed in accordance with the 2000 International Building Code (International Building Code (2000)). For lateral design of the building both wind and seismic effects were considered. The building was treated as an enclosed structure with wind exposure category B. Wind speed in this region is 90 mph and loads shown on the design documents are consistent with the ASCE 7-05 analytical method (Method 2) applicable for low rise structures. For seismic design the structure has been categorized in design category C with importance factor 1.0. The value of mapped structural response S_S and S_1 are 0.38g and 0.11g respectively. For frames type along line 3, 4 and 5 the maximum horizontal deflection is reported as 1.248 in. for the load combination 1.0 D.L. + 1.0 W.L.. For the frame along line 2 and 6, drift has been reported as 1.03 in. for same load combination. As shown in Section 6.3 of this thesis, these deflections are considerably greater than those computed from analytical models developed for this research.

Figure 4-1: Photograph of Exterior of Test Building

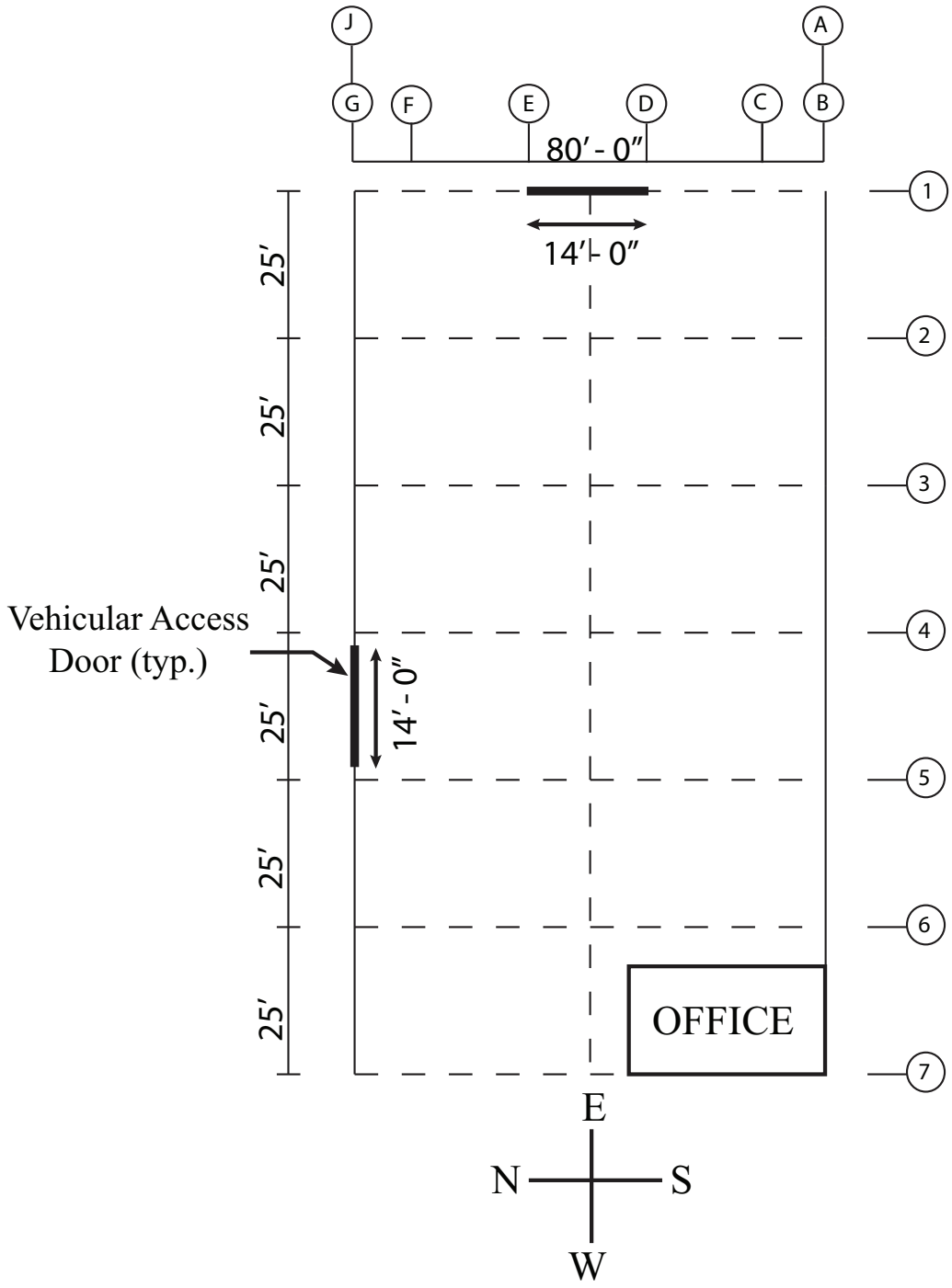

Figure 4-2: Plan of building

4.3 Building Description

4.3.1 Openings in Building

The building has two vehicle access doors as marked in Figure 4-2. The doors are 14 ft wide and 14 ft in height. One of the access doors was located centrally along line 1 and served as the primary entrance to the building. The other door was on grid line J and located centrally between line 4 and 5. Aside from two small personnel access doors (approximately 2.5 ft in width and 7.0 ft in height) there were no other major openings in the structure. Hence, while evaluating the wind loads on building it was considered as an enclosed structure.

4.3.2 Purlin, Girt, Building covering and Connection details

The building is covered with screw-fastened metal roof cladding on the four walls and roof. Figure 4-3 show cross-sectional details of the roof and wall sheeting. The sheeting used was 26 gage and the typical coverage of a panel is 36 in.

Figure 4-4 shows cross-sectional details used for cold formed steel used in building used for end-wall, girts and purlins. The purlins and girts were 8-1/2 in. deep Z-sections. Other cross-sections in the figure were used primarily in the end wall. The details of connection between cladding and purlin are shown in Figure 4-5, which also shows the fastener pattern. Two different screw sizes, 14 x 1 ¼ in. as structural fastener and 14 x 7/8 in. as stitch fasteners were used.

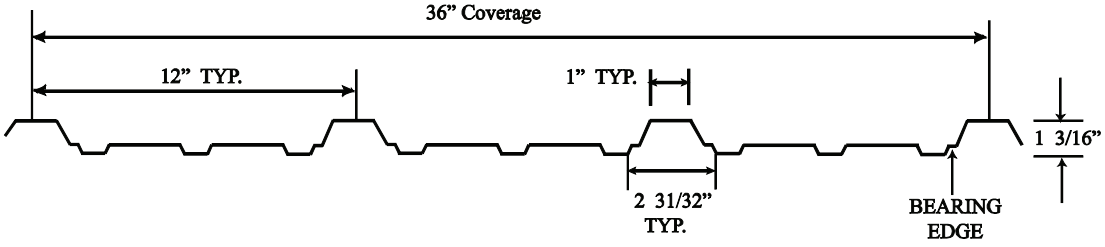

Figure 4-3: Roof and Wall Panel

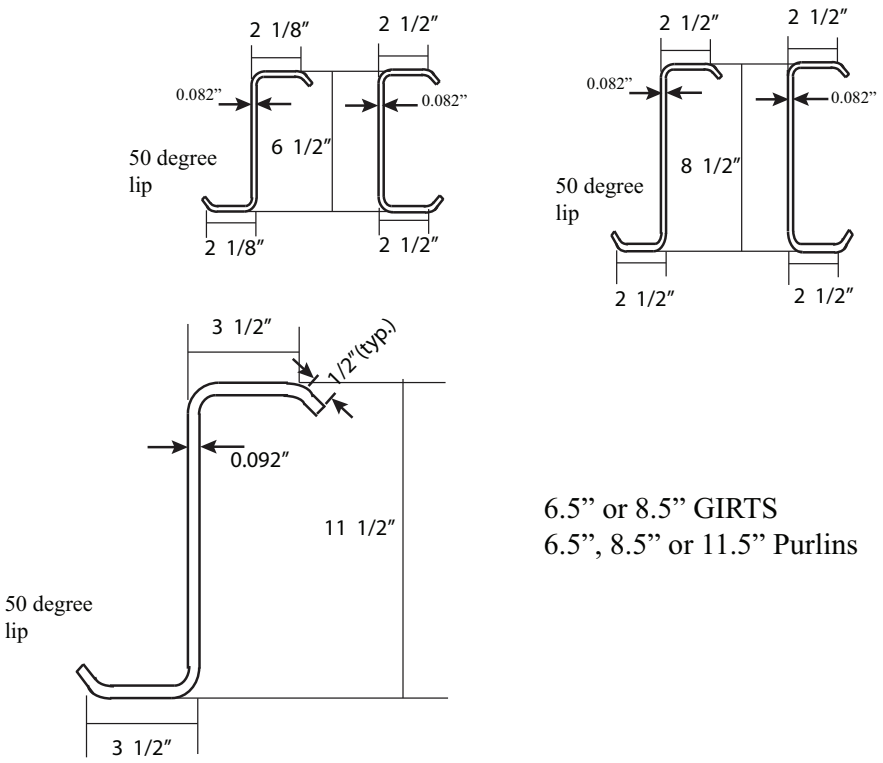

Figure 4-4: Purlin and Girt Cross-sections

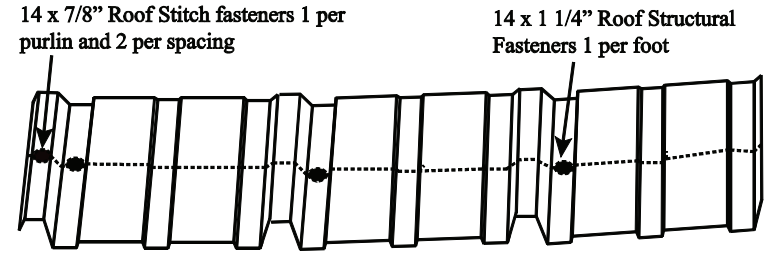

INTERMEDIATE PURLIN FASTENER PATTERN

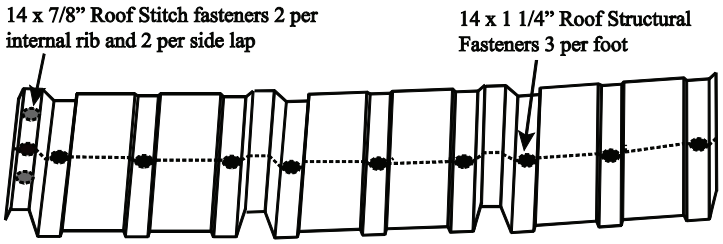

ENDLAP AND RIDGE CAP

Figure 4-5: Fastener Pattern

4.3.3 **Gable Frame Dimensions and Properties**

In this thesis the frames located on grid lines 2 and 6 are referred to as "Exterior" frames, and the frames on lines 3, 4, and 5 are referred to as "Interior" frames.

Dimensions and details for the Exterior Frames are shown in Figures 4-6 through 4-9, and dimensions and details for the Interior Frames are given in Figures 4-10 and 4-13. Note that the depth of the sections at the haunch is greater for the Interior frames (depth = 42 in.) than it is for the Exterior frames (depth = 38 in.). However, the depth at midspan of the Interior frames (depth = 14 in.) is significantly less than that of the Exterior frames (depth = 23 in.). Additionally, the panel zone of the Exterior frames has a diagonal stiffener, whereas the panel zone of the Interior frames does not.

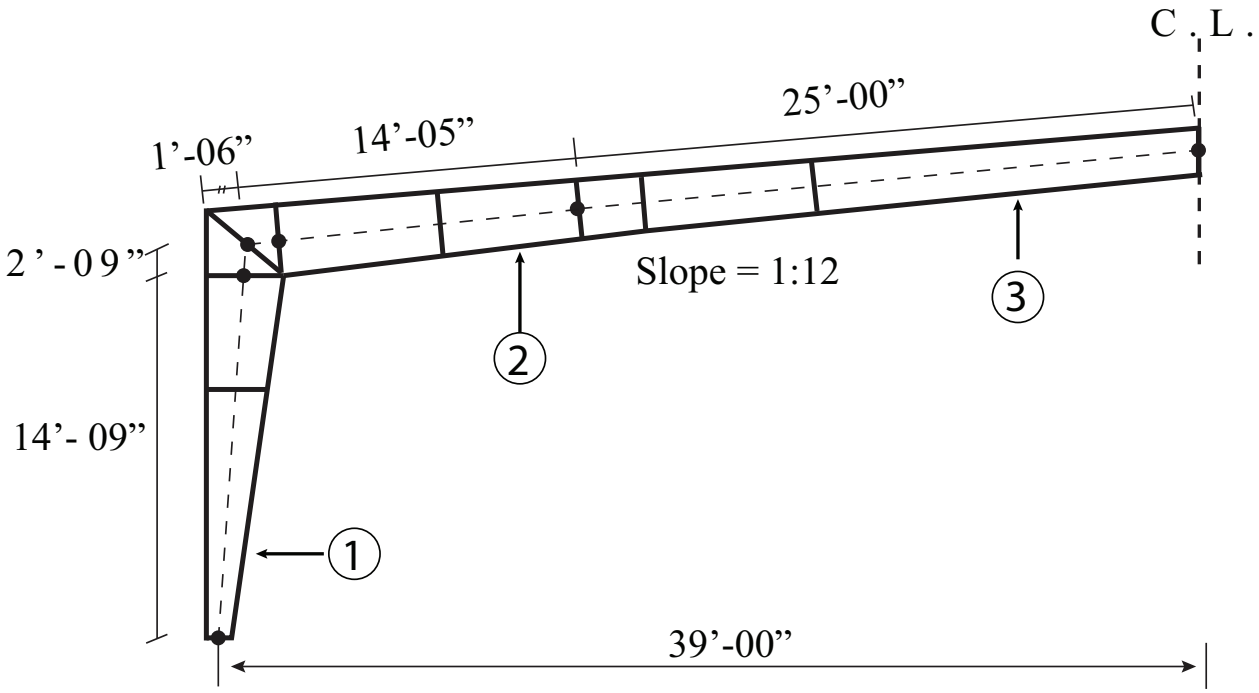

Figure 4-6: Frame along line 2 and 6

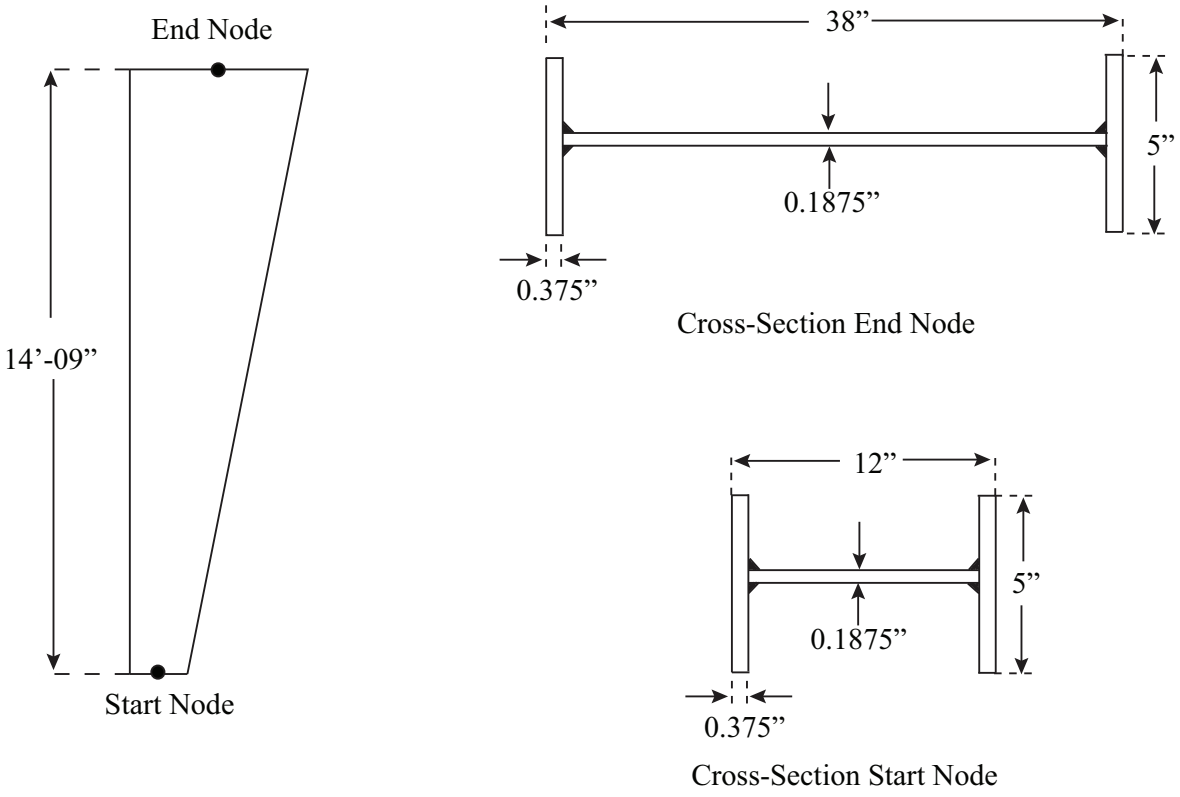

Figure 4-7: Column (Section 1) details

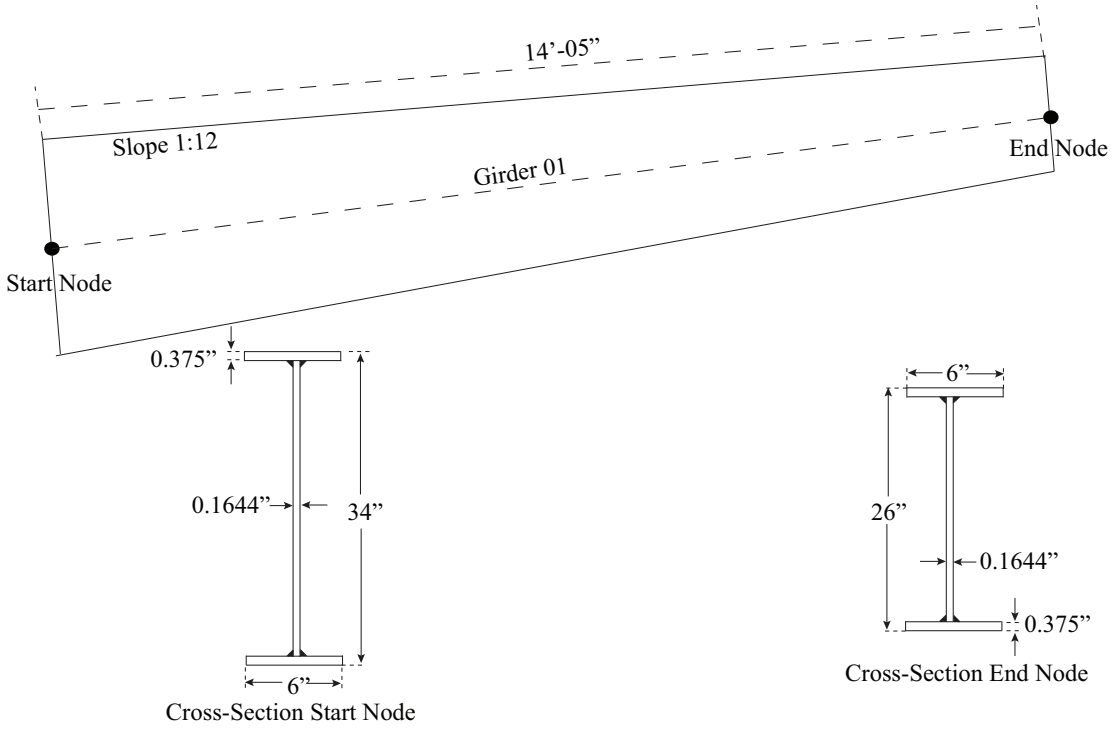

Figure 4-8: Girder 2 details

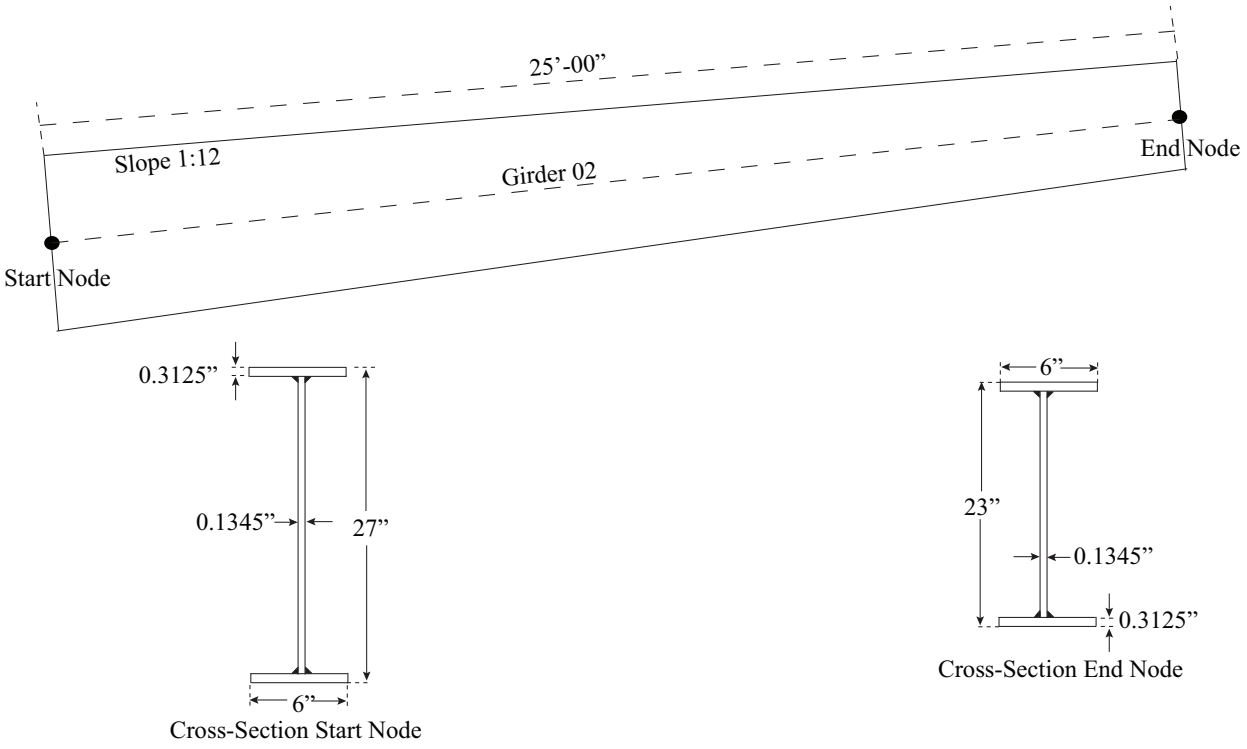

Figure 4-9: Girder 2 details

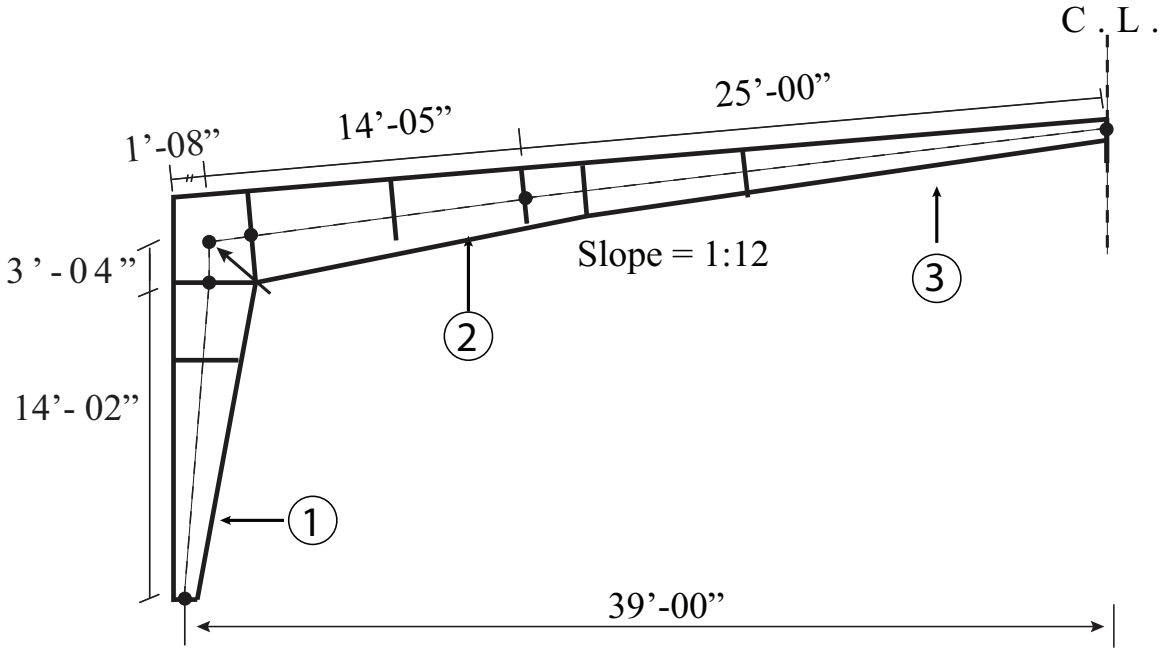

Figure 4-10: Frame along line 3, 4 and 5

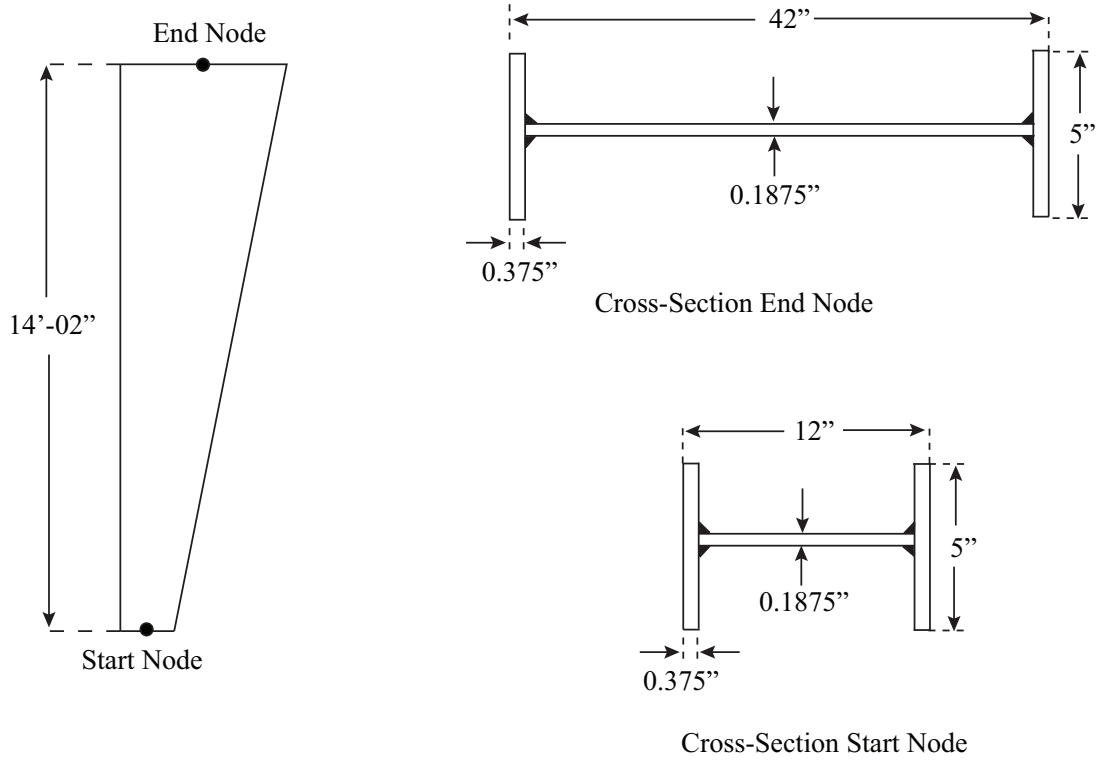

Figure 4-11: Column details along line 3,4 and 5

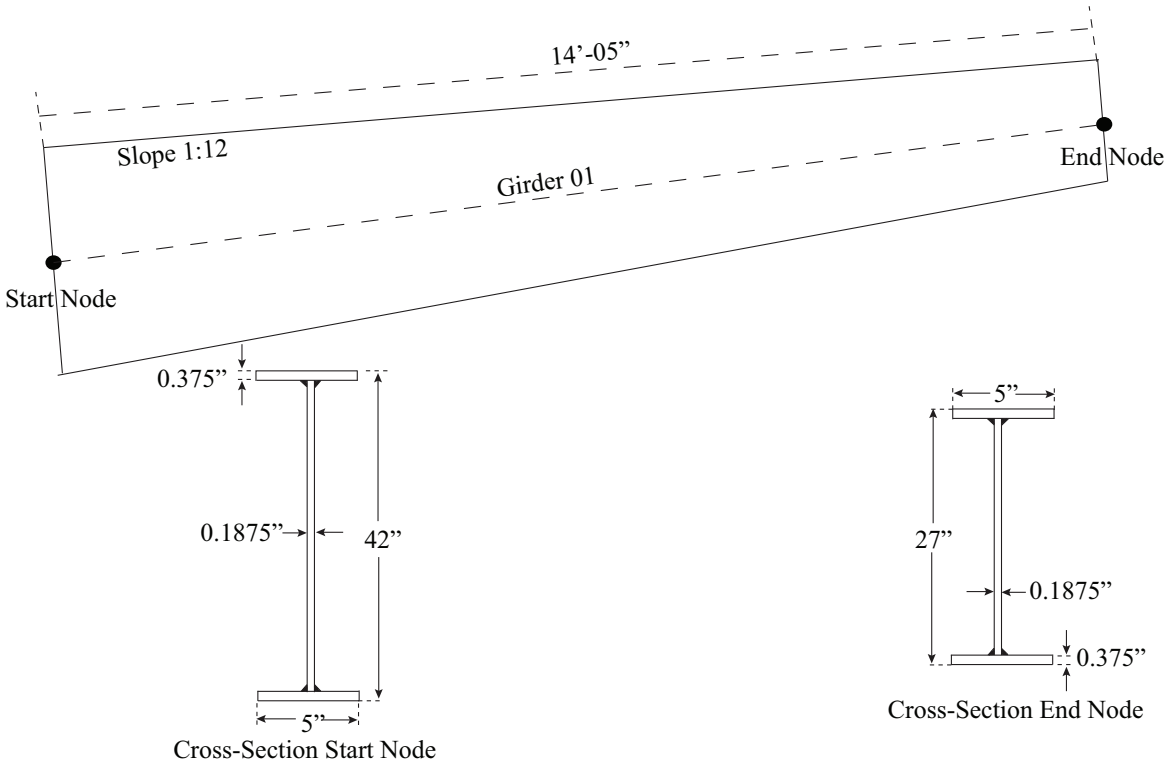

Figure 4-12: Girder 1 details along line 3, 4 and 5

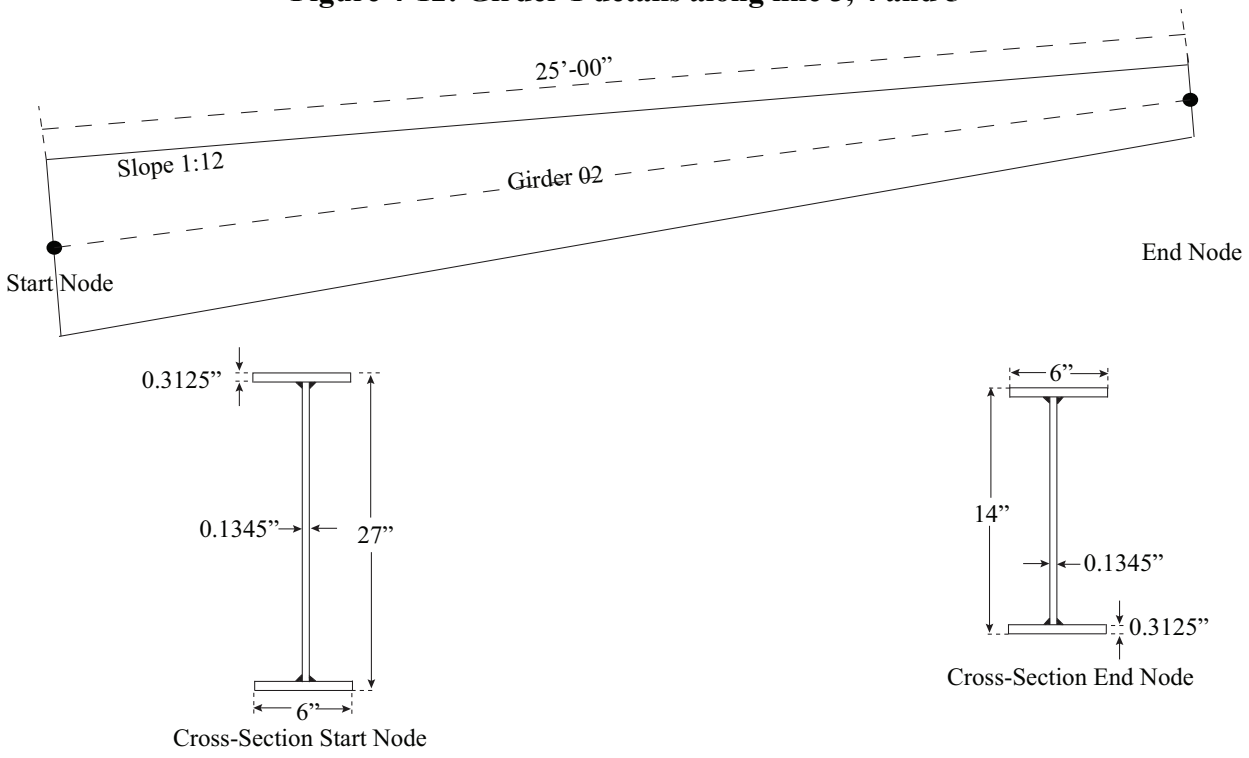

Figure 4-13: Girder 2 details along line 3, 4 and 5

4.3.4 **Column to Slab Connection Details**

The connection of the base of the column to the slab is shown in Figure 4-14. The same detail was used for the Exterior and Interior columns. There is no grout between the base plate and the floor slab. The entire perimeter of the column appears to be fillet welded to the base plate, but the size of the weld is not shown on the drawings. Figure 4-15 shows a photograph of column-base connection.

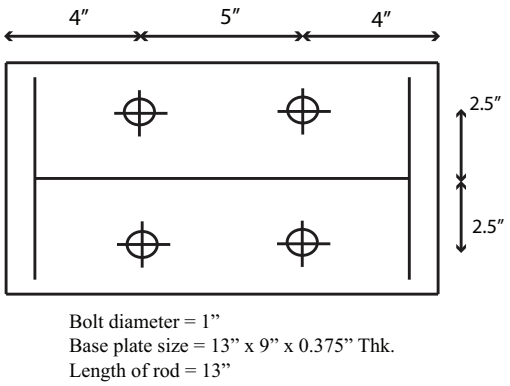

Figure 4-14: Base Plate Details

Figure 4-15: Photograph of typical Column Base Connection

4.3.5 **Foundation Details**

Foundation details were not available in the calculation package as it was designed by a third party.

Chapter 5 Gravity Dead Loads and Wind Loads on Test Building

5.1 Introduction

Dead loads and wind loads on the Test Building are discussed in this Chapter. Dead loads are based on the self weight of the structure, and do not include mechanical, electrical, or insulation (assumed negligible). The loads have been calculated based on two-dimensional frame models.

Wind loads were calculated as per ASCE 7-05 using Method 2. Calculations were performed considering both the approaches listed in the analytical method, i.e. using the general approach applicable for all height structures and the approach applicable for low rise structures. This section provides a summary of the wind load calculation for the test building. The detailed calculations are provided in Appendix A.

5.2 Gravity Dead Loads

Gravity Dead Load considered in the analysis mainly consisted of three components, frame self weight; weight of purlins and girts; weight of sheeting and cladding.

a. Weight of purlins and girts – The weight of a purlin and girt was applied as a concentrated load on the frame being considered for analysis. The magnitude of load was calculated with tributary length equal to half of distance to adjacent frame (12.5 ft. x 2) on each side of frame. The total load comes out as approximately 73 lb for each purlin (Cross-sectional area of purlin times tributary length times unit weight of steel). Figure 5-1 shows the application of load on a typical frame in SAP model.

b. Weight of cladding and sheeting – These were made from cold formed steel with 26 gage as thickness. The load of cladding and roof sheeting was applied as uniformly distributed load along the length of column and rafter respectively. The area load of 26 gage material is 0.75 lb/ft^2 was converted into line load by multiplying it with tributary with corresponding to each frame (half of distance to adjacent frame on each side, 25 ft). This number comes out to be 18.75 lb/ft. Figure 5-2 shows the application of the load.

c. Self weight of gable frame – This was automatically considered by software once the self weight option was selected.

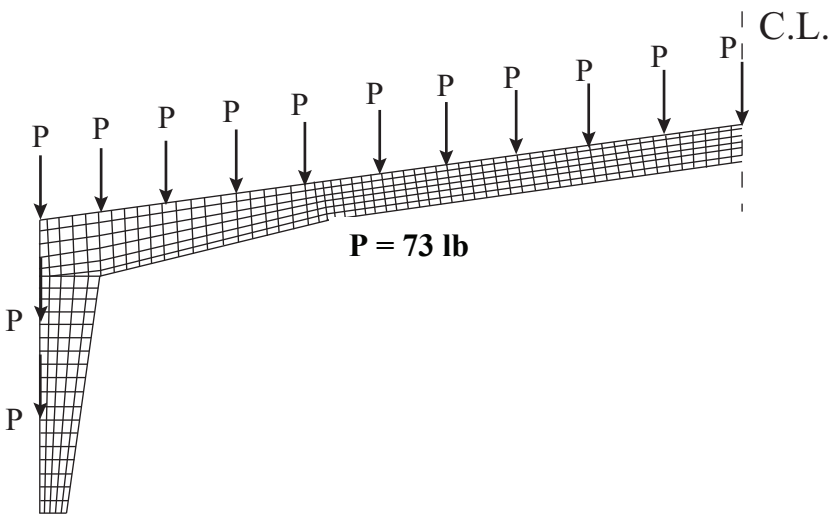

Figure 5-1: Weight of Purlin and Girts applied as Concentrated Load

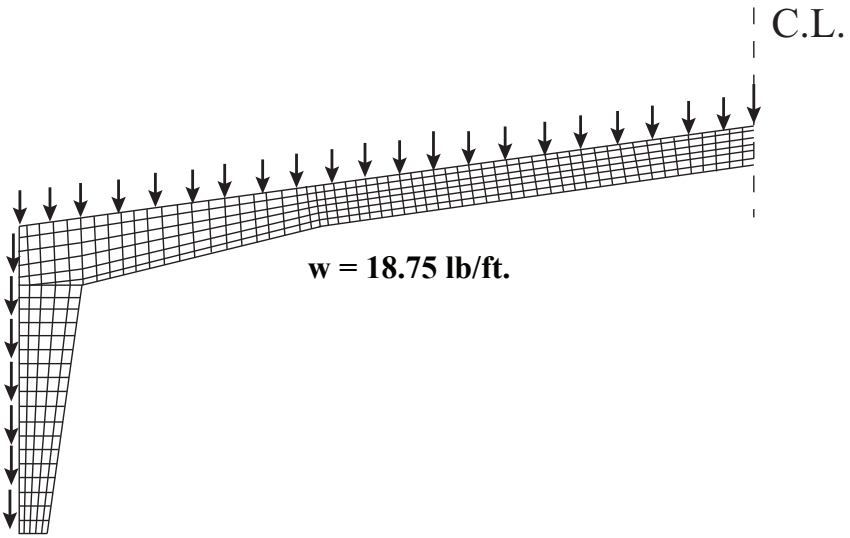

Figure 5-2: Application of load due to roof sheeting and wall cladding

5.3 Wind Loads

5.3.1 Approach I – General approach for all height buildings

The calculations were checked for wind acting along the direction of Main Wind Force Resisting System (MWFRS) as shown in Figure 5-3. The building was classified as an enclosed building in wind exposure category B.

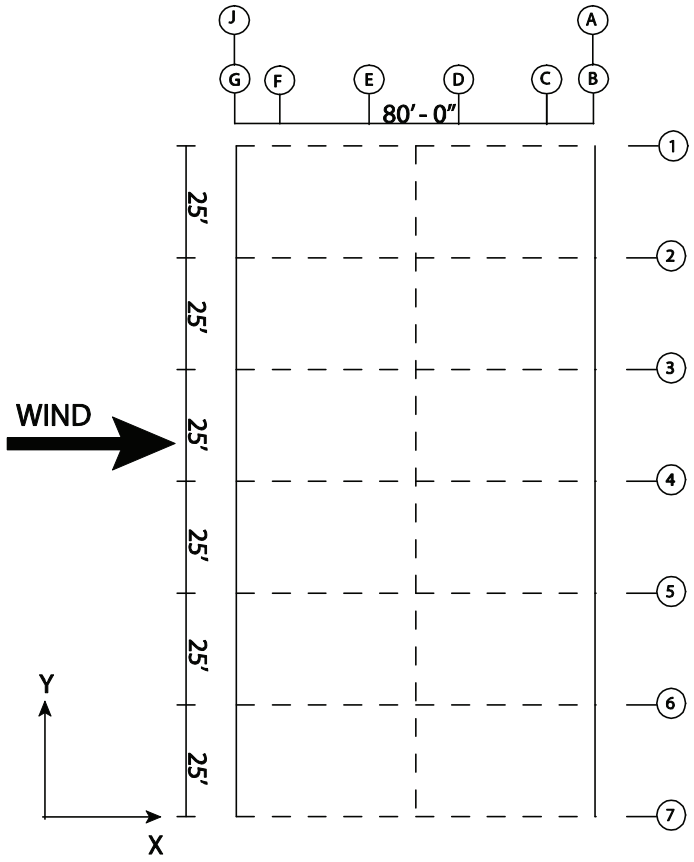

Figure 5-3: Direction of wind loading

Pressure coefficients were calculated using tables and figures provided in ASCE 7-05. Both the cases of positive and negative internal pressure were considered. Figure 5-4 and 5-5 show the pressure acting on the surface of building. The pressure is transformed into uniformly distributed load acting along the length of members of MWFRS (columns and rafters) based upon the tributary width.

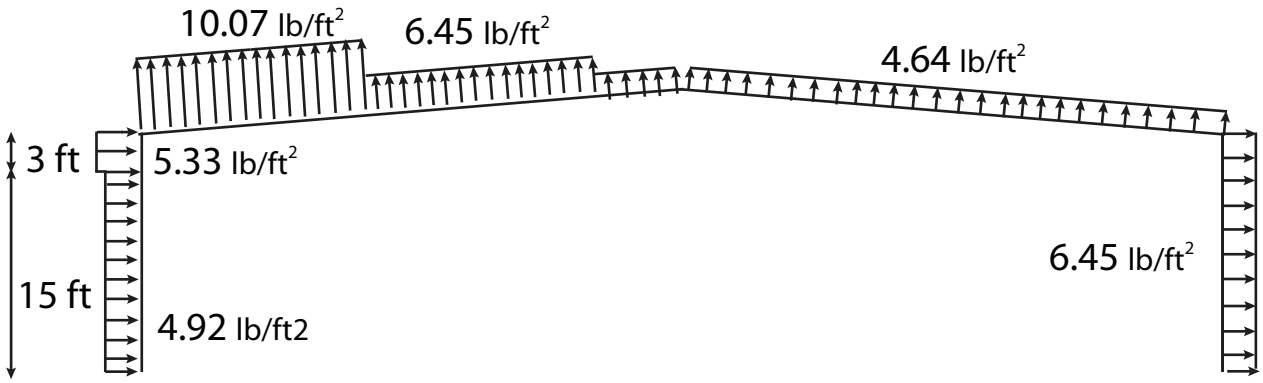

Figure 5-4: Pressure distribution (Positive internal pressure)

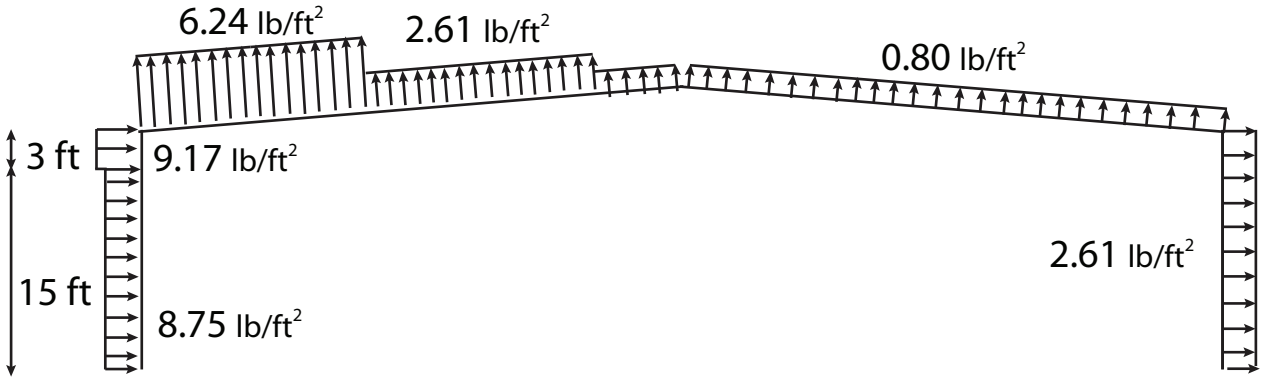

Figure 5-5: Pressure distribution (Negative internal pressure)

To find the magnitude of lateral load that could be safely applied during testing program, pressure obtained using ASCE method (Figure 5-4 and Figure 5-5) is converted into concentrated load acting at the knee location based on the tributary width corresponding to frame. The equivalent load using this approach worked out to be 5100 lb.

5.3.2 Approach II - Approach applicable for low rise buildings

The pressures and loads acting on the surface of the building were worked out in a manner similar as for approach I except that coefficients were used from tables and figures provided for low rise buildings. As already discussed in Section 3.3.2, this approach is conservative and results in higher pressures acting on corners. Figure 5-6 and 5-7 show the pressure acting on a frame. The equivalent concentrated load acting on building at knee location is 6100 lb.

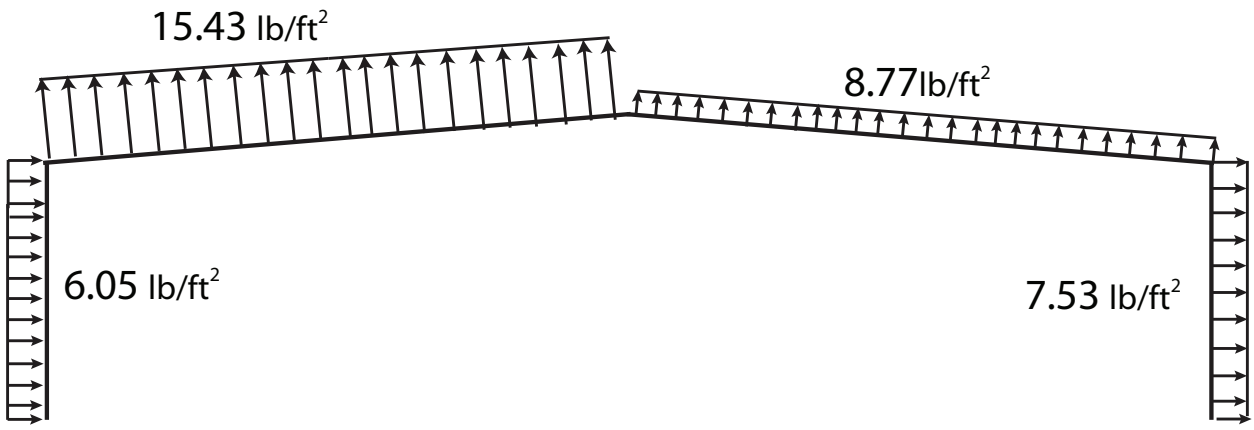

Figure 5-6: Pressure distribution (Positive internal pressure)

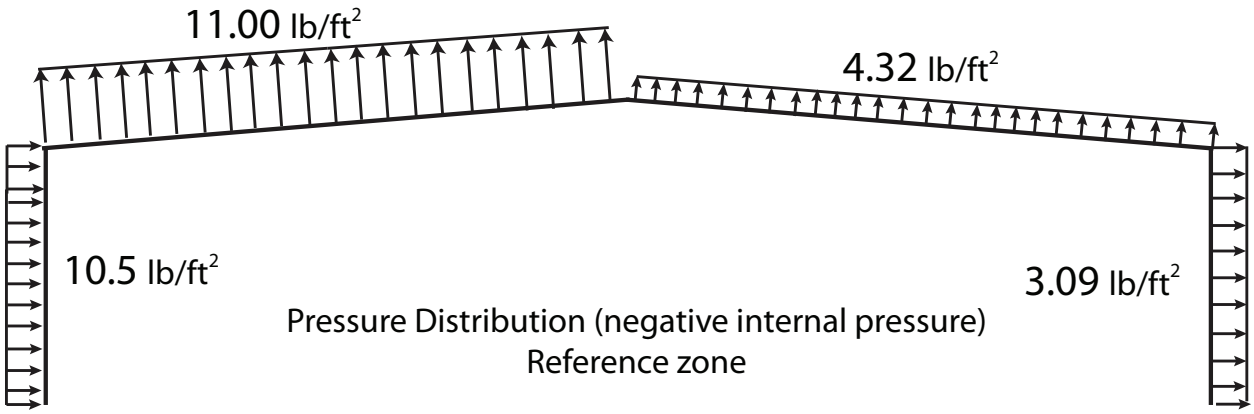

Figure 5-7: Pressure distribution (Negative internal pressure)

Chapter 6 Structural Analysis of Test Building

6.1 Introduction

The two frame types (interior and exterior) of the test building were analyzed by finite element analysis. Two types of analysis were performed:

1. 2-D Frame Analysis, using nonprismatic sections to represent the columns and rafters
2. 3-D Finite Element Analysis, using shell elements to represent the columns and rafters

In each case the column to base connection was modeled in a variety of ways, including pinned connections, simple spring connections, complex spring connections, and fully rigid connections. The modeling approaches and results are presented in this chapter. Correlation with the experimental results is provided in Chapter 9. It is important to note that for this chapter the term "3-D Finite Element Analysis" refers to analysis of individual frames modeled using Finite Elements. It shall not be confused with complete three-dimensional analysis of building which has been discussed in Chapter 8.

6.2 Use of 2-D Frame Analysis

In the 2-D frame analysis, the columns and rafters are modeled as two-dimensional "line elements". The tapering of the members can be handled in one of two ways: by subdividing each member into a number of prismatic frame elements, or by modeling each tapered member with a nonprismatic frame element. The use of nonprismatic elements is generally more convenient because fewer elements are used, and because the accuracy does not depend on how many sub-elements are used to model a main member. All of the 2-D frame analysis reported in this chapter used nonprismatic frame elements.

Analysis was performed using SAP 2000 , and was verified by use of a separate program that was developed in Mathcad. In both cases axial, flexural and shear deformations were included. The SAP 2000 routines are based on the assumption that the moment of inertia of the variable depth I-Sections varies quadratically with depth (which is a reasonable approximation), whereas the Mathcad solution is exact.

Each frame was represented by the analytical model shown in Figure 6-1. As may be seen, eleven nodes and ten elements were used. This is the minimum number of nodes and elements required to model the structure when nonprismatic sections are used. Note that the haunch region of the frame was modeled using short prismatic sections (e.g. between nodes 2 and 3 and

nodes 3 and 4). The controlling geometry for the frame models is provided in Tables 6-1 and 6-2 (b) for the Exterior and Interior frames, respectively. The modulus of elasticity used in the analysis was 29,000 ksi. Poisson's ratio was taken as 0.3.

The base of the columns were pin-supported in the vertical and horizontal directions. A rotational spring of stiffness K_θ was used to represent the rotational restraint column-to-base connection. This stiffness ranged from zero (pinned) to infinity (fixed). A lateral load of 7.5 kip was applied to node 2. This location of load is essentially the same as that used in the testing. The lateral displacements obtained at three key locations are reported in Tables 6-3 and 6-4 for the Exterior and Interior Frames, respectively.

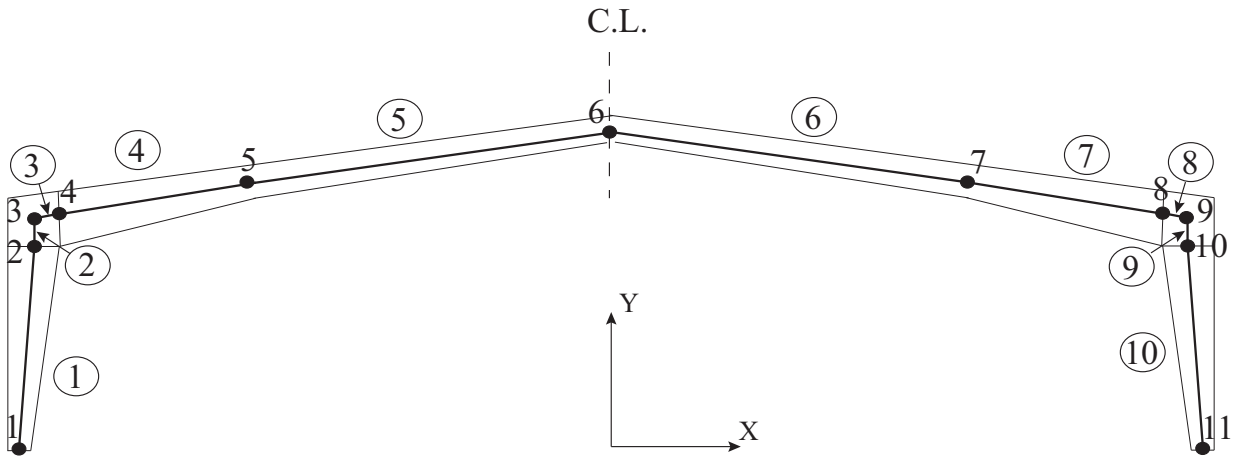

Figure 6-1: 2-D Frame Model

Table 6-1: Geometry and Section Properties Used for 2-D Frame Analysis of Exterior Frame

Node	X Coordinate (in.)	Y- Coordinate (in.)	Depth (in)	Web Thickness (in)	Flange Width (in.)	Flange Thickness (in.)
1	-466	0	12	0.1875	5	0.375
2	-452	177	38	0.1875	5	0.375
3	-452	195	38	0.1875	5	0.375
4	-434	196	34	0.1644	6	0.375
5	-299	210	36	0.1644	6	0.375
6	0	235	23	0.1345	6	0.3125
7	-299	210	36	0.1644	6	0.375
8	-434	196	34	0.1644	6	0.375
9	-452	195	38	0.1875	5	0.375
10	-452	177	38	0.1875	5	0.375
11	-466	0	12	0.1875	5	0.375

Table 6-2: Geometry and Section Properties Used for 2-D Frame Analysis of Exterior Frame

Node	X Coordinate (in.)	Y- Coordinate (in.)	Depth (in)	Web Thickness (in)	Flange Width (in.)	Flange Thickness (in.)
1	-466	0	12	0.1875	5	0.3750
2	-450	170	42	0.1875	5	0.3750
3	-450	191	42	0.1875	5	0.3750
4	-442	192	42	0.1875	5	0.3750
5	-299	215	27	0.1345	5	0.3125
6	0	240	14	0.1345	5	0.3125
7	299	215	27	0.1345	5	0.3125
8	442	192	42	0.1875	5	0.3750
9	450	191	42	0.1875	5	0.3750
10	450	170	42	0.1875	5	0.3750
11	466	0	42	0.1875	5	0.3750

Table 6-3: Results of 2-D Frame Lateral Load Analysis for Exterior Frame

K_θ	SAP 2000 (displacement, in.)			Mathcad (displacement, in.)			Ratio (SAP 2000/Mathcad)		
in-k/rad	ΔX_2	ΔX_6	ΔX_{10}	ΔX_2	ΔX_6	ΔX_{10}	ΔX_2	ΔX_6	ΔX_{10}
Pinned	0.768	0.801	0.731	0.777	0.811	0.739	0.99	0.99	0.99
10^2	0.767	0.800	0.73	0.777	0.809	0.738	0.99	0.99	0.99
10^4	0.707	0.737	0.669	0.714	0.744	0.676	0.99	0.99	0.99
10^6	0.337	0.349	0.304	0.342	0.354	0.308	0.99	0.99	0.99
10^8	0.309	0.320	0.277	0.315	0.325	0.282	0.98	0.98	0.98
Rigid	0.309	0.320	0.280	0.314	0.325	0.282	0.98	0.98	0.99

Haunch modeled as Flexible, Shear Deformation Included

Table 6-4: Results of 2-D Frame Lateral Load Analysis for Interior Frame

K_θ	SAP 2000 (displacement, in.)			Mathcad (displacement, in.)			Ratio (SAP 2000/Mathcad)		
in-k/rad	ΔX_2	ΔX_6	ΔX_{10}	ΔX_2	ΔX_6	ΔX_{10}	ΔX_2	ΔX_6	ΔX_{10}
Pinned	0.682	0.743	0.634	0.695	0.755	0.647	0.98	0.98	0.98
10^2	0.681	0.741	0.634	0.694	0.754	0.646	0.98	0.98	0.98
10^4	0.633	0.687	0.586	0.643	0.698	0.595	0.98	0.98	0.98
10^6	0.302	0.326	0.262	0.309	0.333	0.267	0.98	0.98	0.98
10^8	0.275	0.296	0.236	0.282	0.304	0.242	0.98	0.97	0.98
Rigid	0.274	0.296	0.236	0.282	0.304	0.242	0.97	0.97	0.98

Haunch modeled as Flexible, Shear Deformation Included

Three basic observations may be made from the tables:

1. The SAP 2000 and Mathcad analyses report virtually the same results. This indicates that the use of a quadratically varying moment of inertia for a web-tapered member (as used by SAP 2000) is sufficiently accurate.

2. The lateral deflection at node 10 is somewhat less (5-9 percent) than that at the loaded node (node 2). This is due to axial compression in the rafter and bending in the rafter (deformed shape shown in Figure 7-22).

3. The deflection at node 6 (at midspan) is greater than that at nodes 2 or 10.

4. The displacement is very sensitive to the assumed rotational stiffness of the supports. For the Exterior frame the deflection at node 2 reduces from 0.770 in. for the pinned base to 0.310 in. for the fixed base. For the Interior frame this reduction is from 0.682 in. to 0.274 in.

5. The lateral stiffness of the Exterior frame is somewhat less than that of the Interior frame. For the pin supported Exterior frame the stiffness can be estimated as 7.5/0.768=9.77 kip per in. For the pin supported Interior frame the lateral stiffness is 7.5/0.682=11.0 kip/in. The Interior frame is stiffer than the Exterior frame because of the increased depth at the haunch.

The variation in displacement with support stiffness is further illustrated in Figures 6-2 and 6-3, which are plots of the variation in displacement at node 2 with the rotational stiffness of the support spring. Curves are shown for the 2-D SAP2000 model, the 2-D Mathcad Model, and the 3-D SAP2000 model. The 3-D SAP2000 model is discussed later. Figure 6-2 is for the Exterior frames, and Figure 6-3 is for the Interior frame. Between the pinned-rigid base connection stiffness limits, there is a "transitional region" for which the displacement rapidly decreases with increasing spring stiffness. This region begins at a rotational stiffness of approximately 1000 kip-in./radian, and ends at a stiffness of approximately 1000000 kip-in./radian. The question for the designer is "how much stiffness is provided by the actual support condition, and how do I incorporate that into my model? This issue was discussed in general in Section 2.3 of this thesis, and will be revisited in Section 6.2 of this chapter.

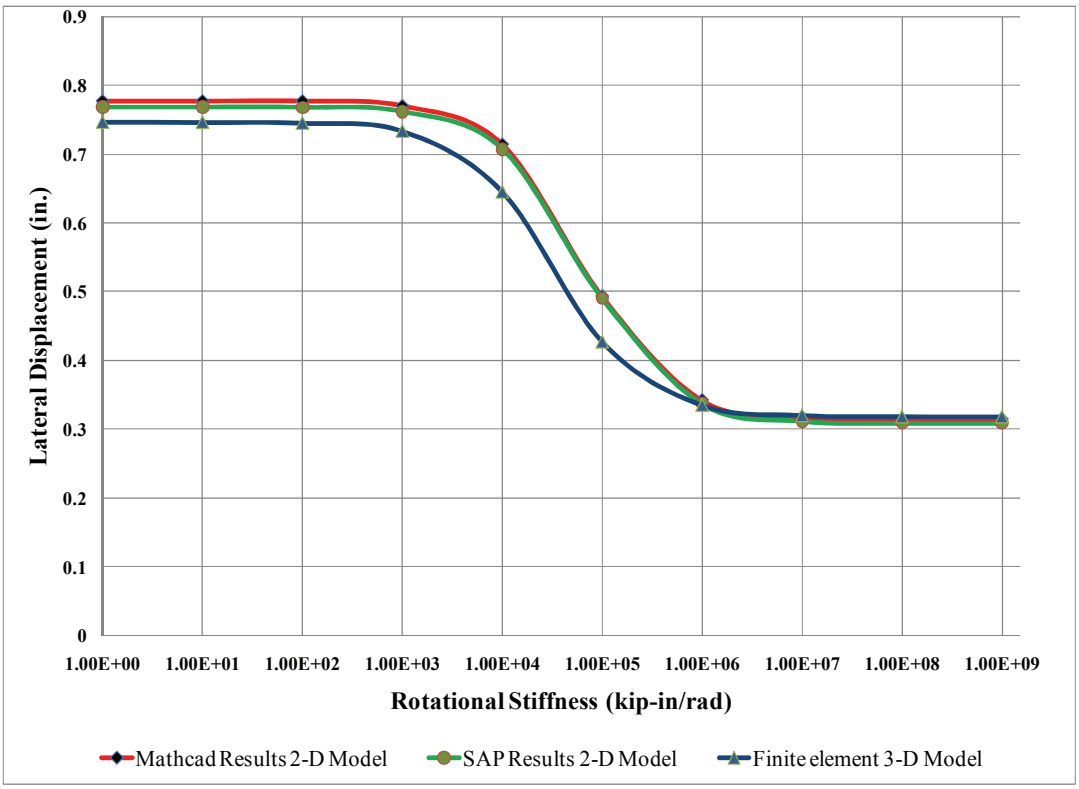

Figure 6-2: Variation in Drift with Support Stiffness, Exterior Frame

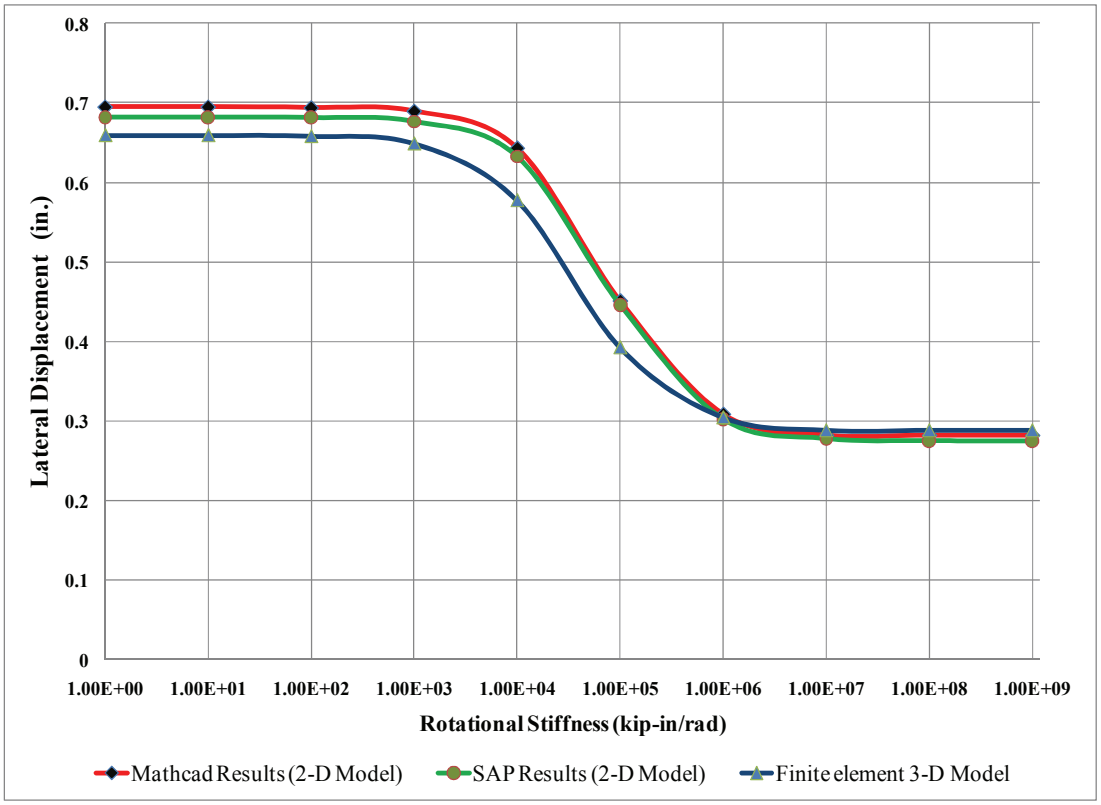

Figure 6-3: Variation in Drift with Support Stiffness, Interior Frame

The analysis presented so-far modeled the "panel zone" with short flexible elements. To determine the influence of the panel zone stiffness, the analysis of the exterior frame was repeated with the haunch region (elements 2, 3, 8, and 9) modeled as rigid. The Mathcad routines were used for this analysis. The results of the analysis are shown in Table 6-7. As may be seen, the effect of haunch stiffness is significant, with the deflection for the pinned base model reducing from 0.777 in. to 0.596 in. (a reduction of 23 percent). Similar reductions in displacement were obtained for the other base conditions. In must be noted, however, that there is no rational basis to model the haunch as fully rigid in an actual structure.

Table 6-5: Influence of Hauch Stiffness on Exterior Frame Displacement

K_θ in-k/rad	Rigid Haunch, Shear Deformations Included (in.)			Ratio (Rigid Haunch to Flexible Haunch)		
	ΔX_2	ΔX_6	ΔX_{10}	ΔX_2	ΔX_6	ΔX_{10}
Pinned	0.596	0.621	0.567	0.77	0.77	0.77
10^2	0.595	0.620	0.566	0.77	0.77	0.77
10^4	0.549	0.573	0.521	0.77	0.77	0.77
10^6	0.269	0.279	0.245	0.79	0.79	0.80
10^8	0.248	0.258	0.224	0.79	0.79	0.79
Fixed	0.248	0.257	0.224	0.79	0.79	0.79

Another item of interest is the influence of shear deformations on the computed stiffness. The original model (with flexible haunches) was re-analyzed with shear deformations neglected. The results, shown in Table 6-8, indicate that shear deformations are responsible for approximately four to seven percent of the drift, with the larger percentage being applicable for the Fixed base condition.

Table 6-6: Influence of Shear Deformation on Exterior Frame Stiffness

K_θ in-k/rad	Flexible Haunch, Shear Deformations Excluded (in.)			Ratio (Shear Deformations Excluded/Included)		
	ΔX_2	ΔX_6	ΔX_{10}	ΔX_2	ΔX_6	ΔX_{10}
Pinned	0.748	0.782	0.713	0.96	0.96	0.96
10^2	0.747	0.781	0.712	0.96	0.97	0.96
10^4	0.688	0.718	0.653	0.96	0.97	0.97
10^6	0.321	0.334	0.291	0.94	0.94	0.94
10^8	0.293	0.305	0.264	0.93	0.94	0.94
Fixed	0.292	0.304	0.262	0.93	0.94	0.93

6.3 3-D Finite Element Models

The 3-D finite element models for the exterior and interior frame are shown in Figure 6-4. The left part of this figure shows the mesh for the Exterior frame, and the right side shows the mesh for the Interior Frame. In these models the elements are 4-node thin shell elements with six degrees of freedom per node. Eight elements were used through the depth of the web, and two elements were used across the width of the flange. Stiffeners were modeled where present. The loading was applied over the width of the column flange as shown in Figure 6-5. The "Pinned" base column-to slab connection was modeled as shown in Figure 6-6, where the "linear springs" were used to provide a rotational stiffness equal to the rotational stiffness K_θ.

The results of the analysis are shown in Tables 6-7 and 6-8 for the Exterior and Interior frames, respectively. The results for the 3- Model are also given graphically in Figures 6-2 and 6-3. As may be observed by the tables and figures, the 3-D model produces displacements and behavior very similar to that produced by the 2-D models where the panel zone region was modeled with flexible prismatic elements, and without explicit panel zone modeling. Hence, there appears to be no justification for modeling panel zone region as rigid.

It is interesting to note that the lateral displacements produced by the SAP2000 model are generally less than those produced from the 2-D models. This is particularly true near the middle of the transitional region (Rotational stiffness approximately 10^4 to 10^5 in.-k/radians).

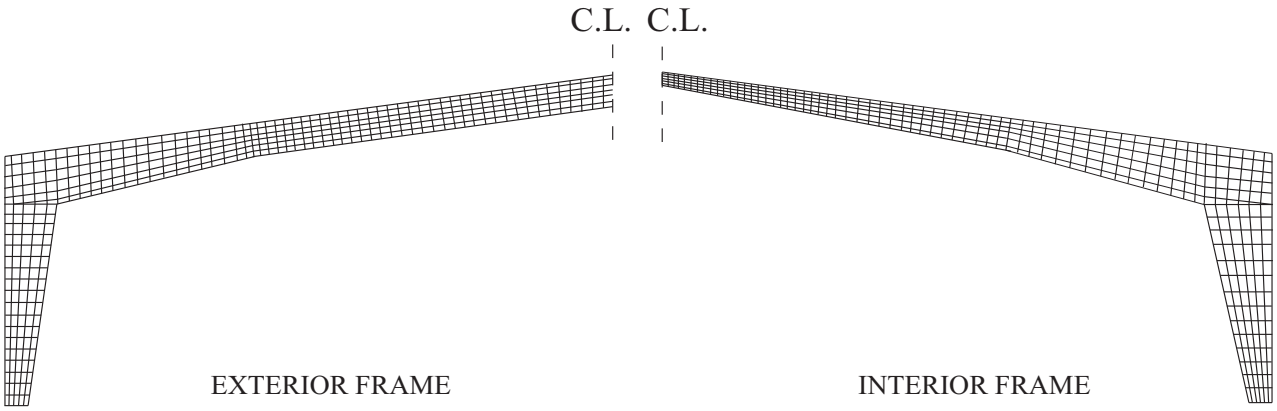

Figure 6-4: Finite element model for interior and exterior frame

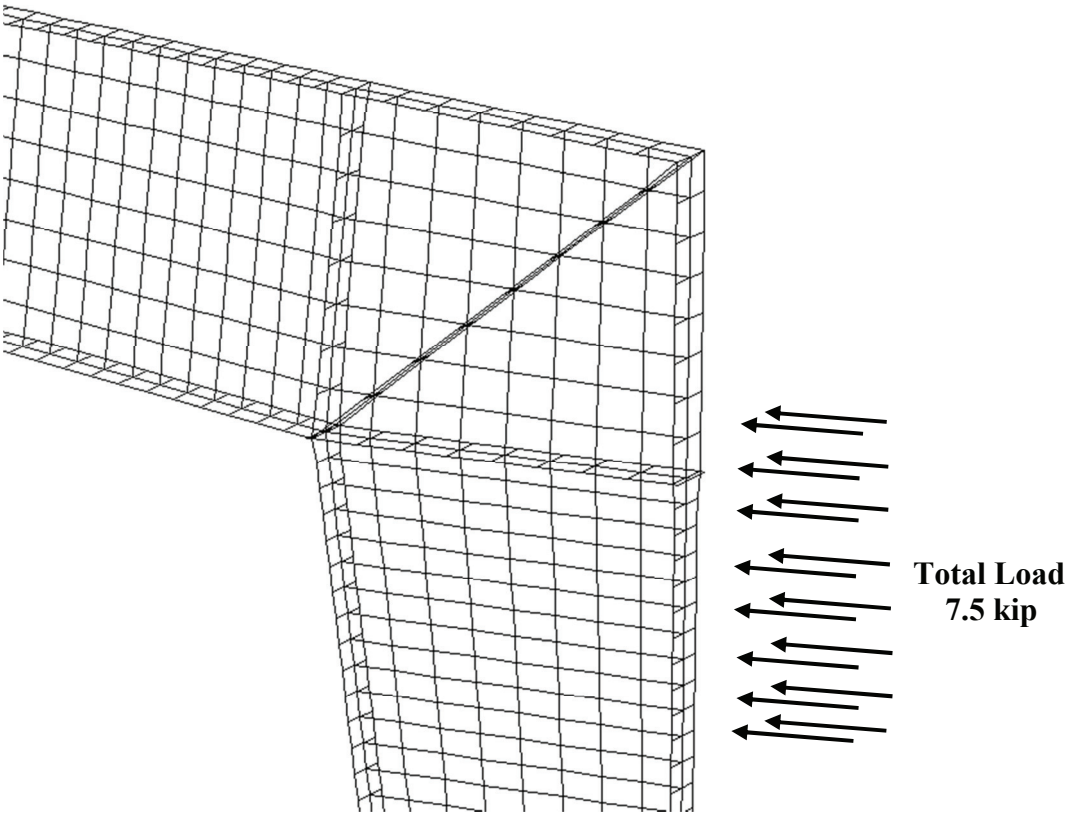

Figure 6-5: Load applied on column flanges

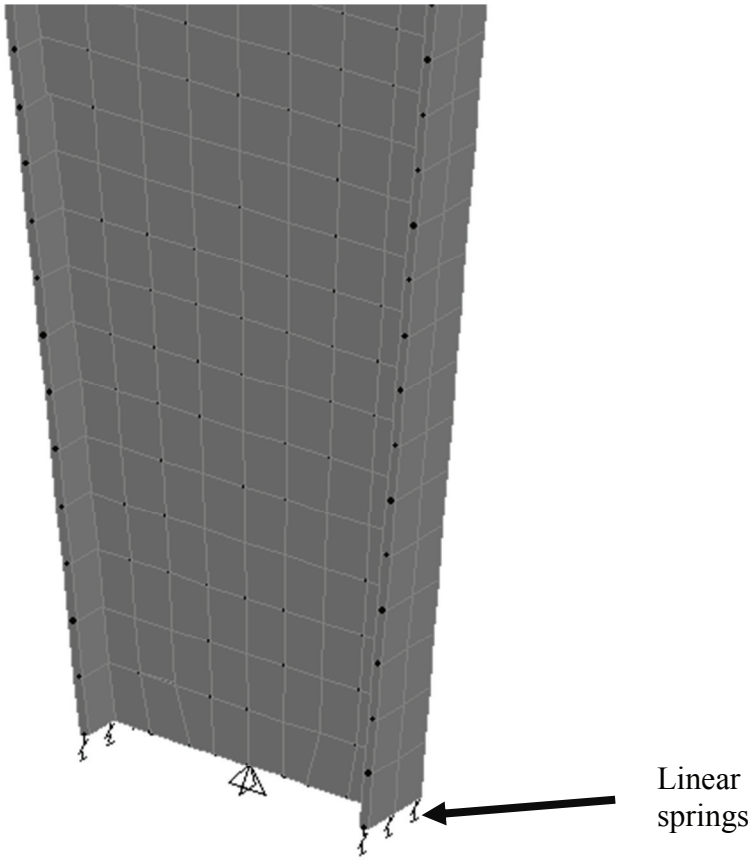

Figure 6-6: Pin connection with rotational restraint provided by linear springs

Table 6-7: 3-D Results for Exterior Frame Displacement

K_θ in-k/rad	Displacements, in.			Ratio (SAP finite element model/Mathcad frame model)		
	ΔX_2	ΔX_6	ΔX_{10}	ΔX_2	ΔX_6	ΔX_{10}
Pinned	0.745	0.745	0.767	0.96	0.92	1.04
10^2	0.745	0.745	0.767	0.96	0.92	1.04
10^4	0.645	0.645	0.662	0.90	0.87	0.98
10^6	0.334	0.334	0.340	0.98	0.94	1.10
10^8	0.317	0.317	0.323	1.01	0.98	1.15
Rigid	0.317	0.317	0.323	1.01	0.98	1.15

Table 6-8: 3-D Results for Interior Frame Displacement

K_θ in-k/rad	Displacements, in.			Ratio (SAP finite element model/Mathcad frame model)		
	ΔX_2	ΔX_6	ΔX_{10}	ΔX_2	ΔX_6	ΔX_{10}
Pinned	0.659	0.659	0.693	0.97	0.89	1.09
10^2	0.659	0.659	0.692	0.97	0.89	1.09
10^4	0.605	0.605	0.635	0.96	0.88	1.08
10^6	0.3149	0.3149	0.326	1.04	0.97	1.24
10^8	0.288	0.288	0.298	1.05	0.97	1.26
Rigid	0.287	0.287	0.297	1.05	0.97	1.26

6.3.1 **Influence of "Actual" Base stiffness on Computed Response**

In the previous section of the thesis the sensitivity of the computed response to the stiffness of the column-to-base connection was evaluated, and it was found that the computed displacements are extremely sensitive to the connection stiffness. In this section of the thesis, the actual stiffness of the base connection will be estimated by three approaches:

Method 1:

This method is based on the assumption that the column base rotates as a rigid body about its centroidal axis (Figure 6-7). Using this method the support rotational stiffness is:

$$K_\theta = 4k_{Rod}d_1^2 \qquad 6\text{-}1$$

Method 2:

This method is based on the assumption that the column base rotates as a rigid body about the compression flange (Figure 6-8). Using this method the support rotational stiffness is:

$$K_\theta = 2k_{Rod}(d_2^2 + d_3^2) \qquad 6\text{-}2$$

In Methods 1 and 2 the term k_{Rod} in equations represent the axial stiffness of the anchor rod. The stiffness is taken as

$$k_{Rod} = \frac{A_{Rod}E}{L_{eff}} \qquad 6\text{-}3$$

Where A_{Rod} is the cross sectional area of the rod, E is the modulus of elasticity, and L_{eff} is the effective length of the rod. The effective length depends on the distribution of stress along the

length of the bar. If this axial stress in the bar is uniform over the length of the bar, the effective length is equal to the actual length. If the stress distribution is linear, ranging from zero at the deepest embedment to a maximum at the slab level the effective length is half of the actual length.

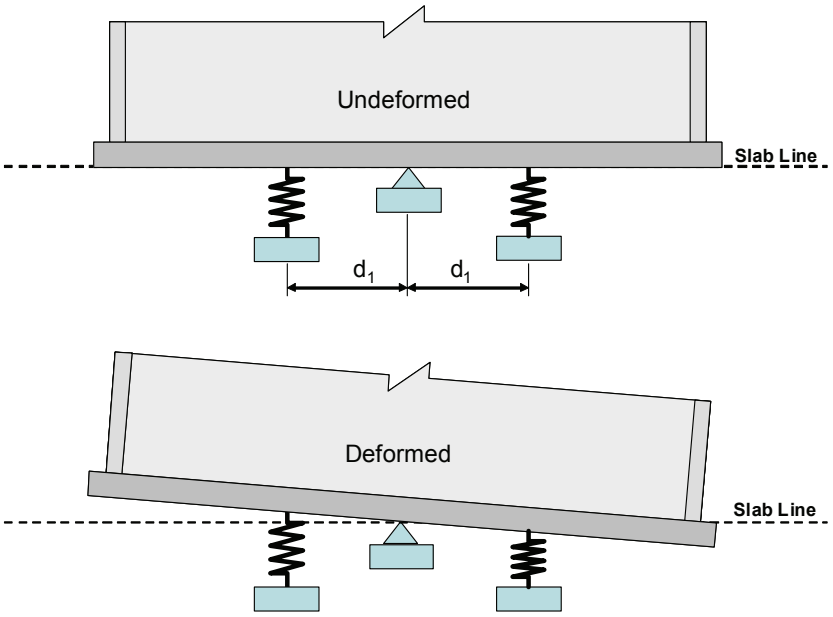

Figure 6-7: Undeformed and Deformed Configuration for Model 1

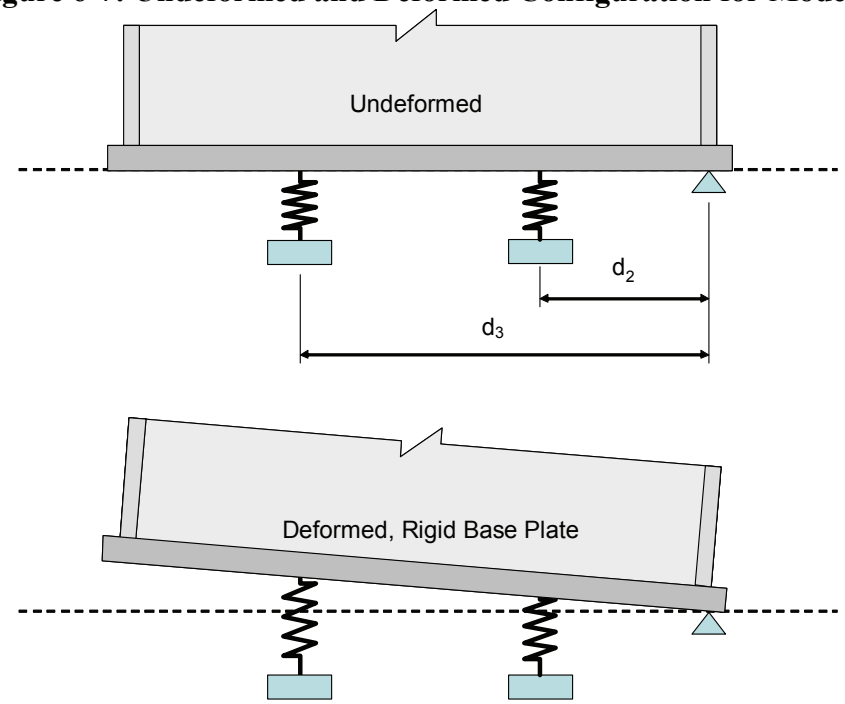

Figure 6-8: Undeformed and Deformed Configuration for Model 2

Method 3:

Method 3 requires a detailed finite element analysis of the entire gable frame. Special attention is paid to modeling the column-to-base connection, wherein the base plate, columns and rafters are modeled using shell elements, the anchor rods are modeled as tension-only springs, and the concrete base is modeled as compression only springs. During the analysis the base plate will deform and "lift off" the slab as shown in Figure 6-9. This method, which is nonlinear (due to tension-only or compression-only) springs, will not produce an explicit stiffness K_θ. However, an equivalent rotational base spring stiffness may be obtained from the lateral displacement produced from the analysis, and from a curve representing the sensitivity of such displacement to the rotational spring stiffness.

To obtain the sensitivity curve, the frame three-dimensional finite element model is run with base connection that is pinned in the lateral and vertical directions, and is partially restrained in the rotational direction by a spring. Analysis is repeated with increasing rotational spring stiffness and a plot of displacement (at point of load) vs spring stiffness is obtained. Using the displacement obtained from the model with the base accurately modeled (using Method 3), the equivalent stiffness is obtained from the curve as shown in Figure 6-10.

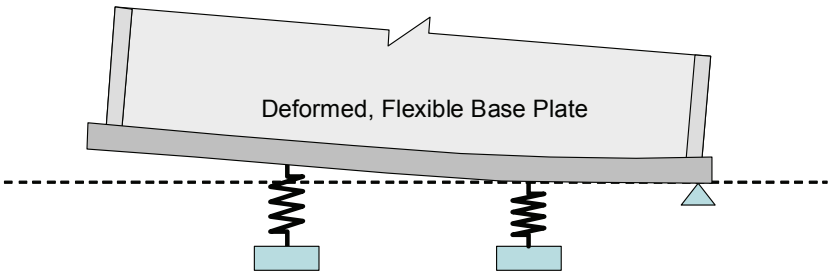

Figure 6-9: Modeling of Column-to-Base Connection when Base Plate is Flexible

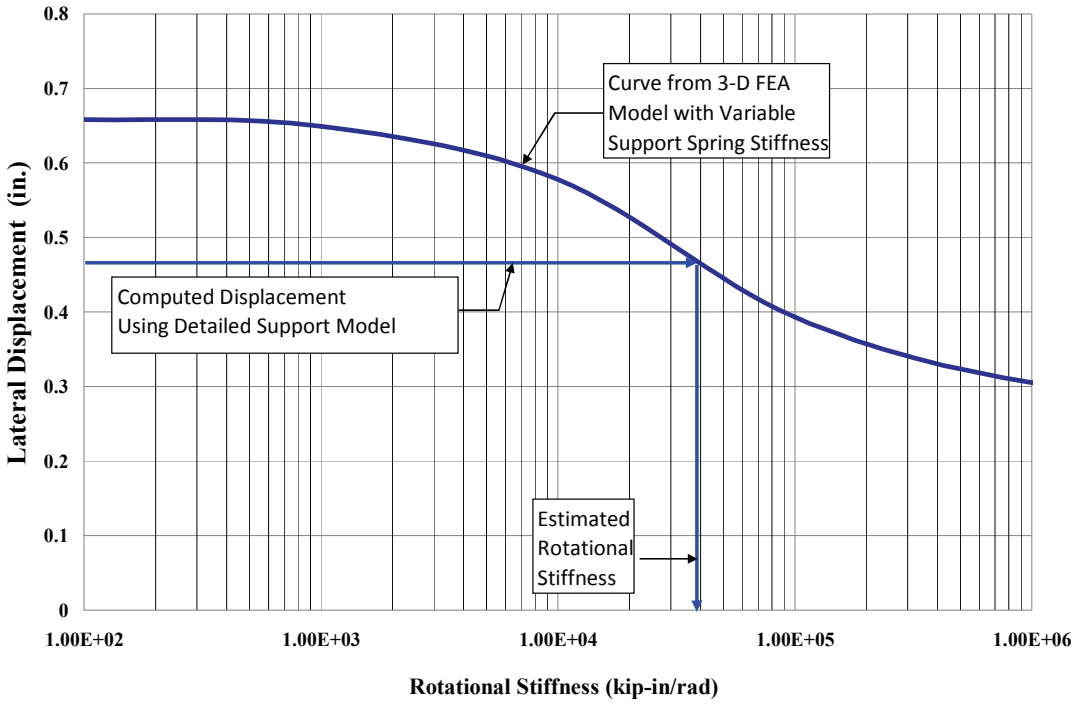

Figure 6-10: Obtaining Equivalent Base Stiffness from Detailed Finite Element Analysis

6.4 Estimates Stiffness of Column-to-Base Connection for Test Building

Using the base plate dimensions shown in Figure 6-11 and an effective length of half of the actual length, the rotational stiffness for both the Exterior and Interior base connections are as follows for the Test Building:

Using Method 1 and Equation 6-1 K_θ= 87,500 k-in/radian

Using Method 2 and Equation 6-2 K_θ= 560,000 k-in/radian

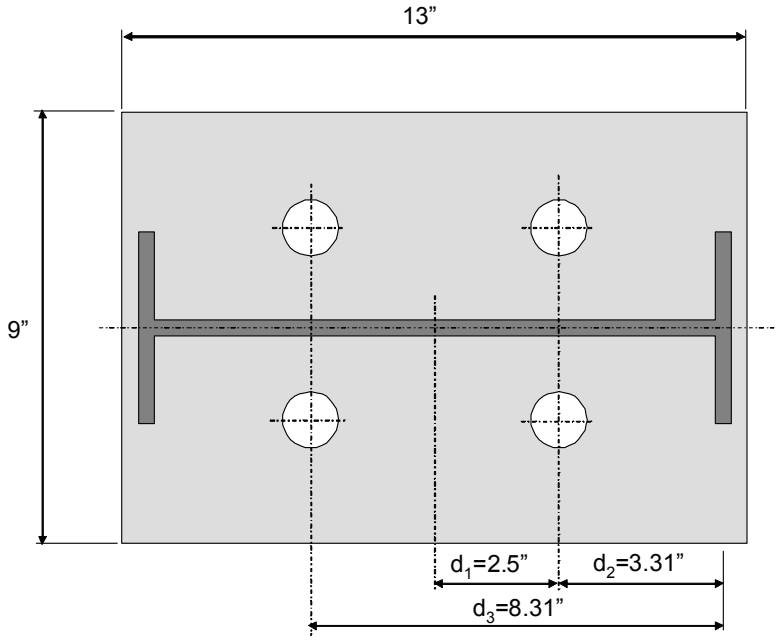

Figure 6-11: Base Plate Dimensions Used for Analysis

The range of results given by the first two methods is very large. On review of the technical basis of the methods it would seem that Equation 6-1 is not reasonable because it is not possible for the base plate rotate below the slab line as shown in Figure 6-7. The deformation pattern used to derive Equation 6-2 is more reasonable physically (only a small length of the base plate physically descends below the slab line). Both equations assume that the base plate is rigid, which is not reasonable.

The results of the Method 3 analysis for the Exterior and Interior frames are shown in Figures 6-12(a) and 6-12(b), respectively. As may be observed, the rotational stiffness recovered for both frames is approximately 20,000 k-in/radian. This stiffness is *significantly less* that computed from Equations 6-1 or 6-2. The most likely source for the difference is out-of-plane bending stiffness of the base plate. This stiffness was assumed to be infinity in Equations 6-1 and 6-2, and the actual plate thickness (3/8 in.) in the 3-D finite element analysis. The other significant factor in the column-base plate connection stiffness is the assumed axial stiffness of the anchor bolts.

To determine the influence of base plate thickness and anchor bolt stiffness the 3-D analysis was repeated using a variety of parameters. The results of the analysis are presented in Figures 6-13(a) and 6-13(b) for the Exterior and Interior frames, respectively. For the system as modeled (with the 3/8 in. base plate, the effective stiffness of the anchor bolt of 3500 k/in.) the influence

of effective anchor bolt stiffness is not significant (doubling or halving the stiffness does not result in a significant change in displacement). When the thicker base plate is used the displacements reduce significantly for all assumed anchor bolt stiffness, and the influence of anchor bolt stiffness on computed displacement is increased.

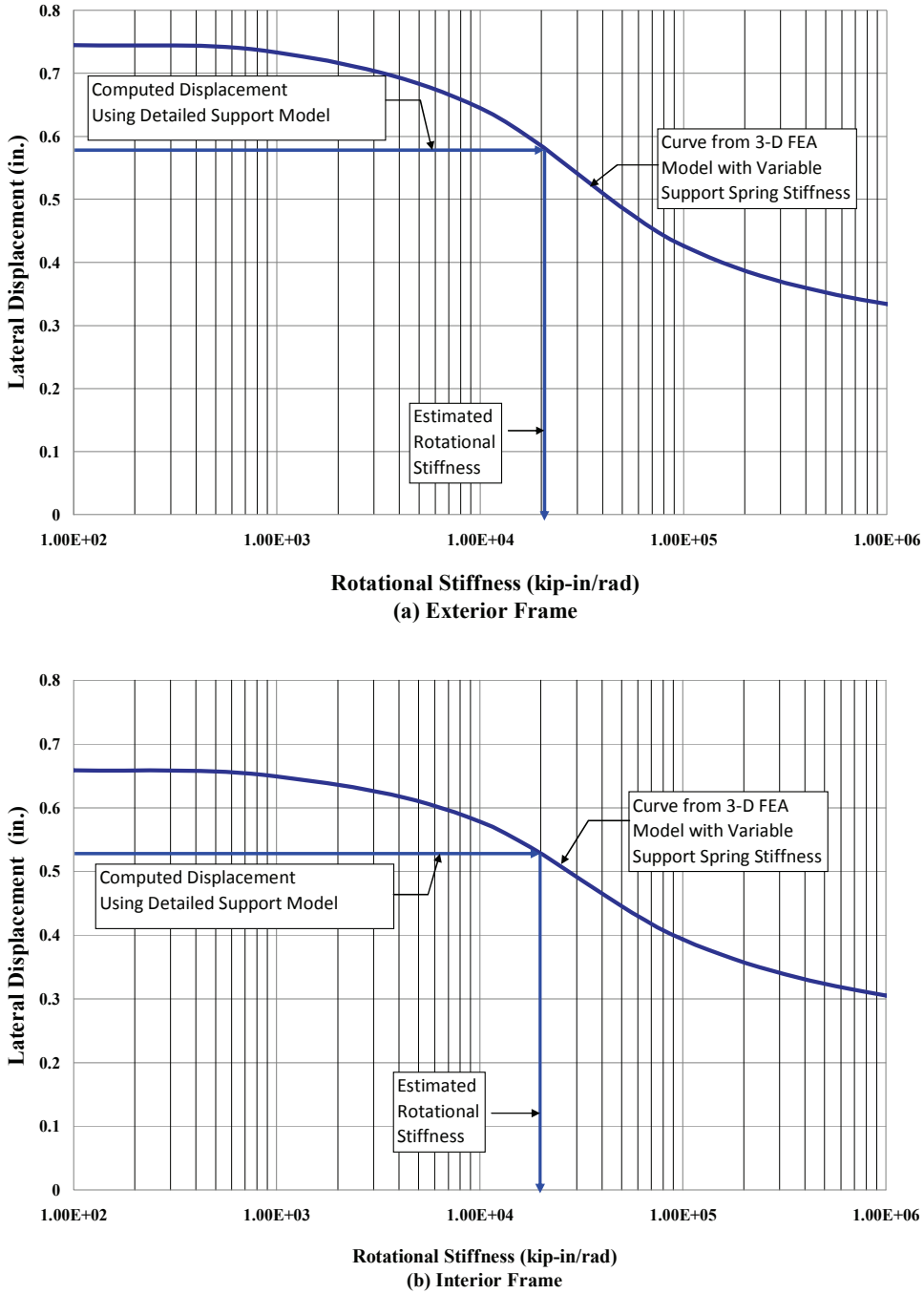

Figure 6-12: Developing Rotational Stiffness from Finite Element Model

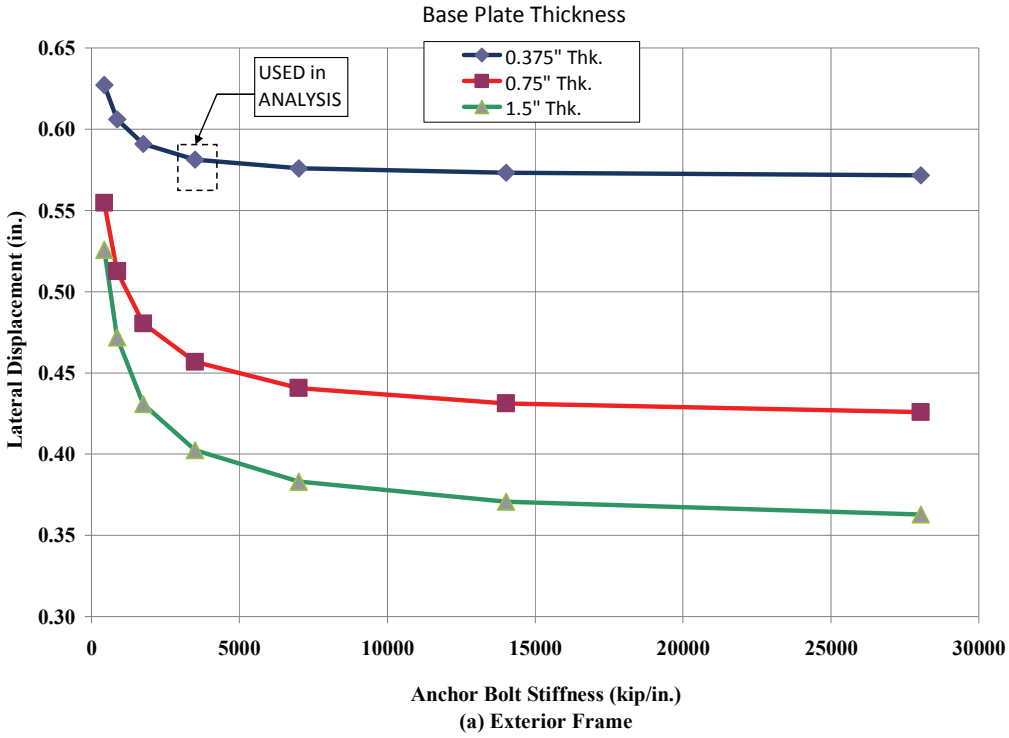

(a) Exterior Frame

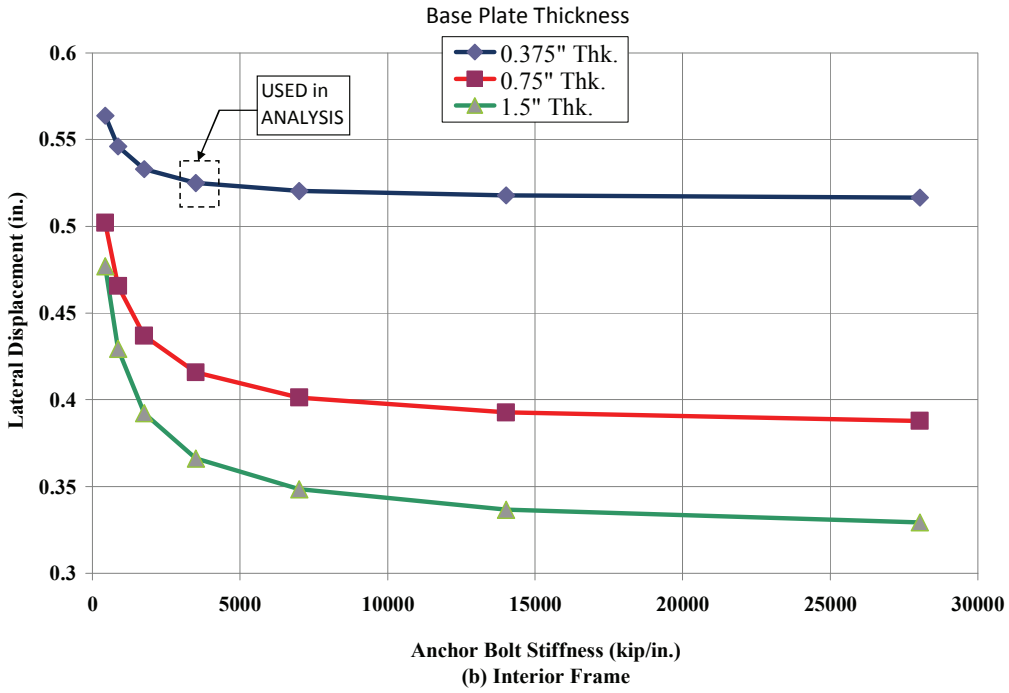

(b) Interior Frame

Figure 6-13: Influence of Base Plate Thickness and Anchor Bolt Stiffness on Deflection

The level of gravity load on the structure has an influence on the stiffness of the base-to-column connections because this loads prevents the base plate from lifting up and thereby deforming during under lateral loads. To investigate this tendency, analysis was performed for four levels of gravity load:

Zero Dead Load
0.5 times Design Dead Load
1.0 times Design Dead Load
2.0 times Design Dead Load

The results of the analysis are shown in Figured 6-14(a) and (b) for the Exterior and Interior frames, respectively. Analysis was run with an anchor bolt stiffness of 2AE/L, and with variable base plate thickness.

As may be seen from the figures, the deflection reduces slightly when the dead load is included. The largest reductions occur for the thinner base plates. For the 3/8 in. base plate (the actual thickness) the deflection under a 7.5 kip lateral force decreases from 0.581 in. to 0.562 in. (3 percent) for the Exterior frame, and from 0.525 in. to 0.508 in. (3 percent) for the Interior frames.

The estimate of the base spring effective stiffness with gravity dead load included is obtained using the sensitivity curves. The results are shown in Figure 6-15(a) and (b) for the Exterior and Interior frames, respectively. In both cases, it appears that the equivalent rotational stiffness of the support is approximately 22,000 k-in./radian.

The discrepancy between the simplified model (Methods 1 and 2) and the 3D Finite Element model are very significant. As mentioned earlier, Method 1 is not kinematically realistic, and should not be used. Method 2 is not realistic for the Test Building because it is based on a rigid base plate, whereas the Finite Element model used the actual plate thickness of 3/8 in. It is interesting to note from Figure 6-13 that increasing the actual base plate thickness from 3/8 in. to 1.5 in. would effectively provide a fixed base condition for the Test Structure.

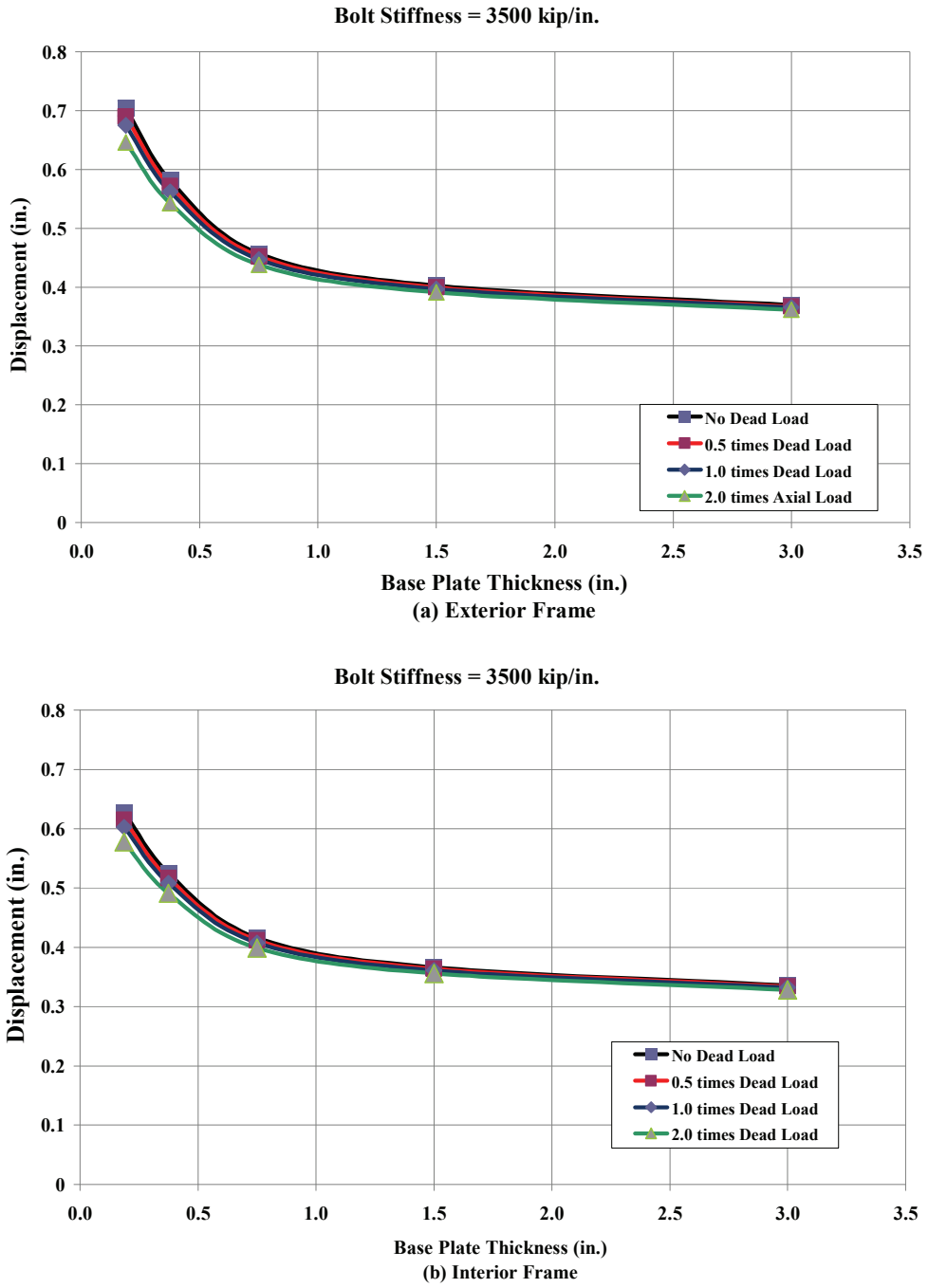

Figure 6-14: Influence of Dead Load on Computed Displacements

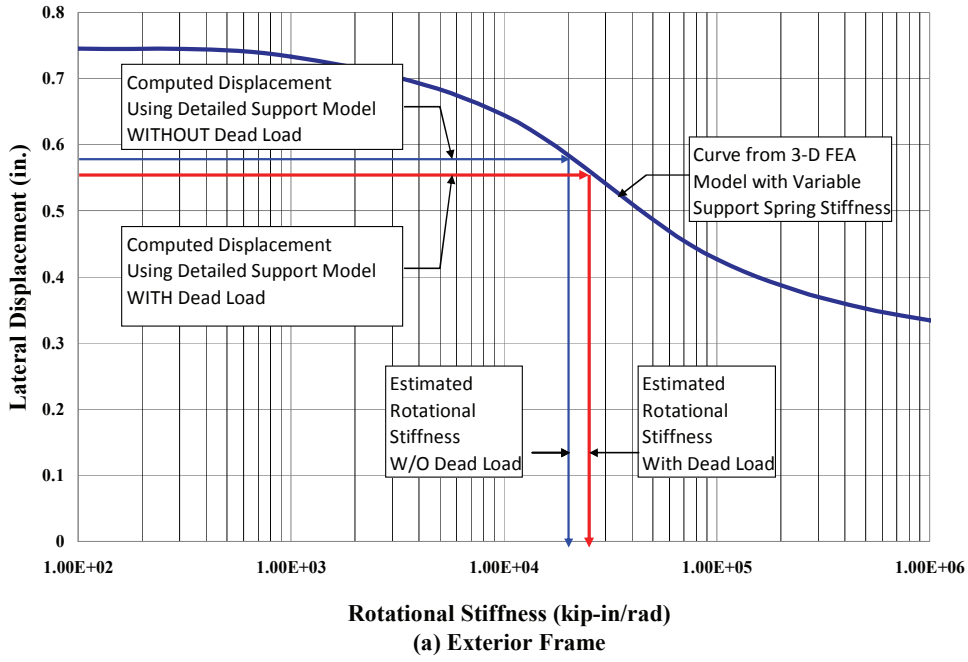

(a) Exterior Frame

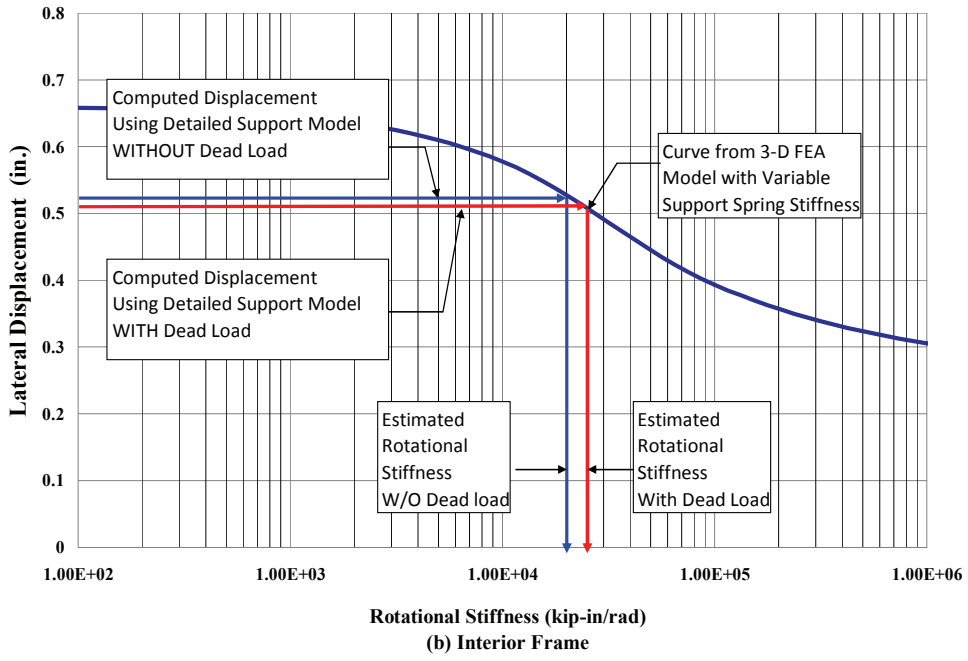

(b) Interior Frame

Figure 6-15: Revised Estimate of Base Stiffness, Including Dead Load Effect

6.5 Analysis of Structure under Design Level Loads

All of the analysis discussed up to this point has been for the structure loaded with a 7.5 kip concentrated lateral force at node 2 in the 2-D model (see Figure 6-1), or a 7.5 kip force distributed over the column flange in the 3-D model (see Figure 6-4). The actual loading on the structure is more complex than used so far, and it is of interest to determine the deflections and base reactions under the actual load. Two loadings will be considered: gravity and wind. Wind loads are based on ASCE 7-05 analytical load method for all height buildings. Both loadings are based on a tributary bay width of 25 ft. The analysis was performed for the Interior frame only, using the 2-D SAP 2000 model. Three support spring stiffnesses were used: pinned, intermediate (K_θ= 22000 k-in./radian) and rigid. The results are presented in Tables 6-9 through 6-11.

Table 6-9: Forces and Displacements under Design Level Dead Loads

Support Stiffness	Reactions at Node 1 (Left Support)			Moment at Knee	Displacement at Node 2 (in.)		Displacement at Node 6 (in.)	
	F_X (k)	F_Y (k)	M_Z (k-in.)	M (k-in.)	Δ_X	Δ_Y	Δ_X	Δ_Y
Pinned	1.86	3.2	0.00	-273	-0.0350	0.0008	0.00	-0.319
Intermed.	1.91	3.2	9.7	-271	-0.0327	0.0002	0	-0.2818
Rigid	2.22	3.2	79.1	-255	-0.0267	0.0002	0.00	-0.282

Table 6-10: Forces under Design Level Wind Loads

Support Stiffness	Reactions at Node 1 (Left Support)			Moment at Knee	Reactions at Node 11 (Right Support)			Moment at Knee
	F_X (k)	F_Y (k)	M_Z (k-in.)	M (k-in.)	F_X (k)	F_Y (k)	M_Z (k-in.)	M (k-in)
Pinned	-4.10	-2.86	0	390	-0.88	-0.38	0	-71
Intermed.	-4.14	-2.8	-37.017	359.49	-0.84	-0.44	22.63	-44
Rigid	-4.37	-2.59	-186.4	252	-0.61	-0.66	68.9	39.0

Table 6-11: Displacements under Design Level Wind Loads

Support Stiffness	Displacement at Node 2 (in.)		Displacement at Node 6 (in.)		Displacement at Node 10 (in.)	
	Δ_X	Δ_Y	Δ_X	Δ_Y	Δ_X	Δ_Y
Pinned	0.254	-0.0200	0.259	0.170	0.213	0.019
Intermed.	0.217	-0.017	0.219	0.1667	0.1765	0.0159
Rigid	0.093	-0.0062	0.087	0.142	0.061	0.006

The following points may be drawn from the Tables 6-9, 6-10, and 6-11:

The net reaction due to gravity plus wind load acts in the downward direction, putting compression at the base of the column. For the intermediate stiffness (K_θ= 22000 k-in./radian) condition the downward reaction is only 400 pounds.

Chapter 7 Experimental Testing Program

7.1 Introduction

Seven full scale tests were conducted on the Test Building, where each frame was loaded individually as shown in Figure 7-1. The plate-welded steel frames were loaded laterally using a custom-designed load frame and rigging assembly. The assembly was fabricated and proof-loaded in the Thomas M. Murray Structural Engineering Laboratory.

For each of five tests along grid line A, the frame was loaded by pulling it towards grid line J. For tests on line J, the frame was pulled towards grid line A. Only two pull tests were possible on grid J due to space limitation inside the building.

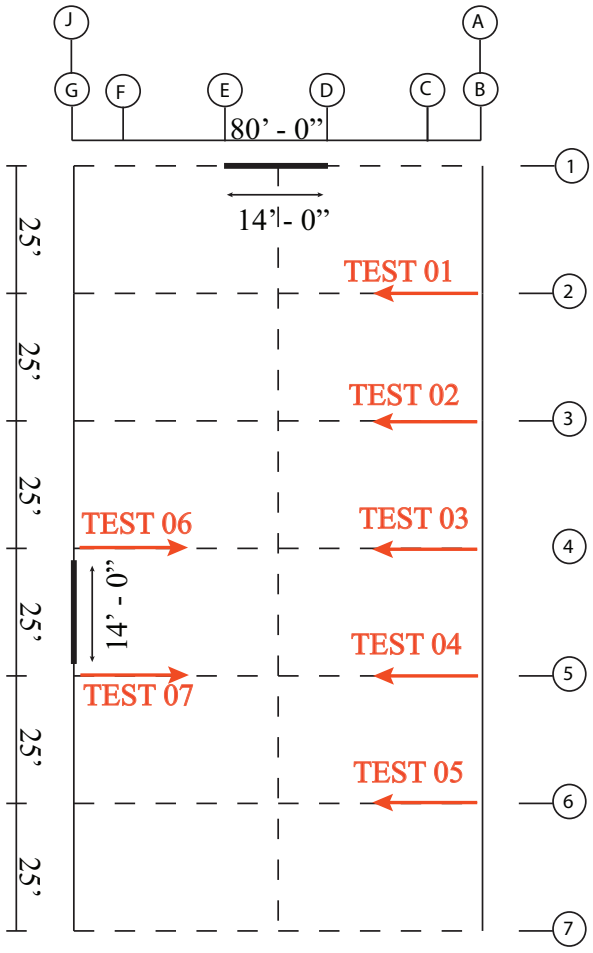

Figure 7-1: Direction of frame loading (Each frame loaded individually)

7.2 Preliminary Analysis

Before deciding upon the magnitude of load to be applied to the building, preliminary analysis of the frames was carried out using a three-dimensional model, shown in Figure 7-2. Analysis was run using SAP2000 in a manner consistent with that described in Section 6.2 of this thesis.

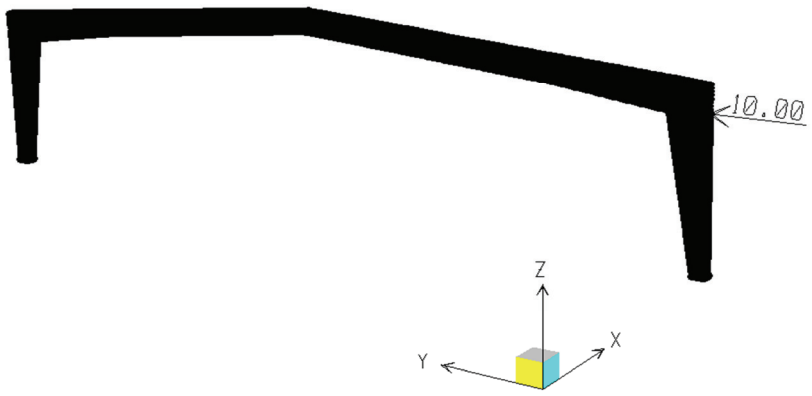

Figure 7-2: SAP model

The objective of the analysis was to reach a value of load which would result in deformation that could be accurately measured with the instrumentation while keeping the frame well below plastic (yield) limit. As a preliminary analysis, isolated frames were modeled. For the analysis the base of structure was considered as pinned. This approach is conservative as it maximizes the bending moments at the knee in the structure. From the analytical model, it was found that the application of 10000 lb laterally resulted in stresses that were less than 15 ksi, which is well below yield limit. Wind load analysis of the building (Chapter 3) using the ASCE 7-05 Low-Rise Method 2 analytical procedure resulted in an equivalent lateral load of 6100 lb. Based on this information, it was decided to test the frames with a load magnitude of 7500 lb.

7.3 Load frame assembly

To pull the building laterally, a load frame assembly was used. The assembly consisted of a steel frame, cables, two hydraulic rams, and concrete ballast. The ballast was needed to provide sufficient vertical normal force to keep the loading assembly from sliding during the experiments. The Figure 7-3 is a photograph of the assembly in-place in the Test Building.

Figure 7-3: Load frame and rigging assembly

The base of the test frame consists of two parallel tracks made of steel box sections (Figure 7-4). A square tube column was welded to a cross beam connecting the two tracks. The column could be extended in height to keep the line of load application as horizontal as possible. The extension was made possible by use of a telescopic interior column which could be lifted using a jack operated with a hydraulic pump. The load frame assembly was designed to resist forces well in excess of the test load.

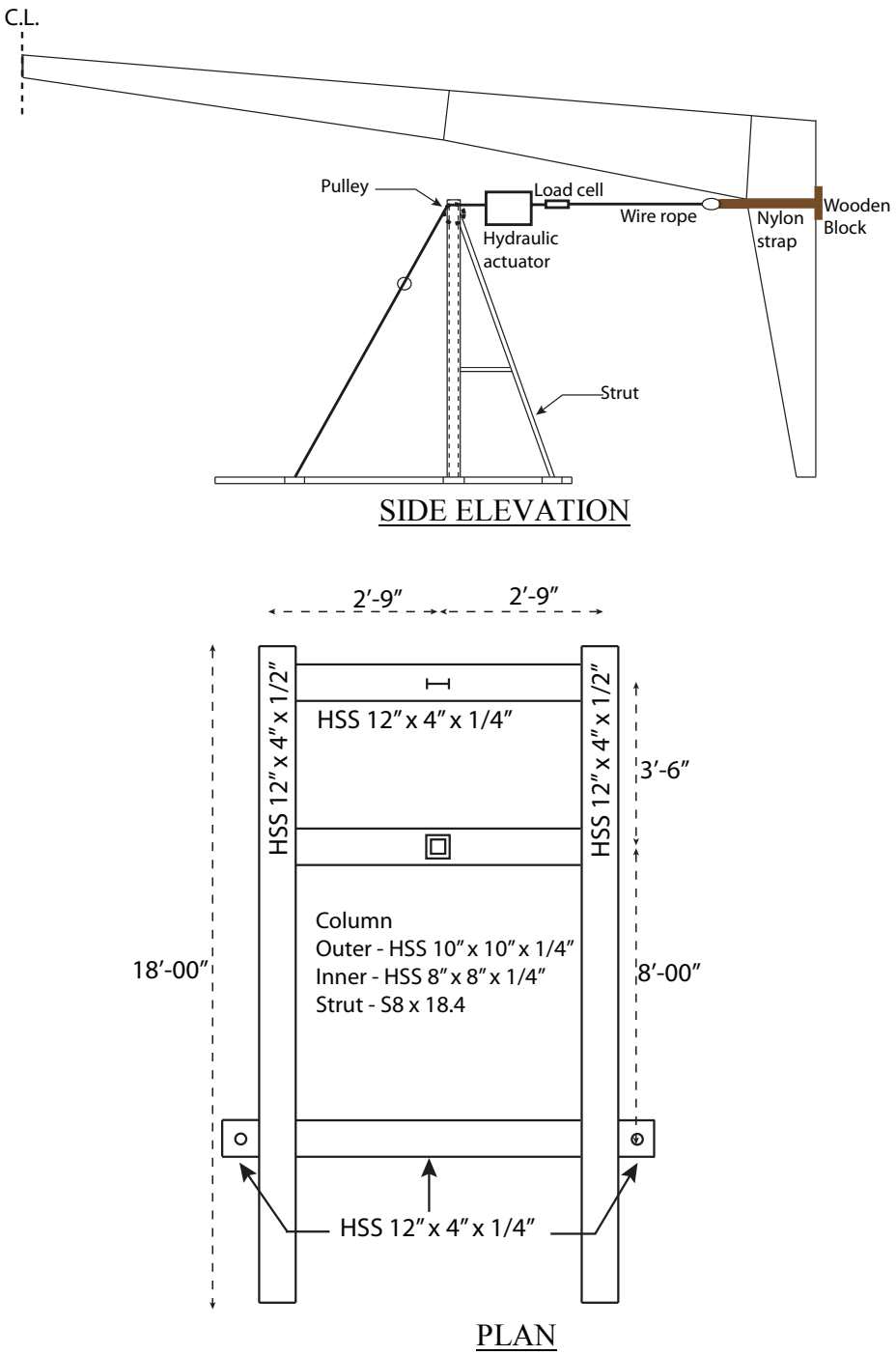

Figure 7-4: Frame dimensions and section sizes

As the wire rope ran over the pulley mounted on the top of column, application of lateral load on the building caused the load frame to slide towards the side of the building being loaded. To avoid this, a normal force was required which had to be more than the lateral load divided by coefficient of friction. The 7500 lb test load resulted in the requirement of a normal load reaction of at least 25000 lb (conservatively assuming the coefficient of friction between steel and concrete as 0.3). To provide this much weight, eight concrete blocks of size 27 in. x 27 in. x

54 in., each weighing approximately 3500 lb, were placed on the tracks as shown in Figure 7-3. The blocks were moved into position by use of a fork lift.

The plate welded steel frames were loaded by use of a cable - hydraulic ram - nylon strap system that was connected between the loading assembly and the frame. A wooden block of size 12" x 6" was used at the location of load application to provide uniform load distribution, and thereby avoid possible damage to the steel structure. A safety factor of 5:1 was used for all the components of the rigging assembly. Figure 7-5 shows the details of rigging assembly.

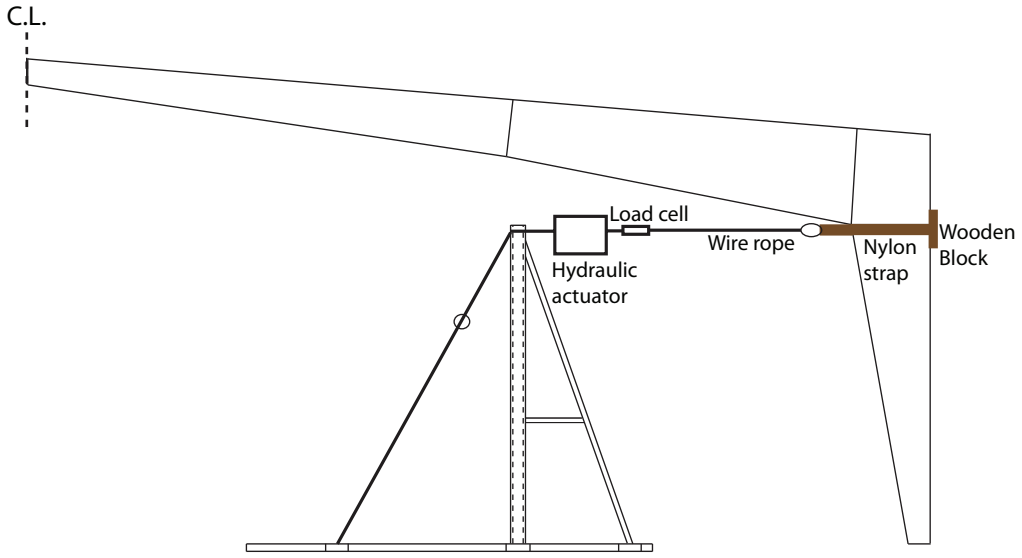

Figure 7-5: Rigging assembly

A load transducer was used in line with the rigging assembly to measure the load being applied to the building. The load cell was pre-calibrated in the laboratory for a load value of 18000 lb.

A hydraulic actuator of capacity 50000 lb was used to apply the test load on the building. It has twin action of compression and expansion. A hand pump was used to operate the actuator where compression (shortening) action made the wire ropes go taut and hence load the building gradually.

7.4 The Data Acquisition Systems

A Vishay Micro measurements data acquisition system 5000 was used to monitor the data. The frequency of measurement was 50 data points per second. The system has the capability to monitor data from 40 different sensors. Out of 32 strain gage channels 24 were used to sense changes in strain in the column flanges. Four of the high level channels were used to read rotation at the base of the column.

An additional data acquisition system by National Instruments "NI PX 1052" was used to read lateral deflections at the knee locations. This system had 16 channels. Fourteen channels were used to read deflection on both sides of all the frames including the cold formed steel end walls. One of the channels was used to read load from the load transducer.

7.5 Instrumentation

7.5.1 Strain Gages

The application of lateral load to the frames caused bending of the columns and rafters. To obtain a moment-rotation response at the base of the columns, the moment was evaluated by measuring strain close to the base of a column. Strain gauges were mounted on the column flanges at an elevation of six in. from the top of base plate. Six strain gauges, four on the inner column flanges and two on the outer column flanges were used. The location of strain gauges is shown in Figure 7-6.

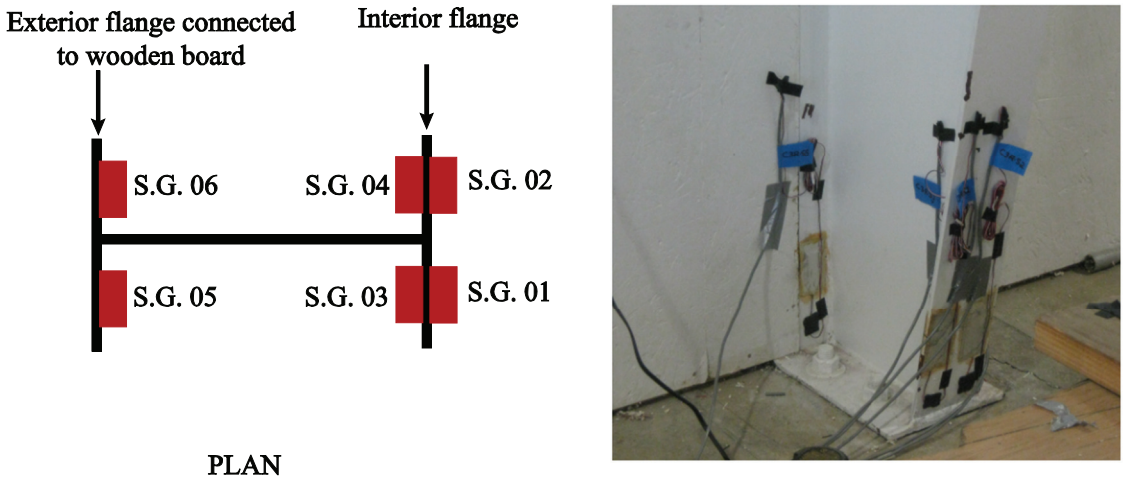

Figure 7-6: Location of Strain Gages

Strain gauges from Vishay micro measurements were used. Uni-axial pre-wired Strain gauge type "C2A-06-250LW-350" were used, which are suitable for metal surfaces. The resistance of strain gauge is 350 ohms. The procedure for installation of strain gage is included in Appendix B.

7.5.2 Inclinometers

In order to find the rotation of the columns near the base, inclinometers were used at the same elevation as the strain gauges. Voltage based inclinometers (NG2U series) manufactured by Reiker Inc. were used. The inclinometers were mounted on the web at mid-depth of the column near the base as shown in Figure 7-7. The inclinometers have a measuring range of ±10 degree

and a resolution of one fiftieth of a degree. The inclinometers were calibrated in the Structures Laboratory using a simply supported beam. The calibration procedure is provided in Appendix C.

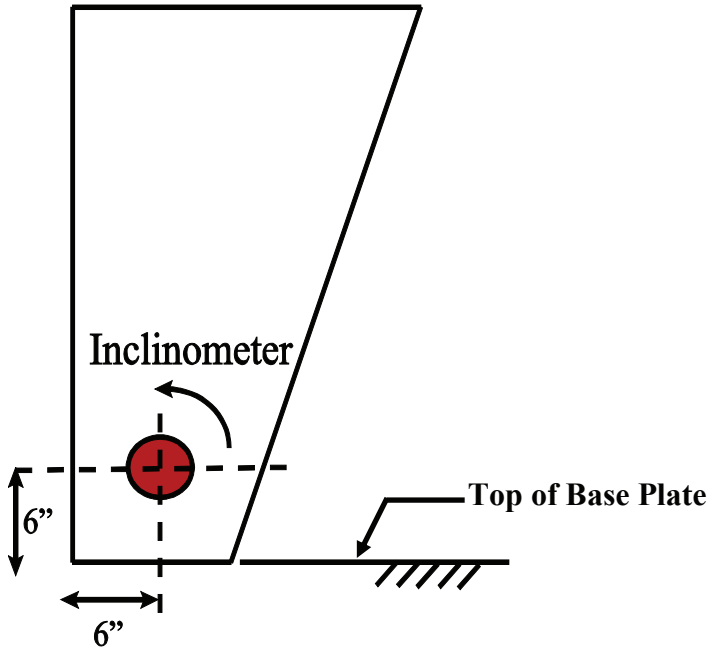

Figure 7-7: Inclinometer location on column web

7.5.3 Linear voltage displacement transducer (LVDT) and wire potentiometers

Lateral deflection of the building was monitored with linear voltage displacement transducers. These instruments were reading deformations at column-rafter interface (Figure 7-8). The LVDT’s are capable of measuring deformation to a resolution of one thousandth of an in.

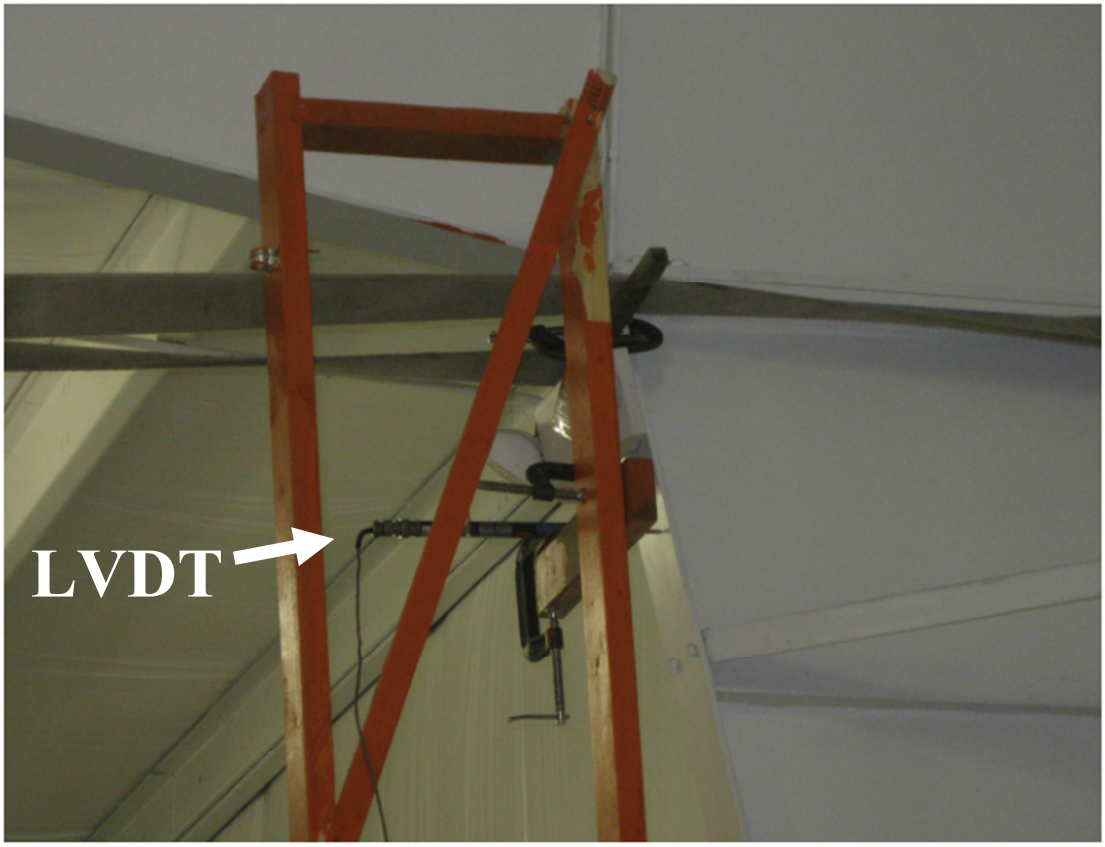

Figure 7-8: Location of Linear voltage displacement transducer

Wire potentiometers were used to measure lateral drift for some of the frames. The wire-pots and LVDTs were fixed to the top of wooden frames using C-clamps. The wooden frames were used to keep the drift measuring instruments in place without coming into contact with the main steel frames. The LVDTs and wire-potentiometers were calibrated in laboratory before taking them out to the site. The procedure for calibration has been provided in Appendix C.

7.6 Test Results

Before starting any test, the load frame was aligned with the frame to be loaded. This was done by matching the center lines of column on the load frame and that of frame being pulled. The rigging assembly was then put in line with the nylon strap going around the column which was to be pulled. Once the assembly was set up, the slack in the wire rope (which was used for pulling) was removed by adjusting the height of the column on the load frame so as to make the line of pull as horizontal as possible. A hand pump was then used which caused the actuator to shorten, inducing tension in the wire rope. This resulted in loading of the frame. While unloading, the pressure from the pump was gradually released. For each frame, three tests (with full loading and unloading cycles) were performed.

7.6.1 **Load-Displacement Response**

Application of lateral load on the test building resulted in near linear load deformation response. The frame which was directly loaded had significant deformations at the loaded end of the frame. The frames which were immediately adjacent to the loaded frame had much smaller deformations. For example the frames along lines 3, 4 and 5, when directly loaded, deformed approximately 0.30 to 0.35 in. when the test load was 7.5 kip. The deformations at the same end of the adjacent frames were approximately 0.010-0.015 in., which is only 3 to 5% of the deformations on the loaded frames. The deflections in which were frames two-bays from the loaded frame were less than the instrument resolution.

The measured deflection at the unloaded end of the test frame was expected to be less than the deflection at the loaded end. In some cases this occurred, but in other instances the deflection at the unloaded end was greater than the deflection at the loaded end. However, in most cases, the difference in loaded and unloaded end deflections was small.

The full set of load-deflection plots obtained from the testing are presented in Appendix D. A sample of these plots are presented and discussed below.

Loading Exterior Frame on Frame Line 02

Figure 7-9 is a plot of the load-deflection response for the frame on line 2 pulled from South to North. Frame 2 is an "Exterior" frame which has less depth at the knee, but greater depth at mid-span when compared to the Interior frames. Displacement responses are shown for both the loaded and unloaded ends. Note that the vertical axis on the plot represents the applied load (from 0.0 to 7.5 kip) but does not necessarily represent the actual load resisted by the frame. The maximum resisted load will be somewhat (approximately eight percent) less than 7.5 kip due to load being distributed to the adjacent frames. Estimates of the load actually resisted by the frame are presented in Chapter 8 of this thesis.

As may be seen by the load-deflection plot for Frame 2, the response was near linear, with the South (loaded) end displacing more than the North end during low-level loads, but displacing less than the North end at loads approaching 7.5 kip. There appears to be a slight change of slope in the North end response at an applied load of approximately 2.5 kip. The maximum displacement attained at the loaded end of the frame was 0.25 in. The slope of the Load-Displacement curve is approximately 7.5/0.25=30 kip per in.

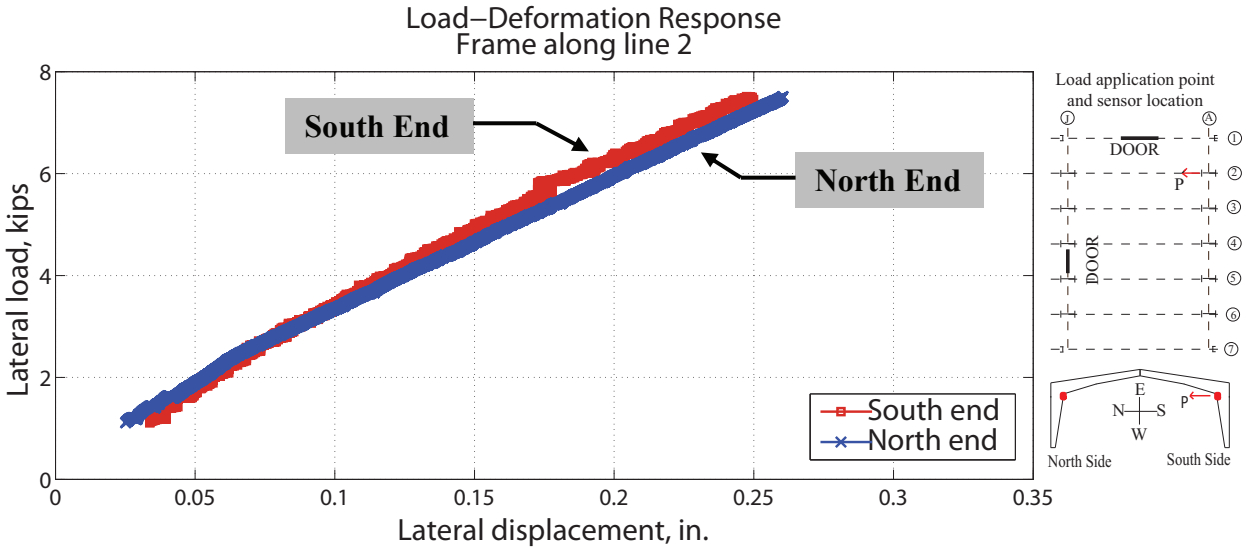

Figure 7-9: Load Displacement Curves for Load Applied on Frame 02

Loading Interior Frame Along Frame Lines 03

The force-displacement plot for Interior frame on Line 03, loaded at the South end, is given in Figure 7-10. As with the Frame on Line 02, the response is near linear, with the deflection at the loaded end being somewhat less than the deflection at the unloaded end. The maximum displacement obtained at the loaded end was 0.23 in. when the applied load was 7.5 kip. The slope of the Load-Displacement curve for the loaded end of the frame is approximately 7.5/0.23=32.6 kip/in.

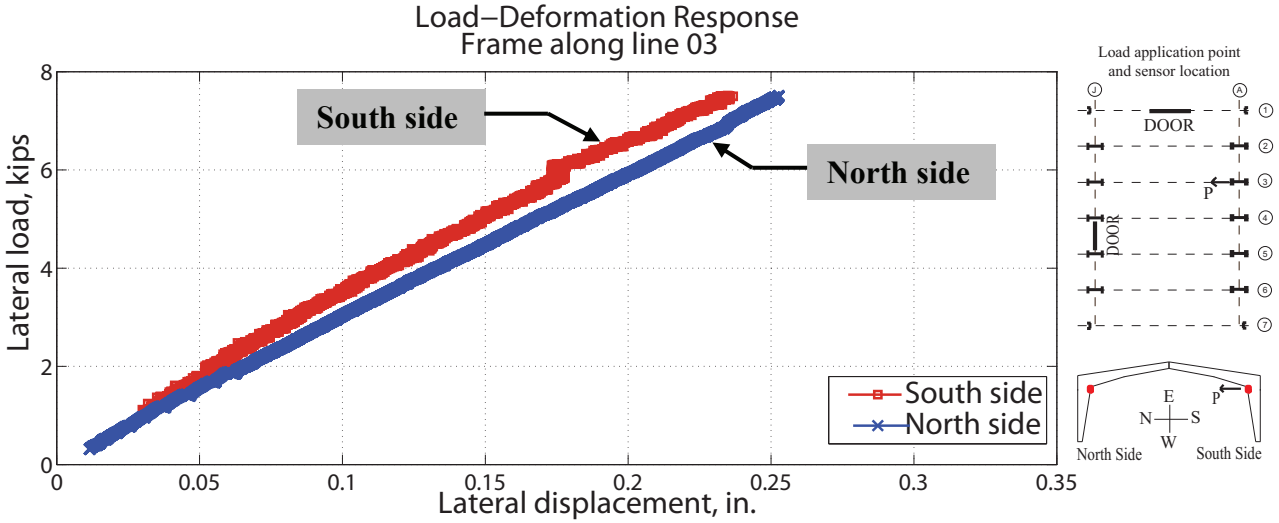

Figure 7-10: Load Displacement Curves for Load Applied on Frame 03

Loading Interior Frame Along Frame Line 04

The load-deflection response for the frame on Line 04, loaded at the South End is presented in Figure 7-11. In this case the responses are linear, and the deflection at the loaded end of the frame is significantly greater than the deflection at the unloaded end. The peak deflection at the loaded end was 0.32 in. when the applied load was 7.5 kip, producing a Load-Displacement slope of 7.5/0.32 = 23.4 kip/in. It is interesting to note that the deflection at the unloaded end of Frame 04, approximately 0.25 in., is nearly identical to the displacement obtained at the unloaded end when Frame 03 was loaded (see Figure 7-10).

When the frame on Line 04 was loaded on the North end, the load-deflection plot shown in Figure 7-12 was obtained. As with the South end loading, the response is linear, and the displacement at the loaded end is greater than the displacement at the unloaded end. However, the displacement at the loaded end of the frame is approximately 0.275 in., which is less than the displacement obtained when the South end was loaded. The Load-Displacement slope of 7.5/0.275=27.3 kip/in. when the frame was loaded on the North end.

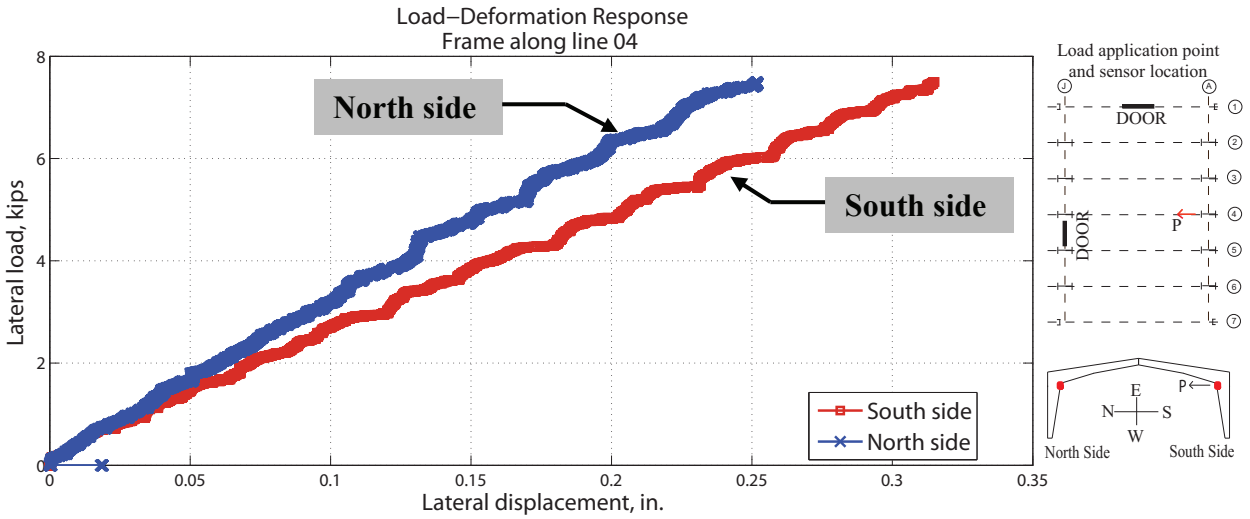

Figure 7-11: Load Displacement Curves for Load Applied on Frame 04

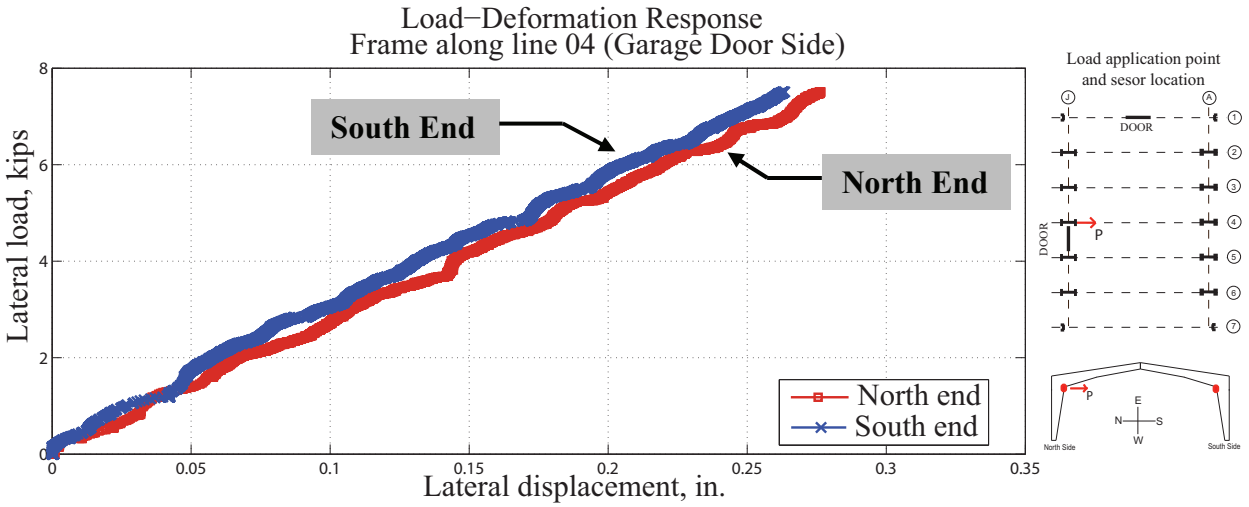

Figure 7-12: Load Displacement Curves for Load Applied on Frame 04

Loading Interior Frame Along Frame Line 05

The load-deflection response for the frame on Line 05, loaded at the South end is presented in Figure 7-13. In this case the responses are linear, and the deflection at the loaded end of the frame is somewhat greater than the deflection at the unloaded end. The peak deflection at the loaded end was 0.28 in. when the applied load was 7.5 kip, producing a Load-Displacement slope of 7.5/0.28 = 26.8 kip/in. As with Frames 03 and 04, the deflection at the unloaded end of Frame 05 is approximately 0.25 in.

The load-deflection plot for frame 05 loaded at the North end is provided in Figure7-14. The deflection at the loaded end is greater than the deflection at the opposite end. The slope of the load deflection plot at the loaded end is 7.0/0.31=24.2 kip/in.

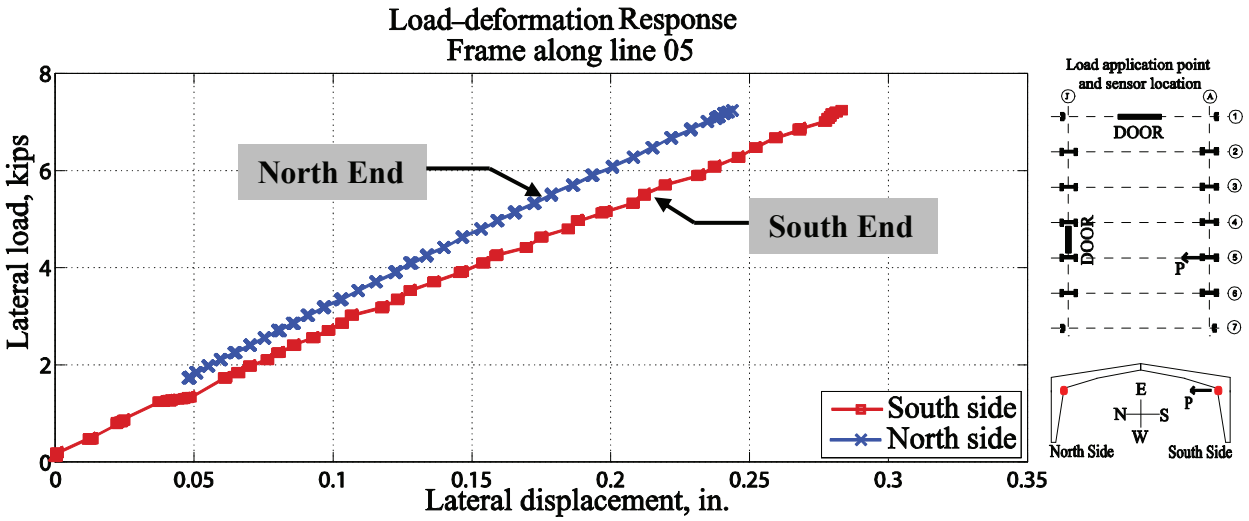

Figure 7-13: Load Displacement Curves for Load Applied on Frame 05

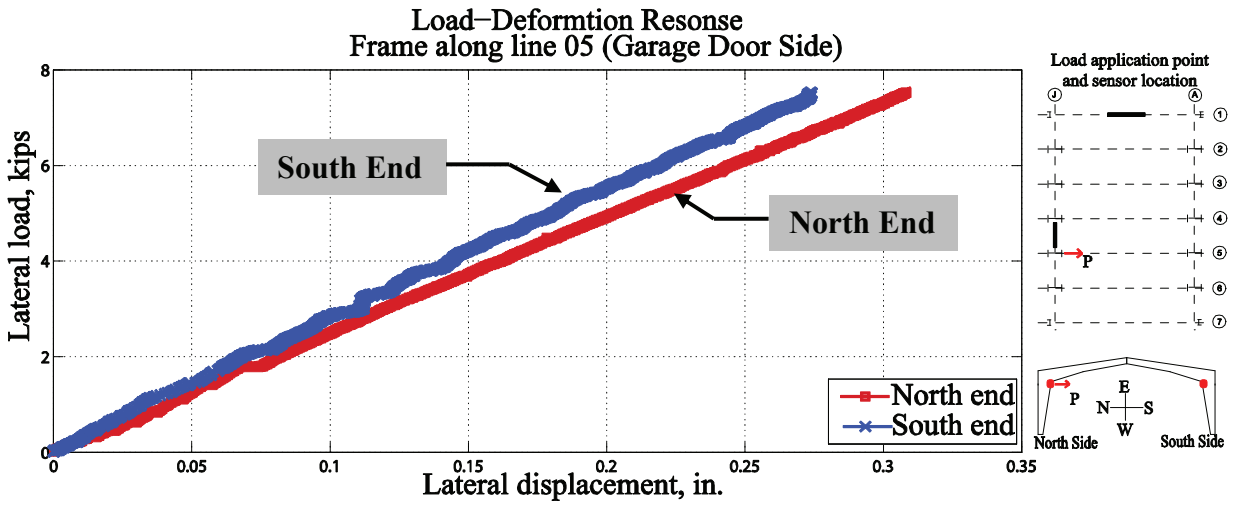

Figure 7-14: Load Displacement Curves for Load Applied on Frame 05

Loading Exterior Frame Along Frame Line 06

The load-deflection plot for frame 06 is given in Figure 7-15. This frame was loaded only at the South end, and the maximum applied load was 6.5 kip. The deflection at the loaded end was greater than the deflection at the unloaded end. The shape of the load-deflection curve for the South end is somewhat erratic. (Among the three plots obtained for this test, the response shown in Figure 7-15 is the least erratic). The slope of the load deflection curve at the loaded end is 6.5/0.21=32.1 kip/in.

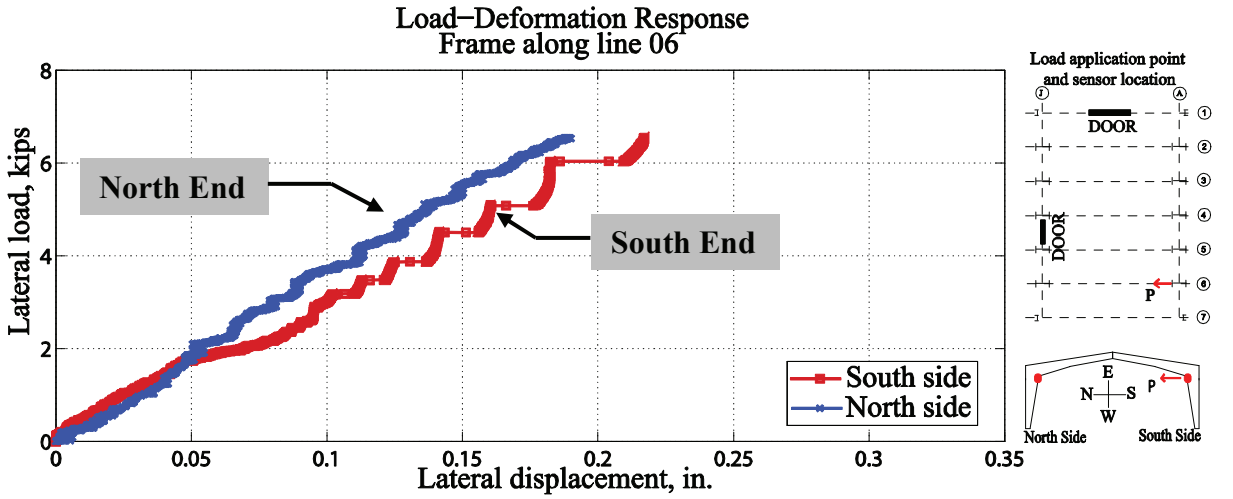

Figure 7-15: Load Displacement Curves for Load Applied on Frame 06

A summary of the results of the tests is shown in Table 7-1. Note that the results for the test on the South End of Frame 6 were adjusted to provide values consistent with a 7.5 kip load.

There is no clear trend in the results, except that the deflections at the loaded end of the Interior frames appear to be somewhat greater than the deflections in the Exterior frames. The exception is Frame 3, which had a measured deflection of only 0.24 in.

Based on the results the average value of load/deflection is approximately 31.0 kip per in. for the Exterior Frames and 26.5 kip/in. for the interior frames. As noted earlier, however, these values do not represent the stiffness of the individual frames because there was some load sharing to the adjacent frames.

Table 7-1: Summary of Load-Deflection Results

Frame	Loaded End	Applied Load (kip)	Loaded End Deflection (in.)	Unloaded End Deflection (in.)	Load/Deflection at Loaded End (kip/in.)	Loaded End Defl./Unloaded End Defl.
2	S	7.5	0.25	0.26	30.0	0.96
3	S	7.5	0.24	0.25	31.2	0.96
4	S	7.5	0.32	0.25	23.4	1.28
	N	7.5	0.28	0.26	26.8	1.07
5	S	7.5	0.28	0.25	26.8	1.12
	N	7.5	0.31	0.27	24.2	1.15
6	S	7.5	0.24	0.20	32.1	1.20

Response of Frames 03 and 05 When Frame 04 is Loaded

Figure 7-16 shows the measured responses at both ends of Frames 03, 04, and 05 when Frame 04 is loaded on the South end. The response of Frames 03 and 05 are shown in expanded form in Figure 7-17. Note that the curves in Figure 7-17 have a somewhat erratic appearance because these measurements are at the low-end of the instrument resolution. Similar results are shown for other loadings in Figures 7-18 through 7-21.

Two observations can be made about the curves presented in Figures 7-16 and 7-17:

1. The deflection at the South (loaded) end of the adjacent frames (approximately 0.013 in.) is significantly less than the deflection South end of the loaded frame (approximately 0.3 in.). If it is assumed that the frames have the same lateral stiffness (all of the frames are interior frames) it can be estimated that 0.3/ (0.3+2x0.013) = 0.92 times the applied load of 7.5 kip, or 6.9 kip is being carried by the loaded frame.

2. The deflection at the North end of the adjacent frames is about half of the deflection of the South end. This can be attributed to the flexibility of the purlins which are "rolled over" when the load is applied.

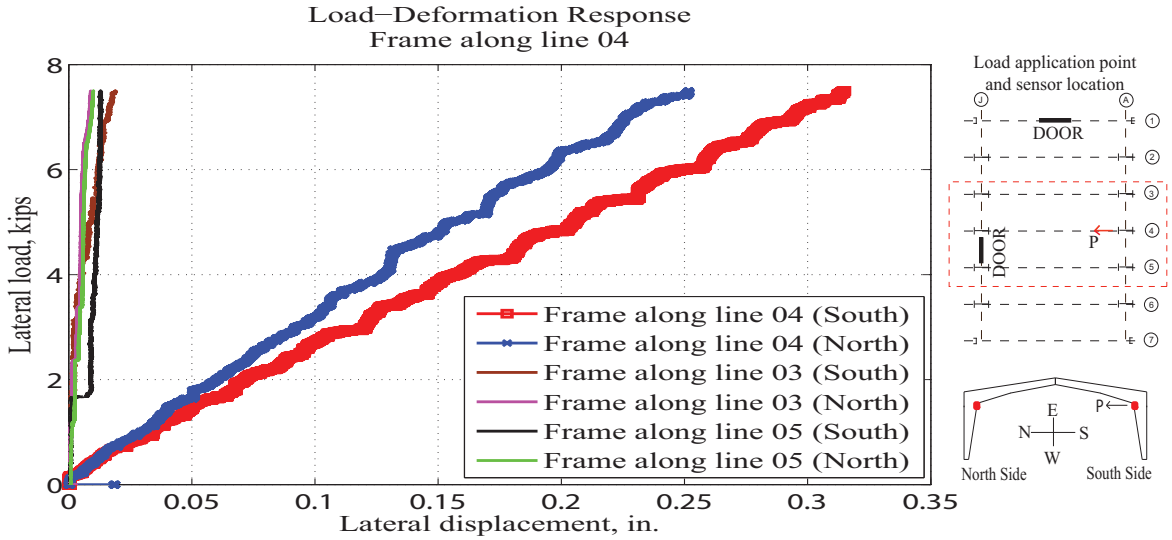

Figure 7-16: Load-Deflection Response loaded and Adjacent Frames, Frame pulled along line 04

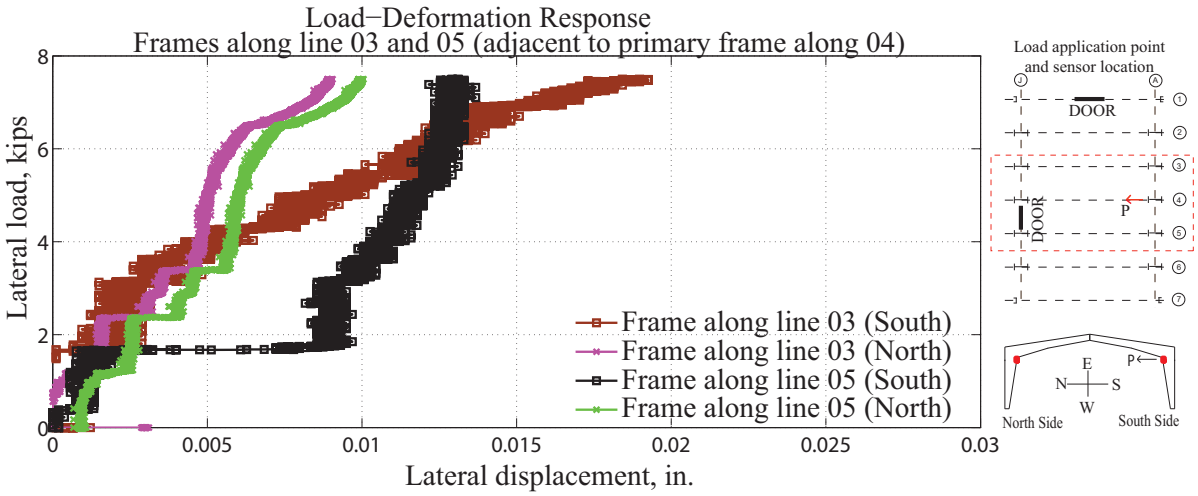

Figure 7-17: Results for adjacent frame, frame pulled along line 04

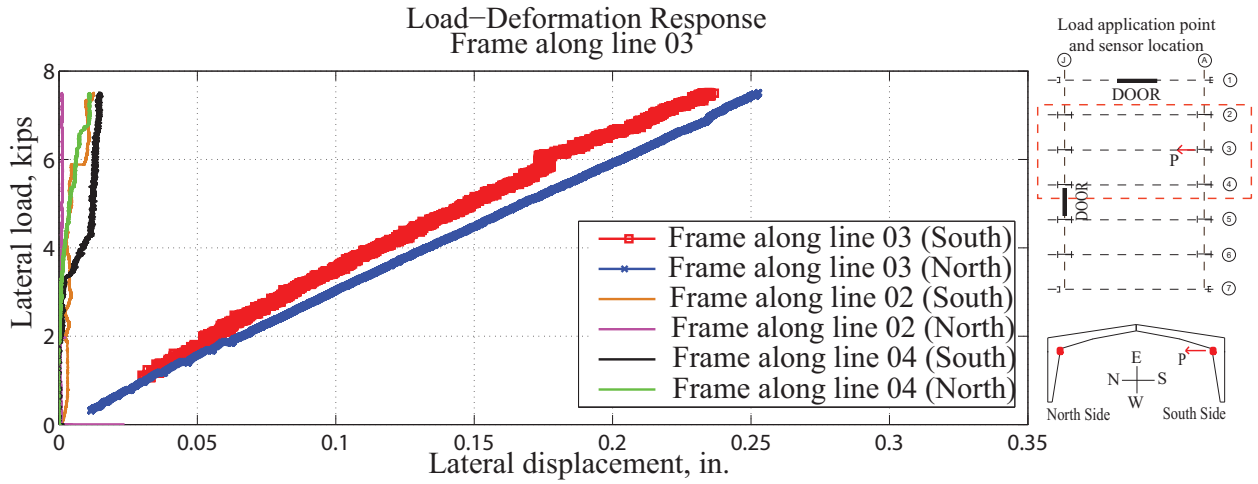

Figure 7-18: Load-Deflection Response loaded and Adjacent Frames, Frame pulled along line 03

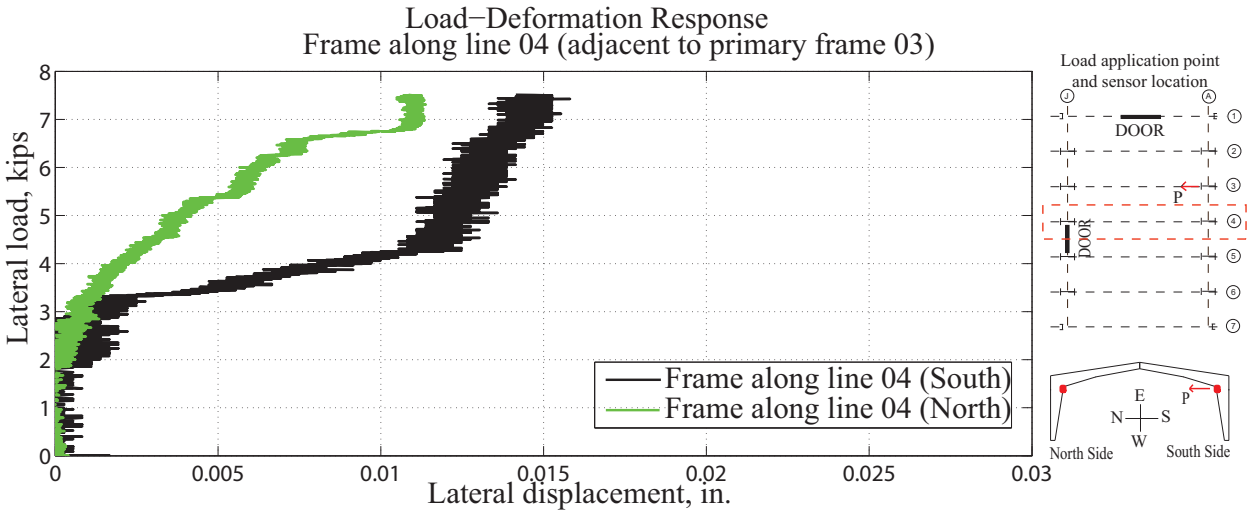

Figure 7-19: Results for adjacent frame, frame pulled along line 03

Displacement sensors along frame 02 did not monitor much deformation as it was a stiff frame and deformations obtained were really small and beyond resolution of instrument.

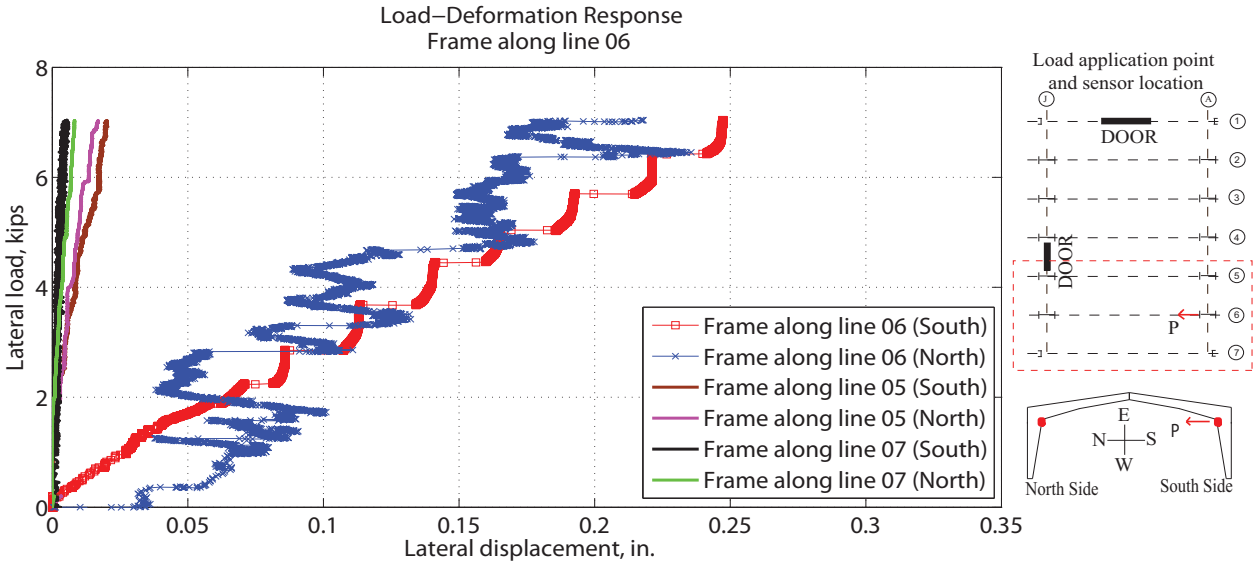

Figure 7-20: Load-Deflection Response loaded and Adjacent Frames, Frame pulled along line 06

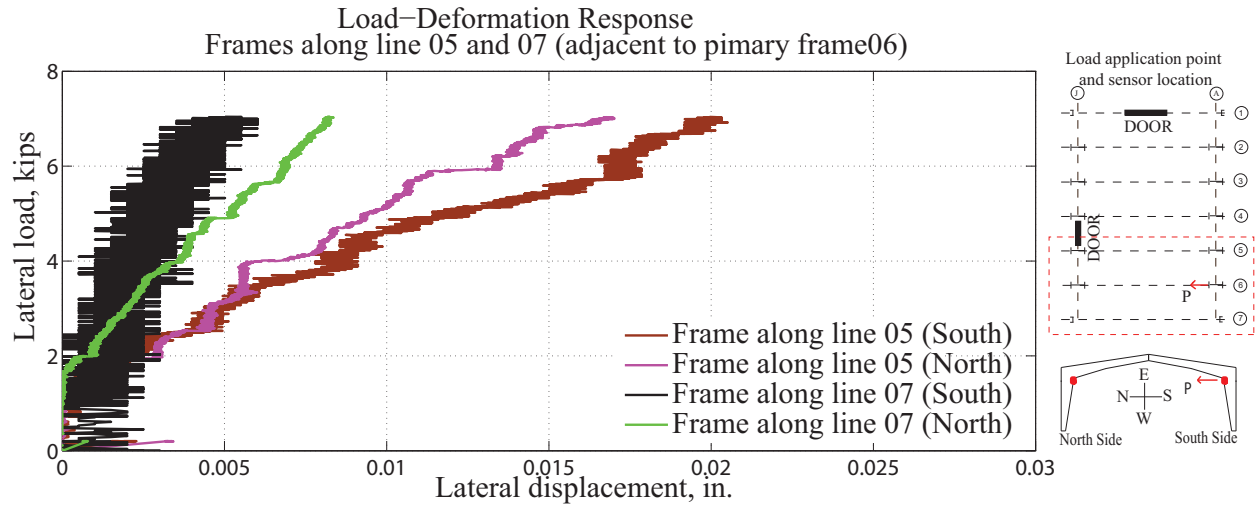

Figure 7-21: Results for adjacent frame, frame pulled along line 06

7.6.2 Moment - Rotation Response

As the building starts to deform laterally under the effect of the applied load, columns and rafters experience bending. The column base experiences moment which is resolved as tension-compression couple acting along the flanges (Figure 7-22).

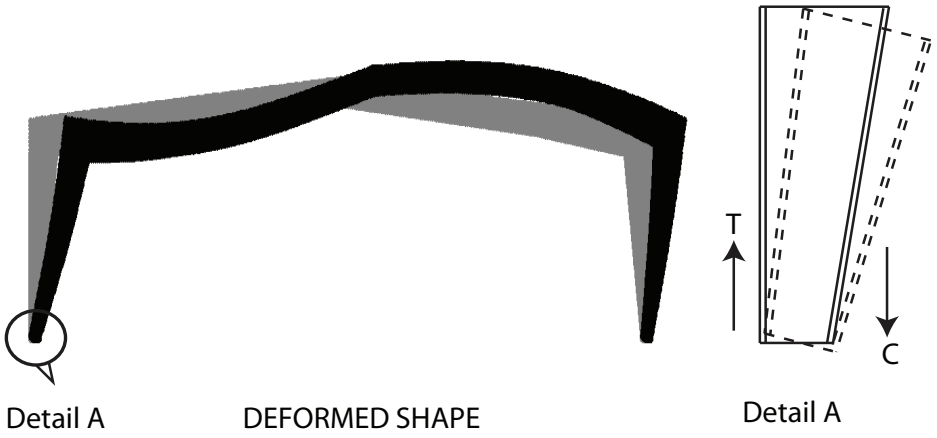

Figure 7-22: Bending of columns and rafters

Strain gauges mounted on the column flanges monitored change in strain. Inclinometers mounted on the webs of the columns were used for measuring the tilt (rotation) at the base. This behavior was measured at the "loaded end" of the loaded frames and the two adjacent frames, and at the unloaded end of the loaded frame. It is noted that all of the strain gage and inclinometer data was of poor quality because the measurements were at the low end of instrument resolution, and electrical noise tended to obscure that part of the data which is of interest. Data obtained at columns adjacent to the loaded columns was indiscernible from the noise, so was not used. While the data for the loaded columns could be extracted but did not provide useful results in most cases.

The moment at base of the column was evaluated in accordance with the calculations provided below.

Resulting axial force (P) and moment (M) are calculated as per expression below.

$$P = \left(\frac{\varepsilon_C + \varepsilon_T}{2} \right) EA$$

$$M = \left(\frac{\varepsilon_C - \varepsilon_T}{2} \right) ES$$

where

ε_C Average strain on compression flange

ε_T Average strain in tension flange

A Cross sectional Area

S Section Modulus

E Modulus of elasticity

In this section plots have been presented for one typical interior frame and one exterior frame. As the load applied to any of the frames caused a very small change in strain, the results obtained were not very consistent. The strain gages are very sensitive to a couple of factors such as any electrical or mechanical noise, length of wire from strain gage to data acquisition system, other voltage instruments connected to same data acquisition system. The noise induced due to these factors was considerable and in same range as the signal sensed by gages. Hence, the data obtained was not always reliable. At some locations some linear trend was observed in moment-rotation plots.

Loading Exterior Frame Along Frame Line 02

The frame was pulled towards North. Figure 7-23 and Figure 7-24 shows the moment rotation response for South (loaded end) and North end respectively. The response was obtained using procedure described in Section 7.6.2. The figure shows a linear trend for the column which is being directly loaded, however, the strain gages on other side does not show any trend. Moreover, it could also be seen from the figures that moment does not start from zero which shows the noise from external sources while monitoring.

For the near end, the slope of the moment-rotation line is approximately 24,500 k-in./radian.

Loading Interior Frame Along Frame Line 04

This frame was loaded on South side and pulled towards North. Figure 7-25 and 7-26 show the moment response for loaded and unloaded end respectively. For this test the loaded end did not show a linear trend as opposed to what was seen for Frame along line 02. However, the end opposite the loaded end displayed an apparent rotational stiffness of 25,000 k-in/radian. This is nearly the same as observed for the loaded end of frame 02.

Moment-rotation plots for the other tests are provided in Appendix D. The slopes of these curves do not display any particular trend, and thus there is a large variation in the experimental "stiffness" of the column to base connections.

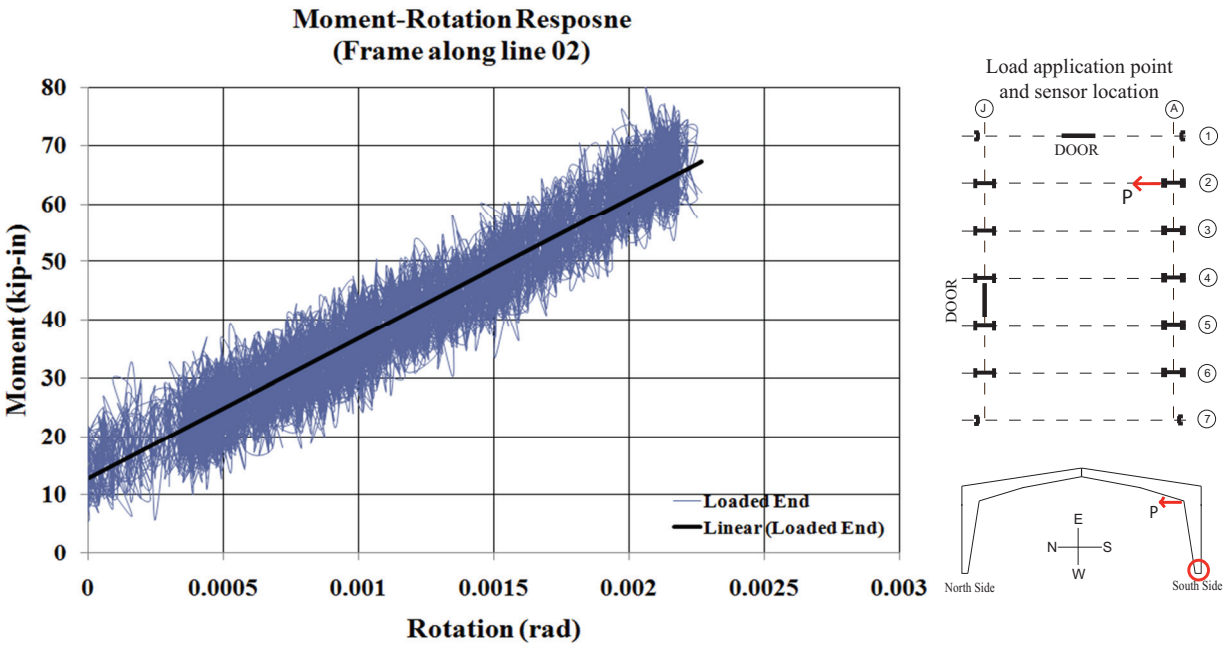

Figure 7-23 Moment-Rotation at Loaded end of Base of Columns for Exterior Frame 02

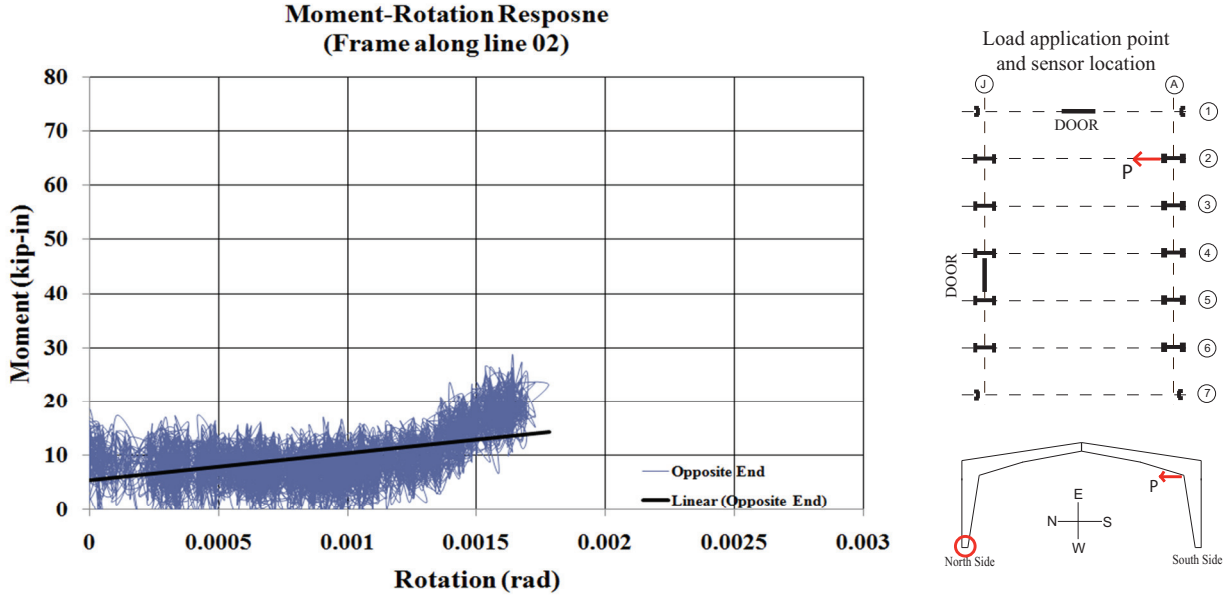

Figure 7-24 Moment-Rotation at Opposite end of Base of Columns for Exterior Frame 02

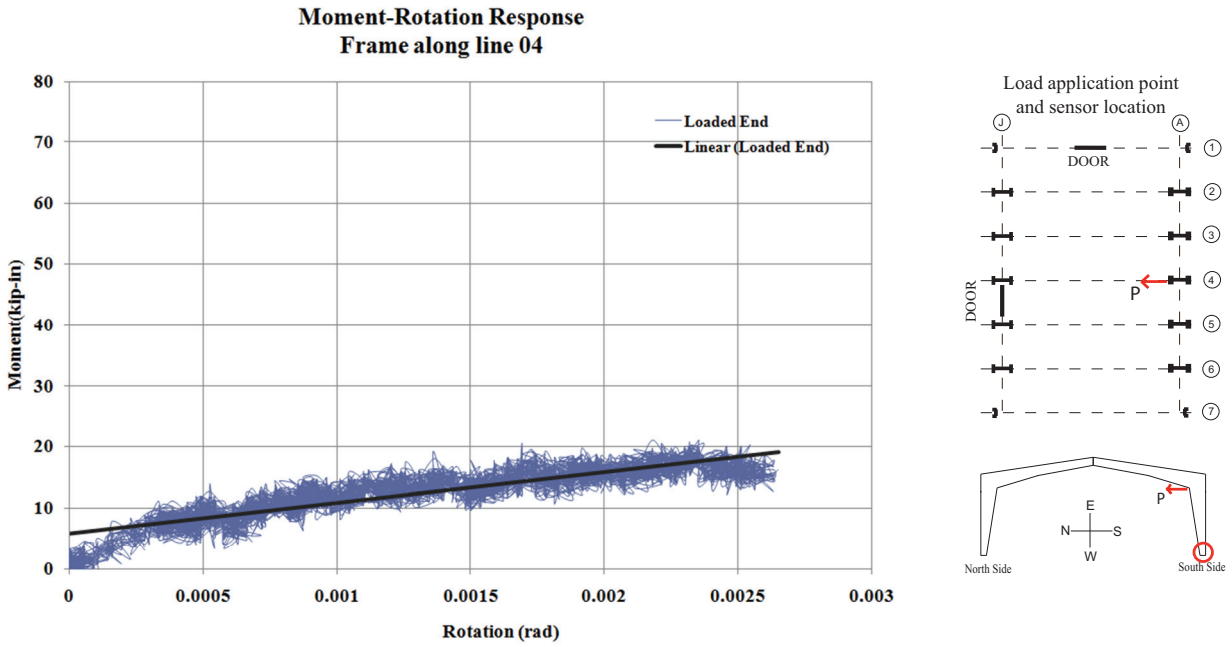

Figure 7-25 Moment-Rotation at Loaded end of Base of Columns for Exterior Frame 04

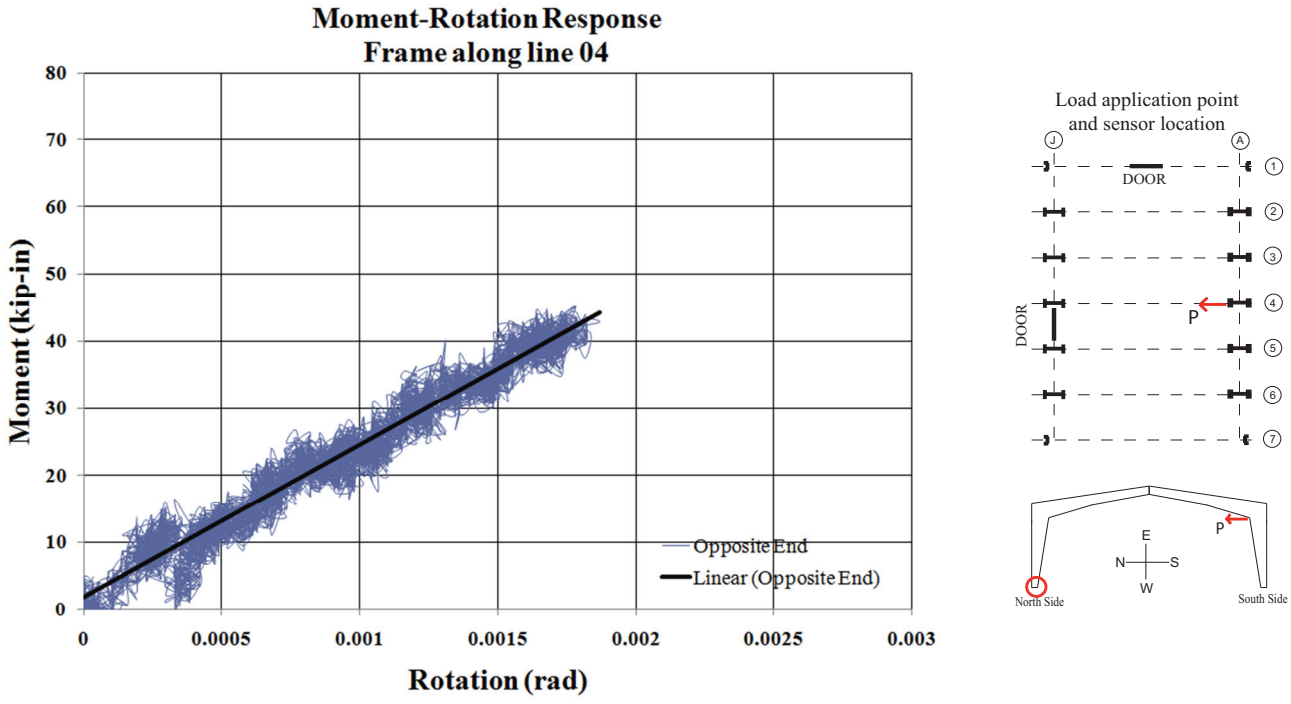

Figure 7-26 Moment-Rotation at Opposite end of Base of Columns for Exterior Frame 04

Chapter 8 Three-Dimensional Modeling

8.1 Introduction

The results obtained from the two-dimensional analysis of individual gable frames were not consistent when compared with those obtained from the experimental testing program, with the experimental results indicating a stiffer structure than obtained from the analysis. Hence, it was decided to use a complete three-dimensional model of the test building to account for a number of factors which were not considered in the two-dimensional planar model. These factors mainly consisted of the effect of secondary steel purlins and girts, and the in-plane diaphragm action of the wall and roof sheeting. The additional flexibility of the diaphragm due to fastener layout and detailing was not considered in this thesis. This chapter provides details of the three-dimensional modeling of the whole building. The modeling and analysis was performed using SAP 2000 (Computers and Structures 2008). Figure 8-1 shows a rendered view of the building modeled in three-dimensions. The model was created in stages in order to check the effects of individual factors. Section 8.2 discusses the details of the various stages of the model creation.

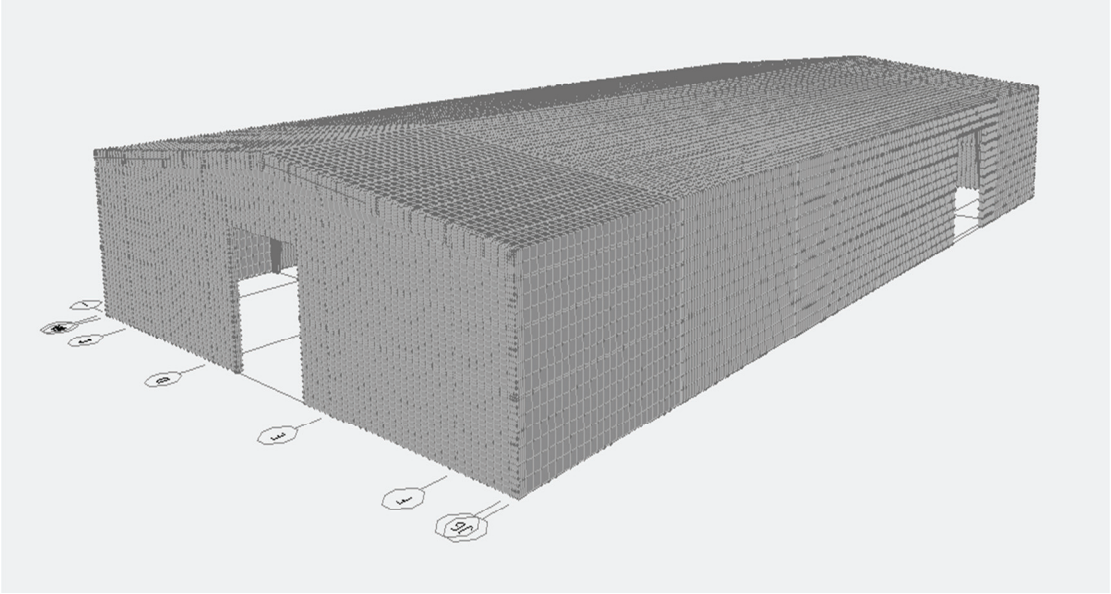

Figure 8-1: Rendered view of three-dimensional Model

8.2 Staged Construction

Starting with the model that was used for two-dimensional analysis, the full three-dimensional model was developed by adding modeling components in a step by step fashion. The following

five stages describe the steps of modeling which range from simple and less time consuming to most complex and modeling intensive.

8.2.1 **STAGE 01 – Interior Gable Frames with Purlins and Girts**

All of the web-tapered steel I-section frames along line 2 through 6 (Figure 4-2) were modeled using four node shell elements. Purlins and girts were modeled with thin shell elements to connect these frames to each other as shown in Figure 8-2. The purpose of this analysis was to account for the stiffness provided by purlins and girts.

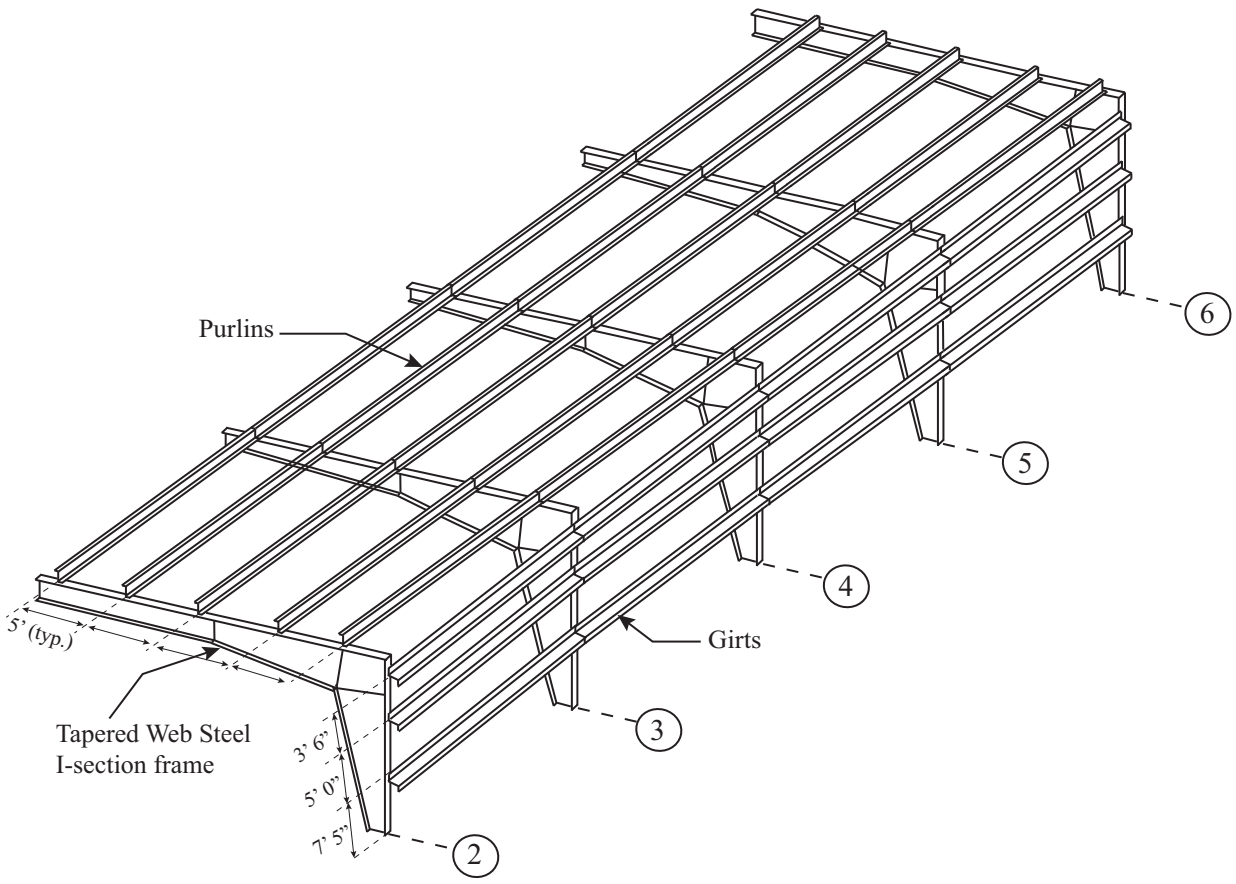

Figure 8-2: STAGE 01 – Web-tapered I-section frames along grid 2 through 6

8.2.2 **STAGE 02**

In this stage metal roof and wall sheeting were added to the model used in STAGE 01 using thin shell elements having isotropic (the same properties in two orthogonal direction) membrane and bending thickness of 0.0179 in. (26 gage). The intent of using isotropic properties was to start

with a simple model and add the orthotropic properties later as the model is developed further. Orthotropic behavior is discussed in following stages. The sheeting was modeled as flat sheets as shown in Figure 8-3. No screw and stitch fasteners were incorporated. The connection between the rafter and purlin, purlin and metal deck, column and girt, and girt and metal deck was defined by overlap of shell elements at respective interfaces. The modeling details at these locations are described in more detail in Section 8.3.

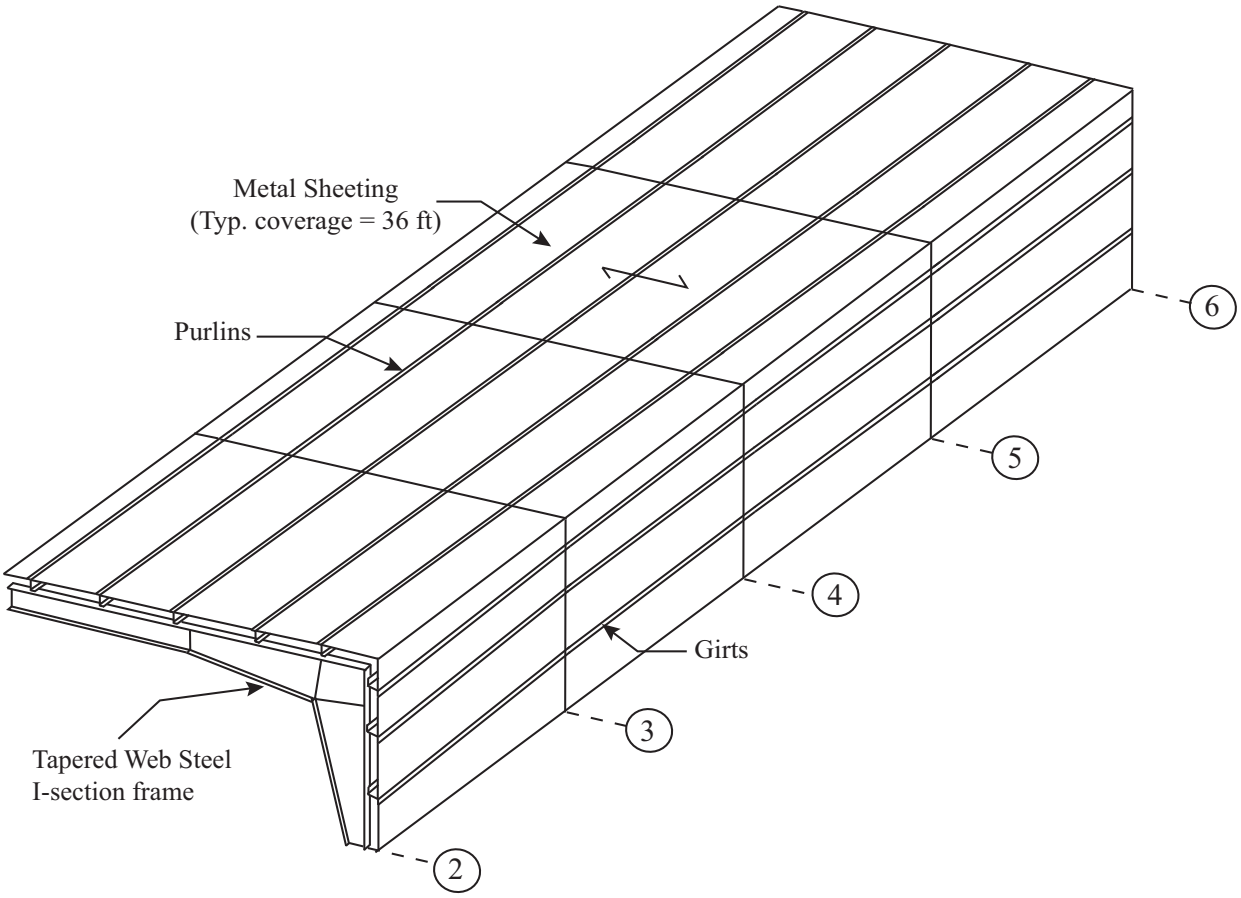

Figure 8-3: STAGE 02 – Web-tapered I-section frames along grid 2 through 6 with metal sheeting

8.2.3 **STAGE 03**

For the actual test building the exterior frame along line 2 was attracting stiffness from the interior frame along line 3 and from the cold formed end wall along line 1. Typically, in a metal building, the end frames are cold formed sections which are expected to provide greater lateral stiffness as compared to the I-section gable frames. In order to verify the effect of the end wall for this building, the end wall was modeled first as a gable frame (STAGE 03), and again as a

true end wall (STAGE 04). For the STAGE 03 model the end frame was modeled using the same web tapered I-sections as were used for the frame along line 02 as shown in Figure 8-4. The analysis was performed and compared with results of the model in STAGE 04 (described in the next section) which has actual cold-formed steel end walls. This gave a measure of the relative stiffness of the end frames modeled using cold formed sections and web tapered I-sections.

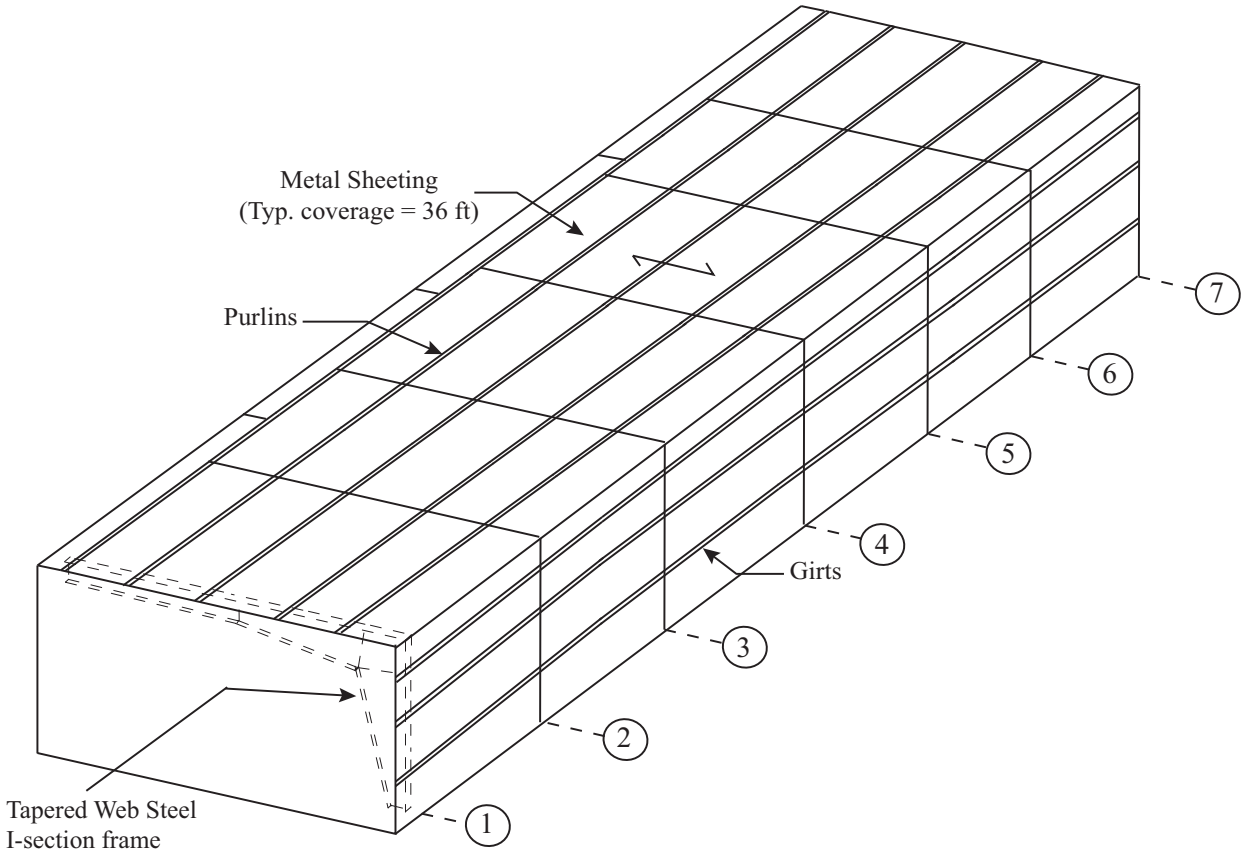

Figure 8-4: STAGE 03 – Web-tapered I-section frames along grid 1 through 7 with metal sheeting

8.2.4 **STAGE 04**

As mentioned before, for the model in STAGE 04, the actual end walls made from cold formed steel were modeled. Girts and wall cladding were also modeled in the end bay as shown in Figure 8-5.

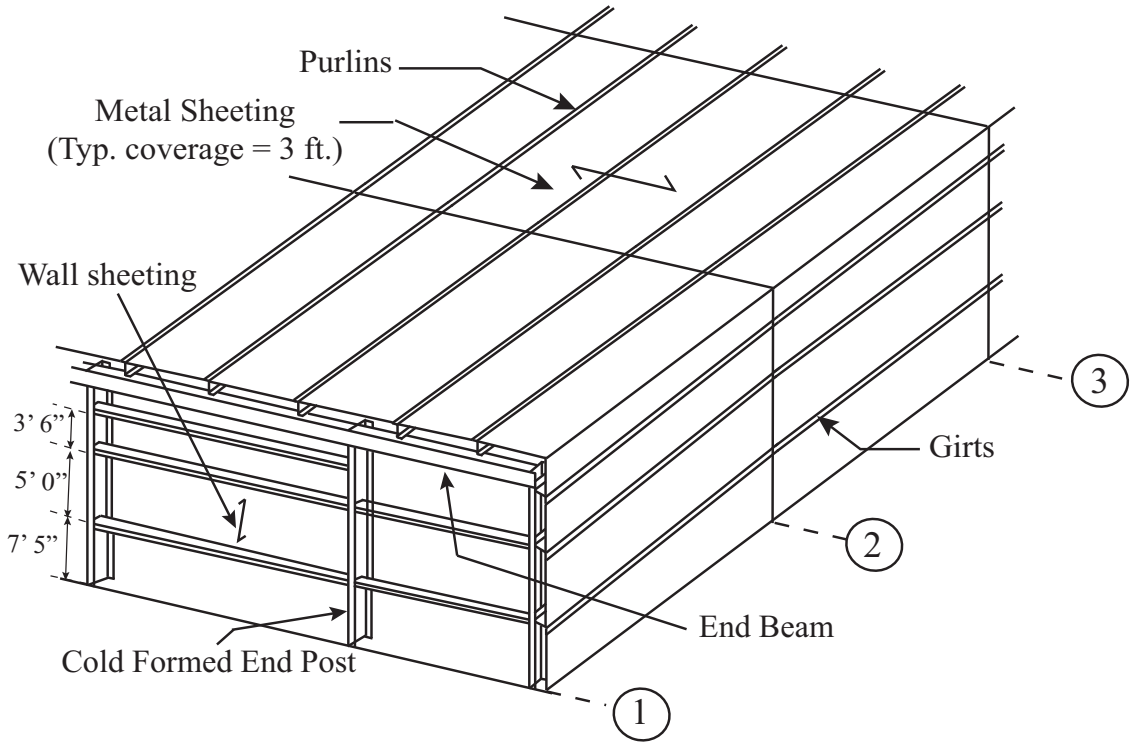

Figure 8-5: STAGE 04 – Web-tapered I-section frames along grid 2 through 6 and cold-formed end walls along line 1 and 7 with metal sheeting

8.2.5 **STAGE 05**

The models developed in STAGE 02 through STAGE 04 had isotropic flat roof and wall diaphragms. However, for the actual test building the metal sheeting was profiled (having ribs to increase the strength and bending stiffness of the sheeting when subjected to gravity and/or wind loads. Thus, the true behavior of the deck is orthotropic (with different properties in orthogonal directions). To capture this effect, the sheeting for the model in STAGE 05 was provided with properties of profiled deck. These properties were recovered by performing another analysis where a panel of profiled deck was modeled and subjected to axial, bending, and shear deformations. Once the orthotropic properties were obtained, analysis was performed for the flat sheeting model (now with orthotropic properties) that was used in the STAGE 04 models.

8.3 Modeling

This section discusses the procedures that were used to model various components of building.

8.3.1 Main Wind-Force Resisting System (MWFRS)

The Main Wind-Force Resisting System was modeled in same fashion as already discussed in Section 6-3. Thin shell elements representing the thickness of the corresponding parts of a member were used to model the columns, rafters and stiffeners. Each shell element had six degrees of freedom at each node. For columns and rafters, the flange was modeled using two elements along the width while the web had eight elements along the depth as shown in Figure 8-6.

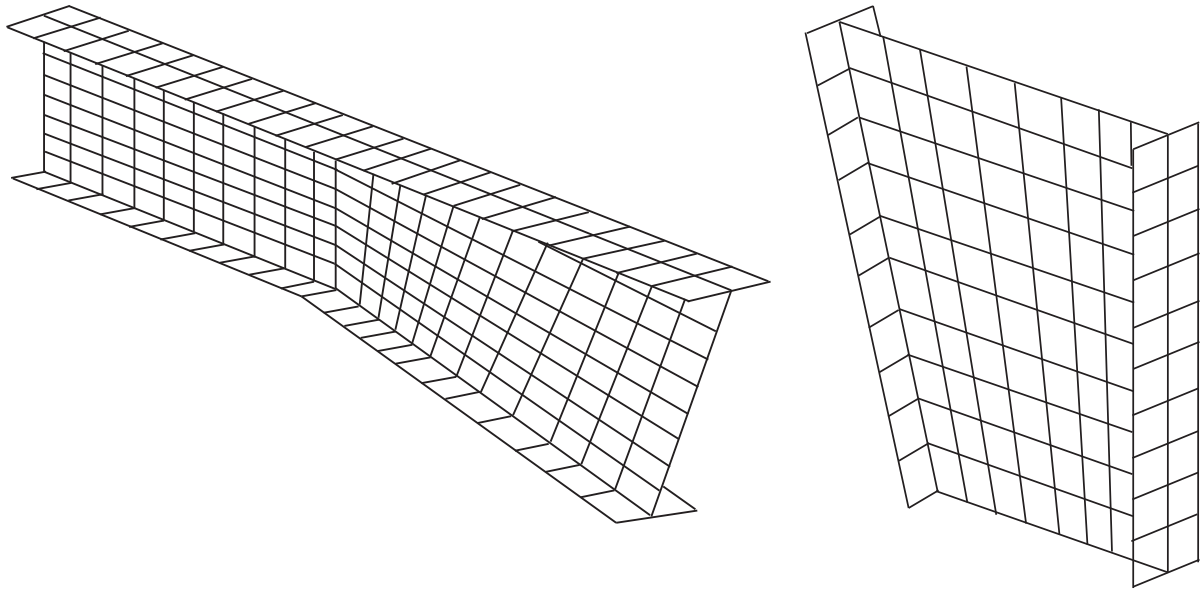

Figure 8-6: Finite element mesh details for column and rafter

8.3.2 End Walls

The end frames were cold formed post and beam construction (channel sections). These were modeled using thin shell elements. The end post had 3.5 in. wide flanges and 11.5 in. deep webs. It was modeled with four elements along depth of web and single elements on both the flanges (Figure 8-7). The beam cross-section was 8.5 in. deep and had a 2.5 in. wide flange. The flanges were modeled using single shell elements while the web had three elements along depth.

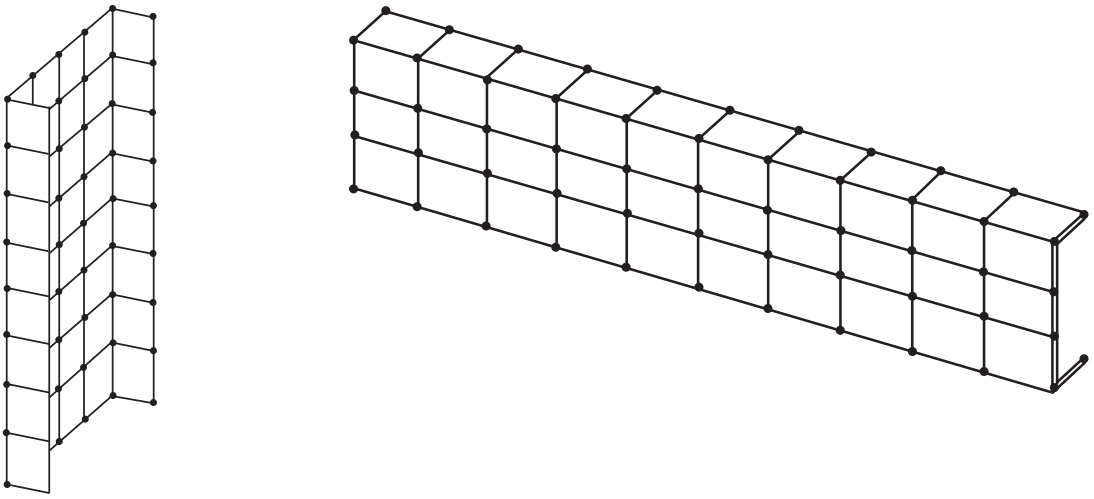

Figure 8-7: Finite element mesh details for end post and end beam

8.3.3 Secondary Steel (Purlins and Girts)

Purlins and girts were modeled using four node shell elements with six degrees of freedom at each node. For simplicity of modeling these sections were modeled as Z-sections with 90° bends and no lips were considered as shown in Figure 8-8. The web was modeled using three elements along the depth while top and bottom flanges were represented by a single shell element.

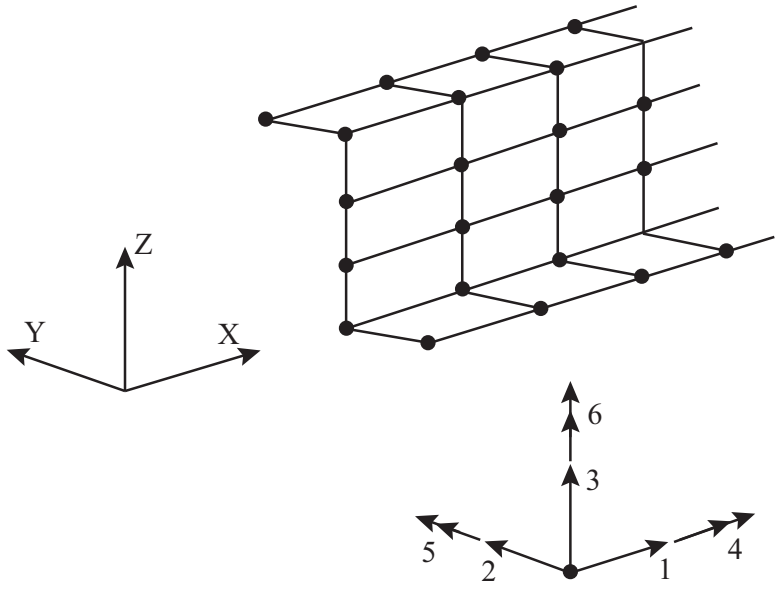

Figure 8-8: Finite element mesh details for secondary steel

Figure 8-9 represents the connection of rafter with purlin. The screw fasteners were not explicitly modeled. At the purlin-rafter interface shell elements representing the rafter flange and purlin

flange were overlapped, and simply connected at four end nodes. The connection at the column-girt interface was modeled in the same fashion.

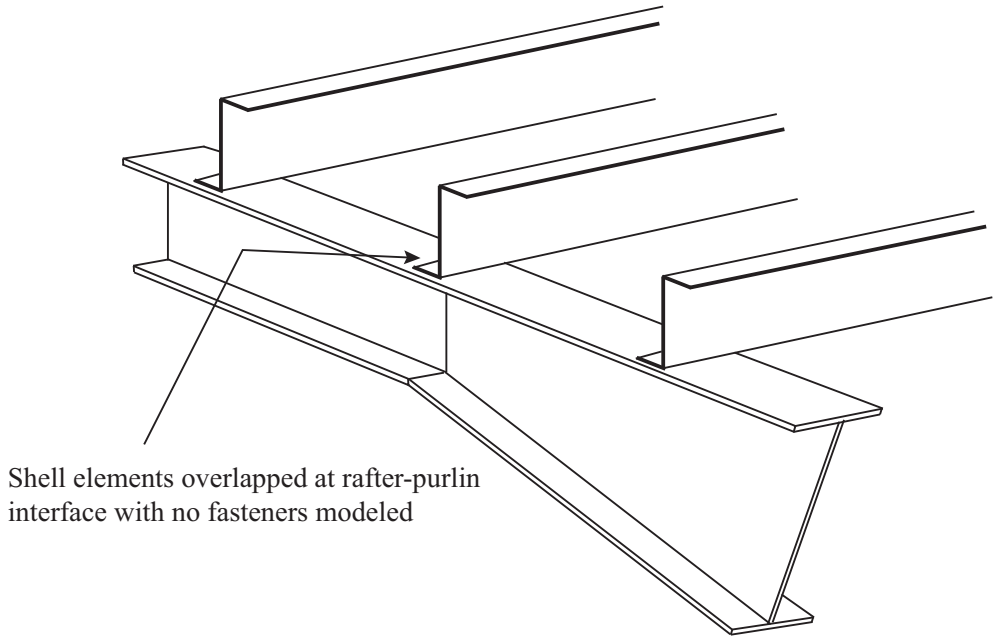

Figure 8-9: Connection at column-rafter interface

.

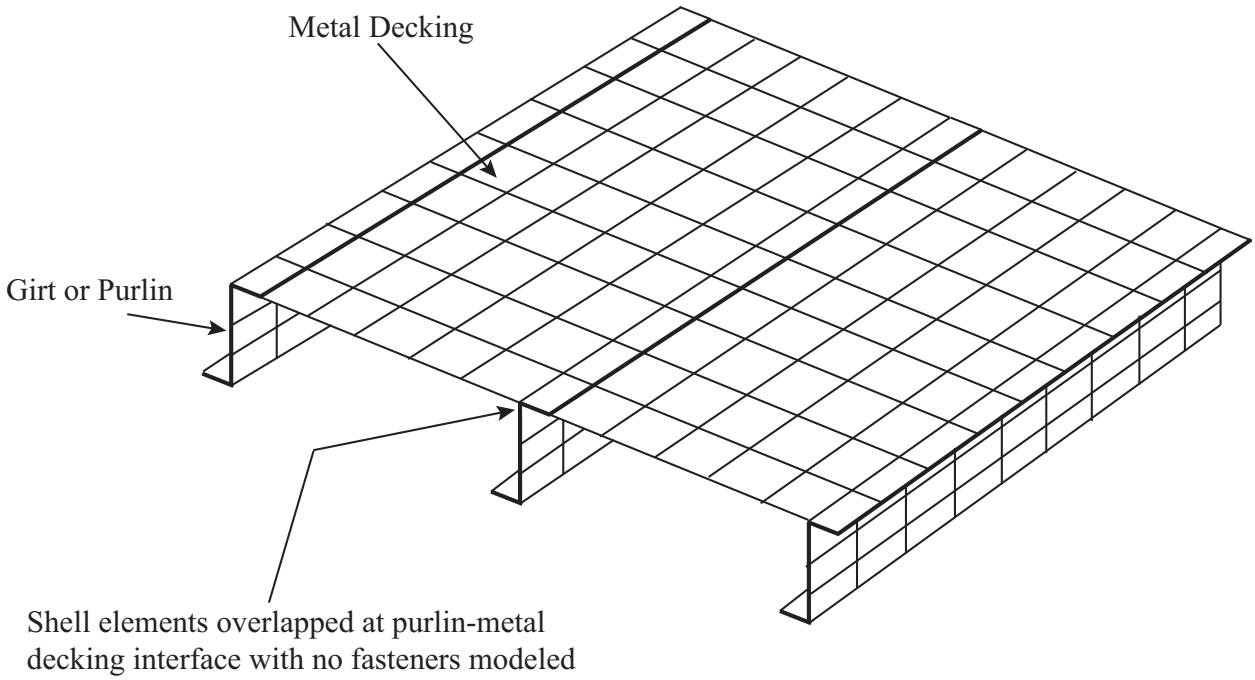

Figure 8-10: Connection between roof-sheeting and purlins

8.3.4 **Wall and Roof Sheeting**

While developing the three-dimensional model of the building in stages, isotropic metal sheeting (similar properties in all directions) was modeled using thin shell elements until STAGE 04 (Section 8.2.4) as shown in Figure 8-10. The connection at the girt-sheeting and purlin-sheeting interface was kept the same, with shell elements simply overlapped and connected at the four end nodes.

The metal sheeting was modeled as a flat sheet as opposed to undulated (profiled) deck. This imparted a behavior which is not true of a profiled sheet, but was good enough for an initial and simple analysis. The intention of doing so was to check if three-dimensional modeling was helping to reach results obtained from experimental testing. If there was any improvement in results, the model could be refined further to include fasteners. If, however, results did not change much with this diaphragm model, there was no point of modeling the fasteners and connection nuances as it would incorporate more flexibility in the analysis model. Moreover, the procedure was modeling intensive and very time consuming.

For the model in STAGE 05 where the roof and wall sheeting were provided actual orthotropic properties, a separate analysis was carried out. The objective of this analysis was to work out axial, bending and shear stiffness parameters in the orthogonal directions. To do so a panel of 180” x 180” was modeled as flat sheet as shown in Figure 8-11. The panel was supported on four edges with roller support provided at all four locations. One end of the panel was restrained against translation in both horizontal directions and rotations about all three axes so as to prevent instability (rigid body motion).

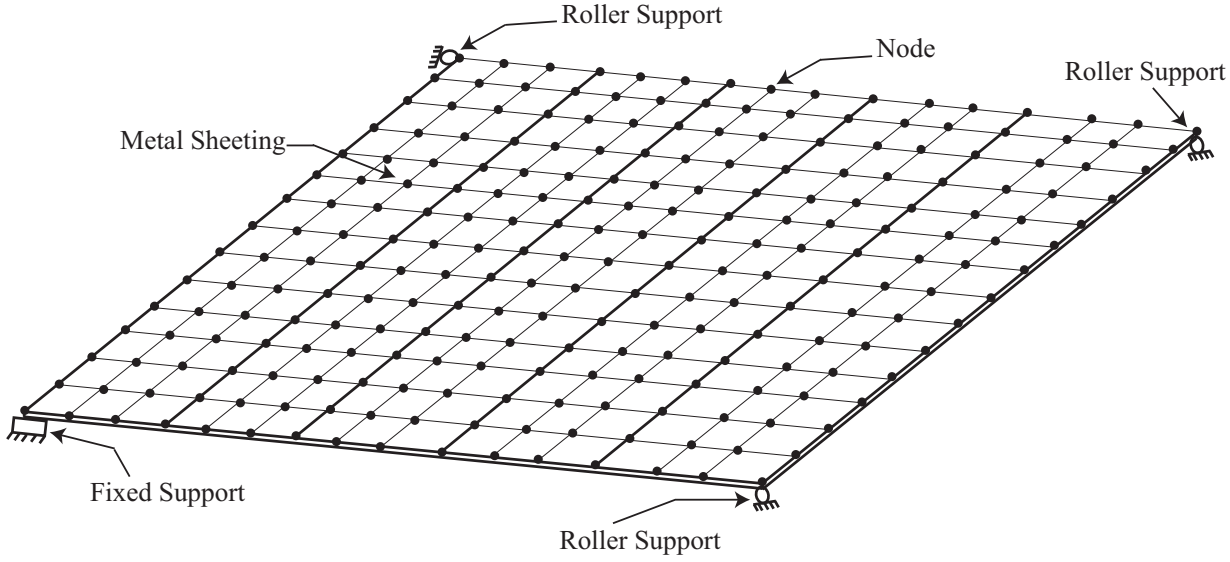

Figure 8-11: Flat roof sheeting with boundary conditions

Another model was created where a panel of same dimensions was modeled having undulations as were present in sheeting on test building. Figure 8-12 shows the shape of the panel with cross-section showing the geometry of the panel. Both the panels were analyzed for axial, shear and flexural loading. For axial stiffness a load of 6 kip was applied causing in plane loading (Figure 8-13), distributed among nodes along the length. The same load was also applied in other direction as shown in Figure 8-13.

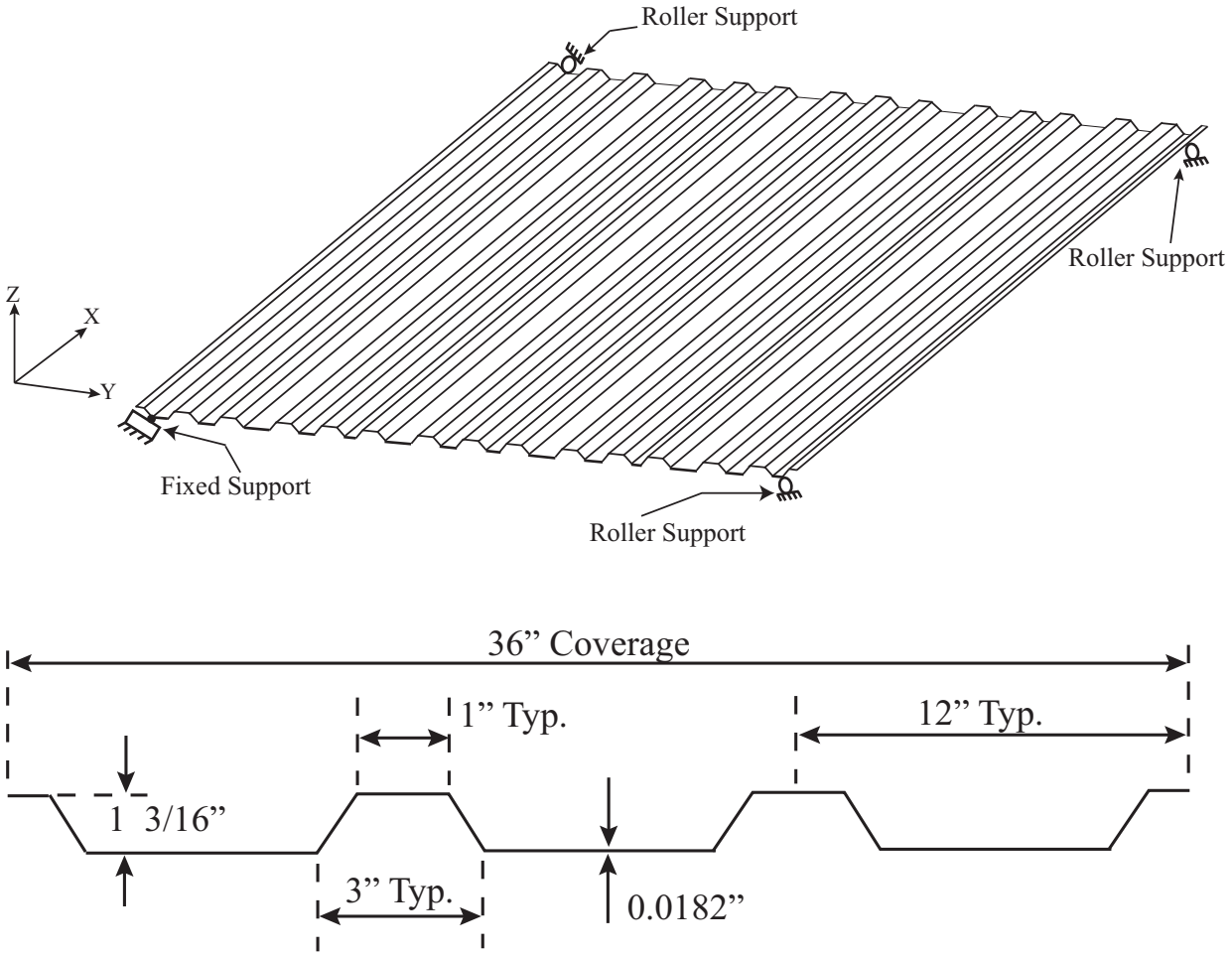

Figure 8-12: Profiled deck with cross-sectional details

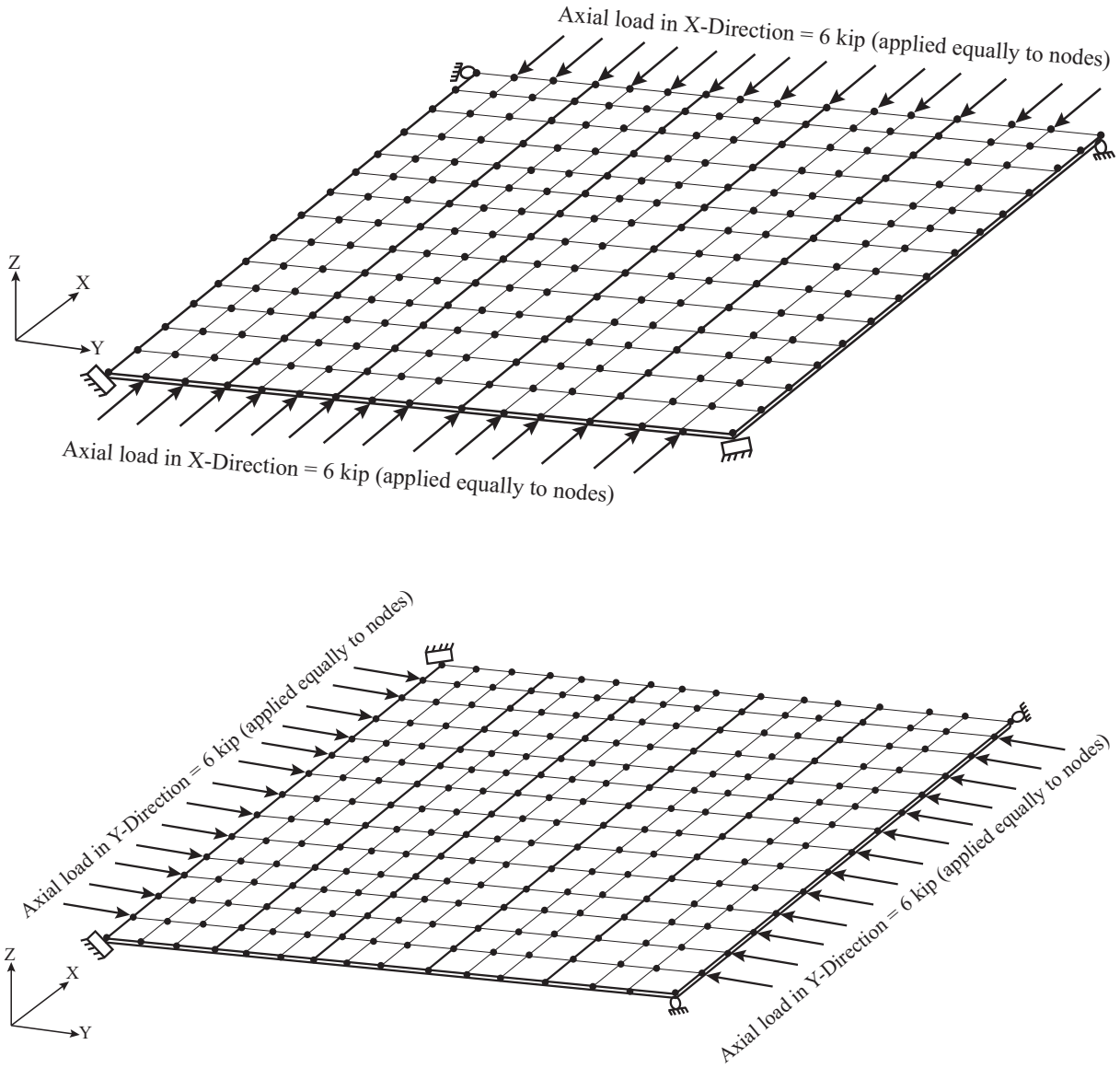

Figure 8-13: Axial load applied in orthogonal direction to get stiffness parameters

Shear stiffness of both the panels was evaluated by using a shear loading in both the directions simultaneously, applied as nodal loads distributed equally. Figure 8-14 shows the application of loading for flat panel.

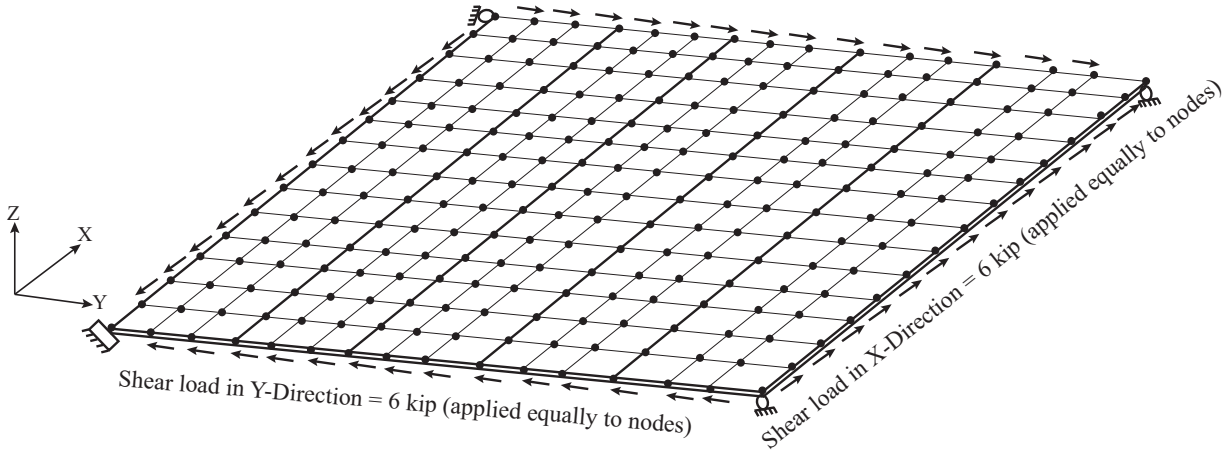

Figure 8-14: Shear load applied in orthogonal directions on flat panel

To account for flexural stiffness, an area load of 25 plf was applied on panels for both the models. Table 8-1 and 8-2 provides the results from the analyses thereby yielding the modification factors that were incorporated in model in STAGE 05 to impart orthotropic properties.

Table 8-1: Axial and bending stiffness parameters for flat and profiled sheeting

Model (deck) Type		Isotropic			Orthotropic		
Stiffness parameter	Direction	Load (kip)	Deformation (in)	Stiff.	Load (kip)	Deformation (in)	Stiff.
Axial (kip/in.)	X - direction	6	0.0089	674	6	77.5	0.08
	Y - direction	6	0.0089	674	6	0.0048	1250
Bending (kip-in. /in.)	X - direction	5.54	94400	5.8e-5	6.2	196.2	0.03
	Y - direction	5.54	94400	5.8e-5	6.2	83500	7.4e-5
Shear (kip/in.)	XY direction	6	401.84	0.015	6	188.9	0.032

Table 8-2: Stiffness modification factors

Modification Factor	Axial	Bending	Shear
X-Direction	1.2e-3	516	2.15
Y-Direction	1.86	1.28	2.15

8.4 Analysis – Results and Discussion

Analyses were performed by applying same magnitude of load (7.5 kip) as in the actual testing. The load was applied on all stages of modeling for both exterior and interior frames. Table 8-3 and 8-4 present the lateral displacements obtained from the analyses.

8.4.1 Exterior Frame

As delineated by Table 8-3, transformation of model from two-dimension to three-dimension draws the resulting drifts closer to true behavior of building. Not only this, the further the model is refined by modeling small details the better results are achieved. In all the analyses results that are presented under column named as "Partially Rigid", column-base connection has been provided a rotational stiffness of 22,000 kip-in./rad as obtained from experimental testing program. To start with, all the interior frames are modeled in three-dimensions connected with just purlins and girts with no decking in STAGE 01. There is reduction of about 1.7 percent for pinned base model. However, if the base connection is provided with rotational stiffness of the actual connection, this reduction is substantial (11 percent). The frames adjacent to the frame being loaded did not show much drift which again highlights the behavior as observed during testing. Hence, reduction in drift or increase in stiffness could be mainly attributed to stiffness added to the system by purlins and girts. It was observed in a separate analysis that girts are far more effective is providing lateral strength (discussed later in Section 8.4.3).

Table 8-3: Lateral Drifts as Obtained from Analyses for Exterior Frame

Analysis Type	Exterior Frame Lateral Drift (in.)				
	Analytical			Exp.	Exp. / Analytical (Partial)
	Pinned	Fixed	Partially Rigid		
Two-Dimensional Model	0.74	0.35	0.56	0.25	0.45
STAGE 01 - 3-D model with girts and purlins in interior bays with no metal decking	0.73	0.36	0.50	0.25	0.50
STAGE 02 - 3-D model with girts, purlins and metal decking in interior bays	0.73	0.34	0.47	0.25	0.54
STAGE 03 - 3-D model with girts, purlins and metal decking in all the bays. End wall modeled with Gable sections	0.62	.31	0.42	0.25	0.60
STAGE 04: 3-D model from STAGE 03 with end walls modeled with cold-formed sections	0.59	0.27	0.37	0.25	0.69
STAGE 05: 3-D model from Stage 04 with metal sheeting given orthotropic properties.	0.58	0.28	0.38	0.25	0.63

For the model in STAGE 02 where metal sheeting for roof and wall has been modeled, lateral drift of system is again reduced. The reduction is about 1.8 percent for conventionally used pin-base connection and 17 percent for partially rigid connection when compared to the drifts obtained from two-dimensional analysis. This additional reduction of drift of about 5 percent in STAGE 02 when compared with model in STAGE 01 is mainly due to in-plane stiffness added to the system by metal sheeting. The drift values and load sharing on adjacent frames increased a small amount, however, was not large enough to be called considerable.

The end walls were not modeled until STAGE 03. Hence the exterior frame in STAGE 02 was missing any stiffness provided by end walls. As discussed in Section 8.2.3, for the model in STAGE 03 the end walls were modeled with same frame properties as the exterior frame. This does not truly represent the test building but the analysis was beneficial to get a measure of lateral stiffness relative to that provided by cold-formed end walls. Analysis results show that even by simply replicating the exterior frame for end walls there is considerable reduction in lateral drift (about 25 percent) for partially rigid connection when compared to the two-dimensional planar frame model.

For the model in STAGE 04 where end walls are modeled using actual cold-formed steel members, it was found that reduction in drift is as high as 35 percent for partially rigid base connection and about 21 percent for pin-base connection. It is interesting to notice that end walls are much stiffer than web-tapered I-section frames. Moreover, incorporating true end wall stiffness further narrows down the difference between analyses results and that obtained from experimental testing program. The difference for exterior frame is about 30 percent using three-dimensional model with cold-formed end walls and partially rigid base as opposed to 53 percent for two-dimensional analysis with partially rigid base condition.

The behavior of the exterior frame as given by model in STAGE 05 which uses orthotropic metal deck properties does not show much improvement in resulting lateral drifts.

8.4.2 **Interior Frame**

For analyses of the interior frame in three dimensional model in STAGE 01 modeling of purlins and girts provided stiffness in addition to the stiffness of frame itself. This resulted in reduction in lateral drift which cannot be overlooked. Table 8-4 shows a reduction of about 8 percent for pin-base condition when compared to drift obtained for two-dimensional model which is far more than the reduction obtained for exterior frame. For the partially rigid connection the reduction is about 11 percent which is about the same number as for the exterior frame.

Consistent with the behavior of exterior frame there is negligible load sharing and deformation of adjacent frames.

Table 8-4: Lateral Drifts as Obtained from Analyses for Interior Frame

Analysis Type	Interior Frame Lateral Drift (in.)				
	Analytical			Exp.	Exp./ Analytical (Partial)
	Pinned	Fixed	Partially Rigid		
Two-Dimensional Model	0.66	0.31	0.51	0.35	0.69
STAGE 01 - 3-D model with girts and purlins in interior bays with no metal decking	0.61	0.32	0.45	0.35	0.77
STAGE 02 - 3-D model with girts, purlins and metal decking in interior bays	0.59	0.30	0.40	0.35	0.87
STAGE 03 - 3-D model with girts, purlins and metal decking in all the bays. End wall modeled with Gable sections	0.58	0.29	0.40	0.35	0.89
STAGE 04: 3-D model from STAGE 03 with end walls modeled with cold-formed sections	0.56	0.29	0.39	0.35	0.89
STAGE 05: 3-D model from Stage 04 with metal sheeting given orthotropic properties.	0.52	0.26	0.35	0.35	0.99

When metal wall and roofing is modeled in STAGE 02, the lateral drift further reduces due to in-plane stiffness provided by sheeting. The results do not improve much for the model with pinned connection when compared to corresponding model in STAGE 01 (less than 2 percent); however, for the partially rigid base condition there is a drop in lateral drift of about 10.7 percent when compared to model in STAGE 01 and about 20 percent when compared to results for a two-dimensional frame. The numbers are close to the numbers yielded by exterior frame for models in STAGE 01 and STAGE 02 (11 percent and 17 percent respectively).

The models in STAGE 03 and STAGE 04 were primarily developed to check the influence of end walls on the exterior frames. Hence as expected, performing the analysis in these STAGES for interior frame did not provide any major increase in stiffness or reduction in drift. However, it should be noted that modeling the building in three-dimensions with partially rigid base reduces the drift by slightly more than 20 percent when compared to two-dimensional analysis. It brings down the difference in lateral drift to 10 percent from 31 percent (given by two-dimensional analysis) when compared with lateral drift obtained from experimental testing.

For the interior frame, the model in STAGE 05 uses orthotropic diaphragm properties and yields a value of lateral drift which is the same as given by experimental testing. The additional stiffness is a result of the high shear stiffness and bending stiffness of orthotropic deck as compared to isotropic deck (almost double for metal sheeting of this building). This, however, does not represent the true behavior as metal sheeting fasteners have been not incorporated in the model so far. Simulation of these connections would induce flexibility in the structure which in turn would result in higher drifts. It can be concluded that test building is stiffer than the analytical model and any further refinement in the model will make it more flexible. This however gives a good estimate of how the real building is behaving when compared to the analytical model.

8.4.3 **Comparison of lateral stiffness provided by girts vs purlins**

By modeling the complete building in three-dimensions in STAGE 01 there was reduction in drift of about 11 percent for both interior and exterior frames. At this stage gable frames were connected with girts and purlins. Another set of analyses were run within this stage with an intent to compare relative stiffness provided by girts and purlins individually. For this an analysis was run where building frames were connected with each other with only girts and no purlins as shown in Figure 8-15. For second analysis the model had only purlins and no girts as shown in Figure 8-16.

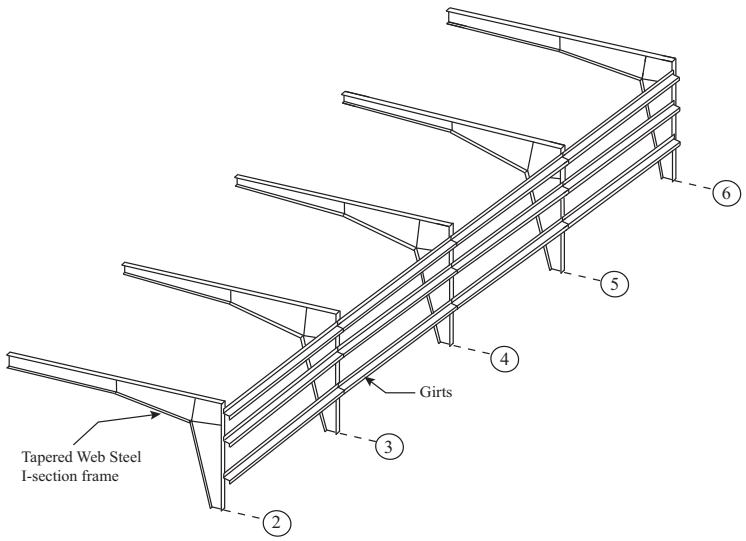

Figure 8-15: Three-Dimensional model connected with girts only

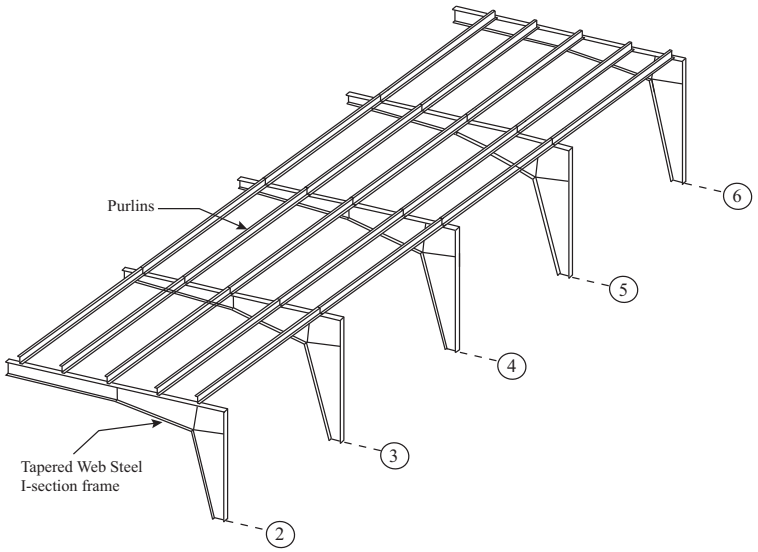

Figure 8-16: Three-Dimensional model connected with purlins only

Table 8-5: Reduction in drift due to addition of girts and purlins individually

Exterior Frame			
Model Type	Displacement (in.)	Percent reduction from 2-D Model	Relative contribution in drift reduction
2-D Model	0.56	--	--
3-D Model full	0.50	11	--
3-D Model with girts	0.52	7.7	70
3-D Model with purlins	0.55	2	23
Interior Frame			
Model Type	Displacement (in.)	Percent reduction from 2-D Model	Relative contribution in drift reduction
2-D Model	0.51	--	--
3-D Model full	0.45	11.8	--
3-D Model with girts	0.47	7.4	63
3-D Model with purlins	0.49	3.2	26

The results obtained from analyses have been presented in Table 8-5. From the results it can be stated that the continuous girt spans are providing much more stiffness when compared to stiffness provided by purlins for both interior and exterior frames.

8.5 Behavior of building for vaious methods of load application during analysis

The objective of this research was to evaluate the behavior of a metal building against wind load. However, while performing experimental testing program and validating results through analysis, the test building was subjected to a point lateral load at column-rafter junction. This does not really represent the way wind load will act on the building. This section has been

included in the thesis to draw comparison between lateral drifts resulting for different loading methods. Two types of loadings have been considered to in this section, namely point load and area load. Figure 8-17 and 8-18 show the point load and area load application respectively.

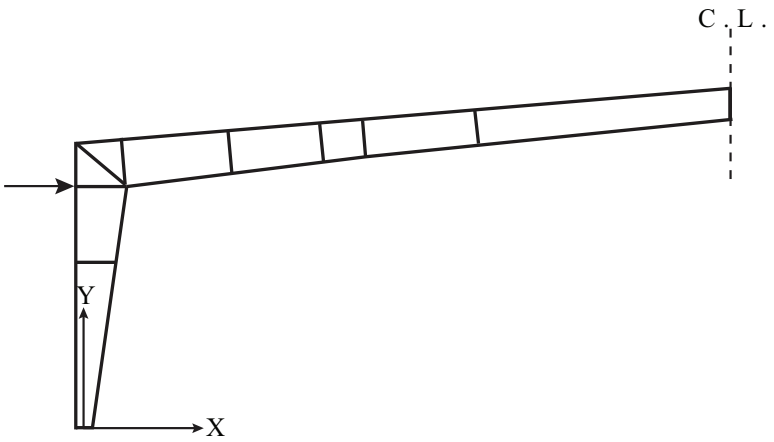

Figure 8-17: Point Load applied at knee location

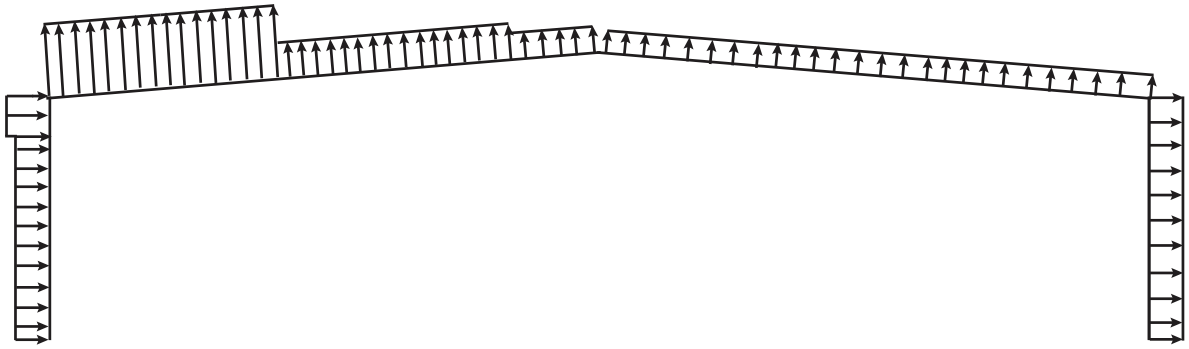

Figure 8-18: Area load applied along the length of member of a frame

8.5.1 Load types and Load cases

For the analysis of a building with a point load of 7.5 kip (same value that was used while testing) was applied. While performing area load analysis, pressure acting on the surface was calculated using tables and figures given in Chapter 6 of ASCE 7-05. Based on the tributary width of each frame this load was then converted to an area load acting across the width of flanges of rafters and columns of the frame. This load when converted to total lateral load acting on the frame, comes out to be 6.1 kip which is less than 7.5 kip. Hence, after carrying out linear analysis of the building, resulting deformations were scaled with a modification factor so as to

match the area load with point load. Four different load cases were considered for analysis with both area load and point load as shown in Figure 8-19.

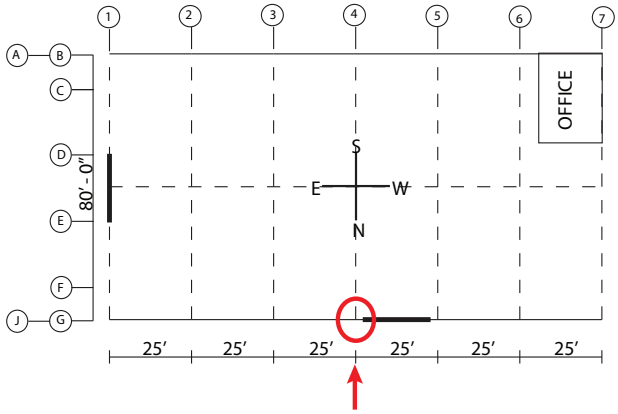

Case 01-Interior Frame along line 04 loaded

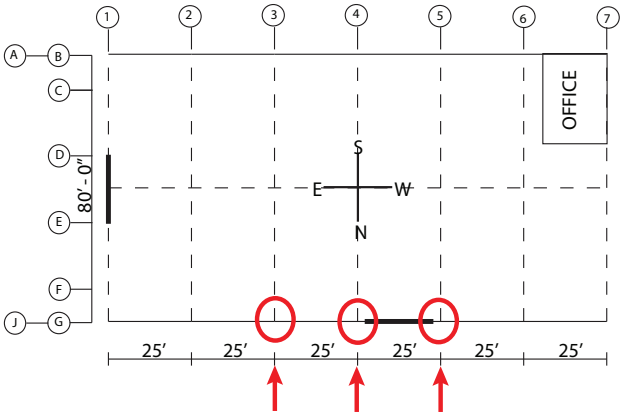

Case 02-Interior Frame along line 04 and first adjacent frames loaded

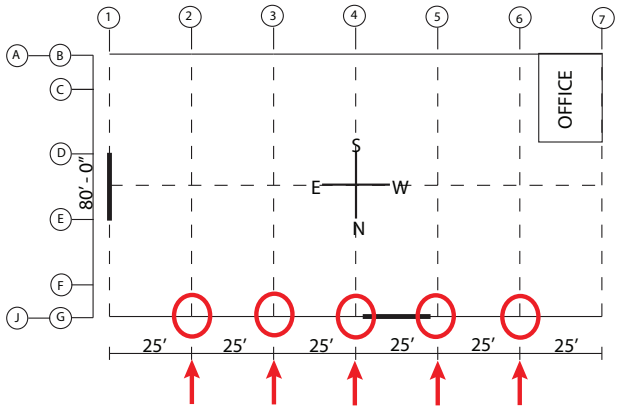

Case 03-Interior Frame along line 04, first and second adjacent frames loaded

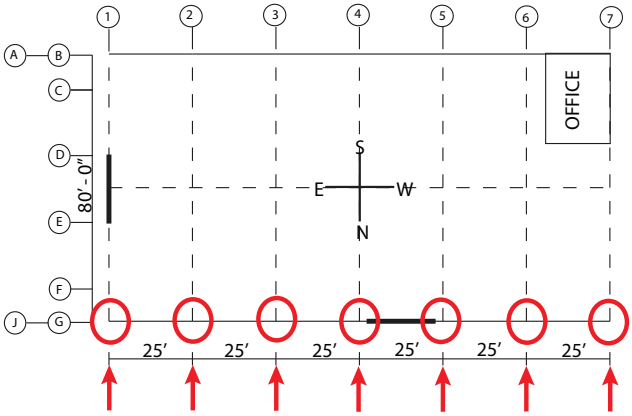

Case 04-All frames loaded

Figure 8-19: Different Load Cases

8.5.2 Analysis – Results and Discussion

The plot shown below in Figure 8-20 represents the difference in analytical behavior of building when it is subjected to area load as opposed to point load. For the first set of loading considered load was applied only to interior frame along line 04. The analysis performed with a point load at the knee location results in lateral drift which is almost twice the drift resulting from area load analysis. A second analysis was considered of all frames along line 01 through 07 subjected to area load and point loads at knee. Similar behavior was observed thereby resulting in high drift values for analysis with point load application. This substantiates that significant difference in results could occur for different loading methods used in analysis.

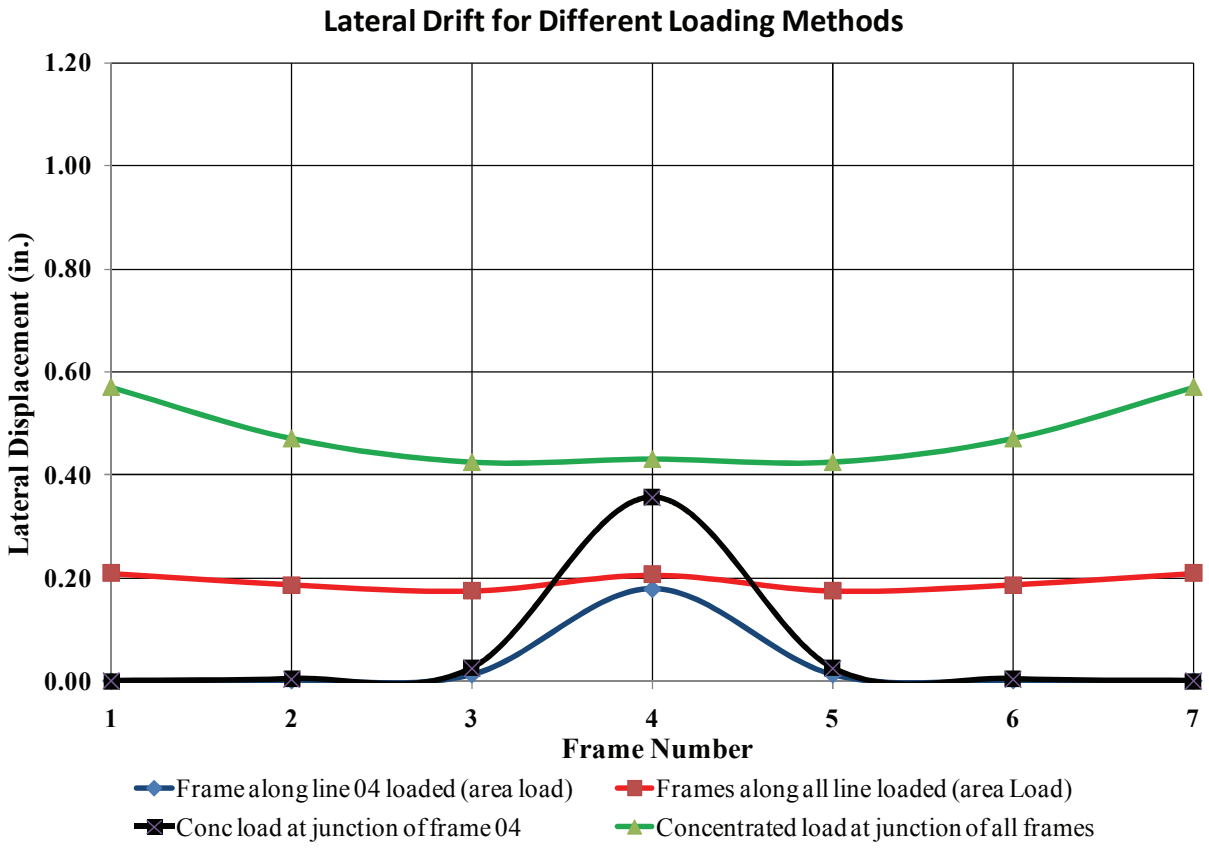

Figure 8-20: Comparison between drift values resulting from area Vs point load application.

Area Load Application

Further analyses were performed to check behavior of individual frames when subjected to different loading patterns as shown in Figure 8-19. The intent of these analyses was to check relative stiffness of the frames and compare to behavior during experimental testing. Figure 8-21 shows the analysis results for frames subjected to area load. For Load Case 01 when the interior frame is subjected to an area load across the width of frame members, primarily the loaded frame is showing the most lateral drift. The adjacent unloaded frames do not undergo major deformations which is consistent with the behavior represented bny building during full-scale testing. Similarly for Load Case 02 where frame along line 04 and adjacent frames are loaded, exterior frames along line 02 and 06 do not show much lateral drift.

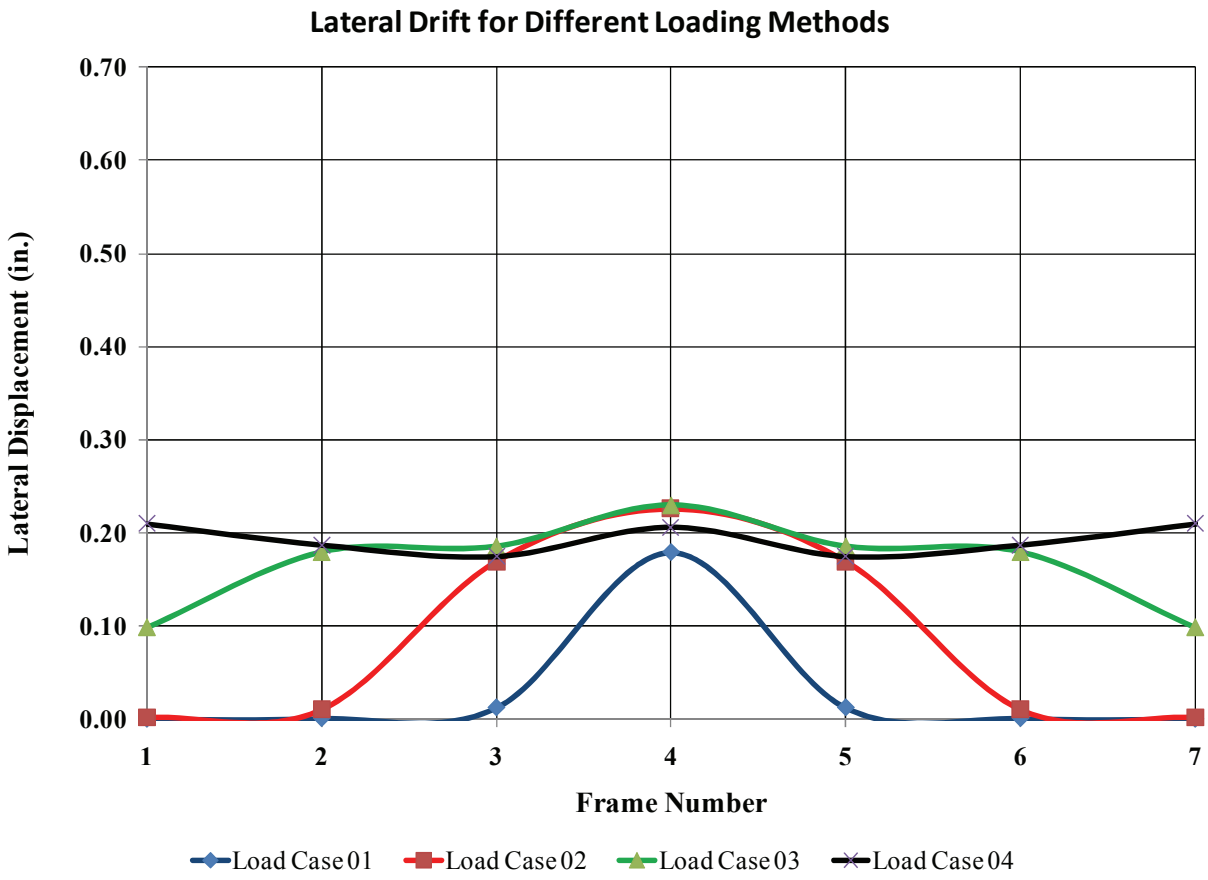

Figure 8-21: Lateral Drift for different patterns of area load applied

It is interesting to note that for Load Case 03 where all web-tapered I-section plate-welded frames are loaded, frames along line 02 and 06 (Exterior frames) deform less as compared to frames along line 03 through 05 (Interior Frame). This again shows that exterior frames are stiffer than interior frames as seen during experimental testing. However, this behavior is not supported by analysis for Load Case 04 when all frames are loaded simultaneously. The exterior frames tend to deform slightly more than interior frames. One of the possible reasons for this could be the way area load is applied. Though the load is applied as pressure but still it is mainly distributed along the depth of the end walls posts. This results in high local stresses and deformations in end walls along line 01 and 07. This drags the adjacent frame along line 02 and 06, thereby showing more lateral drift than the interior frames.

Point Load Application

For the set of analyses performed in this section, variation in lateral drift was compared for different loading patterns as shown in Figure 8-22. Load Case 01 and 02 show similar behavior to the area load application case except that resulting drift values are almost twice when compared to the drift values obtained from area load analysis.

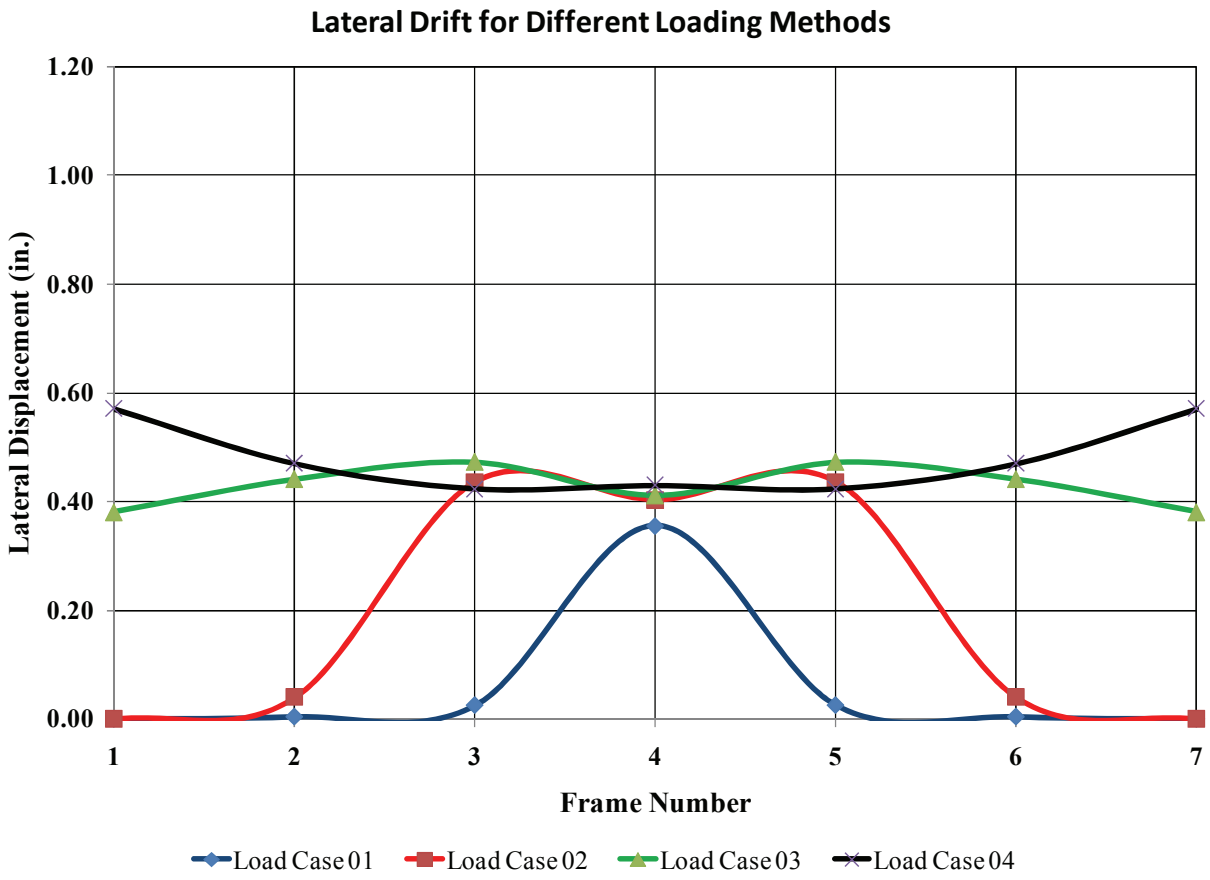

Figure 8-22: Lateral Drift for different patterns of point load applied

While performing analysis for Load Case 03 it is important to note that exterior frames along line 02 and 06 are resulting in more drifts than interior frame. This is opposite to the behavior shown by the building in during testing where exterior frames are stiffer than the interior ones. The deviation is due to different section properties for exterior and interior frames. Interior frames along line 03 through 05 have relatively deep rafters and column sections at location where load is being applied. This makes the interior frames stiffer than exterior frames at that location thereby resulting in higher local drift values for exterior frames. This does not happen in the case of area load analysis as the load is applied throughout the length of frame members and hence exterior frames do not see major local deformations. For Load Case 04 the behavior is again similar to the area load application where cold-formed end wall members deform excessively and drag the adjacent exterior frames.

8.5.3 **Conclusion**

From all the different analyses presented in this section it can be concluded that results vary significantly just based on the method of load application in an analysis model. The experimental testing and most of the analyses performed to validate the results were performed for point load applied at column-rafter location. As discussed previously that for such load application method the resulting drifts are far more than that would result from actual wind load. Nonetheless, the research gives in-depth knowledge for the behavior of base-connection stiffness and behavior of most of the components present in a typical metal building.

Chapter 9 Correlation of Analytical and Experimental Results

9.1 Introduction

The correlation of the experimental and analytical responses of the Test Structure is presented in this Chapter. The discussion concentrates on the deflections measured at the point of loading, which is at the base of the "panel zone" of the column-rafter connection. Recall that a force of 7.5 kip was applied in all of the analyses, and in all experiments except for the loading of Frame 6, in which a maximum force of 6.5 kip was applied. For consistency with all other values reported, the results of the test on Frame 6 are multiplied by the ratio of 7.5/6.5.

9.2 Correlation of lateral displacements

A summary of the analytically and experimental deflections at the load point are provided in Table 9-1. The analysis results are given for pinned, intermediate, and rigid column-to-base connections. The rotational stiffness for the intermediate base connection analysis was taken as 22,000 k-in./radian, which corresponds to the "best guess" stiffness from the 3-D finite element analysis and that obtained from experimental testing.

Table 9-1: Correlation of Analytical/Experimental Results using Applied Load = 7.5 kip

Frame Tested	Experimental Displacement (in.)	Frame 3-D FEA Analytical Displacement (in.)		
		Pinned Base	Intermediate Base K_θ=22,000 k-in./radian	Rigid Base
2	0.25	0.745	0.562	0.317
3	0.24	0.659	0.507	0.287
4	0.35	0.659	0.507	0.287
5	0.29	0.659	0.507	0.287
6	0.24	0.745	0.562	0.317

As may be observed from the table, the experimentally determined displacements are significantly less than those determined from the analysis, and in some cases, are less than the analytical values with the column-to-base connection considered as rigid.

As noted in Chapter 7, not the entire 7.5 kip experimental lateral load is resisted by the frame that is experimentally loaded. Part of this load is shed to the adjacent frames. Based on the deflections in the adjacent frames and in the loaded frames, it was estimated in Chapter 7 (Section 7.6.1) that approximately 6.9 kip is actually resisted by the loaded frame when the 7.5

kip load is applied to the structure. Adjusting the FEA results to an applied force of 6.9 kip per frame produces the results shown in Table 9-2.

Table 9-2: Correlation of Analytical/Experimental Results using Scaled Load = 6.9 kip

Frame Tested	Experimental Displacement (in.)	Frame 3-D FEA Analytical Displacement (in.)		
		Pinned Base	Intermediate Base using K_θ=22,000 k-in./radian	Rigid Base
2	0.25	0.685	0.517	0.291
3	0.24	0.606	0.466	0.265
4	0.35	0.606	0.466	0.265
5	0.29	0.606	0.466	0.265
6	0.24	0.685	0.517	0.291

With this adjustment, the experimentally determined displacements are still significantly less than those obtained analytically, and in most cases, are less than the analytical displacements when the column base is considered to be rigid.

There are several possible reasons why the experimental displacements are less than the analytical values. Aside from experimental or analytical error, differences can only be attributed to the fact that the base of the column is actually stiffer than that modeled analytically, or that the cladding system (including purlins, grits and sheeting) is providing some additional stiffness that has not been modeled.

To investigate the influence of the cladding system, complete three-dimensional model of the test buildings was used. The model was created in stages in order to check the influence (stiffness added) of individual components of the system. Addition of building components in each stage resulted in refinement of the model and brought the analytically obtained displacements closer to those obtained from the testing. The results for each step have been already discussed in Chapter 8. Table 9-3 presents the results obtained from the best model developed in this research. The model takes care of stiffness or flexibility provided by all the components of building except the flexibility added by screw fasteners.

Table 9-3: Correlation of Analytical/Experimental Results using complete 3-D Model

Frame Tested	Experimental Displacement (in.)	Building 3-D FEA Analytical Displacement (in.)		
		Pinned Base	Intermediate Base using K_θ=22,000 k-in./radian	Rigid Base
2	0.25	0.58	0.38	0.28
3	0.24	0.52	0.35	0.26
4	0.35	0.52	0.35	0.26
5	0.29	0.52	0.35	0.26
6	0.24	0.58	0.38	0.28

9.3 Correlation of Analytical and Experimental Moment-Rotation Response

As mentioned in Chapter 6, the analytically determined stiffness of the column-to-base connections was 22,500 k-in./radian. This value correlates very well with the maximum stiffness obtained from the moment-rotation plots determined experimentally. This value, obtained from a number of tests, was 25,000 k-in./radian. It is noted, however, that significantly less stiffness was obtained in a few of the loadings.

Chapter 10 Summary, Conclusions, and Recommendations

10.1 Introduction

This chapter provides a summary of the research, a summary of the basic conclusions, and recommendations for future work.

10.2 Summary of Research

The research described in this thesis was performed as a "pilot" study to determine what, if any, modifications should be made to the wind drift serviceability analysis and design of metal buildings. The main focus of the research was a coordinated experimental-analytical research program in which a full size Test Building was loaded in the field, and analyzed by use of a variety of approaches. The analysis concentrated on the modeling of the column-to-base connection, as the stiffness of this connection was observed to be very significant in assessing the behavior of the whole building system.

10.3 Conclusions

10.3.1 Loads

The two main methods for determining wind loads were reviewed. Method 1, used for low rise "diaphragm" buildings is generally not used for low-rise metal buildings, so the research concentrated on Method 2. Method 2 may be applied rigorously, wherein pressure distributions are determined analytically, or, for low rise buildings, may be based on tables of pressure coefficients. For the test building it was found that the use of pressure coefficients resulted in somewhat larger overall design wind loads (6.1 kip of total lateral force per 25 ft bay) than did the analytical method (5.1 kip per bay). These are the unfactored design level loads, which are based on a 50 year mean recurrence interval load.

10.3.2 Basic Correlation of Analytical and Experimental Results

The correlation of analytical results obtained from planar analysis with experimental results was not good in terms of displacement. The lateral displacements produced by the field testing of the Test Building were on the order of 1/2 of the deflections predicted by finite element analysis. This indicates that the actual stiffness of the test building is twice the analytical stiffness.

Regarding moment-rotation behavior at the column-to-base connections, it was found that the computed rotational stiffness (22,000 k-in/radian), correlated very well to the maximum stiffness

measured in the tests (25,000 k-in./radian). However, this good correlation was found in only a few tests.

The most likely source of the difference in the analytical-experimental displacements is the modeling of the column-to-base connection, which was found to be highly influential in predicting displacements. The good correlation obtained in base-of-column stiffness (for some of the tests) appears to discount this as a significant source of error, however.

Another potential source of the difference in displacements is three dimensional structural-diaphragm interactions. This source of interaction does seem likely, however, as the diaphragms appeared to be fully flexible in-plane in the Test Building. This flexibility was evident from the fact that gable frames adjacent to the loaded gable frames had deflections that were only a fraction (approximately 1/20th) of the deflections of the loaded frames.

It is also possible that the lack of correlation is associated with errors in the experimental measurements, the analytical computations, or both. It is unlikely that there are significant errors in the analysis as three independently developed models, using two independently developed programs, produced very similar results. The most likely problem with the experimental results would be in the calibration of the load cell[1], because this instrument was used in each of the tests. Errors in calibration of displacement transducers is less likely because of the large number of transducers used, and the apparent consistency in measurements between the individual instruments. It is noted, however, that several of the displacement transducers were in the very low range of resolution.

10.3.3 **Modeling**

10.3.3.1 Full Building Analysis as opposed to Planar Frame Analysis

For the building tested and analyzed in this research (for which there was no in-plane roof bracing) the roof sheeting appeared to have negligible in-plane stiffness because the frames adjacent to the loaded frames deflected only a small percentage of the deflection observed for the loaded frames. Given the flexibility of the roof diaphragm in the test building there does not appear to be any advantage to performing a 3-Dimensional analysis of the entire building. However, 3-D building models would be useful for buildings in which X-bracing is used in the plane of the roof *and* for which the end-frames are significantly stiffer than the gable frames. Modeling of the roof sheeting and attachment to the rafters via purlin connections is not

[1] The load cell was recalibrated on March 31, 2010, and it was found that the calibration used in the loading of the Test Building was accurate.

straightforward, however. Such sheeting should not be included in analysis unless realistic procedures are developed for modeling the sheeting system and its connectivity.

10.3.3.2 Modeling Individual Frames

Where individual gable frames are modeled, the analyst has two basic choices:

1. Using 3-Dimensional frame elements
2. Using 2-Dimesnional shell elements

The use of 3-Dimensional shell elements provides the most versatility and accuracy. While the geometry and modeling is complex, such models could be automatically generated by use of only a few parameters. Advantages of the 3-D shell element approach include accurate representation of the panel zone region and the ease of implementing the modeling of the column-to-base connection. The primary difficulty of the use of such models is transforming individual shell element results (in terms of stresses) into cross-sectional results (in terms of force and moment). The computational time required for the analysis is negligible, even for a highly refined mesh.

The use 2-Dimensional frame element appears to provide sufficient accuracy, with predicted deflections being somewhat greater than those predicted by use of 3-D shell element models. When 2-D frame elements are used the elements should be modeled with nonprismatic members. For variable depth I-sections the moment of inertia should be set to vary quadratically with depth, and the shear area and axial area should vary linearly with depth. More accuracy can be provided if the "exact" variations of element property along the length are included in the formulation of the element stiffness matrices and fixed-end force vectors. The panel zone region of the column to rafter connection should be modeled explicitly with short elements in the joint region (or by use of more accurate models such as the Krawinkler or Scissors models). The panel zone region should not be represented as rigid end zones in the column or rafter elements.

10.3.3.3 Modeling the Column-to-Base Connection

There appears to be a significant advantage to modeling the column-to-base connection as partially rigid. However, the development of this model is not straight forward as the stiffness of the connection depends on:

- The size and stiffness of the column
- The plan dimensions of the base plate
- The thickness of the base plate
- The arrangement of anchor bolts
- The pretension in the anchor bolts
- The axial stiffness of the anchor bolts (which depends on anchorage details)

- Thickness and properties of grout
- The axial load present in the column prior to the application of lateral load
- The flexibility of the foundation underlying the anchor bolt.

Each of the above items may be represented in a detailed finite element model of the column-to-base connection, but only if the column and base plate are modeled with 3-D shell elements. Simplified models, consisting of several linear springs or even a single rotational spring may be used if the base plate can be assumed to be rigid in out-of-plane bending. Such rigidity could only be assumed if the base plate thickness was (say) four times thicker than the column flange. The proposition relating base plate thickness with thickness of column flange for considering the base as rigid is, however, true only for the test building. In order to generalize any such rule additional study is required to account for a number of factors such as width of column flange, allowable bending stresses and span of the frame. The intent of proposing such rules is to allow a design engineer to incorporate the stiffness of connection easily without detailed finite element modeling.

10.3.3.4 Modeling the Cladding System

Very preliminary analysis was carried out to determine the effect of the cladding on the stiffness of the test building. In this analysis, the purlins were modeled as studs, and the sheeting was modeled as a tension/compression membrane. The analysis indicated that the cladding was not contributing to the lateral stiffness of the structure.

10.3.3.5 P-Delta Effects

P-Delta effects were not considered in the analysis reported herein. It would seem that such effects, when included, would increase the computed displacements.

10.3.3.6 Finite Element Analysis of Full 3-D building System.

One of the original goals of the research reported herein was to perform a 3D finite element analysis of the full building system, wherein the entire structure was modeled in great detail. In such a model, the sheeting, purlins, girts, gable frames, connectors, and column-to-base connections would be modeled in sufficient detail to determine how the structure behaves in three dimensions. The lack of correlation between experimental and analytically determined displacement indicates that such interaction may exist, and may be very significant. It is possible that 3D analysis would expose these "hidden" sources of stiffness. Such analysis, while valuable in itself, would be tremendously enhanced through phased testing and coordinated analysis of a building under construction.

It is also very important to note that the analysis of a full building with a concentrated force applied to one gable frame, as applied in all analysis considered herein, is not a "natural" loading. Wind pressures are applied over the full surface. The behavior of a building under these different types of loading may be substantially different, as the demands on the diaphragm are less extreme when all frames are loaded uniformly.

The three-dimensional analyses have been performed in various stages. Complete model has been created by sequentially adding components of the buildings. For the initial three-dimensional analysis internal tapered I-section frames along grid lines 2 through 6 (Figure 4-2) connected with purlins and girts have been modeled and analyzed. For next stage end walls were included in the model. Following this, metal sheeting was added to model and analysis was carried out. The results obtained from analysis at every stage were compared with results obtained from two-dimensional analysis and experimental testing. It was observed as the models were refined the difference between results obtained from experimental analysis and three-dimensional analysis reduces. The final model which has all purlins, girts, orthotropic deck properties yields results almost same as given by experimental tests. In the model fastener connections have not been modeled. Incorporation of these connections is very time consuming and modeling intensive. However, the final model gives a good estimate of stiffness provided by individual components of building and validated the purpose of three-dimensional modeling.

From the three-dimensional analysis, it can be concluded that purlins, girts and metal sheeting provide substantial stiffness to building against lateral loads. For same magnitude of load, using a two-dimensional analysis can give drifts almost twice that would be given by a real building subjected to same magnitude of load.

10.4 Recommendations for Future Research

10.4.1 Additional Full Building testing

The results reported herein are limited because only one building was tested, and this building was tested in the as-built condition with all cladding in place. The results of the analytical/experimental program indicate that there is a significant source of lateral stiffness in the Test Building that was not represented in the analytical model. From an experimental perspective, the best way to determine the source of the difference would be to test a building under various phases of construction. Doing so would allow the researchers to observe construction procedures, and to test the structure in various phases of completion. An example of a building under construction is shown in Figure 10-1. This building, in southwest Arizona, is constructed only up to the bare frame.

Figure 10-1: Photograph of Metal Building under Construction

If it is possible to test a building under construction, lateral stiffness tests should be performed for the following stages of construction:

1. Bare frame only, without rod bracing and metal roofing (but with sufficient lateral bracing).
2. Bare frame with rod (X) bracing but without roof sheeting.
3. Full structure with rod bracing and roof sheeting in place.

The building should be tested in both directions, and the end-frame should be tested in addition to the gable frames. If at all possible, a variety of column-to-base connection details should be used in the construction.

The main advantage of such testing is that all uncertainties associated with the participation of cladding would be eliminated.

10.4.2 Laboratory Testing of Column-to-Base Connections

It would be worthwhile to test a variety of column-to-base connections to determine the true behavior of the connections and to provide data for correlated finite element modeling. Such

tests should be performed at full scale in a structural engineering laboratory. All of the factors included in Section 10.3.3.3 of this thesis should be considered as parameters in the test program.

10.4.3 **Improved Modeling of Column-to-Base Connection.**

While the analysis used for the column-to-base connection was of sufficient resolution to estimate the stiffness of the column-to base connection, the model was not particularly rigorous from a finite element perspective. The main issue with the analysis is that the base plate and column were modeled with shell elements, and the anchor rods were modeled with single-point springs. These aspects of modeling would tend to underestimate the stiffness. Improved predictions of behavior could be obtained with models in which the column, base plate, and anchor rods are modeled with 3D solid elements.

10.4.4 **Development of Finite Element "Wizard" for Column-to-Base Modeling**

The only way to develop an accurate column-to-base connection model is through the use of 3-D finite element analysis. Given such analysis, an equivalent rotational spring could be developed for use in the more traditional 2-D frame models.

To use this Wizard the user would provide only the most basic information about the column-to-base connection detail. The Wizard, written as an executable Matlab program (not requiring Matlab for use), would automatically model the connection, run the analysis, and provide an equivalent spring stiffness for use in 2-D frame analysis. The Wizard could be written as a pre-processor for a standard finite element analysis program, or could be developed as a standalone program.

It is noted, however, that for thick base plates, Equation 6-2 may be used to predict rotational stiffness, and that the results using this stiffness approach the fixed-base condition. The only difficulty in using this approach is in knowing how thick the plate must be such that its behavior is in fact as described by Equation 6-2. Use of the wizard would allow this factor to be determined on a general basis, wherein simple rules may be used. The rule might read, for example, as "if the base plate is four times thicker than the column flange, the base plate may be assumed rigid". As mentioned before, the rule proposed as an example, relating base plate thickness with thickness of column flange for considering the base as rigid is, however, true only for the test building. The development of wizard would require extensive research considering all other factors as mentioned in Section 10.3.3.3

10.4.5 **Optimization of Column-to-Base Connection Stiffness**

The stiffness of the column-to-base connection can be increased through a number of approaches, and can very likely be increased to the extent that the connection is effectively rigid. However, such rigidity, while desirable for wind drift analysis, may not be desirable for developing the structure's strength under combined wind and gravity loads. Optimization may produce a connection design that provides the maximum benefit with both serviceability and strength based designs are considered.

REFERENCES

ASCE (1998). Minimum Design Loads for Buildings and Other Structures (ASCE 7-98), American Society of Civil Engineers, Reston Virginia.

ASCE. (2006). Minimum Design Loads for Buildings and Other Structures (ASCE 7-05), American Society of Civil Engineers, Reston Virginia.

Berding, D. (2006). Wind Drift Design of Steel Framed Buildings: An Analytical Study and a Survey of the Practice, M.S. Thesis, Department of Civil and Environmental Engineering, Virginia Tech, Blacksburg, Virginia.

Bradley, F. Coffman (2010). "Wind Effects on Low-Rise Metal Buildings: Database-Assisted Design versus ASCE 7-05 Standard Estimates", Journal of Structural Engineering, V136, No 6, pp 744-748.

Case, P.C., and Isyumov, N., (1998). "Wind Loads on Low Buildings with 4:12 gable roofs in open Country and Suburban Exposure", Journal of Wind Engineering and Industrial Aerodynamics, 77&78, pp 107-118.

Charney, F.A. (1990). "Wind Drift Serviceability Limit State Design of Multistory Buildings", Journal of Wind Engineering and Industrial Aerodynamics, 36, pp 203-212.

Charney, F.A. Iyer, H, and Spears, P.W. (2005). "Computation of Major Axis Shear Deformations in Wide Flange Steel Girders and Columns", Journal of Constructional Steel Research, 61 pp 1525-1558.

Charney, F.A., and Marshall, J., (2006). "A Comparison of the Krawinkler and Scissors Models for Including Beam-Column Joint Deformations in the Analysis of Moment Resisting Steel Frames", AISC Engineering Journal, V43, No 1, pp 31-48.

Charney, F.A., and Pathak, R. (2007a), "Sources of Elastic Deformations in Steel Frame and Tube Structures, Part 1: Simplified Subassemblage Models", *Journal of Constructional Steel Research*, V64, No 1, pp 101-117.

Charney, F.A., and Pathak, R. (2007b), “Sources of Elastic Deformations in Steel Frame and Tube Structures, Part 2: Detailed Subassemblage Models”, *Journal of Constructional Steel Research*, *Research*, V64, No 1, pp 1118-135.

Computers and Structures (2008). "SAP API Documentation." Computers and Structure Inc., Berkeley, CA.

Ellingwood, B., Galambos, T., McGregor, J., and Cornell, C.A. (1980). Development of a Probability Based Load Criteria for American National Standards A58, National Bureau of Standards, Washington, D.C.

Fisher, J. M., and West, M.A. (2004). Serviceability Design Considerations for Steel Buildings, Steel Design Guide 3, 2nd Ed American Institute of Steel Construction, Chicago, IL.

Griffis, L. (1993). “Serviceability Limit States Under Wind”, Engineering Journal, AISC, First Quarter.

Hamizi, M., and Hannachi, N.E. (2007). "Evaluation by a finite element method of the flexibility factor and fixity degree for the base plate connections commonly used." Strength of Materials, 39(6), 588-99.

Hon, K.K., and Melchers, R.E. (1988). "Experimental behaviour of steel column bases." Journal of Constructional Steel Research, 9(1), 35-50.

International Building Code (2000). International Code Council, Country Club Hills, IL.

Main, J. A., and Fritz, W.P. (2006). “ Database-assisted design for wind: Concepts, software, and examples for rigid and flexible buildings.” *NIST building science series 180,* http://www.itl.nist.gov/div898/winds/pdf_files/Main-Fritz_DAD_BSS180.pdf (April 22, 2008)

Picard, A., and Beaulieu, D. (1985). "Behaviour of a simple column base connection." Canadian Journal of Civil Engineering, 12(1), 126-136.

Newman, A. (1997). Metal Building Systems, McGraw-Hill, New York.

Murakami, S. (2002). "Setting the Scene: CFD and Symposium Overview", Wind and Structures, v5, no 2-4, pp83-88.

Simiu, E., and Stathopoulos, T. (1997). "Codification of Wind Loads on Buildings Using Bluff Body Aerodynamics and Climatological Data Bases", Journal of Wind Engineering and Industrial Aerodynamics, 69-71, pp 497-506.

Surry, D., Kopp, G., and Bartlett, M., (2005). "Wind Load Testing of Low Buildings to Failure and Model and Full Scale", Natural Hazards Review, August, 2005, pp 121-128.

Uematsu, Y., and Isyumov, N., (1999). "Wind Pressures on Low Rise Buildings", Journal of Wind Engineering and Industrial Aerodynamics, 82, pp 1-25.

Whalen, T., Simiu, E., Harris, G., Lin, J., and Surry, D. (1998). "The use of Aerodynamic Databases for the Effective Estimation of Wind Effects in Main Wind-Force Resisting Systems: Application to Low Buildings", Journal of Wind Engineering and Industrial Aerodynamics, 77&78, pp 685-693.

`

APPENDIX A : Wind Load Calculations for test Building

A.1 Method-1: ACSE 7-05 Analytical approach for buildings of all heights.

Direction of wind: +X-Direction (Figure A-1).

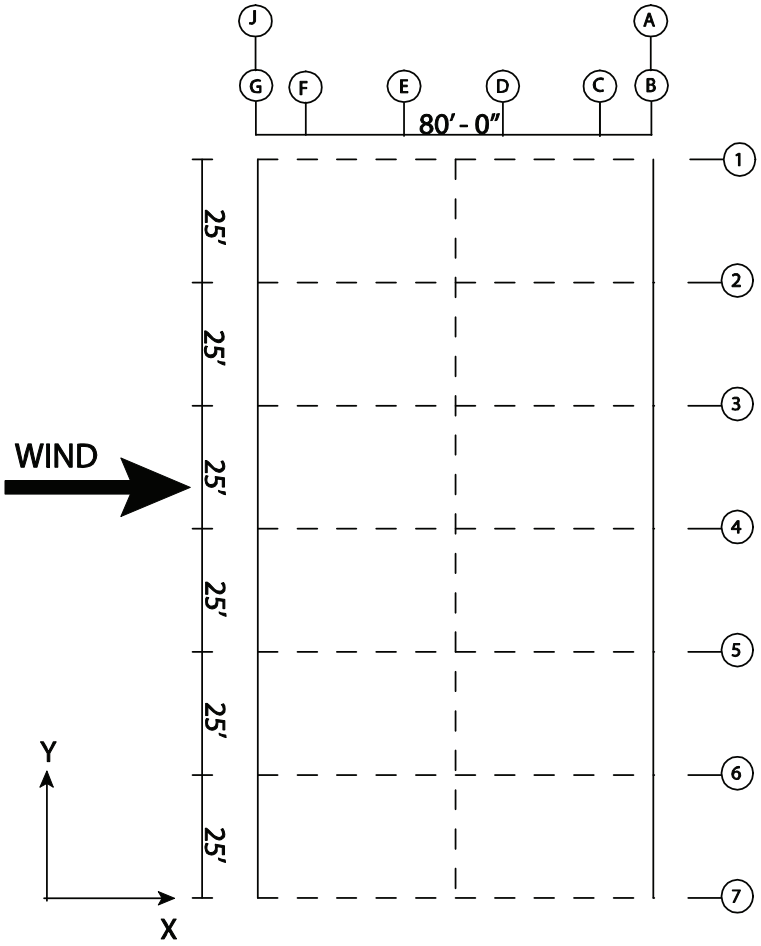

Figure A-1: Direction of wind loading

A.1.1 Building and site information

Width of building = 150 ft = 1800 in.

Length of building = 80 ft = 960 in.

Height at eave = 18 ft = 216 in.

Slope of building roof = 1:12

Height at ridge = (18 + 40/12) x 12 = 256 in.

Basic wind speed = 90 mph (Figure 6.1, ASCE 7-05 (ASCE 2005))

Wind exposure = Enclosed

Wind exposure category = B

Class = II

A.1.2 Wind load calculations

Mean roof height = 18 ft (As slope of roof is less than 10 degree, so eave height is taken as mean roof height)

Topographic factor, $K_z = (1+K_1.K_2.K_3)^2 = 1$ (Eq. 6-3, ACSE 7-05 (ASCE 2005))

Wind directionality factor, $K_d = 0.85$ (Table 6-4, ASCE 7-05 (ASCE 2005))

Velocity pressure exposure coefficient, K_z (Table 6-4, ASCE 7-05 (ASCE 2005))

for $15 \text{ ft} \le z \le z_g$

$$K_h = 2.01\left(\frac{h}{z_g}\right)^{\left(\frac{2}{\alpha}\right)}$$

$$K_h = 0.605$$

for $z \le 15$ ft

$$K_h = 2.01\left(\frac{z}{z_g}\right)^{\left(\frac{2}{\alpha}\right)}$$

$$K_z = 0.57$$

Velocity pressure,

$q_z = 0.00256\, K_z . K_{zt}. K_d . V^2 . I$ (lb/ft^2) (Eq. 6-5, ASCE 7-05(ASCE 2005))

$q_h = 0.00256\, K_h . K_{zt}. K_d . V^2 . I$ (lb/ft^2) (Eq. 6-5, ASCE 7-05(ASCE 2005))

Table A-1: Velocity Pressure Coefficients

Height (ft)	K_z	K_h	q_z (lb/ft^2)	q_h (lb/ft^2)
0-15	0.57	0.605	10.05	10.66
18	0.605	0.605	10.66	10.66

A.1.3 Pressure Distribution

$P = qGC_p - q_i(GC_{pi})$ (lb/ft$_2$) (Eq. 6-17, ASCE 7-05(ASCE 2005))

Where,

$q = q_z$ for windward walls evaluated at height z above ground

$q = q_h$ for leeward walls, side walls, and roofs, evaluated at height h

$q_i = q_h$ for windward walls, leeward walls, side walls, and roofs of enclosed buildings.

G = Gust factor = 0.85 (Section 6.5.8, ASCE 7-05(ASCE 2005))

C_p = external pressure coefficient (Figure 6-6, ASCE 7-05(ASCE 2005))

(GC_{pi}) = internal pressure coefficient (Figure 6-5, ASCE 7-05(ASCE 2005))

Using values of variables from corresponding equations, figures, tables and section of ASCE 7-05 (ASCE 2005), Table A-2 and A-3 present the resulting pressure distribution on windward and leeward side for two possible orientations of internal pressure.

Table A-2: Windward Side Pressure Distribution

Height (ft)	q_z (lb/ft^2)	Pressure (positive internal pressure) (lb/ft^2)	Pressure (negative internal pressure) (lb/ft^2)
0-15	10.05	=(10.05)(0.85)(0.8) – (10.66)(0.18) = 4.915	=(10.05)(0.85)(0.8) – (10.66)(-0.18) = 8.75
18	10.66	=(10.66)(0.85)(0.8) – (10.66)(0.18) = 5.33	=(10.66)(0.85)(0.8) – (10.66)(-0.18) = 9.17

Table A-3: Leeward Side Pressure Distribution

Height (ft)	q_h (lb/ft^2)	Pressure (positive internal pressure) (lb/ft^2)	Pressure (negative internal pressure) (lb/ft^2)
All heights	10.66	=(10.66)(0.85)(-0.5) – (10.66)(0.18) = -6.45	=(10.05)(0.85)(-0.5) – (10.66)(-0.18) = 2.61

A.1.4 Roof

For wind blowing normal to ridge, pressure acting normal to the surface of roof has been evaluated and presented in Table A-4.

Table A-4: Roof pressure distribution

Distance from windward edge (ft.)	q_h (lb/ft^2)	Pressure (positive internal pressure) (lb/ft^2)	Pressure (negative internal pressure) (lb/ft^2)
0-9	10.66	=(10.66)(0.85)(-0.9) – (10.66)(0.18) = -10.07	=(10.66)(0.85)(-0.9) – (10.66)(-0.18) = -6.24
9-18	10.66	=(10.66)(0.85)(-0.9) – (10.66)(0.18) = -10.07	=(10.66)(0.85)(-0.9) – (10.66)(-0.18) = -6.24
18-36	10.66	=(10.66)(0.85)(-0.5) – (10.66)(0.18) = -6.45	=(10.66)(0.85)(-0.5) – (10.66)(-0.18) = -2.61

36-80	10.66	=(10.66)(0.85)(-0.3) – (10.66)(0.18) = -4.64	=(10.66)(0.85)(-0.3) – (10.66)(-0.18) = -0.80

Figure A-2 shows the distribution of pressure on building.

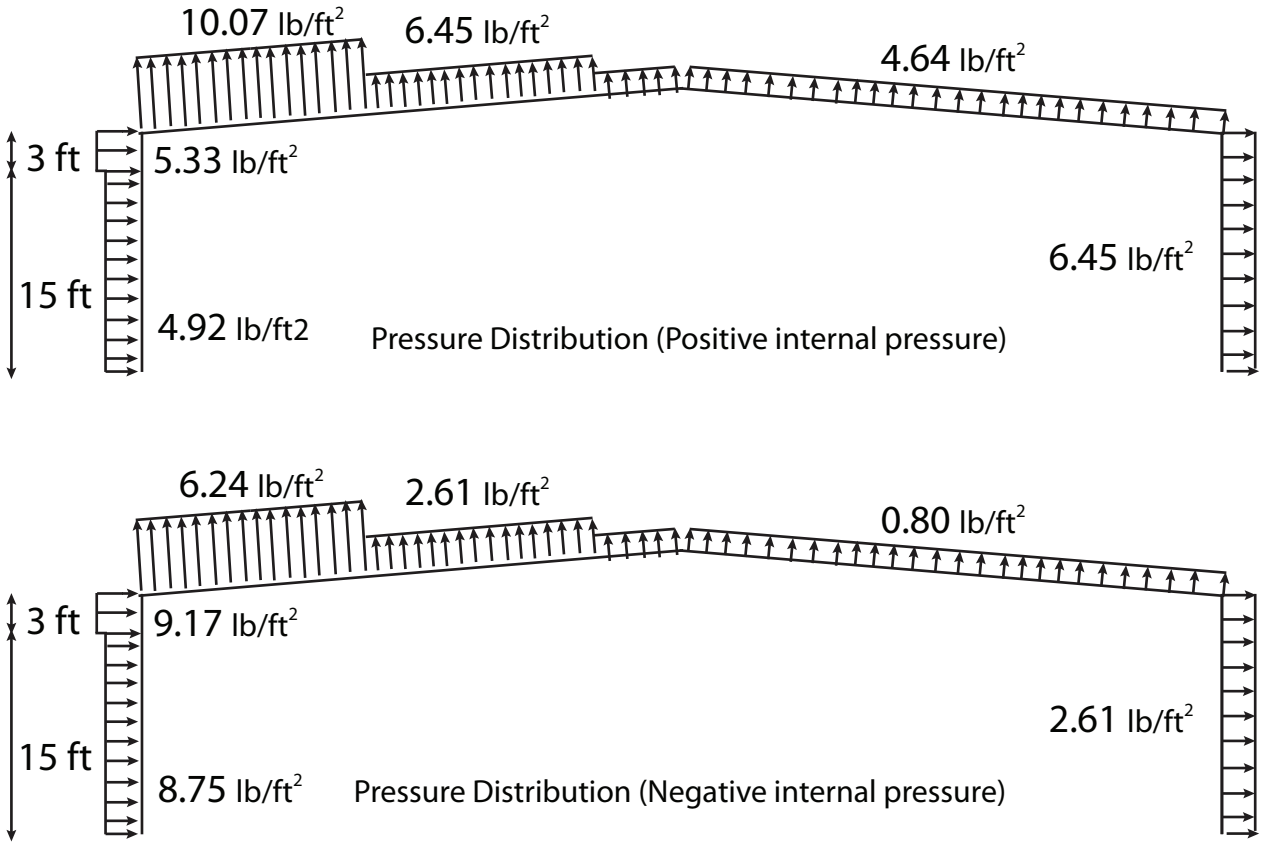

Figure A-2: Pressure distribution

A.1.5 Equivalent uniform lateral load

The frames are spaced at twenty-five center to center. So, considering same tributary width equivalent uniform loading acting along the frame is calculated (Figure A-3).

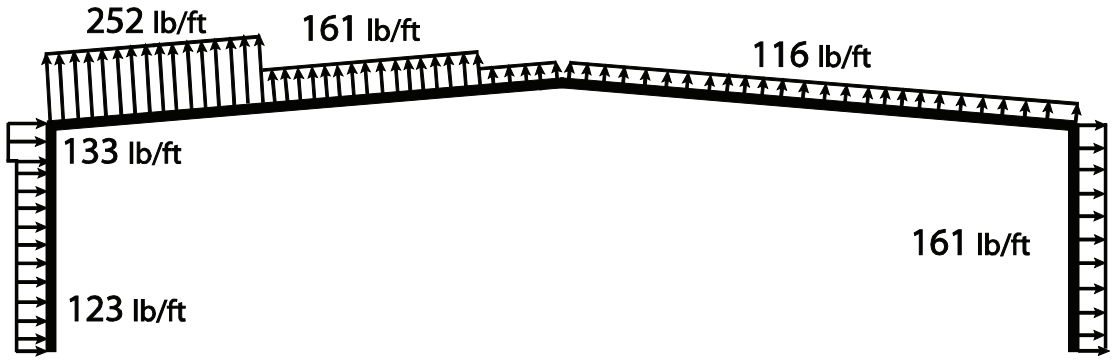

Uniform load (Positive internal pressure)

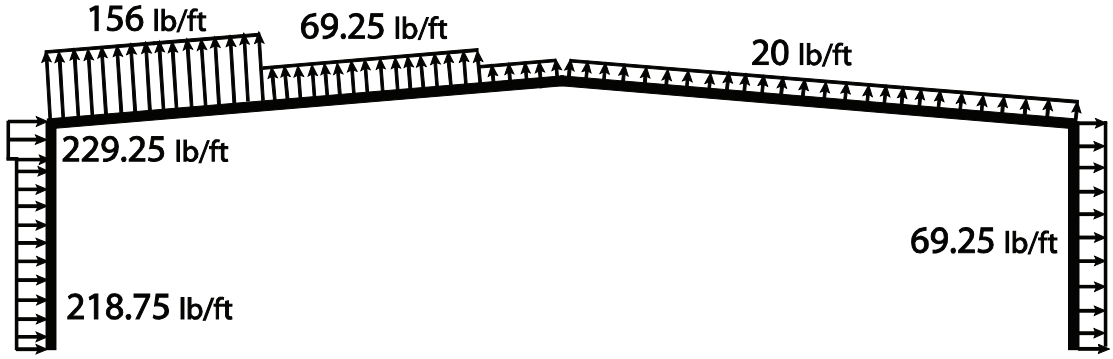

Uniform load (negative internal pressure)

Figure A-3: Uniform load acting on frame

A.1.6 Equivalent concentrated lateral load

Equivalent concentrated lateral load has been calculated by using uniform load distribution and height of the frame. The calculation is as shown below.

P (positive internal pressure) = 5100 lb

P (negative internal pressure) = 5100 lb

A.2 Method-2: ACSE 7-05Aanalytical approach for low-rise buildings (height < 60 ft)

In case of a building for which wind loading is being calculated using this method, load is calculated using different pressure zone coefficients as shown in Figure A-4. The figure shows wind acting from one direction, while designing a building using this method wind from all four directions is considered for both positive and negative internal pressure cases. Hence a building is designed for eight different load cases. In this report, however, building being symmetric only one load direction (both positive and negative internal pressure) has been considered.

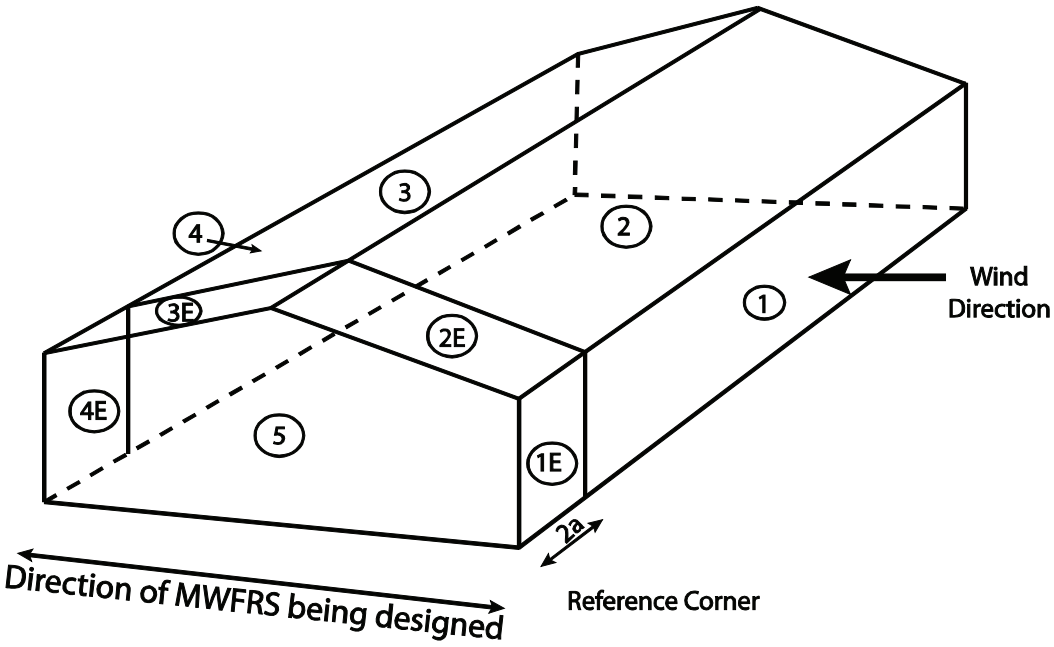

Figure A-4: Pressure coefficient Zones

A.2.1 Building and site information

Width of building = 150 ft = 1800 in.
Length of building = 80 ft = 960 in.
Height at eave = 18 ft = 216 in.
Slope of building roof = 1:12
Height at ridge = (18 + 40/12) x 12 = 256 in.
Basic wind speed = 90 mph (Figure 6.1, ASCE 7-05 (ASCE 2005))
Wind exposure = Enclosed
Wind exposure category = B
Class = I

A.2.2 Wind load calculations

Width of reference zone = 2a = 14.4 ft

where, 'a' is 10 percent of least horizontal dimension or 0.4h, whichever is smaller, but not less than either 4 percent of least horizontal dimension or 3 ft.

Mean roof height = 18 ft (As slope of roof is less than 10 degree, so eave height is taken as mean roof height)

Topographic factor, $K_z = (1+K_1.K_2.K_3)^2 = 1$ (Eq. 6-3, ACSE 7-05 (ASCE 2005))

Wind directionality factor, $K_d = 0.85$ (Table 6-4, ASCE 7-05, (ASCE 2005))

Velocity pressure exposure coefficient, K_z (Table 6-4, ASCE 7-05, (ASCE 2005))

for 15 ft ≤ z ≤ 30	for z ≤ 15 ft
$K_h = 0.70$	$K_z = 0.70$

Velocity pressure,

$q_z = 0.00256\ K_z\ .\ K_{zt}.\ K_d\ .\ V^2\ .\ I$ (lb/ft^2) (Eq. 6-5, ASCE 7-05, (ASCE 2005))

$q_h = 0.00256\ Kh\ .\ K_{zt}.\ K_d\ .\ V^2\ .\ I$ (lb/ft^2) (Eq. 6-5, ASCE 7-05, (ASCE 2005))

Table A-5: Velocity Pressure Coefficients

Height (ft)	K_z	K_h	q_z (lb/ft^2)	q_h (lb/ft^2)
0-15	0.70	0.70	12.35	12.35
18	0.70	0.70	12.35	12.35

A.2.3 Pressure Distribution

$P = q_h.(G.C_{pf}) - q_i.(GC_{pi})$ (lb/ft^2) (Eq. 6-17, ASCE 7-05, (ASCE 2005))

where,

q_h = velocity pressure evaluated at mean roof height (Section 6.5.6.3, ASCE 7-05, (ASCE 2005))

(GC_{pf}) = external pressure coefficient (Figure 6-10, ASCE 7-05, (ASCE 2005))

(GC_{pi}) = internal pressure coefficient (Figure 6-5, ACSE 7-05, (ASCE 2005))

Using values of variables from corresponding equations, figures, tables and section of ASCE 7-05 (ASCE 2005) , Table A-6 and Table A-7 present the resulting pressure distribution on windward and leeward side for two possible orientations of internal pressure.

Table A-6: Windward pressure distribution

Windward side

Load Case	Reference Corner (Zone 1E)	Other (Zone 1)
Positive internal pressure	12.35 (0.67-0.18) =6.05 lb/ft^2	12.35 (0.40-0.18) =2.72 lb/ft^2
Negative internal pressure	12.35 (0.67+0.18) =10.5 lb/ft^2	12.35 (0.40+0.18) =7.16 lb/ft^2

Table A-7: Leeward pressure distribution

Leeward side

Load Case	Reference Corner (Zone 4E)	Other (Zone 4)
Positive internal pressure	12.35 (-0.43-0.18) = -7.53 lb/ft^2	12.35 (-0.29-0.18) = -5.80 lb/ft^2
Negative internal pressure	12.35 (-0.43+0.18) = -3.09 lb/ft^2	12.35 (-0.29+0.18) = -1.36 lb/ft^2

Roof

For wind blowing normal to ridge, pressure acting normal to the surface of roof has been evaluated and presented in Table A-8.

Table A-8: Roof Pressure

Windward roof

Load Case	Reference Corner (Zone 2E)	Other (Zone 2)
Positive internal pressure	12.35 (-1.07 -0.18) = -15.43 lb/ft^2	12.35 (-0.69-0.18) = -10.75 lb/ft^2
Negative internal pressure	12.35 (-1.07+0.18) = -11.0 lb/ft^2	12.35 (-0.69+0.18) = -6.30 lb/ft^2

Leeward roof

Load Case	Reference Corner (Zone 3E)	Other (Zone 3)
Positive internal pressure	12.35 (-0.53 -0.18) = -8.77 lb/ft^2	12.35 (-0.37 -0.18) = -6.8 lb/ft^2
Negative internal pressure	12.35 (-0.53+0.18) = -4.32 lb/ft^2	12.35 (-0.37 +0.18) = -2.35 lb/ft^2

Figure A-5 shows the distribution of pressure on reference zone and other area.

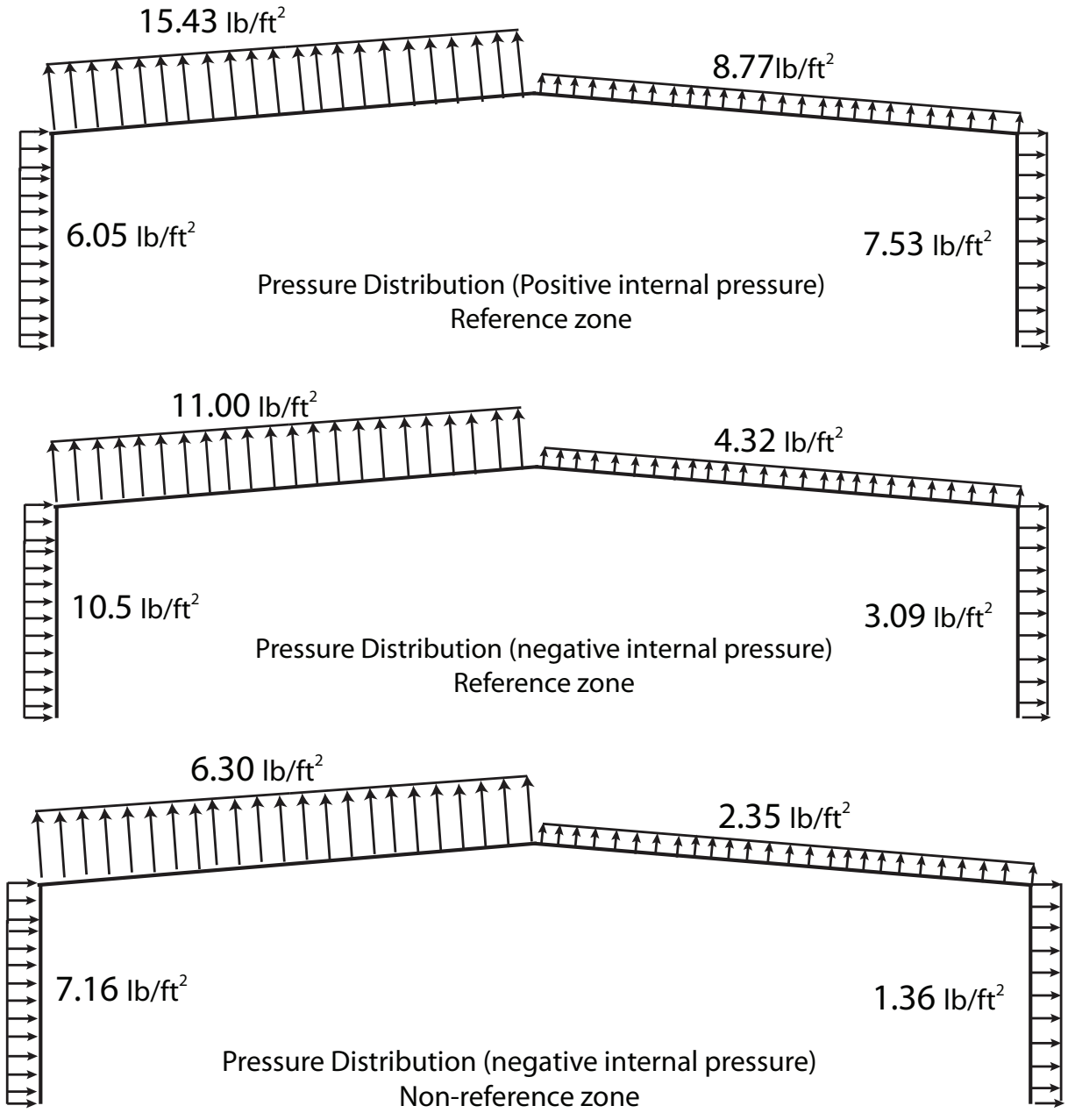

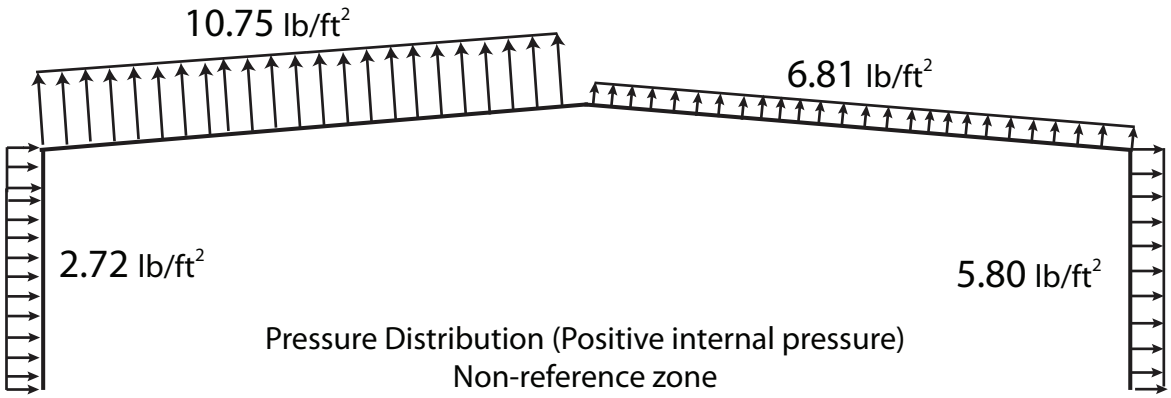

Figure A-5: Pressure distribution for reference and non-reference zone

A.2.4 Equivalent uniform lateral load

The frames are spaced at twenty-five center to center. So, considering same tributary width equivalent uniform loading acting along the frame is calculated (Figure A-6). Reference zone which is more critical has been considered while calculating uniform load.

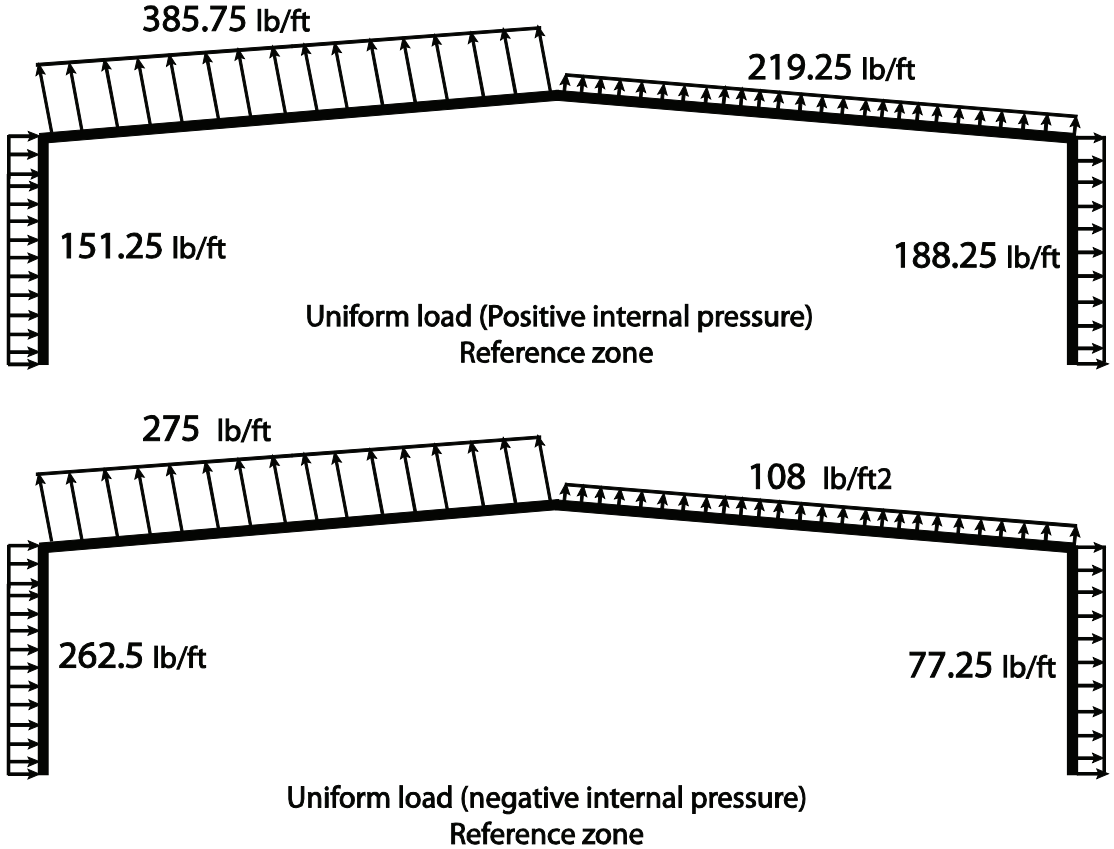

Figure A-6: Uniform load distribution for reference

A.2.5 Equivalent concentrated lateral load

Equivalent concentrated lateral load has been calculated by using uniform load distribution and height of the frame. The calculation is as shown below.

P (positive internal pressure) = 6100 lb

P (negative internal pressure) = 6100 lb

APPENDIX B - Procedure for applying Strain Gages

Uni-axial pre-wired Strain gauge type "C2A-06-250LW-350" has been used to which are suitable to be used for metal surfaces. The resistance of strain gauge is 350 ohms. The following procedure was used to apply the strain gages to the columns of the Test Building:

1. Column flanges are degreased and cleaned with a surface cleaning cloth.
2. Surface is sanded with a grinder and using 220-grit paper.
3. Vishay micro measurement's MCA-2M- PREP CONDITIONER A is used to wash the surface off any particles left after sanding. Surface is then wiped with a clean gauze pad. This has to be done in single stroke across the sanded area.
4. Strain gage location is marked by making cross hairs with a ball point pen.
5. Surface is again sanded using 320-grit paper and cleaned wiped using conditioner A.
6. Using a Q-tip and conditioner A, wipe until a fresh Q-tip stays clean after wiping.
7. Once the surface is clean, using MN5A-2 M-PREP NEUTRALIZER 5A and a Q-tip scrub the cleaned surface. Wipe the excess Neutralizer off using a gauze pad, again staring from inside in a single stroke.
8. A separate surface is cleaned with conditioner and neutralizer.
9. Using a pair of tweezers, strain gauge is taken out and placed on the cleaned surface with shinning side up.
10. Lightly place tape down in the strain gauge and then peel the tape off of the surface at a shallow angle.
11. Hold the tape ends of tape and place the strain gauge on cross hairs marked on the surface.
12. Tape is peeled off once again at a shallow angle with strain gauge completely lifted off with other tape still attached to the surface.
13. Catalyst is applied to the strain gage and edge of tape. It is then allowed to dry for a minute.
14. A drop of M-bond adhesive is applied at the middle bottom edge of gauge
15. Grabbing the free end of the tape, hold the tape taut over the gauging area and press thumb on the bottom edge of the gauge. Move thumb to the top of the gauge, forcing the adhesive to spread evenly throughout the gauge surface.
16. Keeping firm pressure on the gauge with thumb. Let the adhesive cure for 1 min.
17. Check the installation by peeling back (at a 45^{o} angle) the tape and picking at the edges of the gauge with a dental pick. Place the tape back on the gauge until ready for soldering.

18. Apply a piece of Teflon tape that covers the strain gauge and any exposed wires.
19. Cut a piece of (sticky) butyl rubber that extends half an in. beyond all edges of the strain gauge as well as beyond the grey outer covering of the wire. Remove on side of the paper backing, and press the expose butyl rubber down all around the edges, as well as wrap the butyl rubber underneath the grey cable. Remove the other paper backing
20. Cut a piece of neoprene rubber that is about ¼ in. smaller on all edges of the butyl rubber and place on the butyl rubber.
21. Cut a length of foil tape that covers the butyl rubber and the neoprene pad.
22. Seal the edges of the tape with the Nitrile rubber. Allow the rubber to dry and apply a second coat.

APPENDIX C - Calibration of Instruments

C.1 Strain Gages

Change in strain at the column bases was recorded on Vishay Micro measurements data acquisition system 5000 which has the capability of calibrating strain gauges internally. The system can calculate the gauge factor associated with length of wire and perform shunt calibration.

C.2 Linear Voltage Displacement Transducer and Wire Potentiometer

Both Linear Voltage Displacement Transducer (LVDT) and Wire potentiometers (Wire Pots) are voltage based devices. In order to calibrate the devices a known value of displacement is given to the instruments using a scale. Corresponding to the displacement values, a change in voltage is read. The process repeated for a number of values results in voltage-displacement plot, which when entered into data acquisition system calibrates the device.

C.3 Load transducer

The load transducer was calibrated in laboratory using the universal materials testing machine (SATEC, Figure C-1). Similar to the calibration procedure for the LVDT, the change in voltage is read for a known change in load applied. Voltage-Load plot results in the calibration of Load cell.

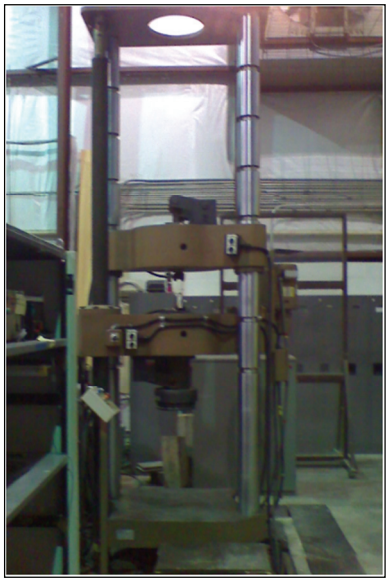

Figure C-1: Universal Testing Machine

C.4 Inclinometer

Voltage based inclinometers (NG2U series) manufactured by Reiker Inc. were used. The inclinometers were mounted on the web at mid-depth of column near base as shown in Figure 7-7. The inclinometers have a measuring range of ±10 degree and a resolution of one fiftieth of a degree. Inclinometers were calibrated using a simply supported beam. The inclinometer was mounted at one end of beam vertically above one of the supports. At the other end of beam a jack was placed. The beam was instrumented with an LVDT at same location. Using the jack, beam was lifted, and the displacement was monitored through by the LVDT. With the length of beam and lift known, the angle by which inclinometer rotates was calculated. The calibration apparatus is shown in Figure C-2.

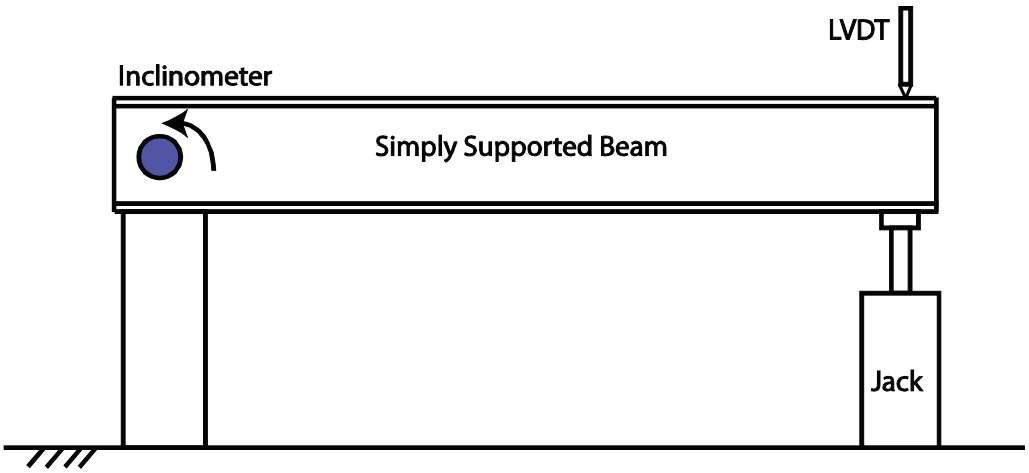

Figure C-2: Simply supported beam for calibrating LVDT

APPENDIX D – Test Results (Load-Deformation Response)

D.1 Frame along grid line 2

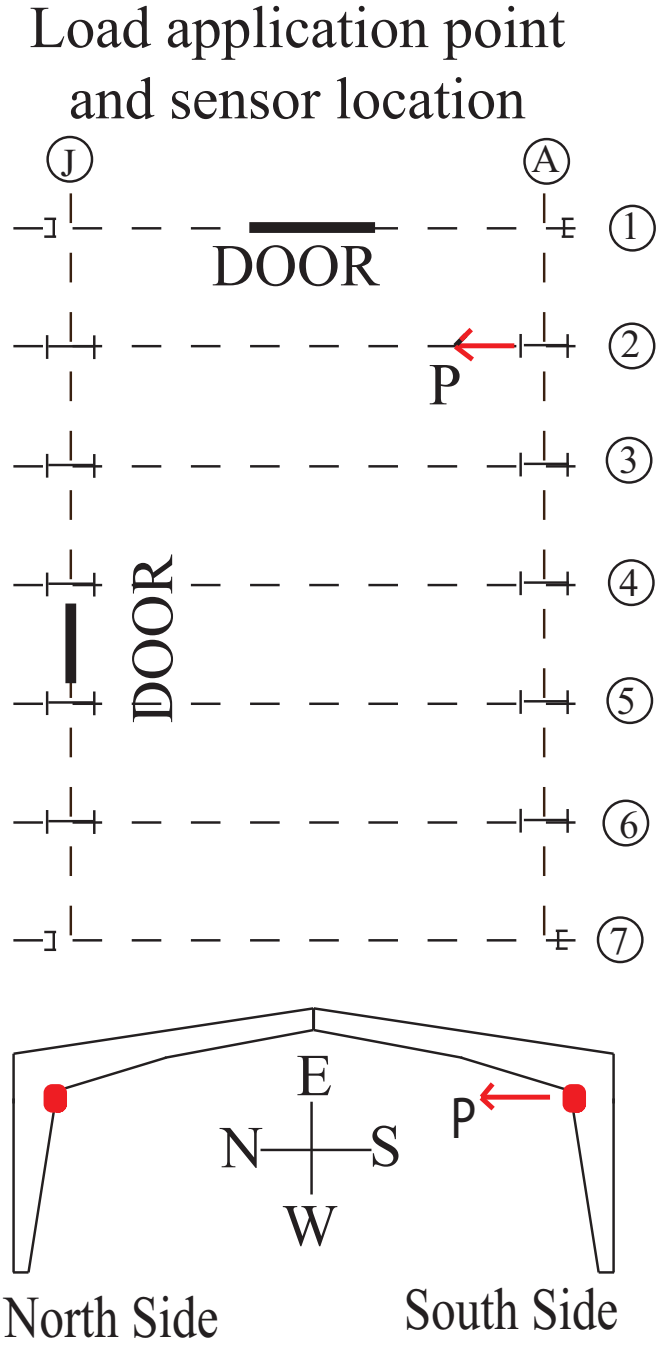

Figure D-1: Location of frame along line 2 and load application points

D.1.1 Test 01

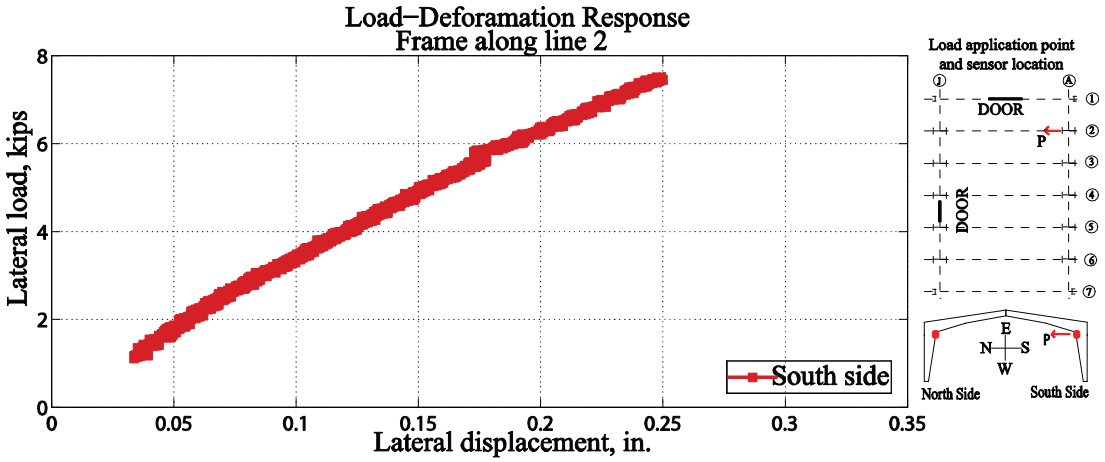

Figure D-2: South end column response of frame along line 2

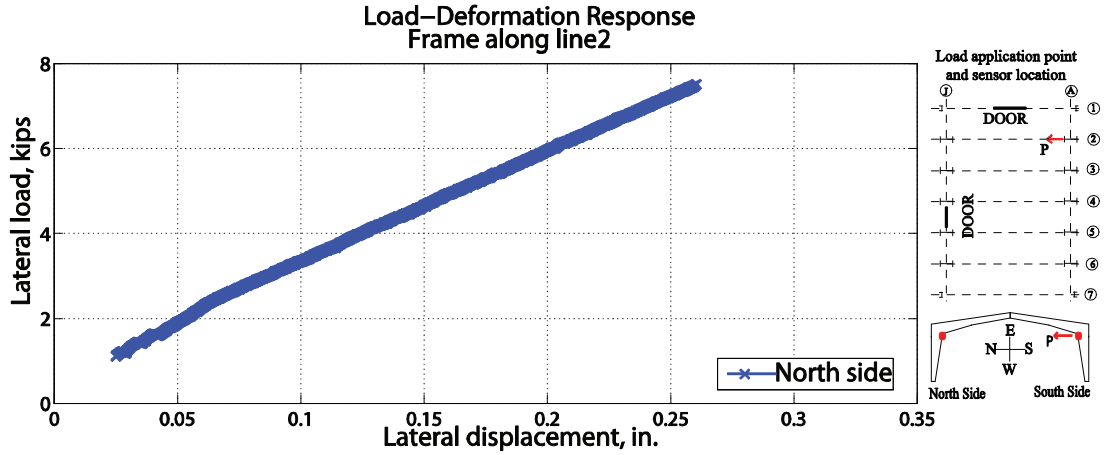

Figure D-3: North end column response of frame along line 2

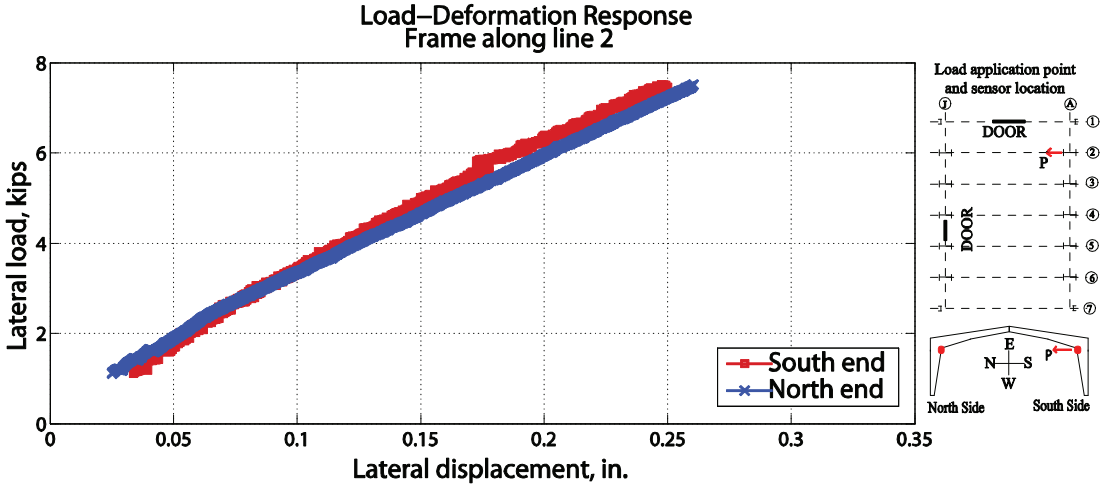

Figure D-4: Deformation on two sides of frame along line 2

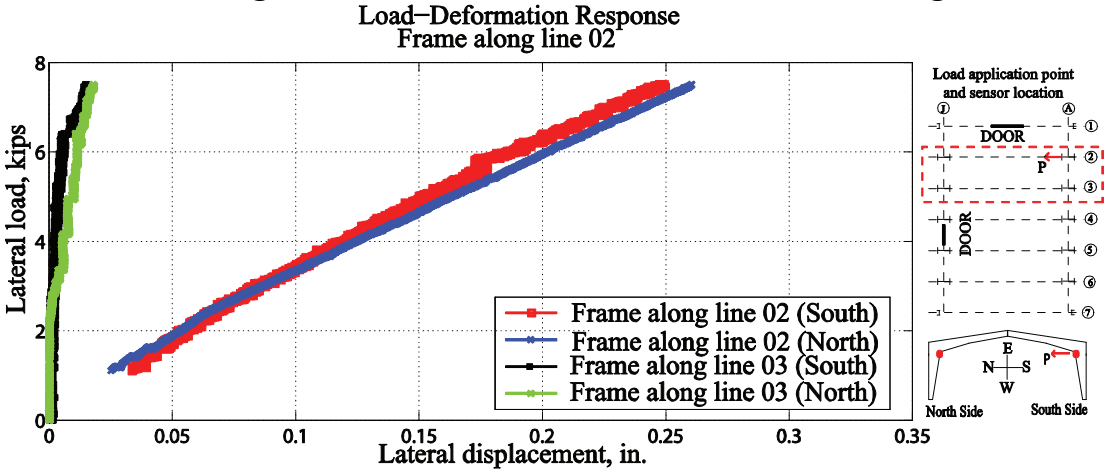

Figure D-5: Deformations on primary frame along line 2

D.1.2 Test 02

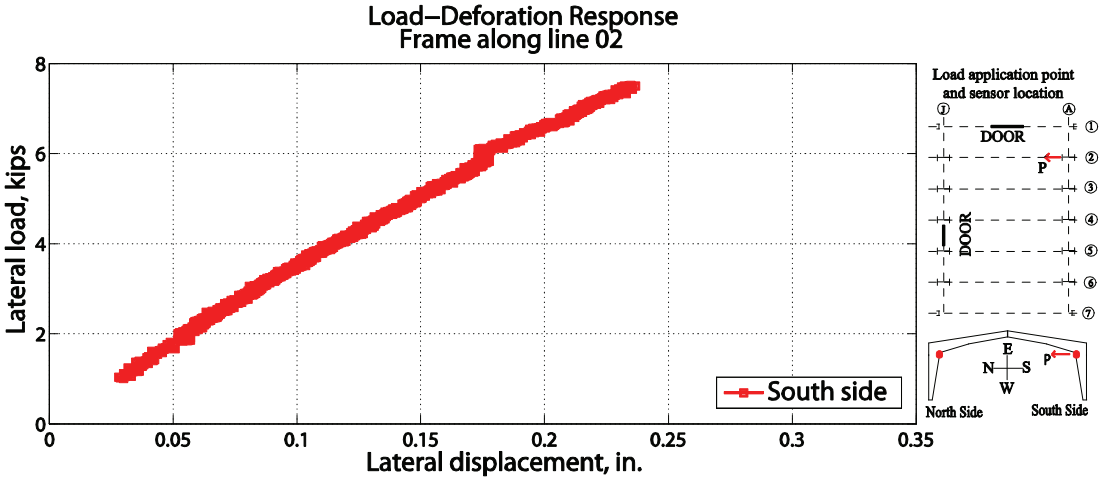

Figure D-6: South end column response of frame along line 2

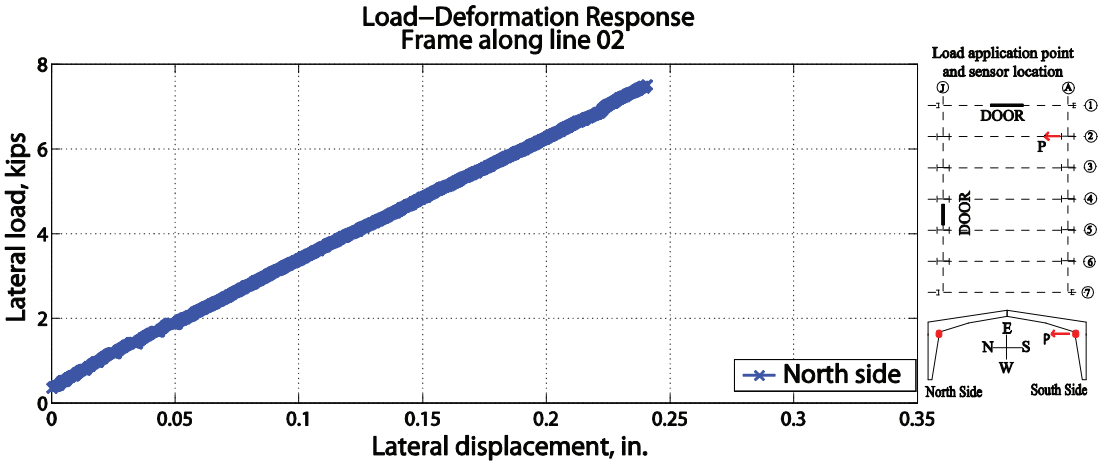

Figure D-7: North end column response of frame along line 2

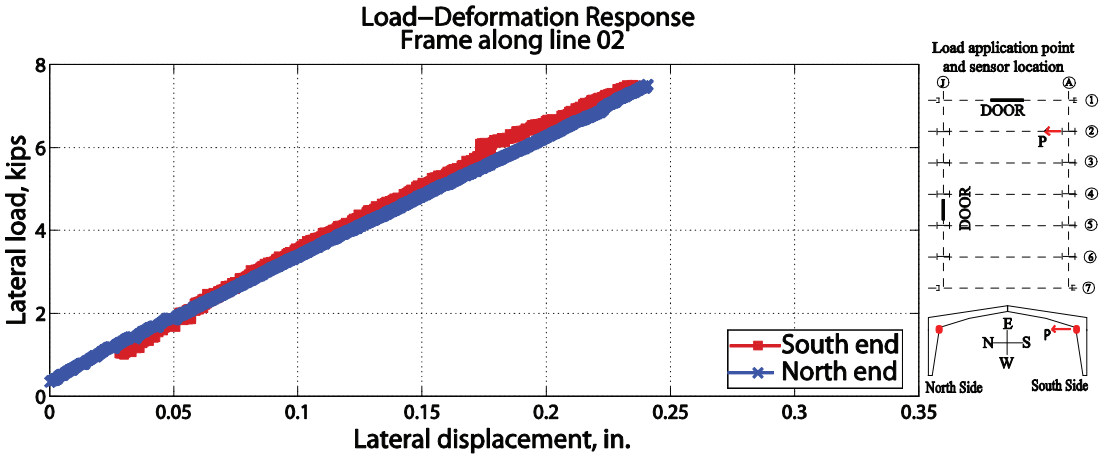

Figure D-8: Deformation on two sides of frame along line 2

D.1.3 Test 03

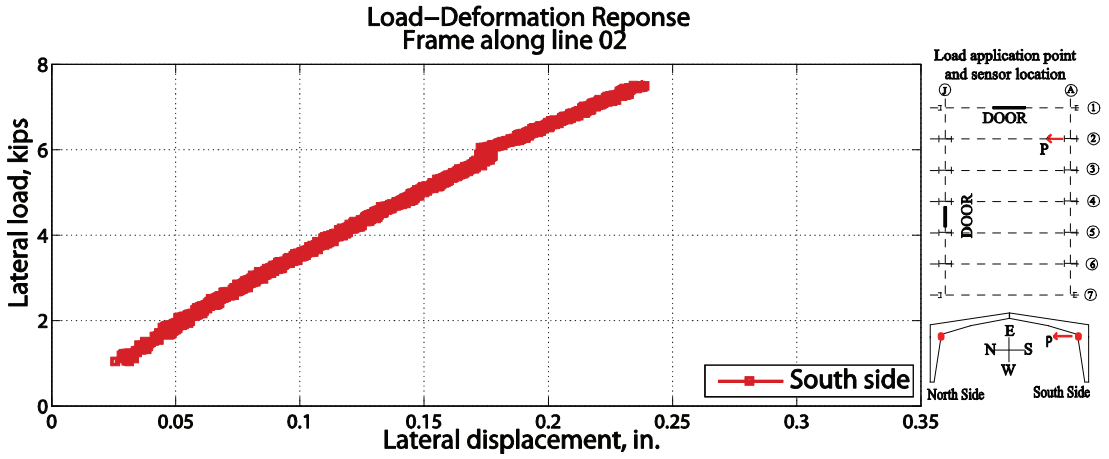

Figure D-9: South end column response of frame along line 2

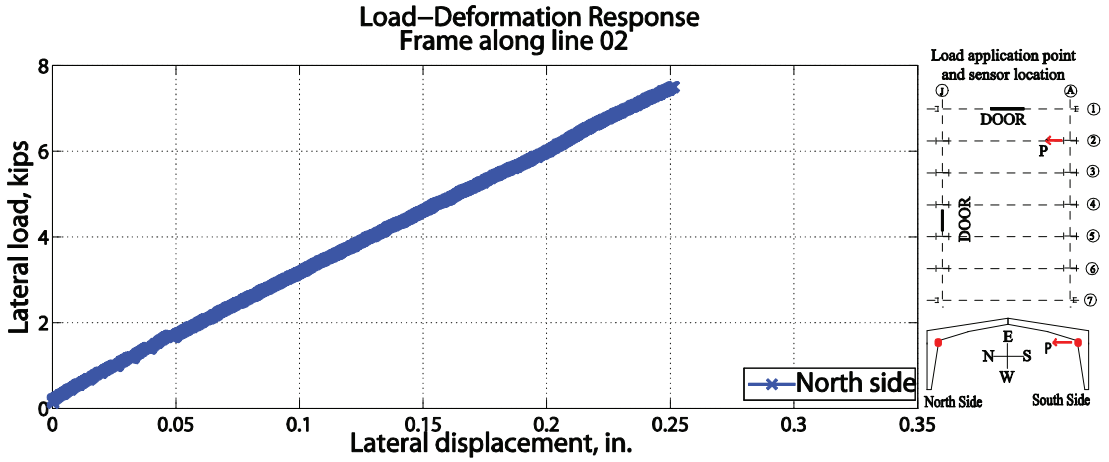

Figure D-10: North end column response of frame along line 2

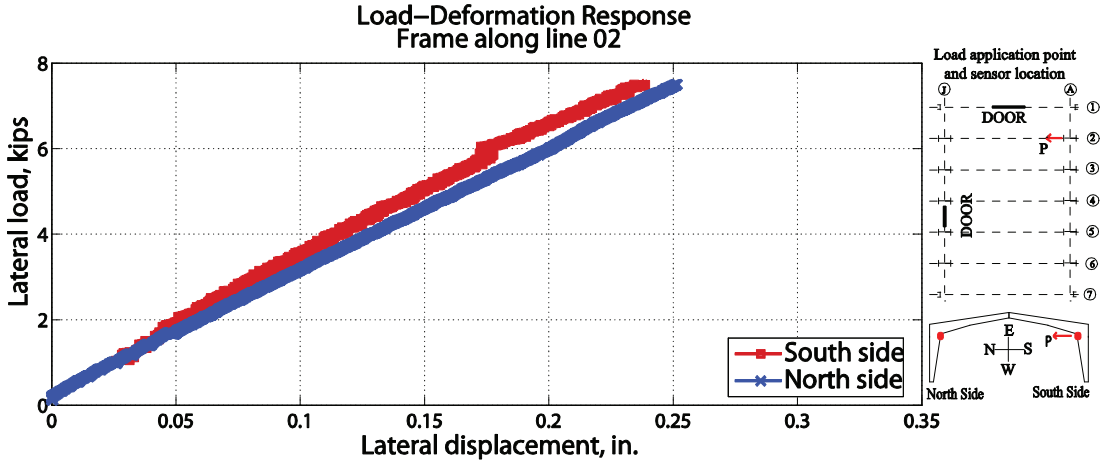

Figure D-11: Deformation on two sides of frame along line 2

D.2 Frame along grid line 3

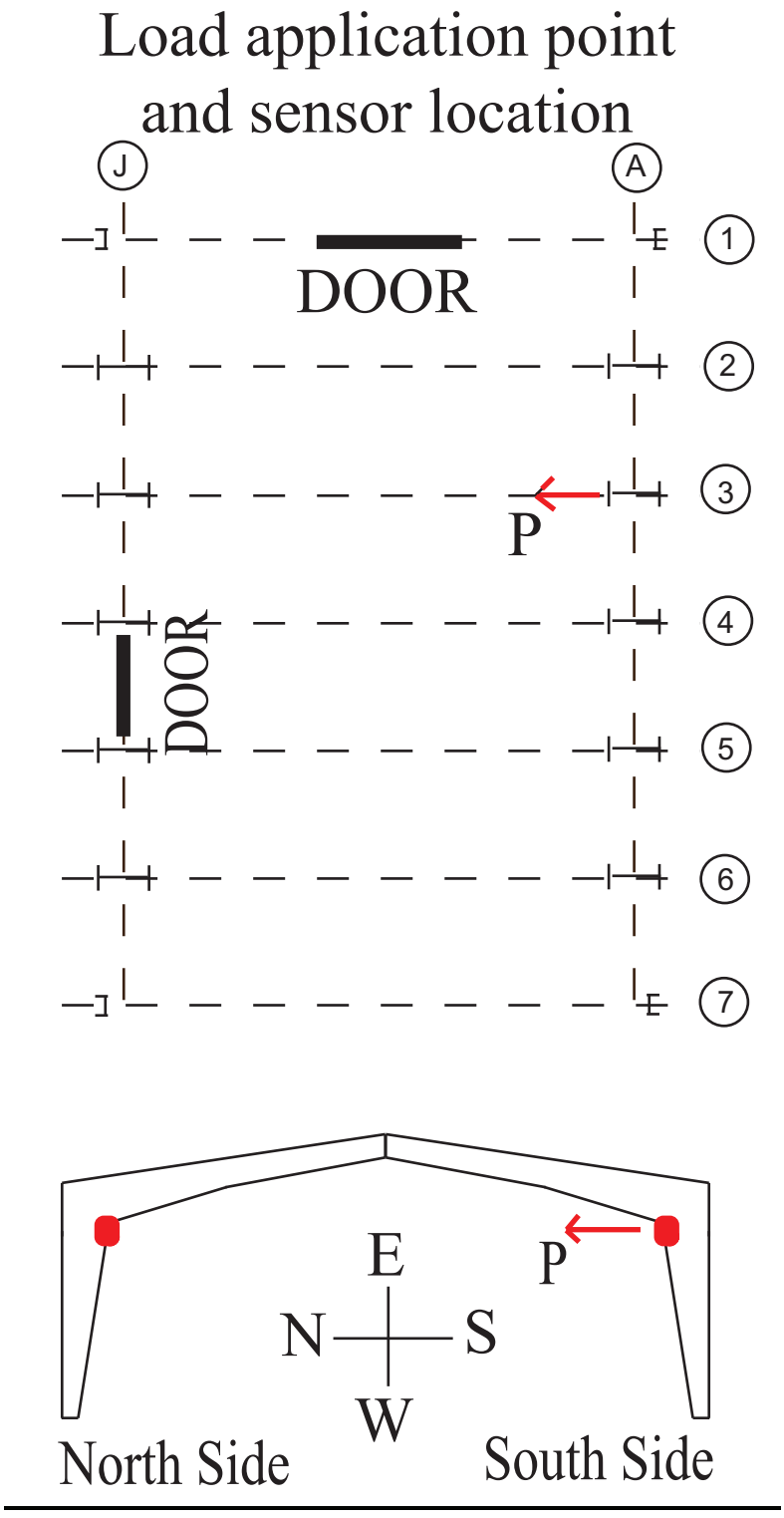

Figure D-12: Location of frame along line 3 and load application points

D.2.1 Test 01

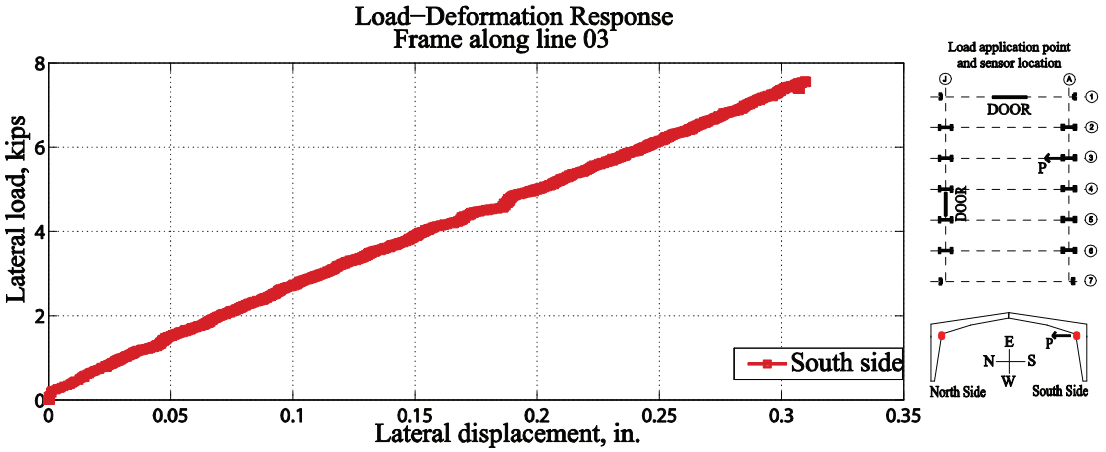

Figure D-13: South end column response of frame along line 2

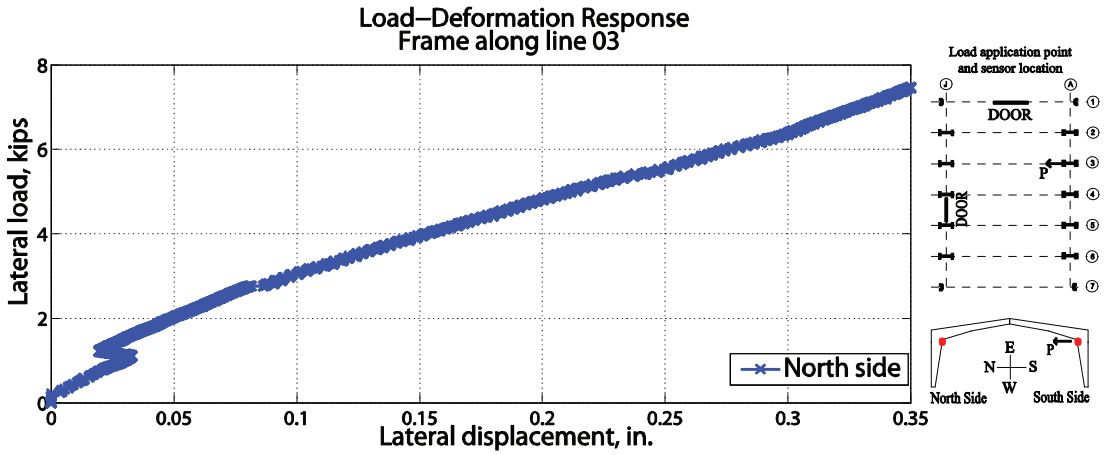

Figure D-14: North end column response of frame along line 2

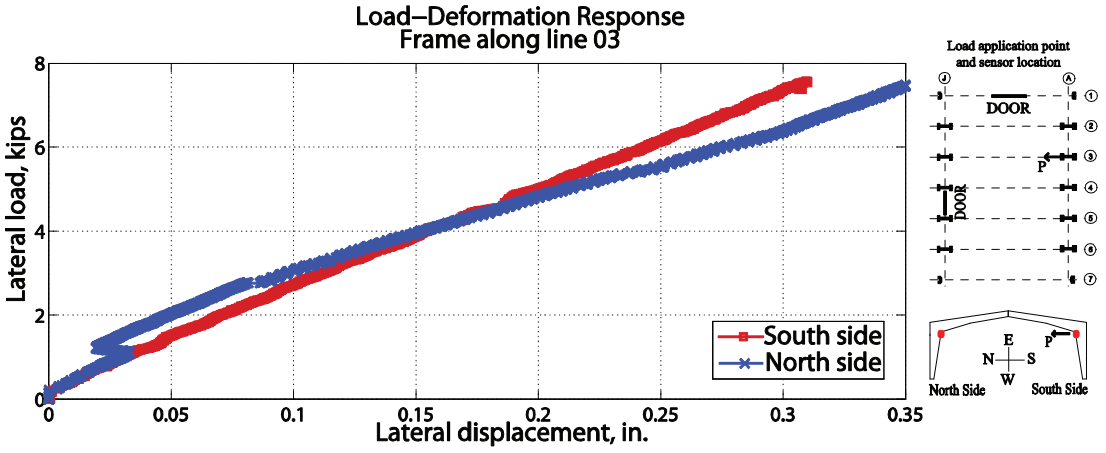

Figure D-15: Deformation on two sides of frame along line 2

D.2.2 Test 02

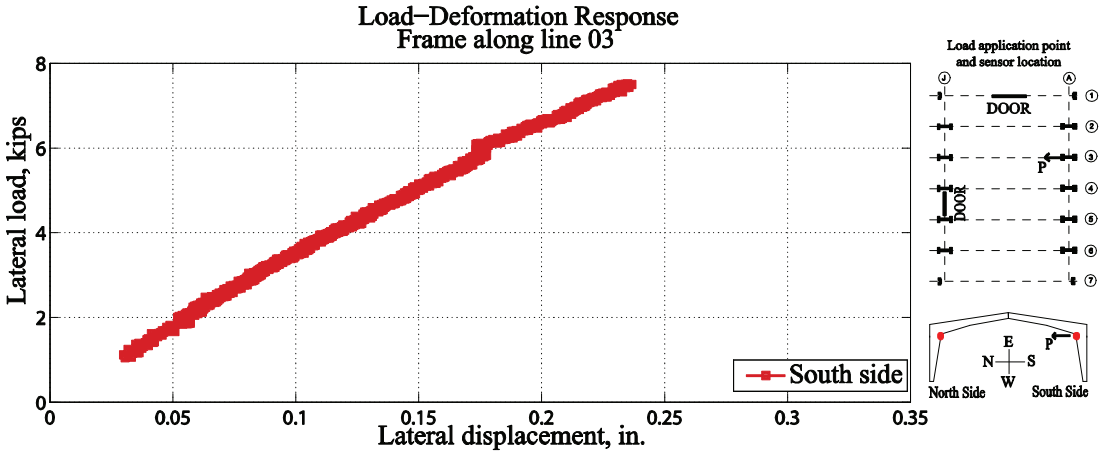

Figure D-16: South end column response of frame along line 2

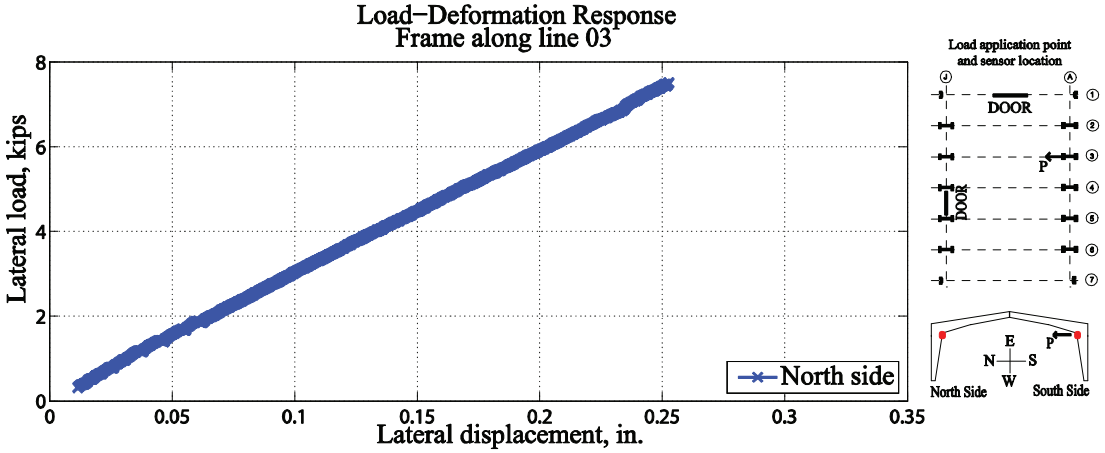

Figure D-17: North end column response of frame along line 2

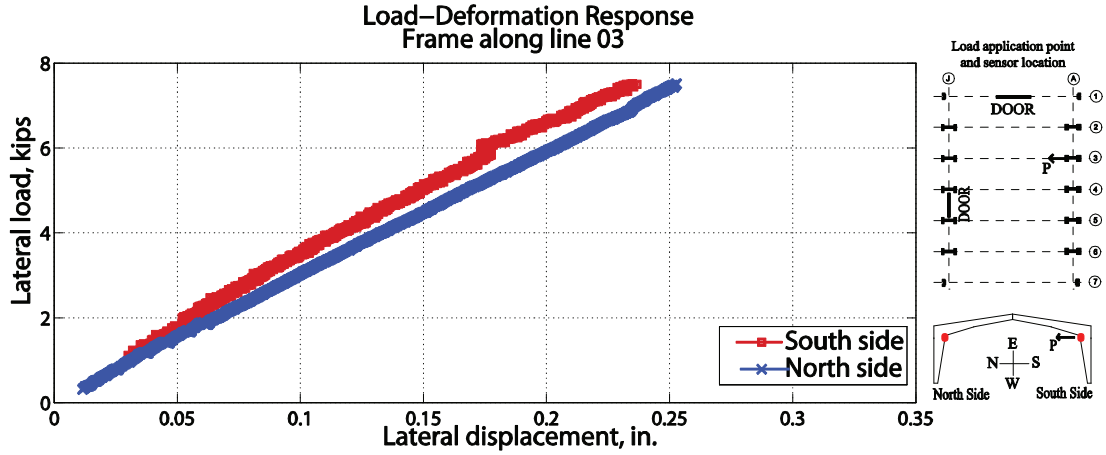

Figure D-18: Deformation on two sides of frame along line 3

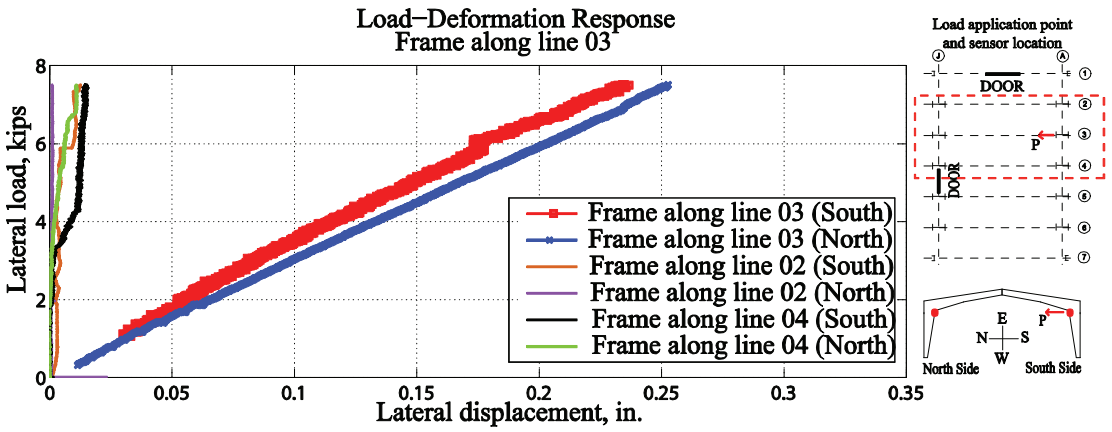

Figure D-19: Deformations on primary frame along line 3

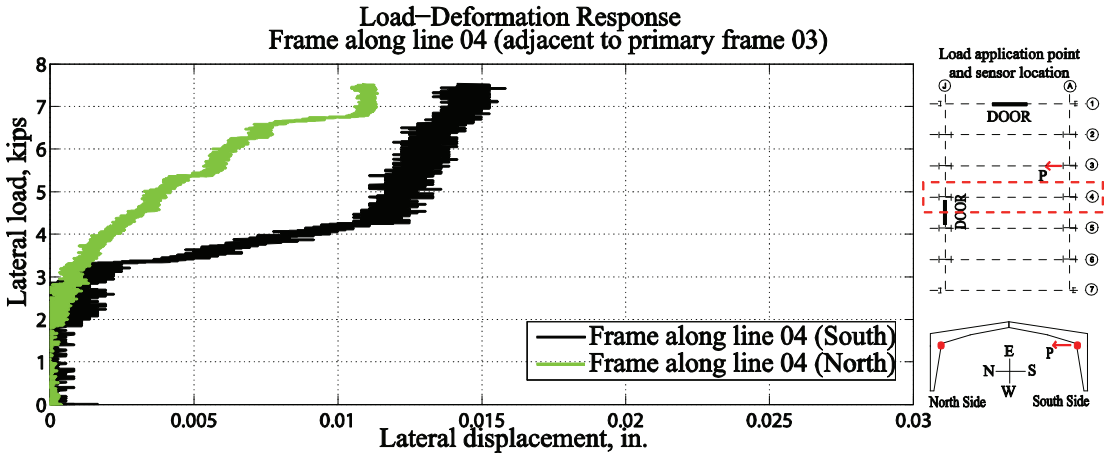

Figure D-20: Deformations on frame along line 4

D.2.3 Test 03

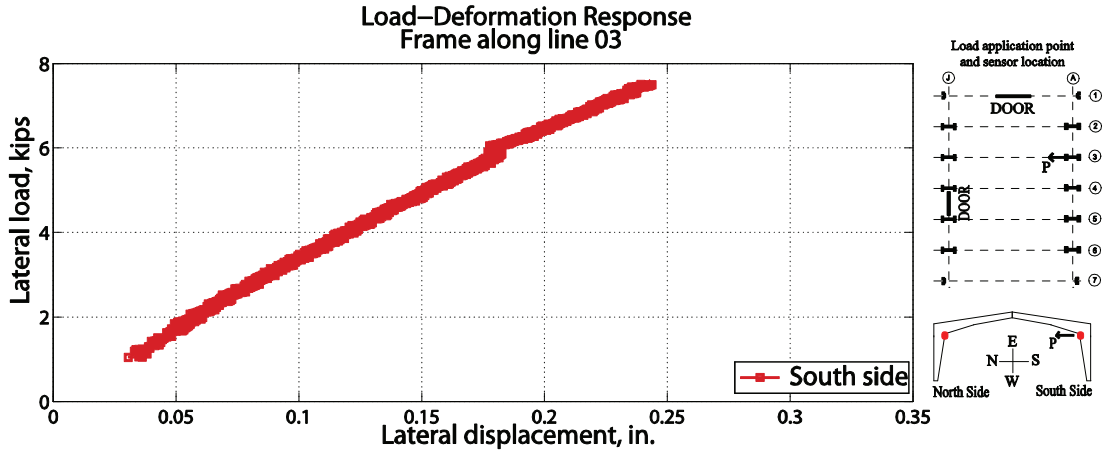

Figure D-21: South end column response of frame along line 3

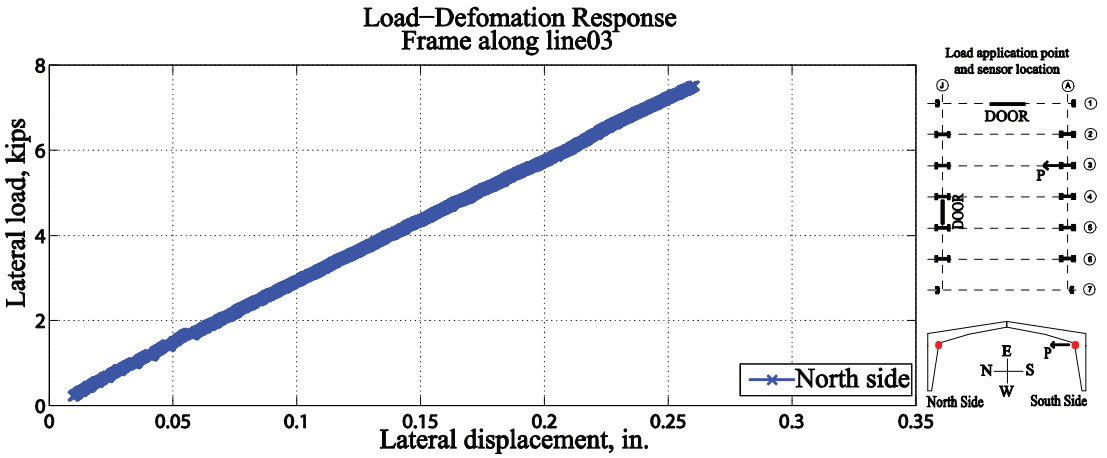

Figure D-22: North end column response of frame along line 3

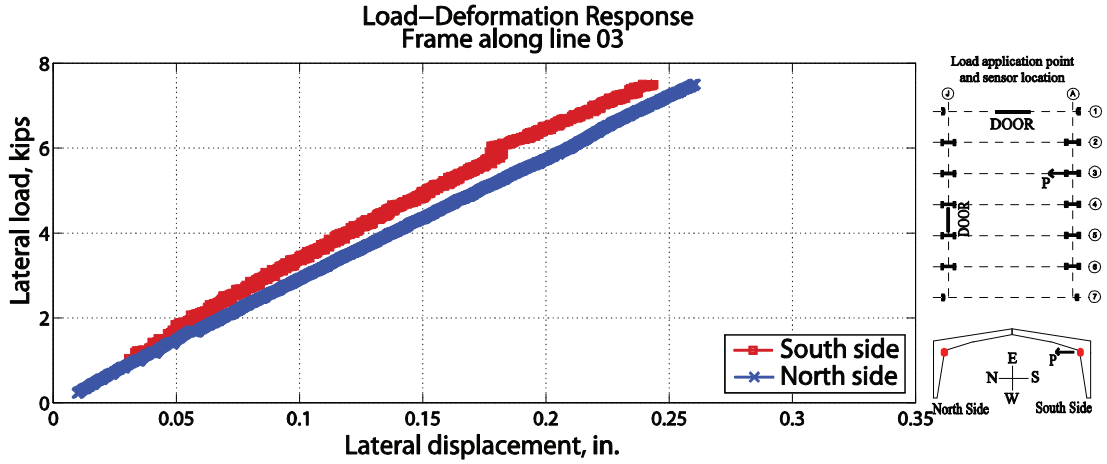

Figure D-23: Deformation on two sides of frame along line 3

D.3 Frame along grid line 4

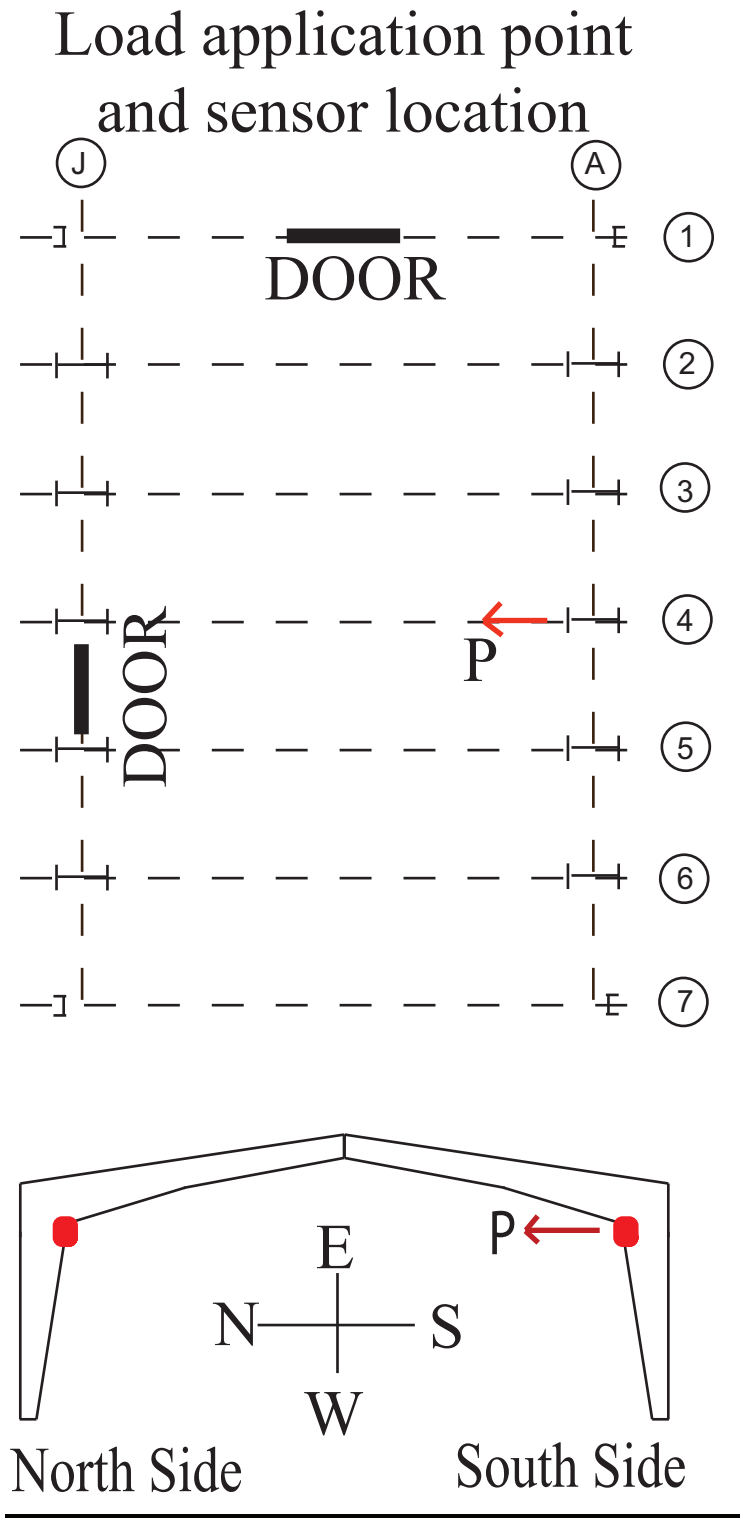

Figure D-24: Location of frame along line 4 and load application points

D.3.1 Test 01

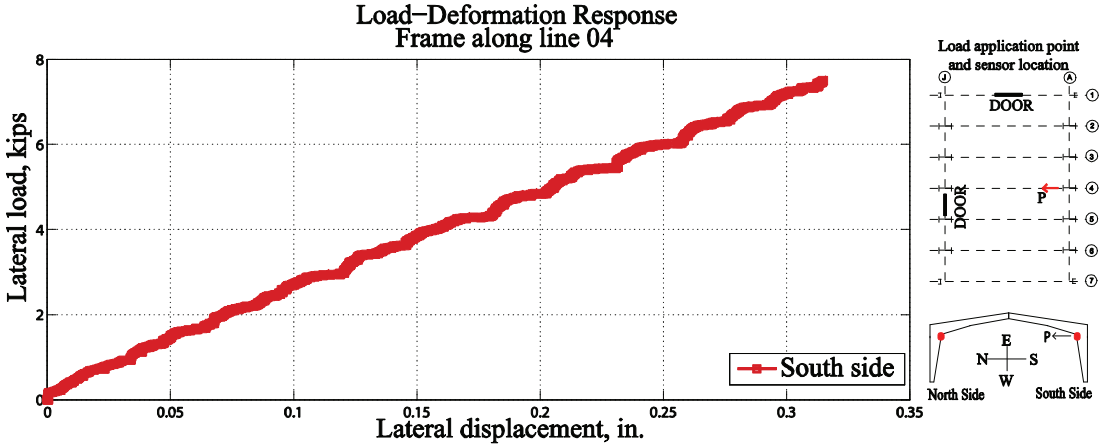

Figure D-25: South end column response of frame along line 4

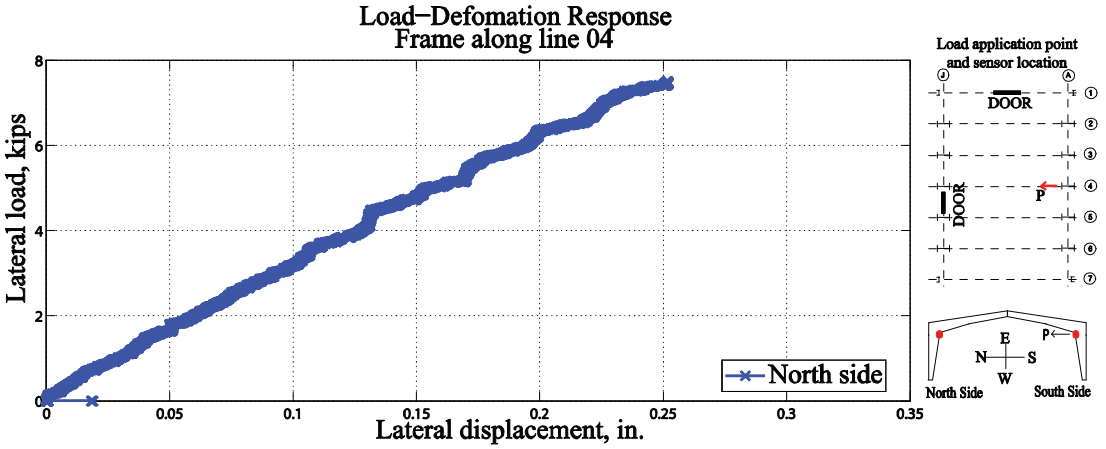

Figure D-26: North end column response of frame along line 4

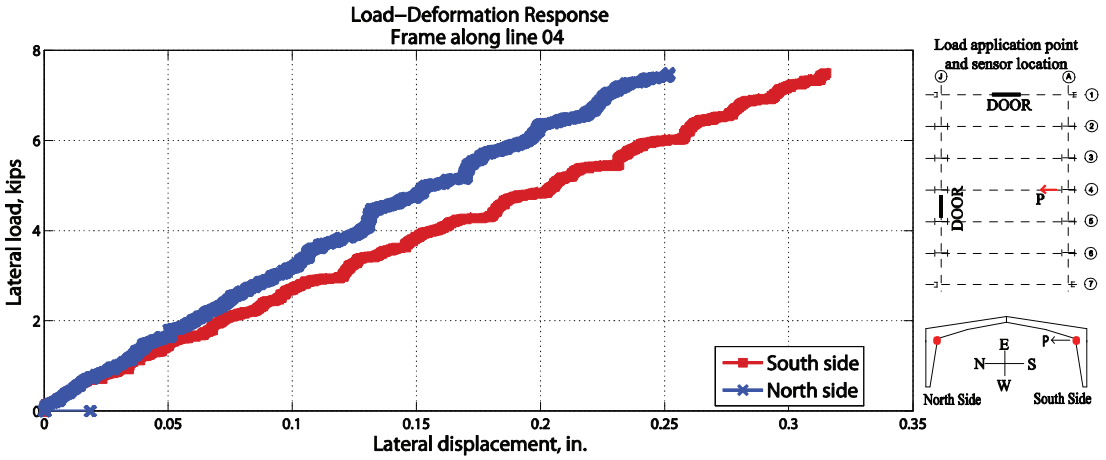

Figure D-27: Deformation on two sides of frame along line 4

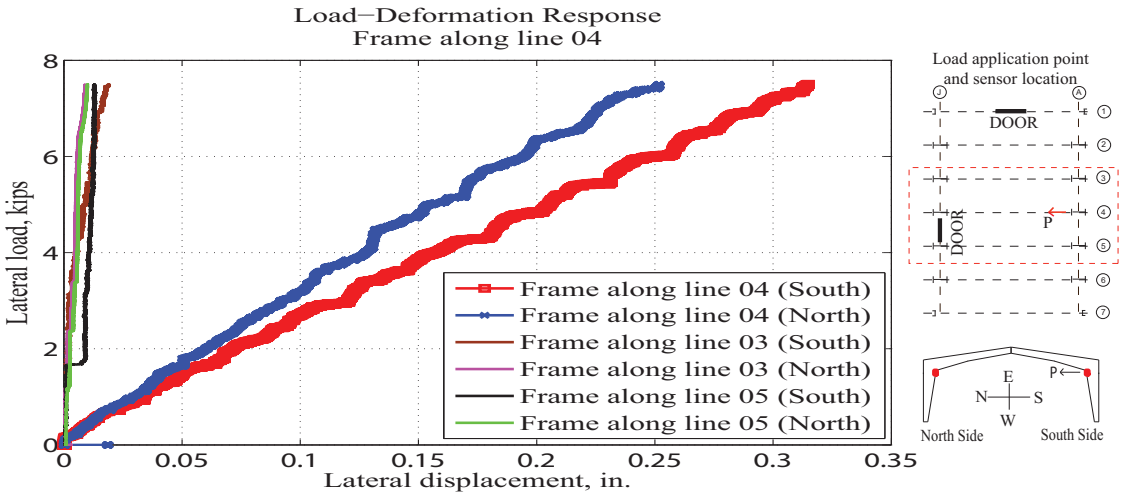

Figure D-28: Deformations on primary frame along line 4 and adjacent frames along line 3 and line 5

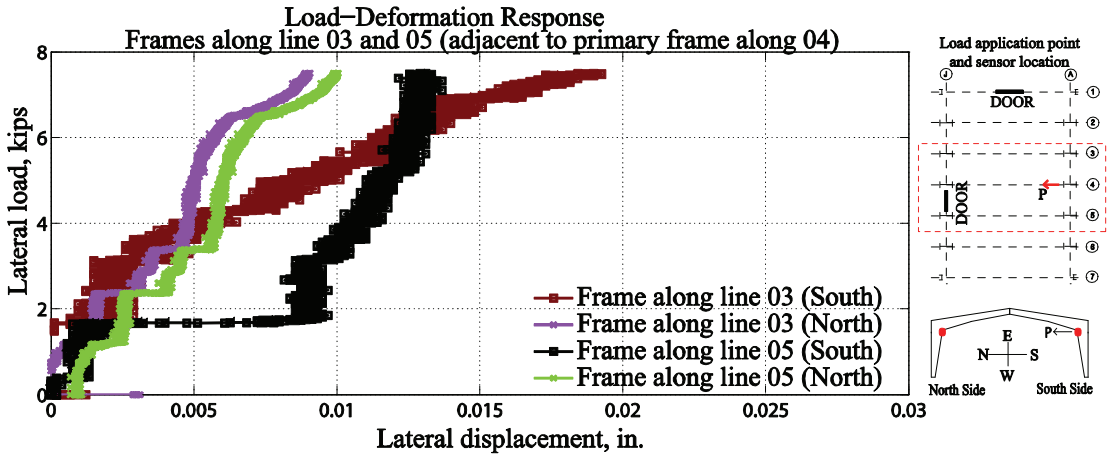

Figure D-29: Deformations on frame along line 3 and line 5

D.3.2 Test 02

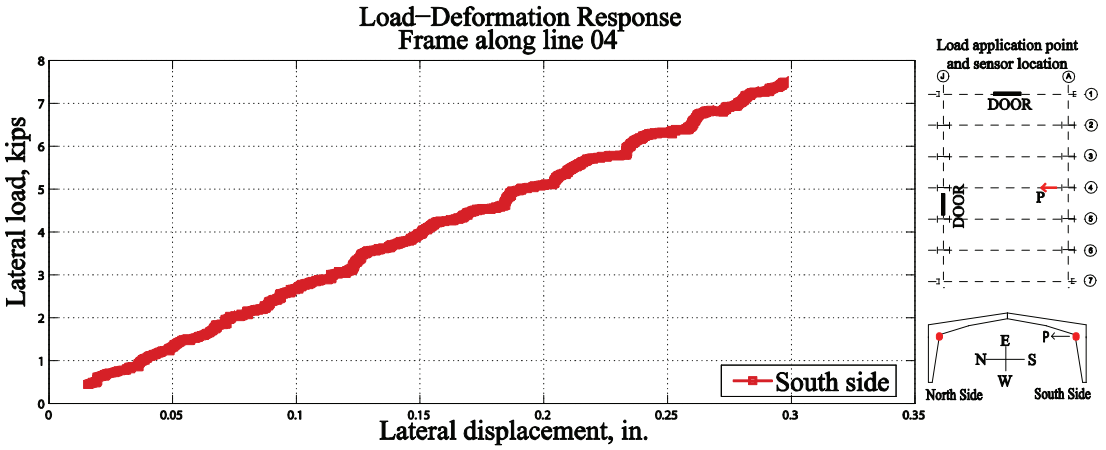

Figure D-30: South end column response of frame along line 4

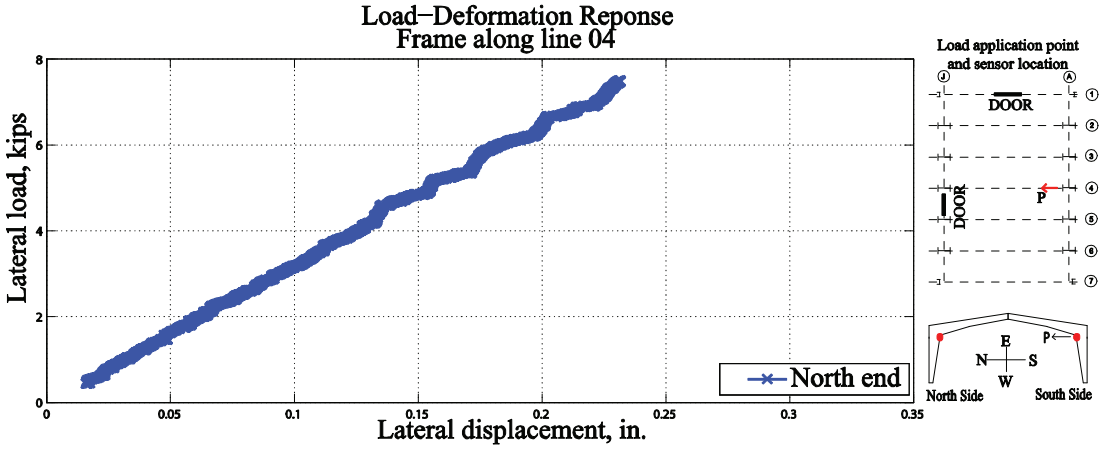

Figure D-31: North end column response of frame along line 4

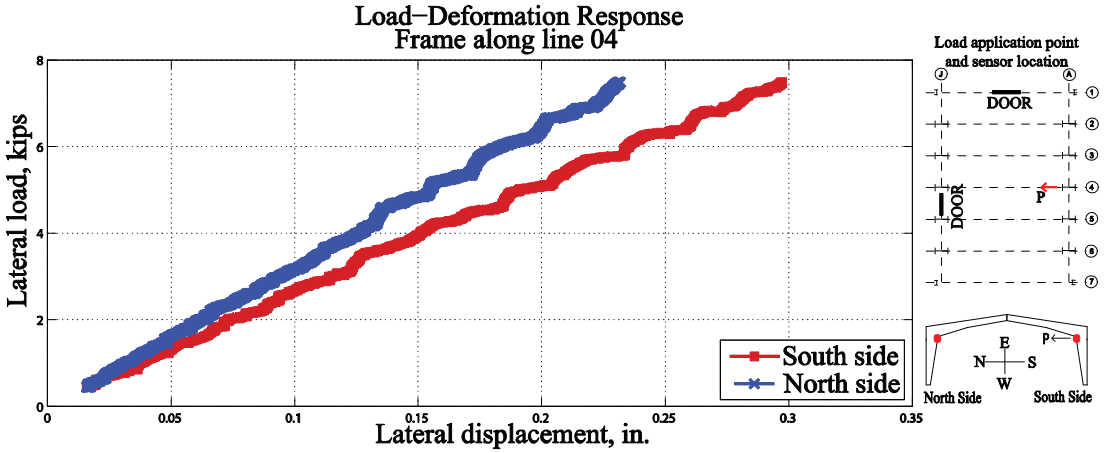

Figure D-32: Deformation on two sides of frame along line 4

D.3.3 Test 03

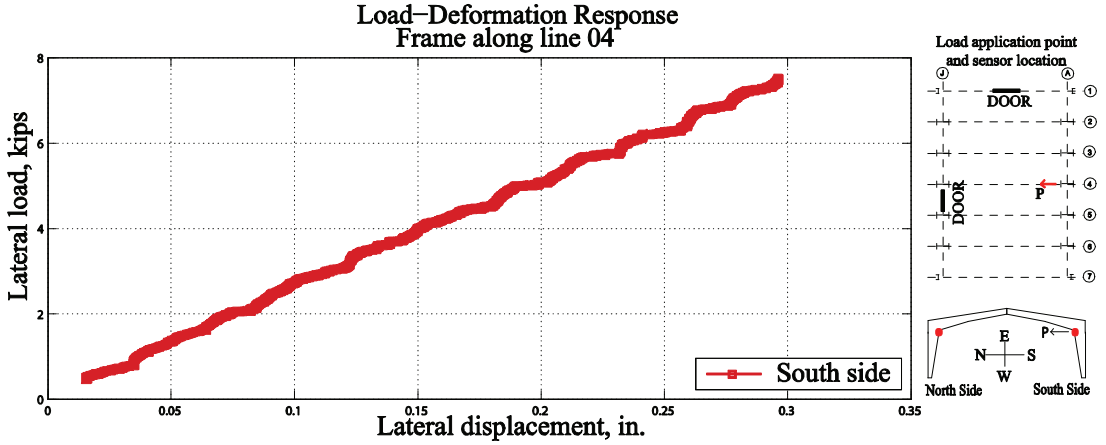

Figure D-33: South end column response of frame along line 4

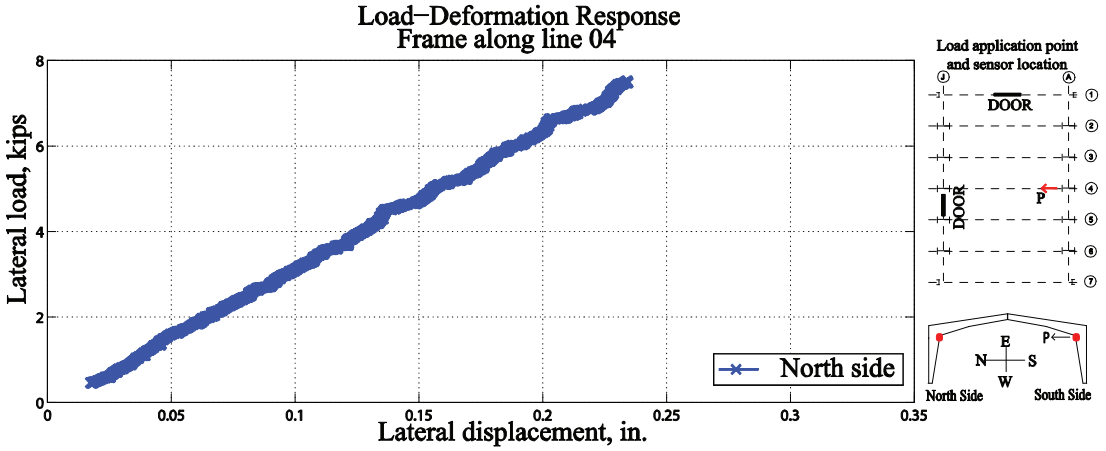

Figure D-34: North end column response of frame along line 4

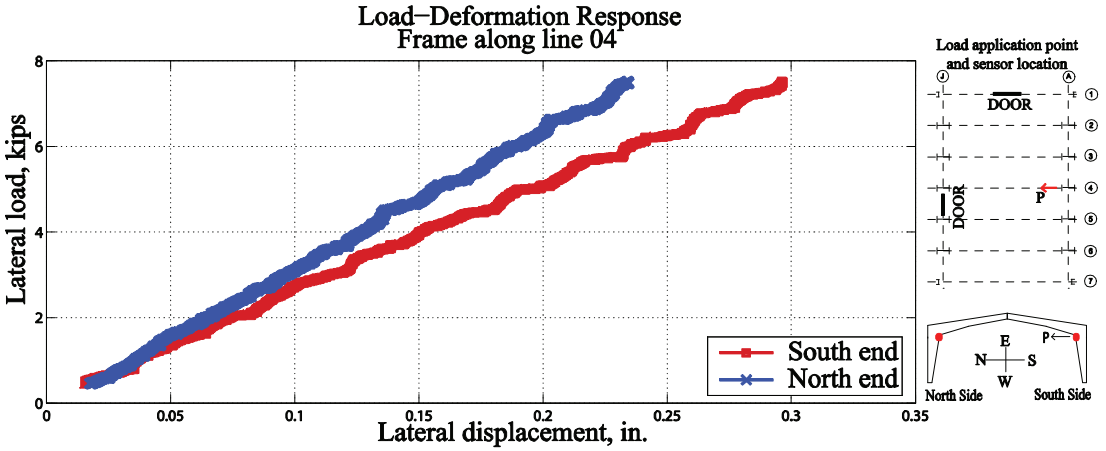

Figure D-35: Deformation on two sides of frame along line 4

D.4 Frame along grid line 5

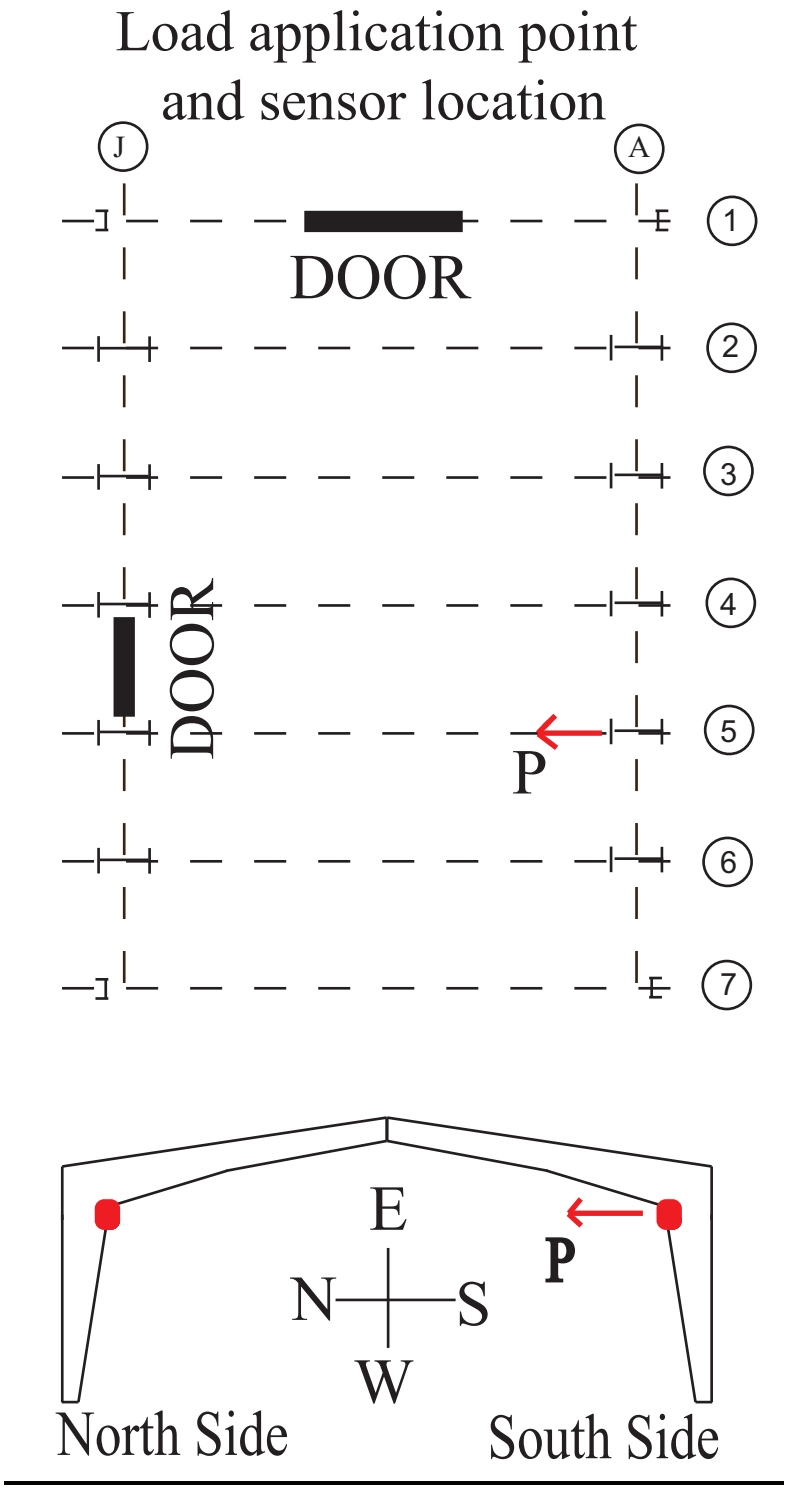

Figure D-36: Location of frame along line 5 and load application points

D.4.1 Test 01

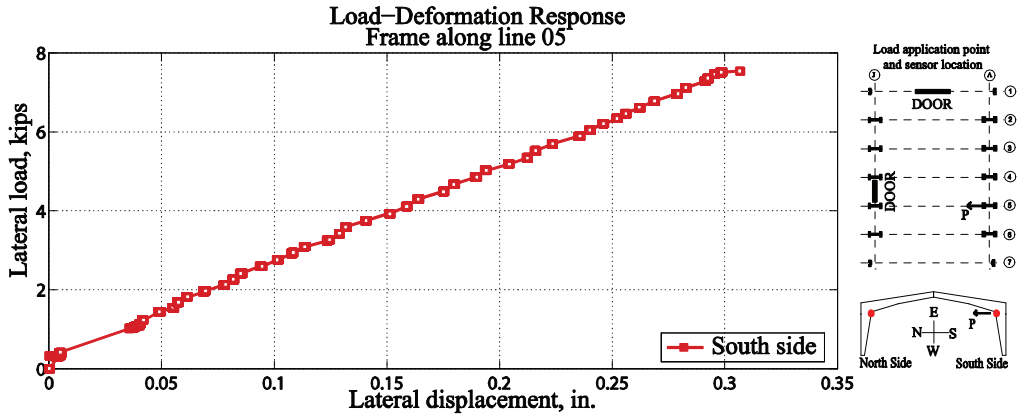

Figure D-37: South end column response of frame along line 5

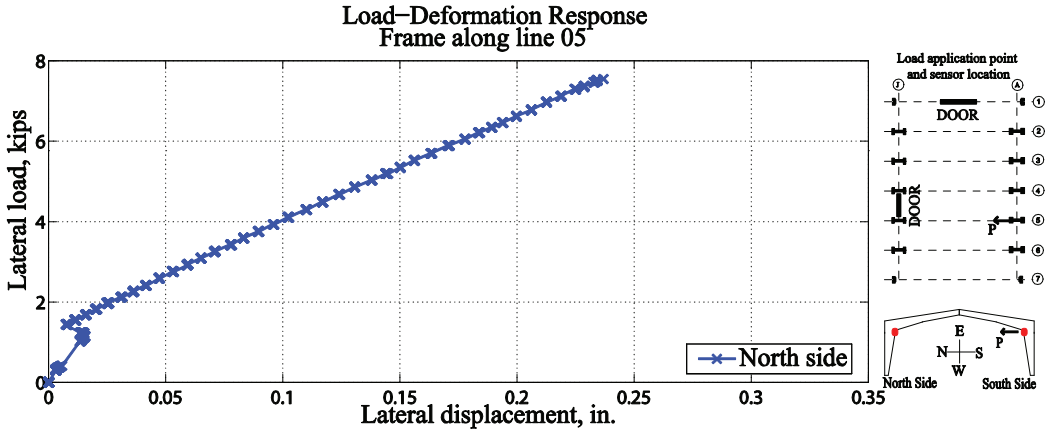

Figure D-38: North end column response of frame along line 5

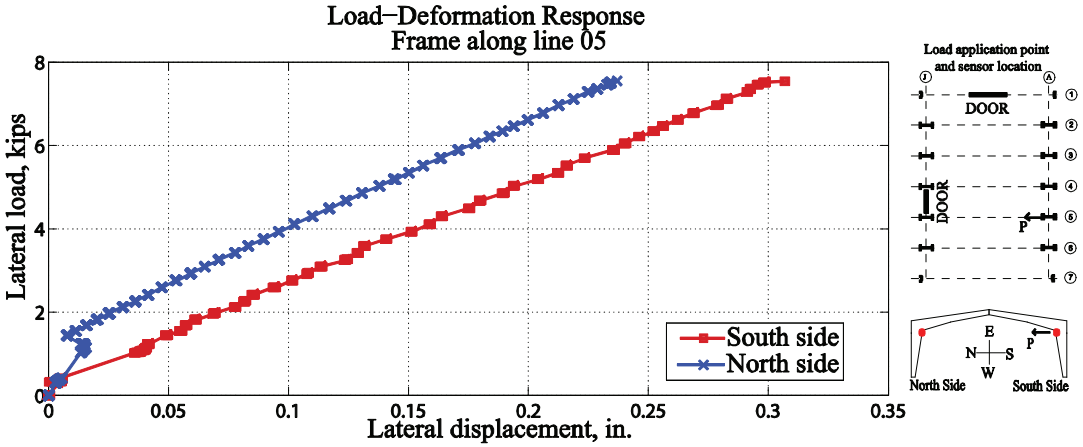

Figure D-39: Deformation on two sides of frame along line 5

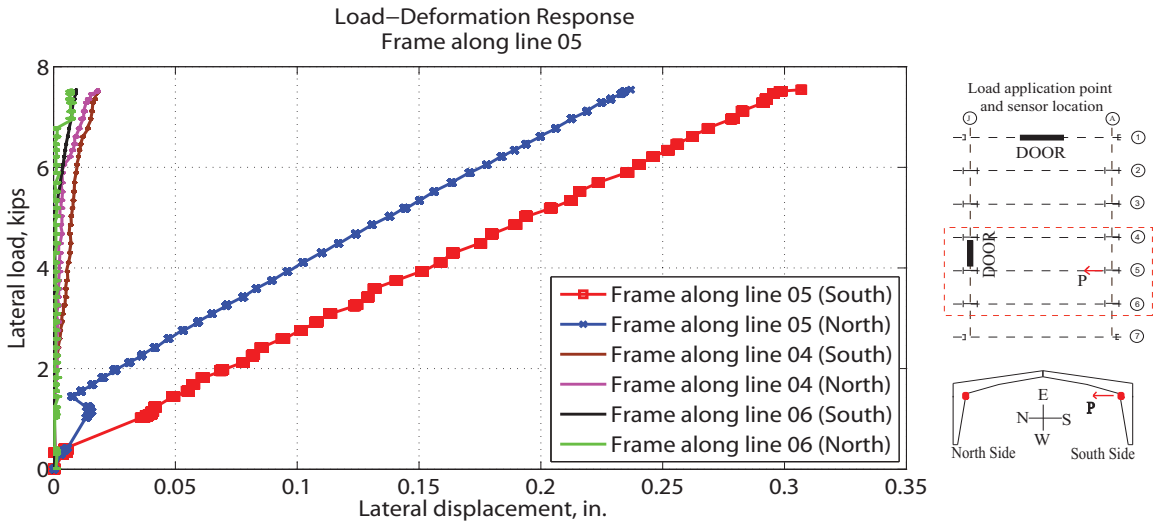

Figure D-40: Deformations on primary along line 5 and adjacent frames along line 4 and line 6

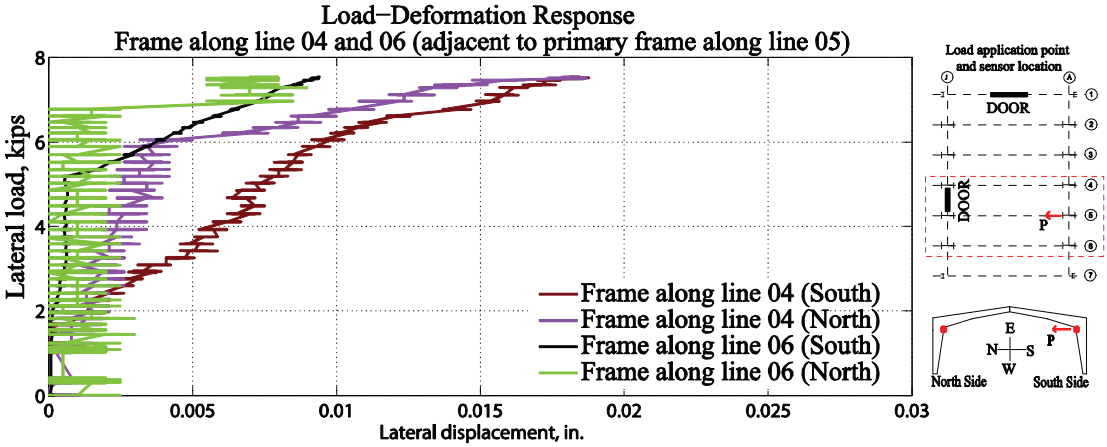

Figure D-41: Deformations on frames along line 4 and 6

D.4.2 Test 02

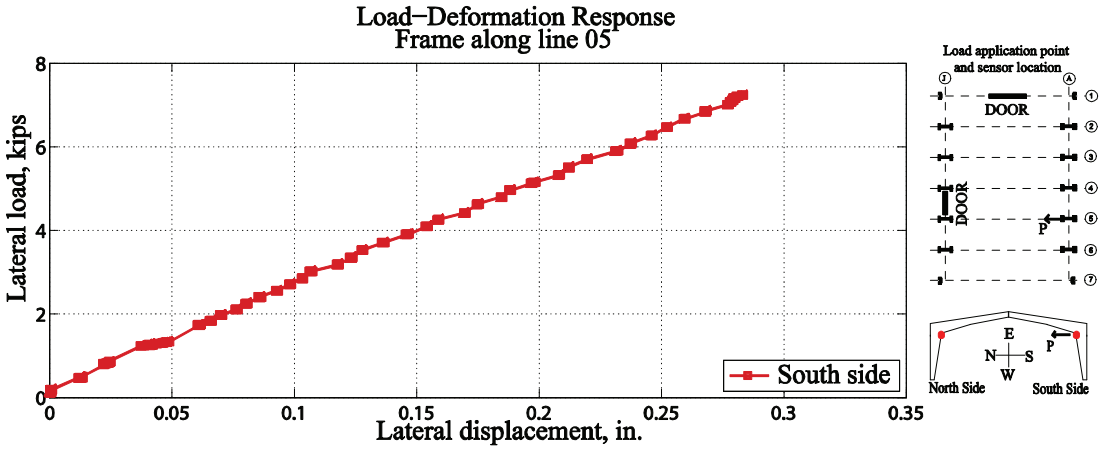

Figure D-42: South end column response of frame along line 5

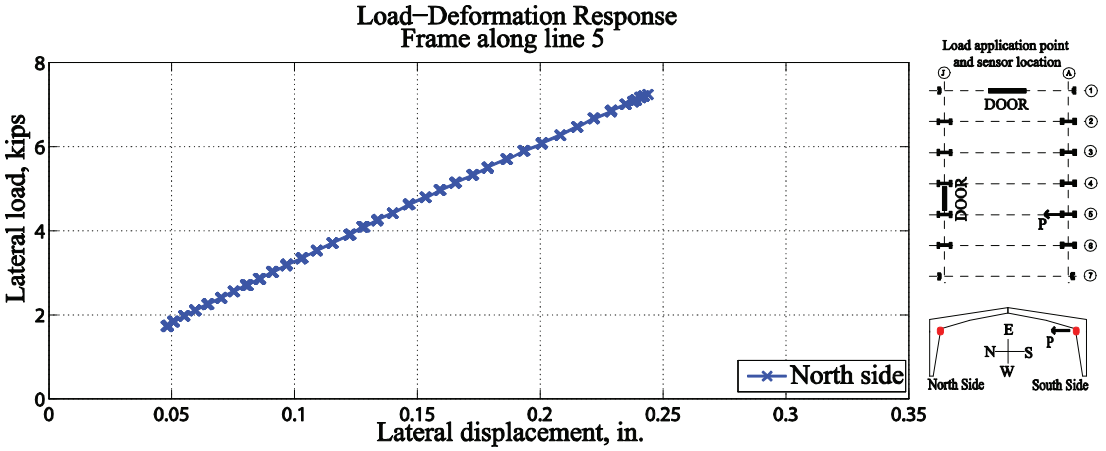

Figure D-43: North end column response of frame along line 5

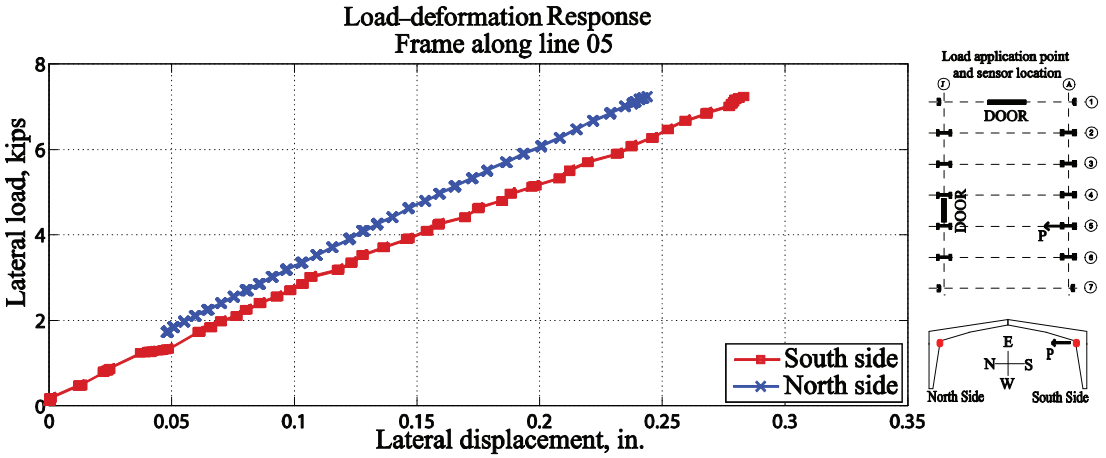

Figure D-44: Deformation on two sides of frame along line 5

D.4.3 Test 03

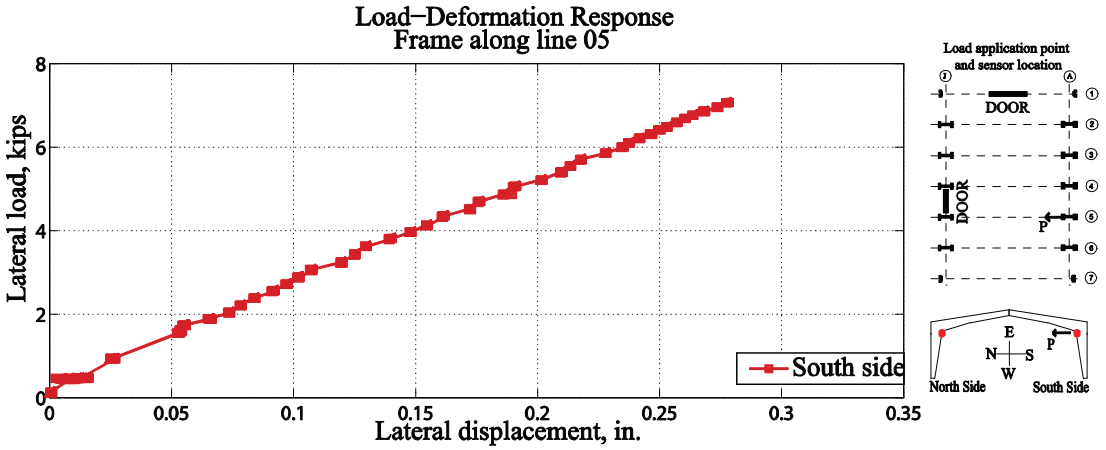

Figure D-45: South end column response of frame along line 5

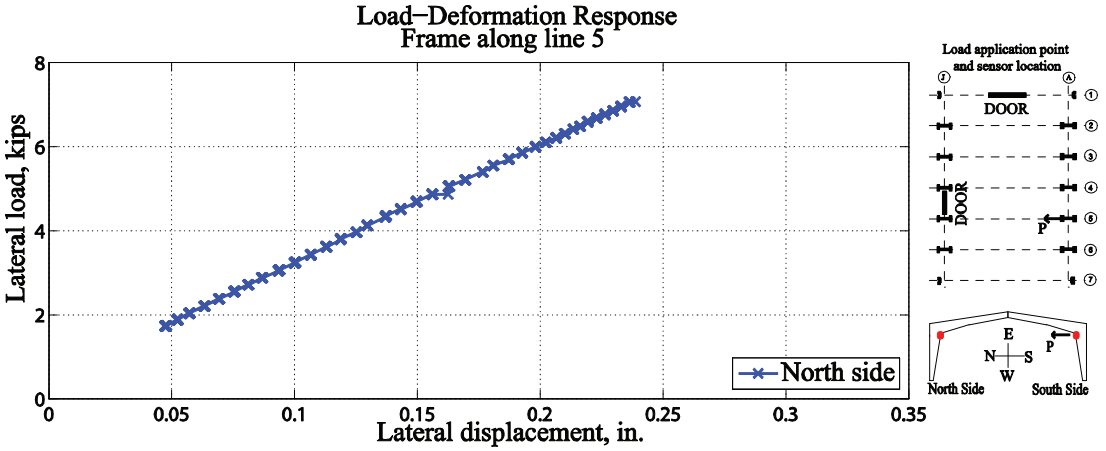

Figure D-46: North end column response of frame along line 5

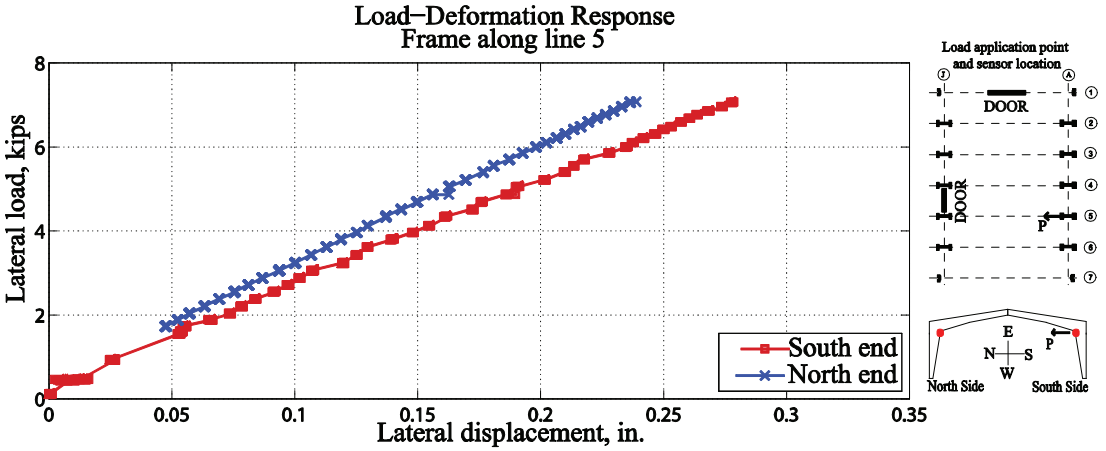

Figure D-47: Deformation on two sides of frame along line 5

D.5 Frame along grid line 6

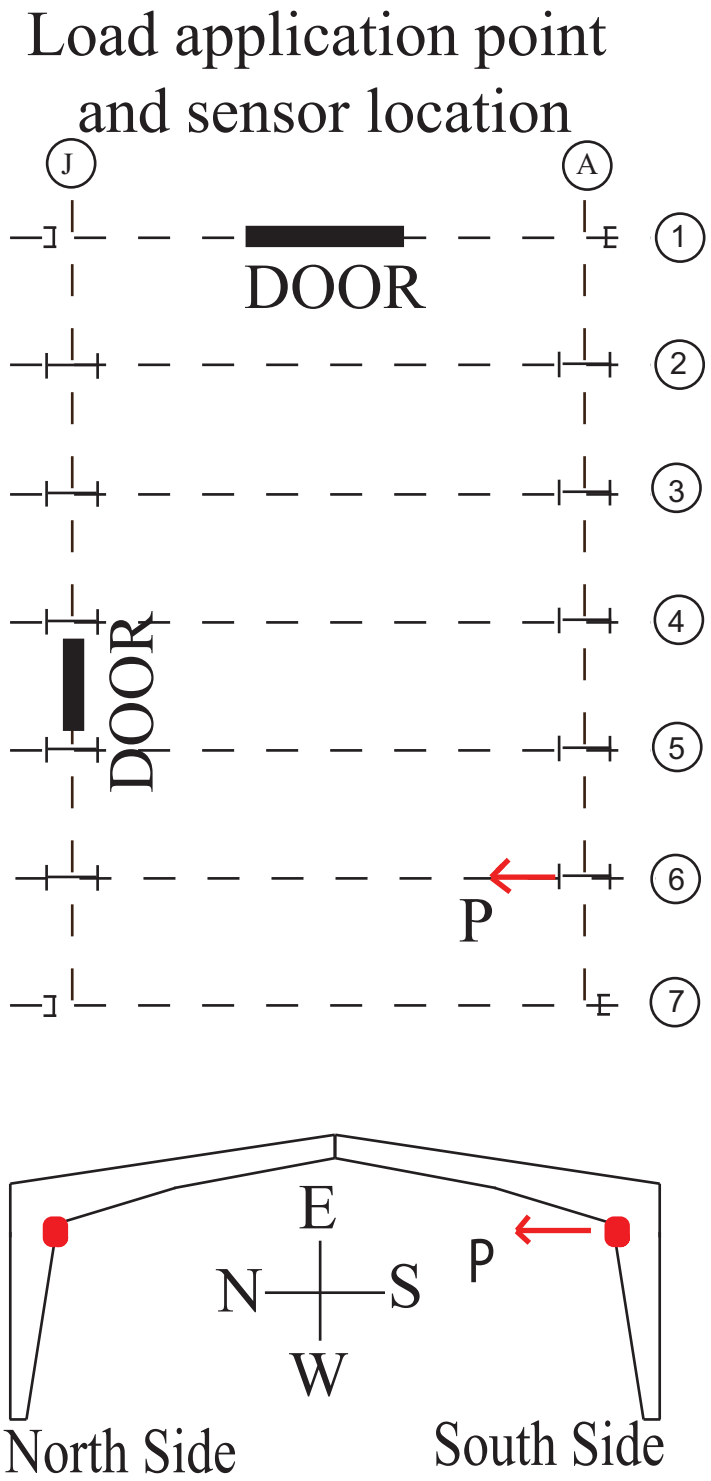

Figure D-48: Location of frame along line 6 and load application points

D.5.1 Test 01

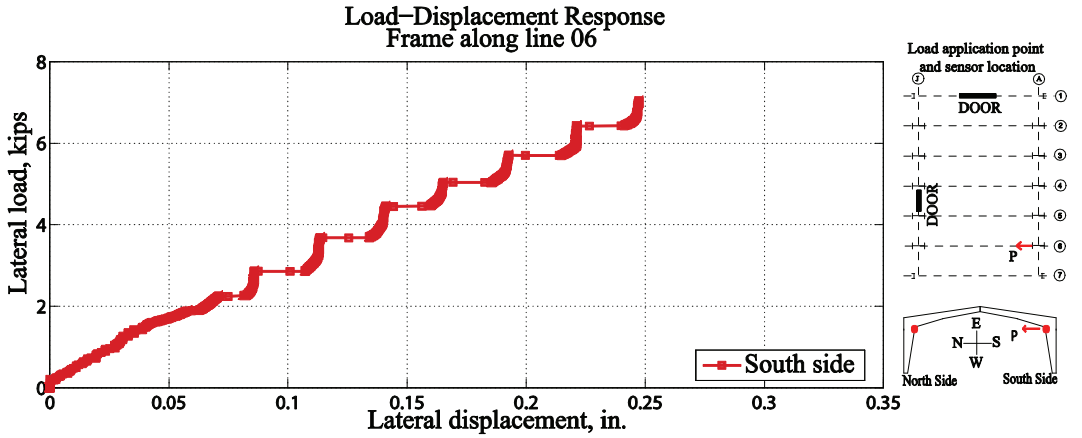

Figure D-49: South end column response of frame along line 6

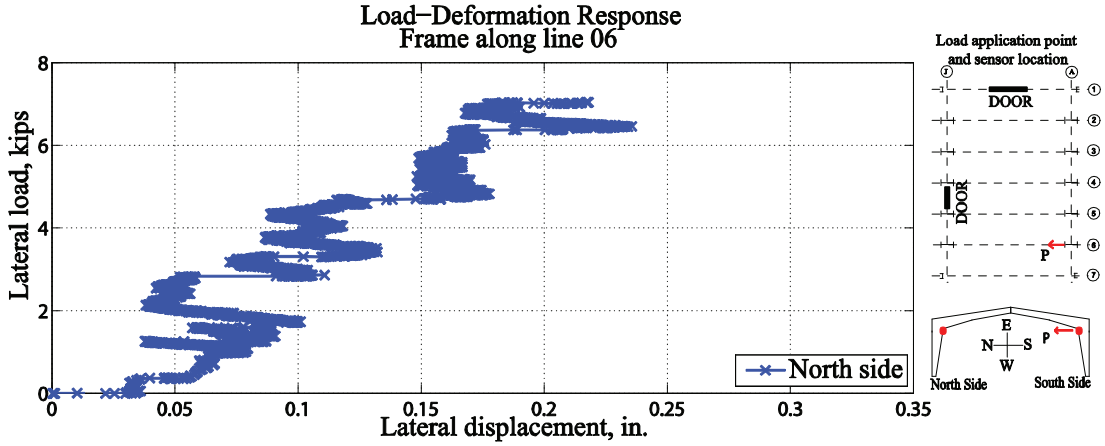

Figure D-50: North end column response of frame along line 6

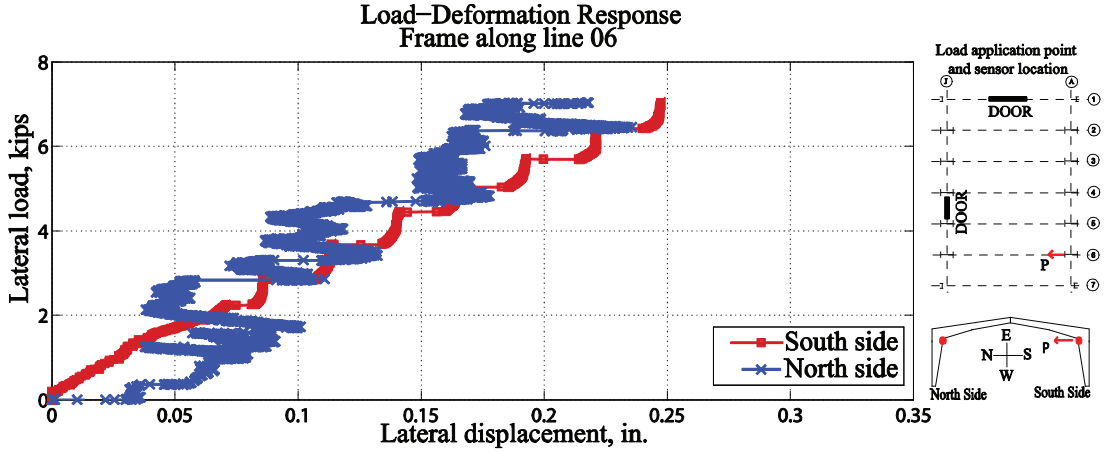

Figure D-51: Deformation on two sides of frame along line 6

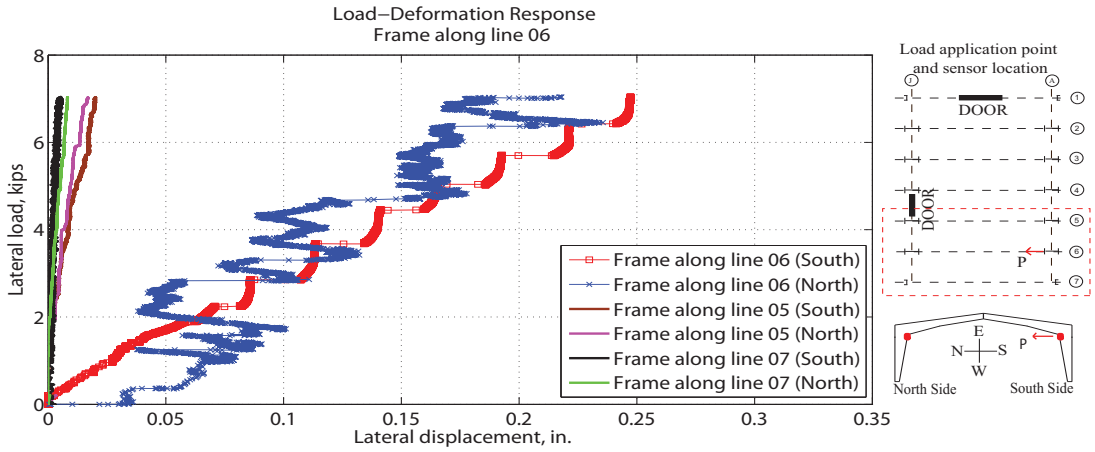

Figure D-52: Deformations on primary frame along line 6 and adjacent frames along line 5 and 7

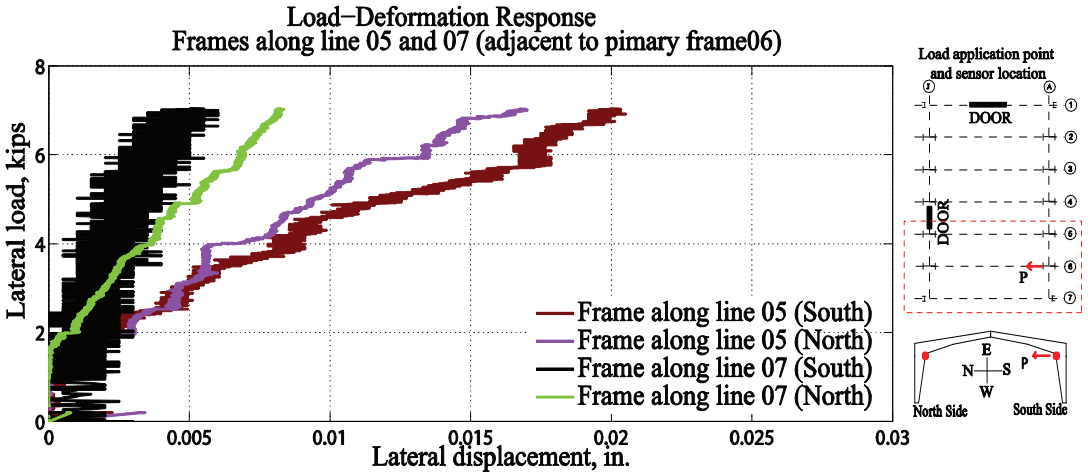

Figure D-53: Deformations on adjacent frames along line 5 and 7

D.5.2 Test 02

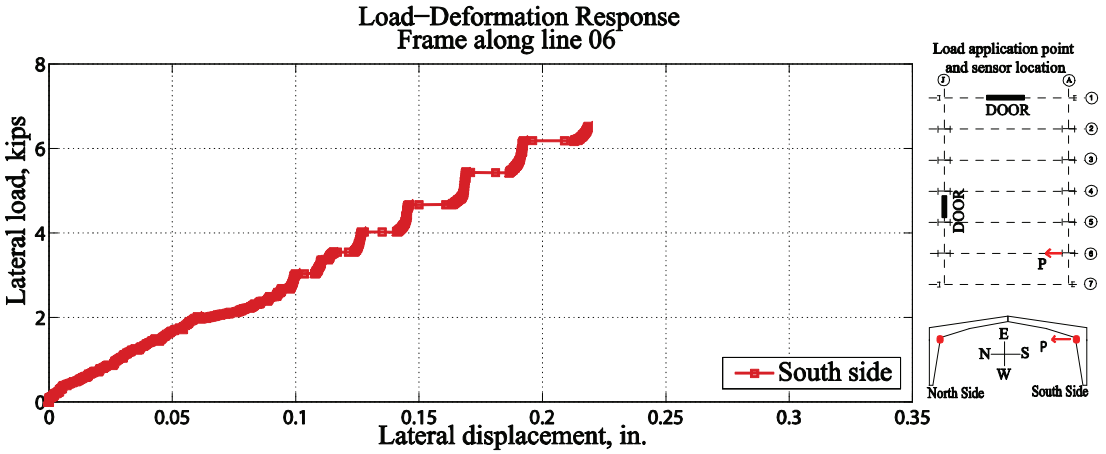

Figure D-54: South end column response of frame along line 6

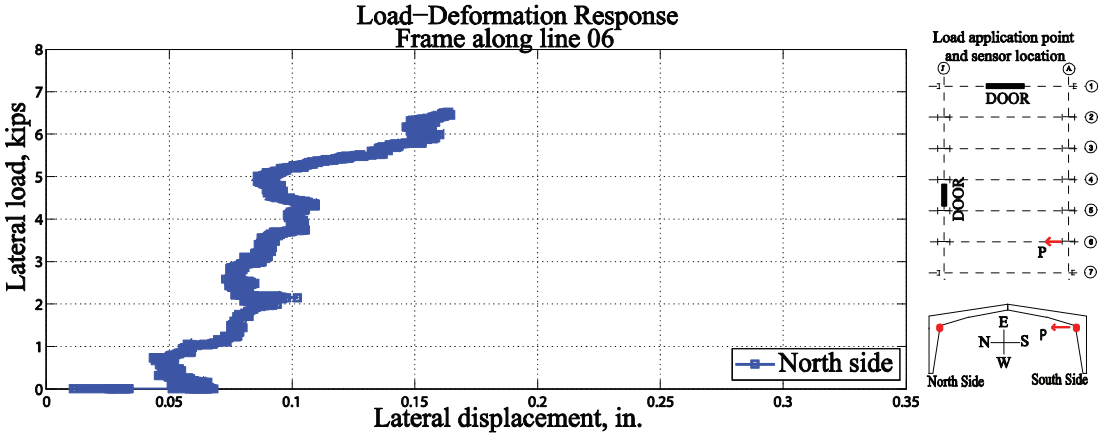

Figure D-55: North end column response of frame along line 6

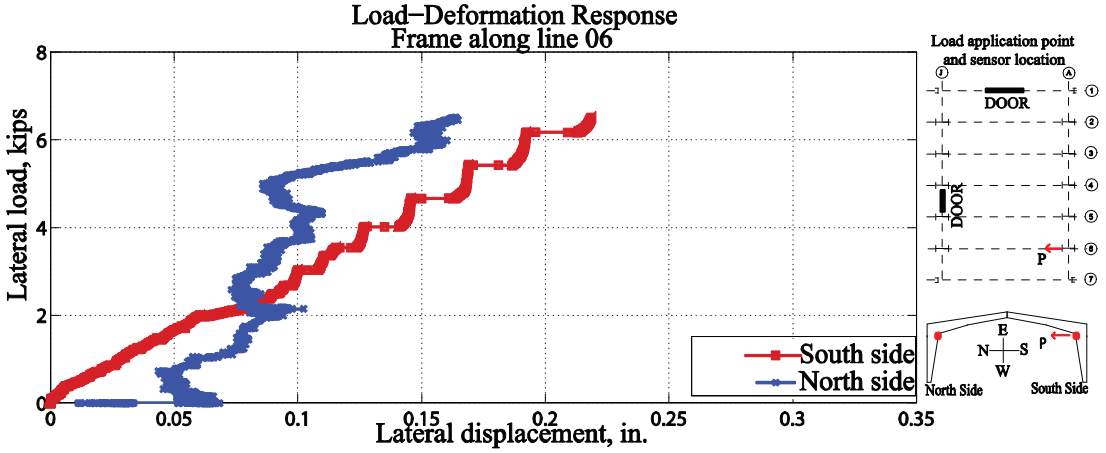

Figure D-56: Deformation on two sides of frame along line 6

D.5.3 Test 03

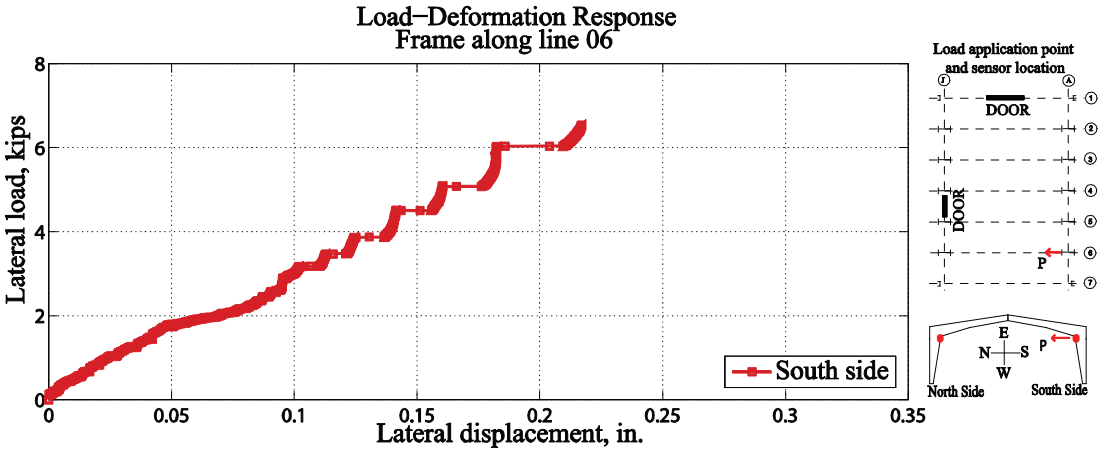

Figure D-57: South end column response of frame along line 6

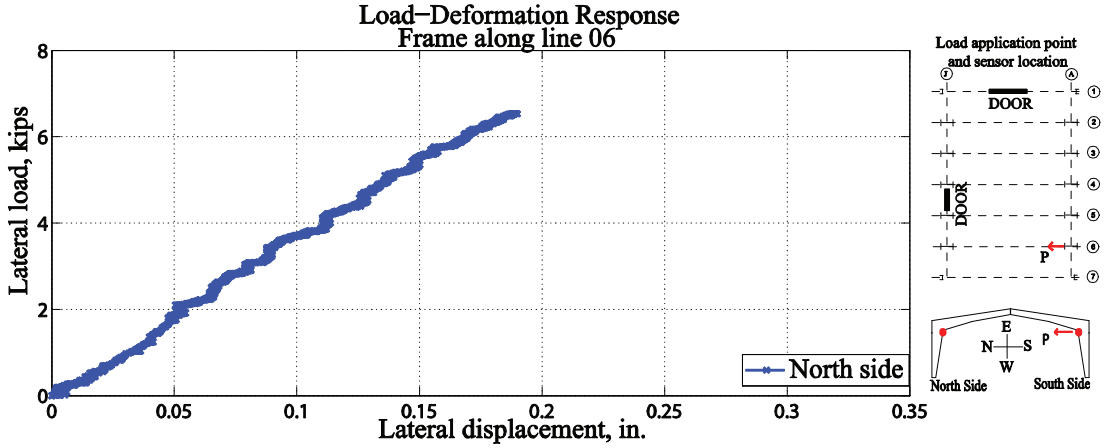

Figure D-58: North end column response of frame along line 6

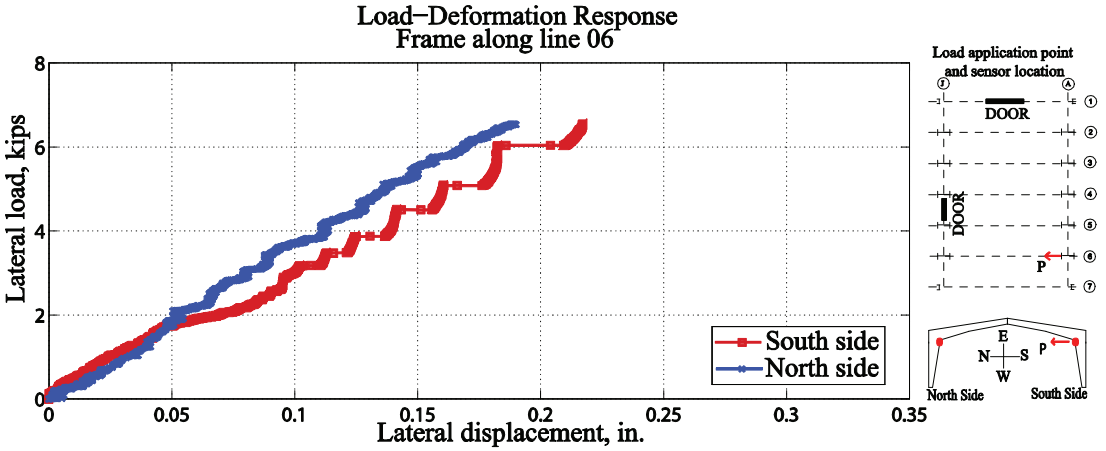

Figure D-59: Deformation on two sides of frame along line 6

D.6 Frame along grid line 4 (Garage Door Side)

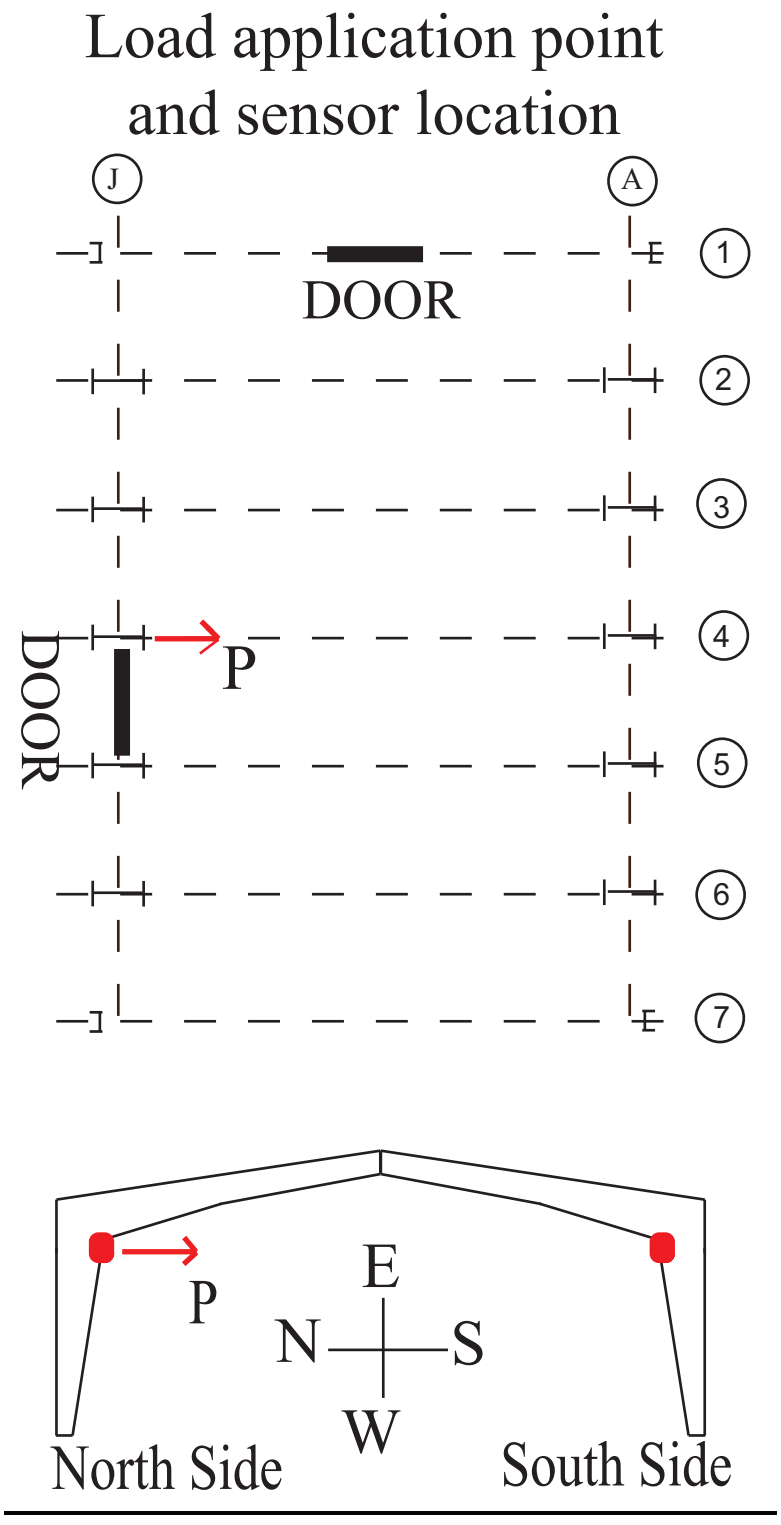

Figure D-60: Location of frame along line 4(Garage Door Side) and load application points

D.6.1 Test 01

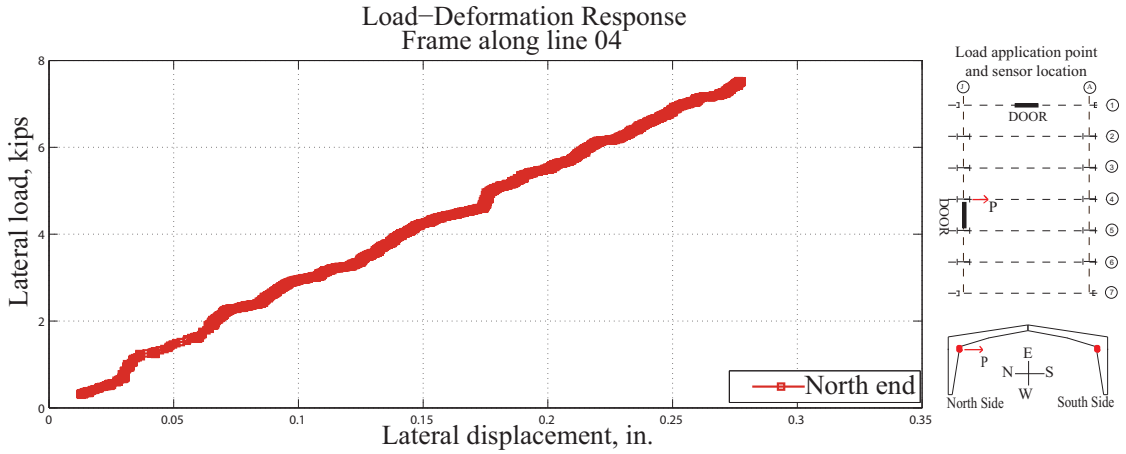

Figure D-61: North end column response of frame along line 4 (Garage Door Side)

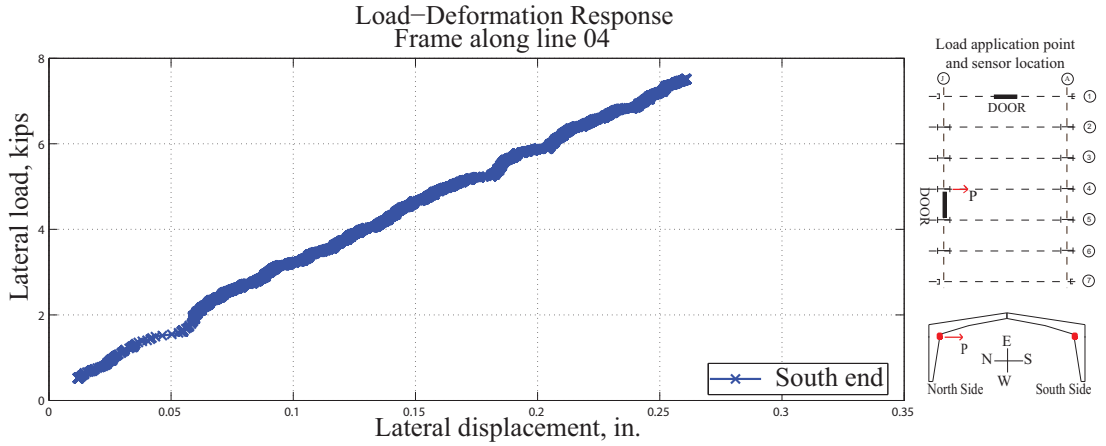

D-62: South end column response of frame along line 4 (Garage Door Side)

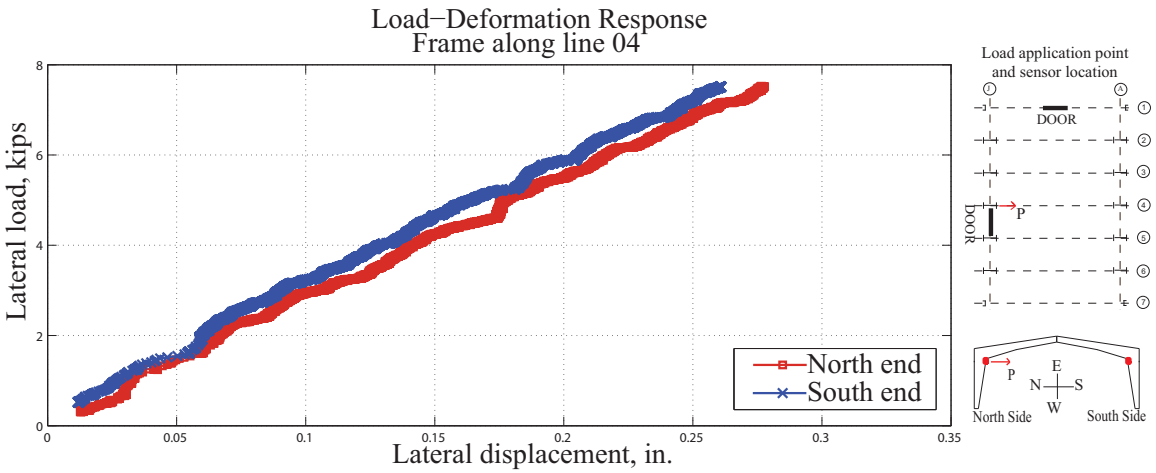

Figure D-63: Deformation on two sides of frame along line 4 (Garage Door Side)

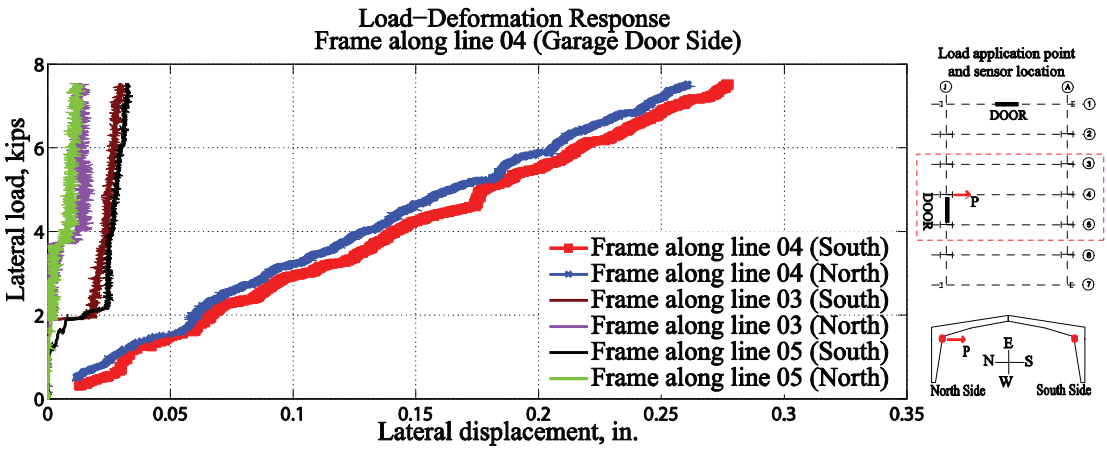

Figure D-64: Deformations on primary frame along line 4 (Garage Door Side) and adjacent frame along line 3 and line 5

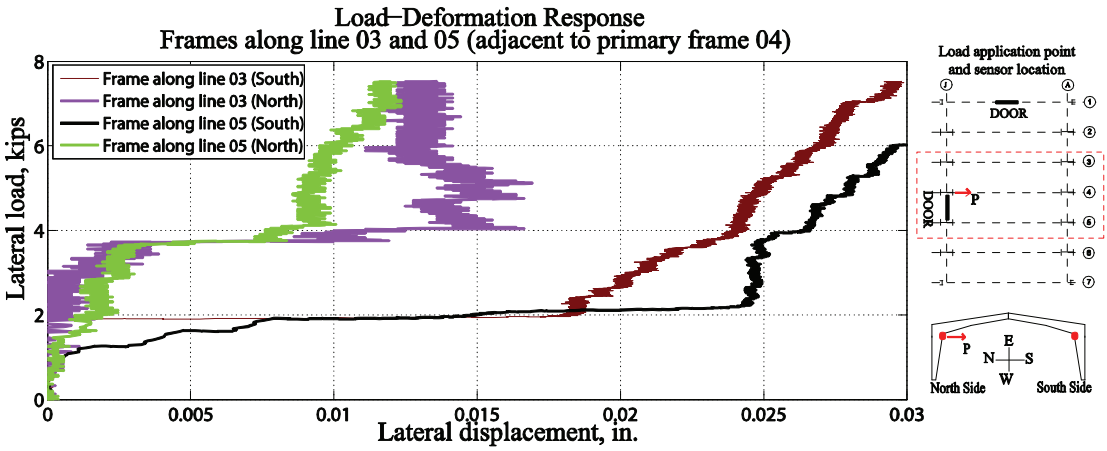

Figure D-65: Deformations on adjacent frames along line 3 and line 5

D.6.2 Test 02

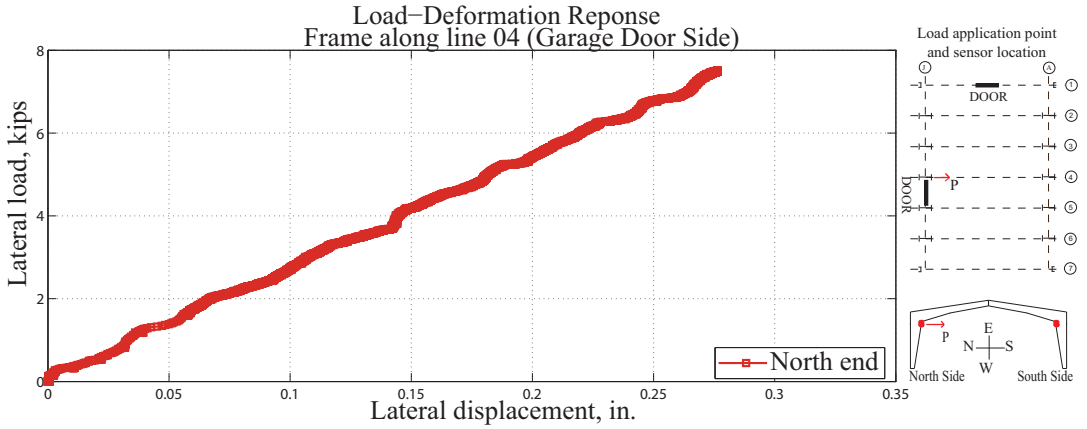

Figure D-66: North end column response of frame along line 4 (Garage Door Side)

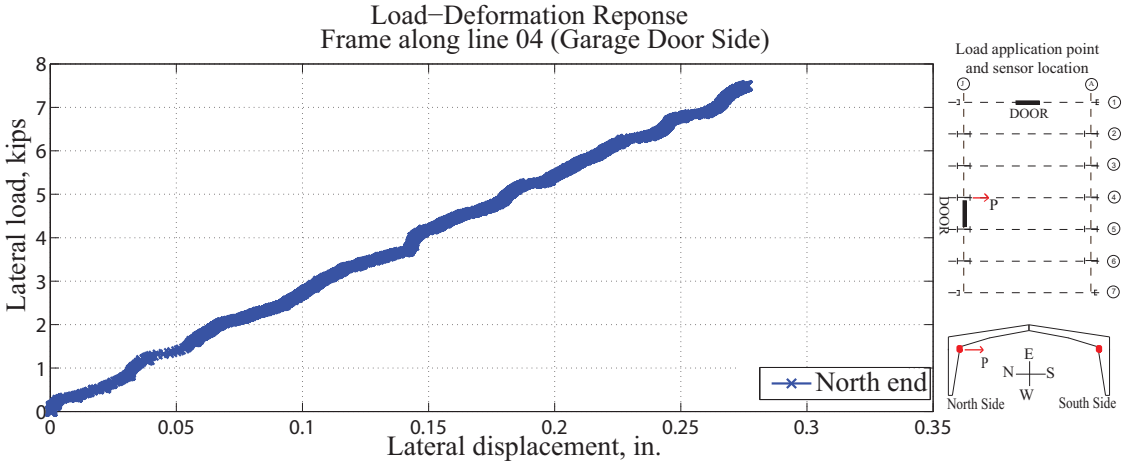

Figure D-67: South end column response of frame along line 4 (Garage Door Side)

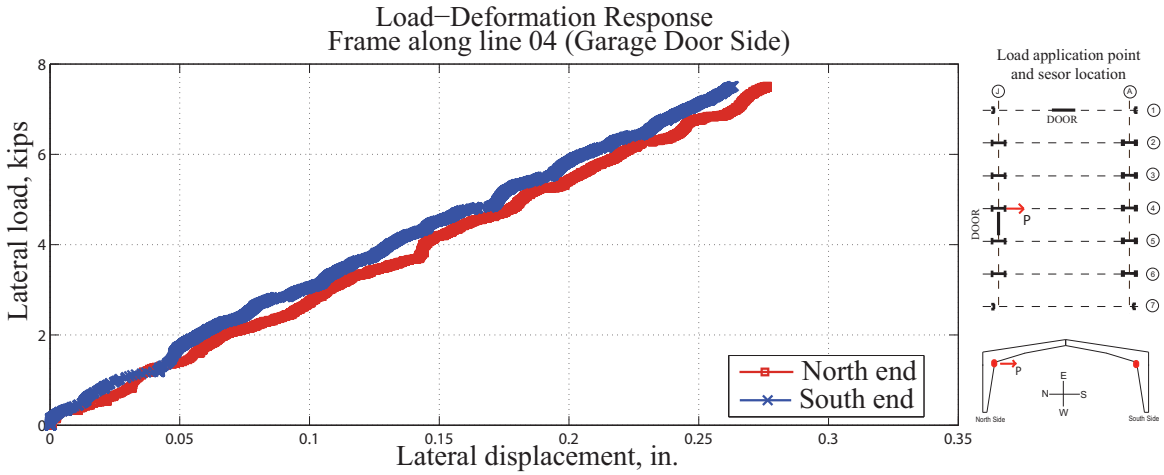

Figure D-68: Deformation on two sides of frame along line 4 (Garage Door Side)

D.7 Frame along grid line 5 (Garage Door Side)

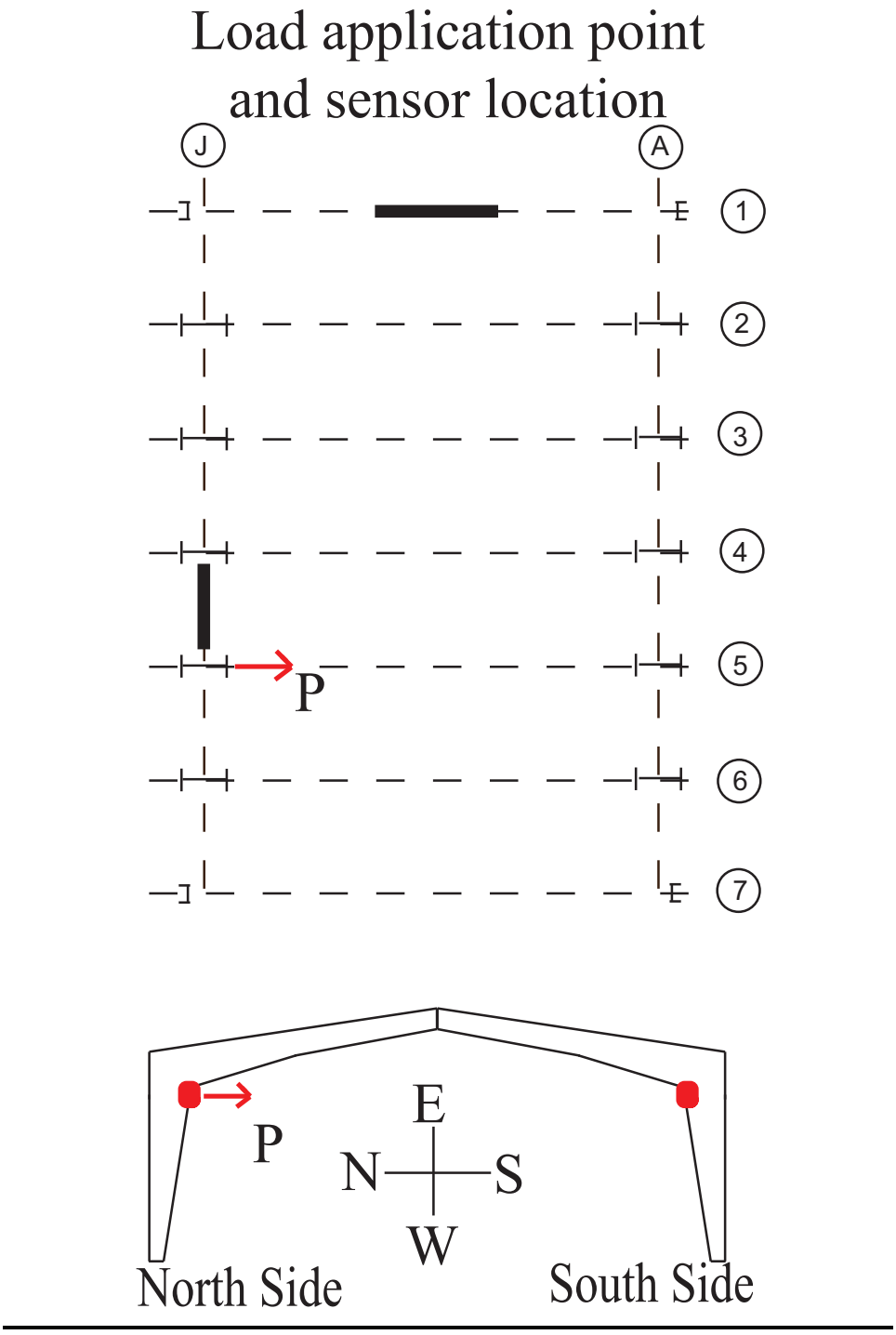

Figure D-69: Location of frame along line 5(Garage Door Side) and load application points

D.7.1 Test 01

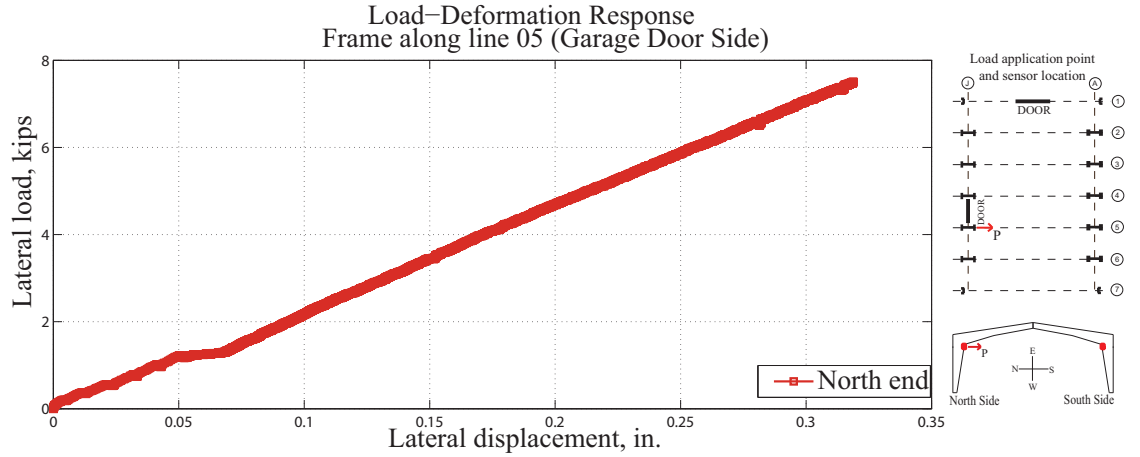

Figure D-70: North end column response of frame along line 5 (Garage Door Side)

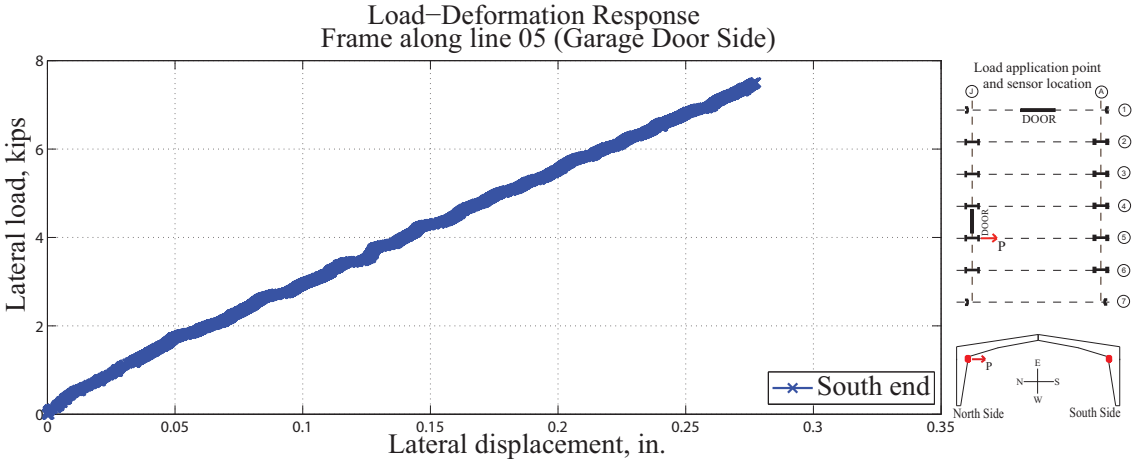

Figure D-71: South end column response of frame along line 5 (Garage Door Side)

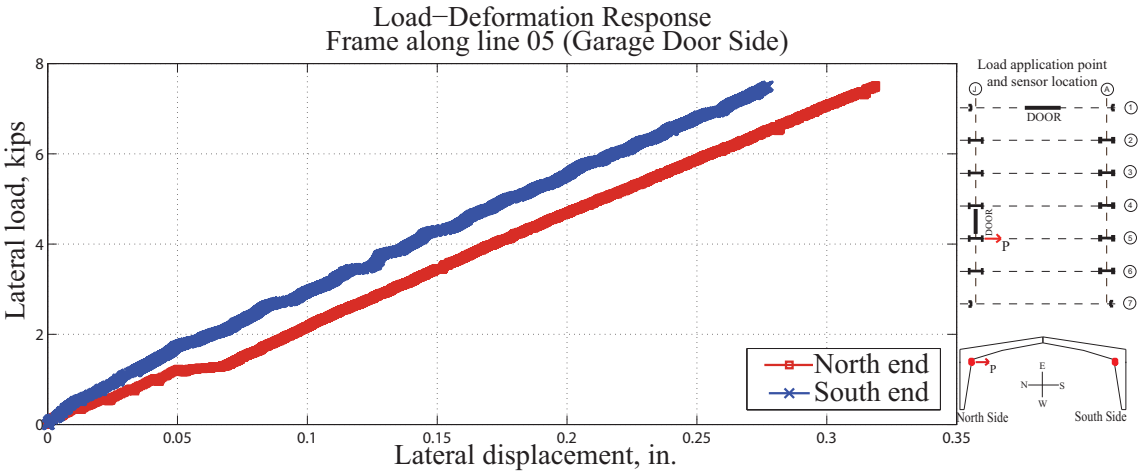

Figure D-72: Deformation on two sides of frame along line 5 (Garage Door Side)

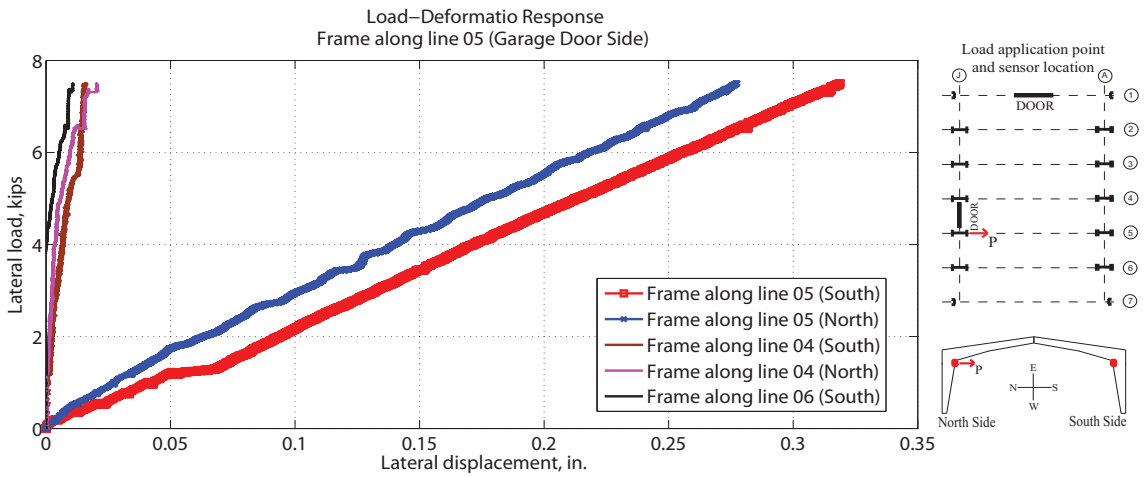

Figure D-73: Deformations on primary frame of frame along line 5 (Garage Door Side) and adjacent frames along line 4 and line 6

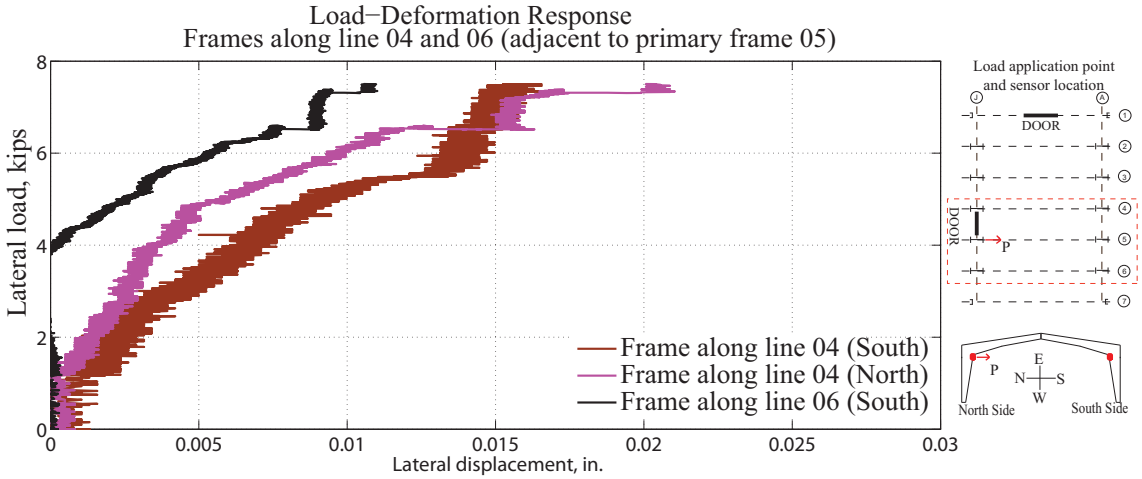

Figure D-74: Deformations on adjacent along line 4 and 6

D.7.2 Test 02

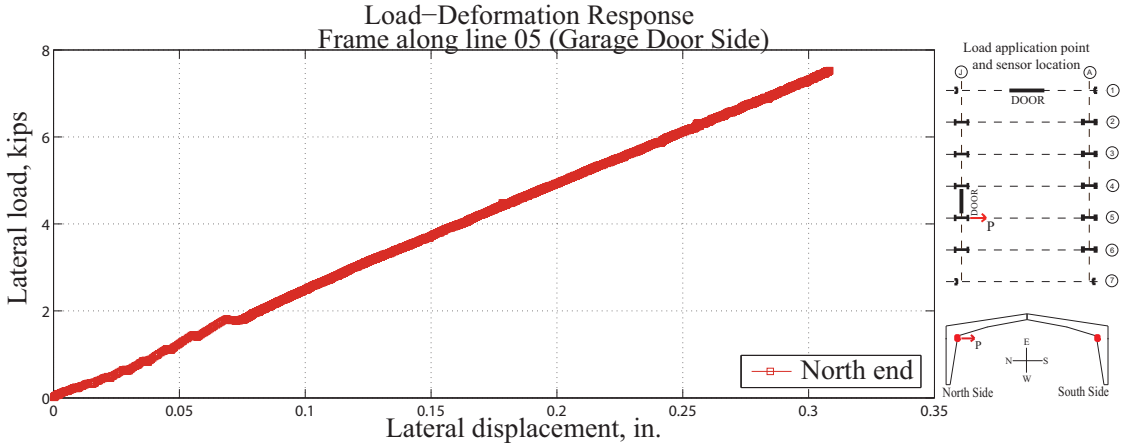

Figure D-75: North end column response

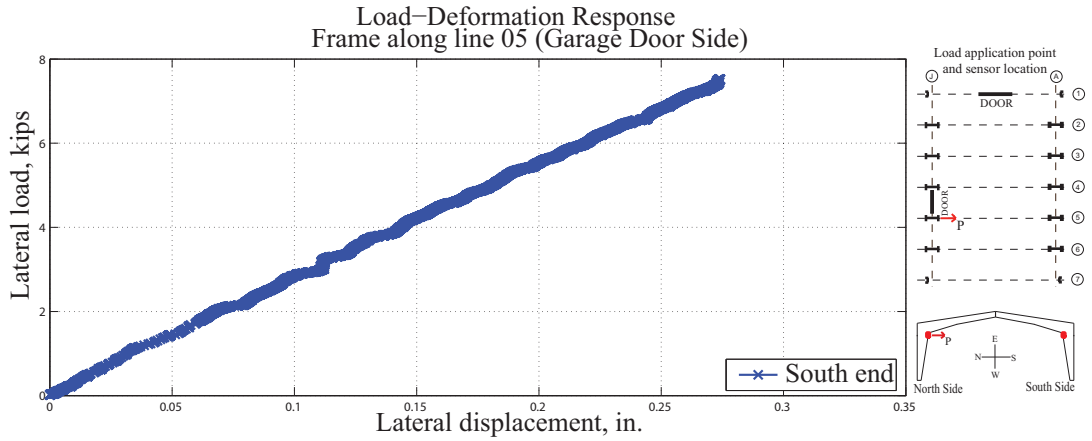

Figure D-76: South end column response

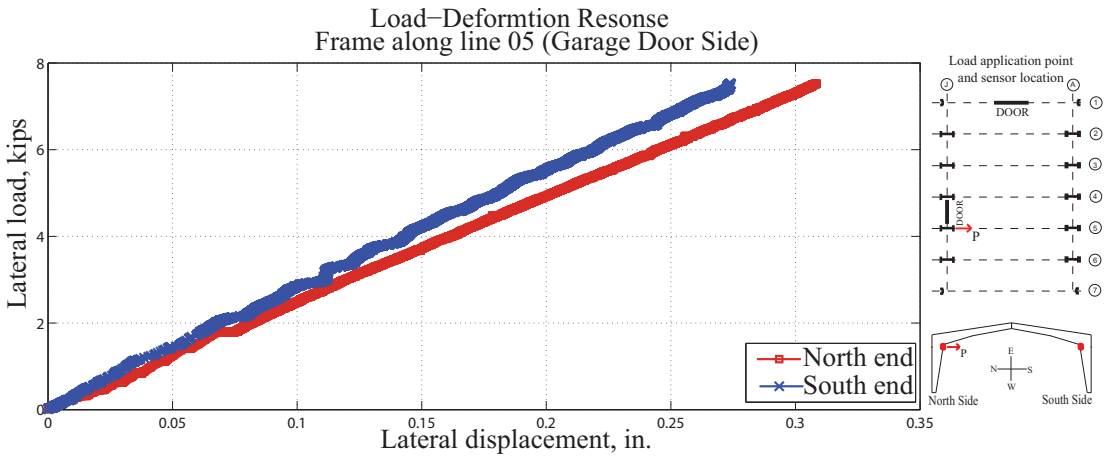

Figure D-77: Plot showing overlap of deformation on two sides

D.7.3 Test 03

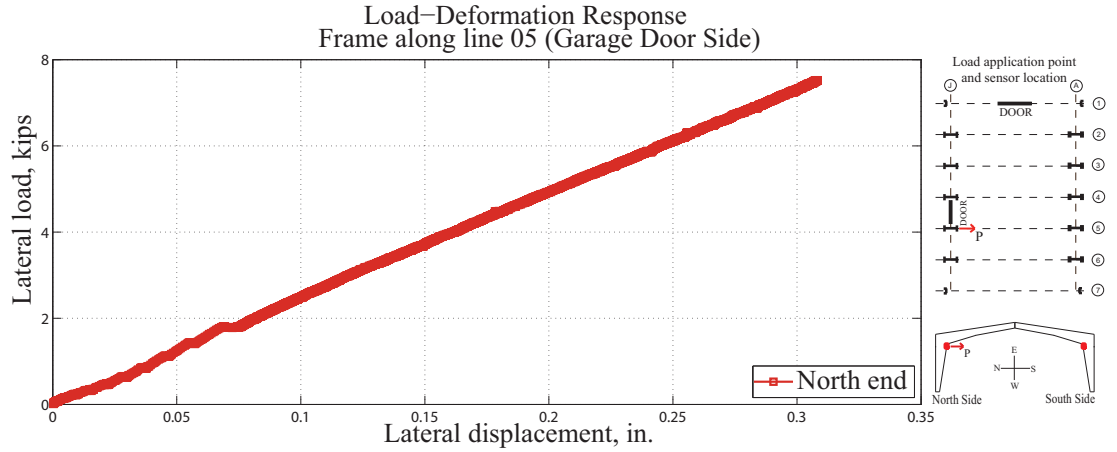

Figure D-78: North end column response

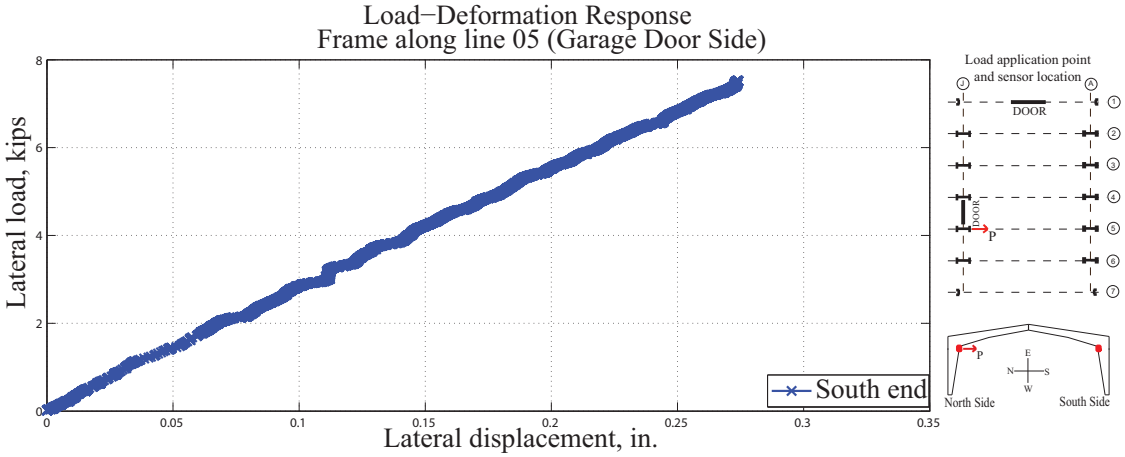

Figure D-79: South end column response

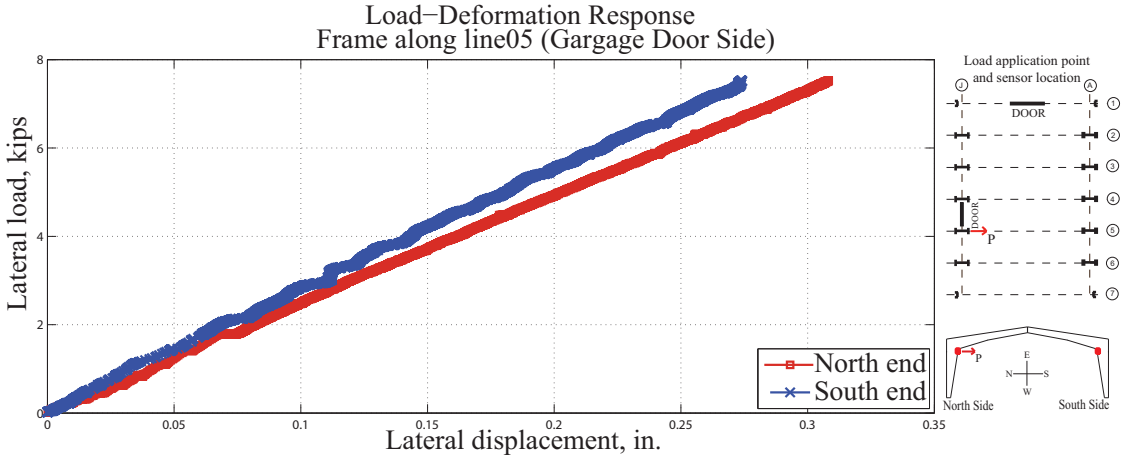

Figure D-80: Plot showing overlap of deformation on two sides

APPENDIX E

E.1 Frame along line 02

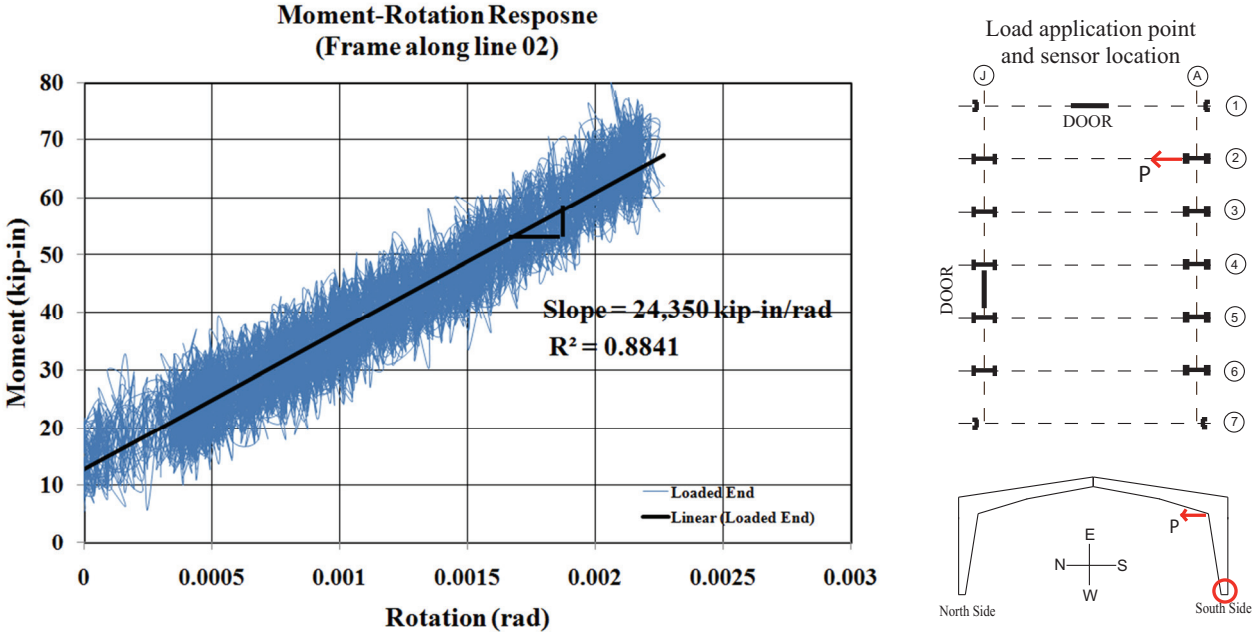

Figure E-1: Loaded End, Frame along line 02

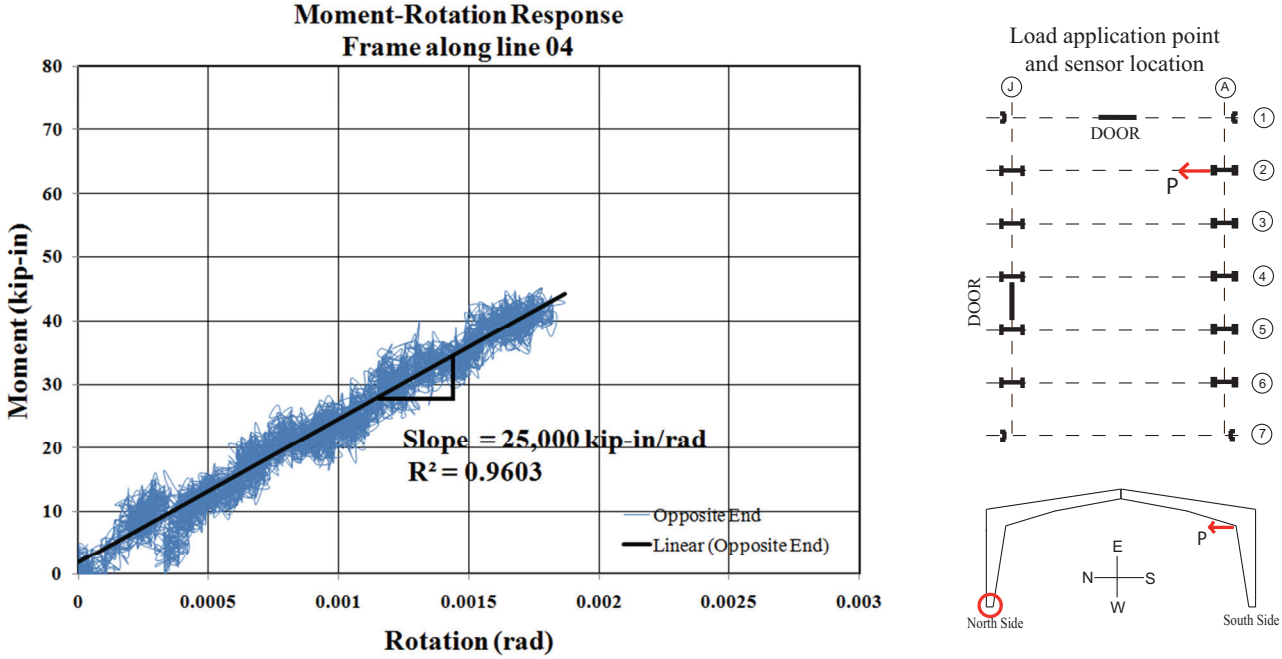

Figure E-2: Opposite End, Frame along line 02

E.2 Frame along line 03

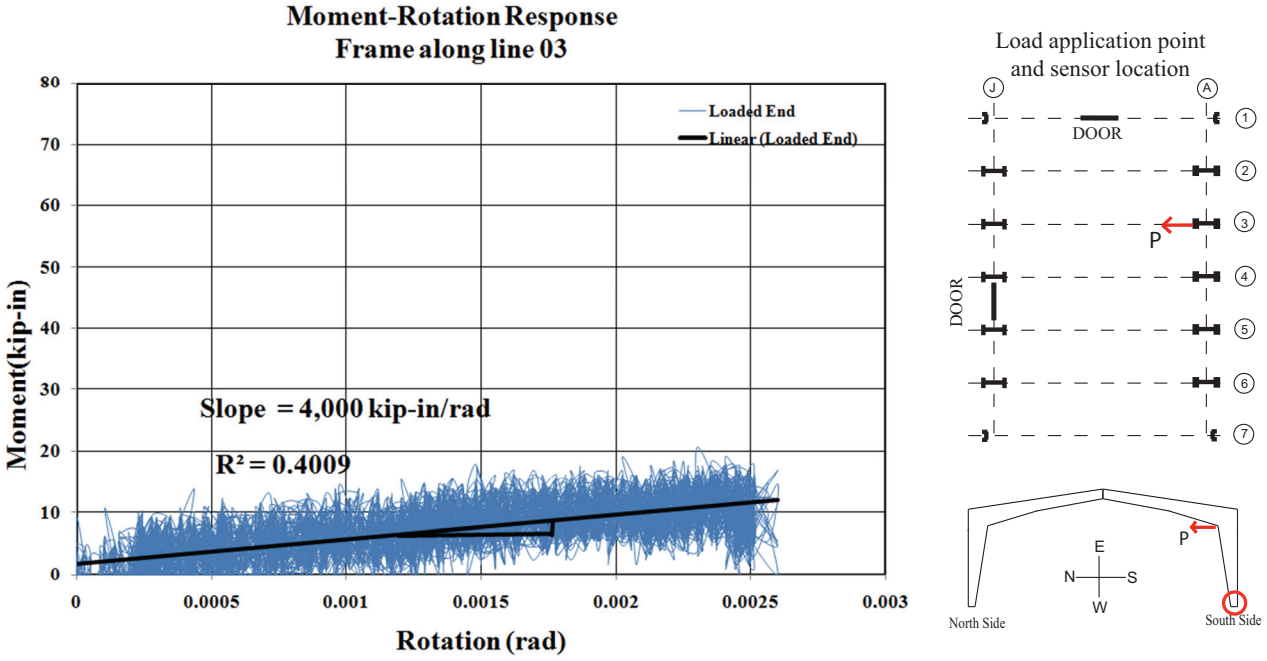

Figure E-3: Loaded End, Frame along line 03

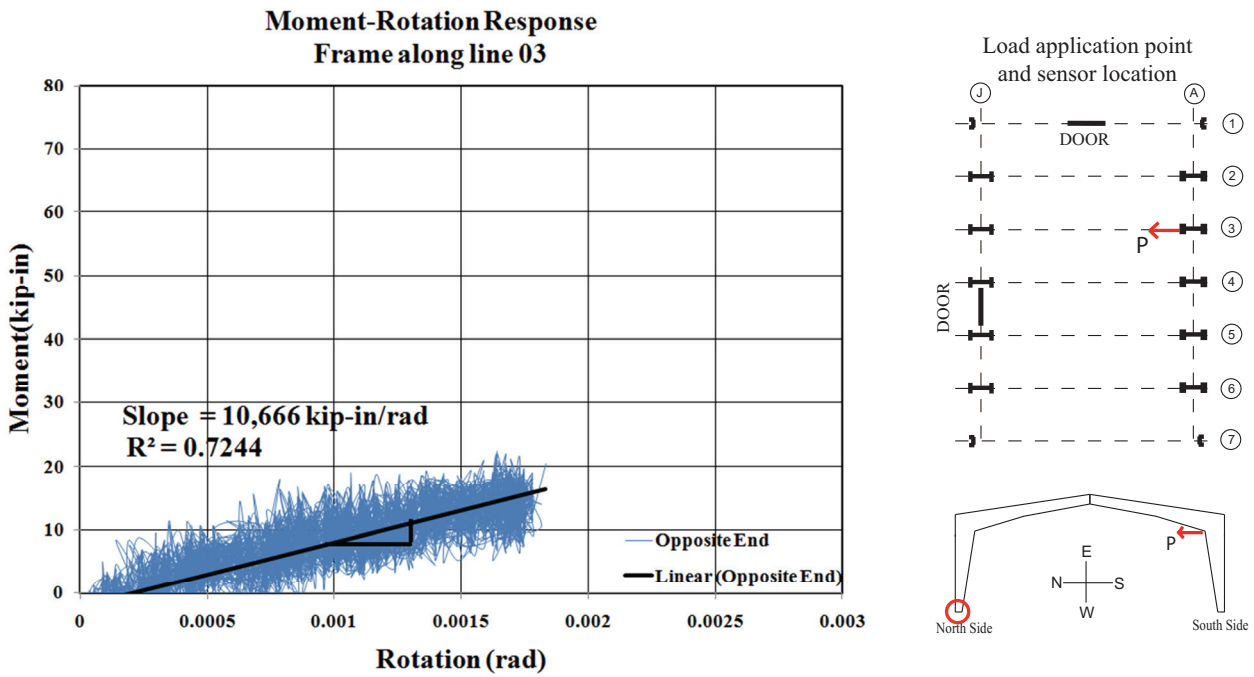

Figure E-4: Opposite End, Frame along line 03

E.3 Frame along line 04

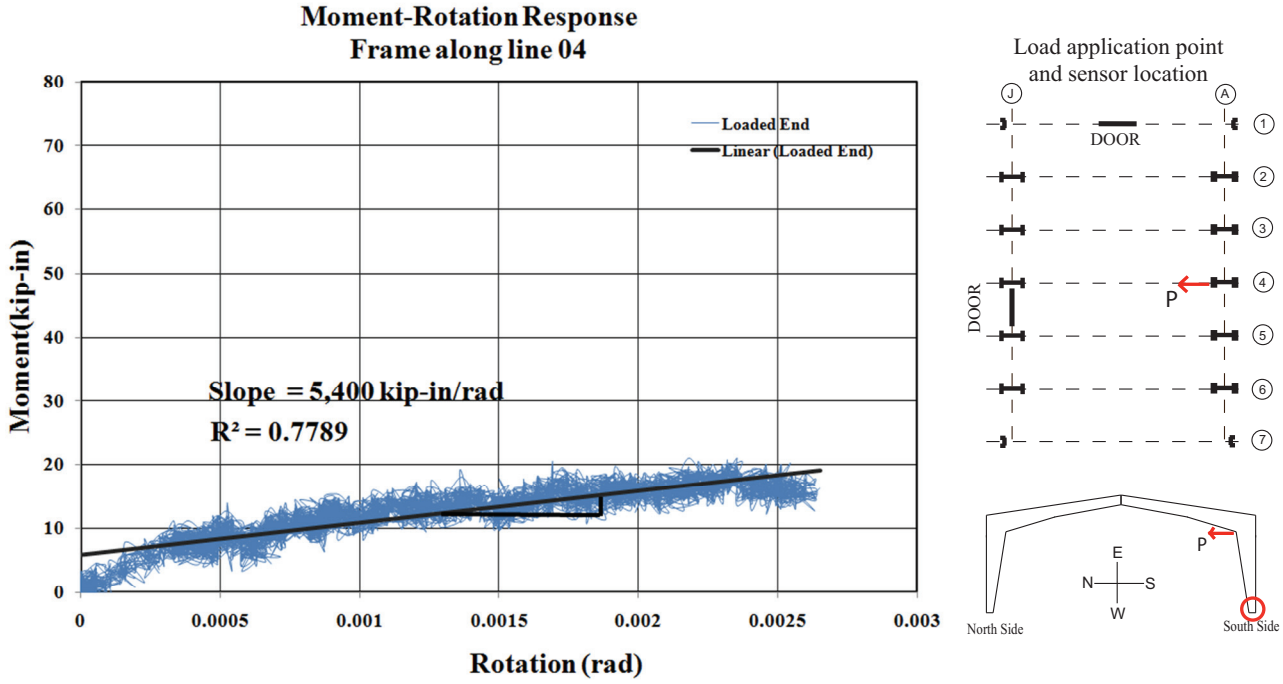

Figure E-5: Loaded End, Frame along line 04

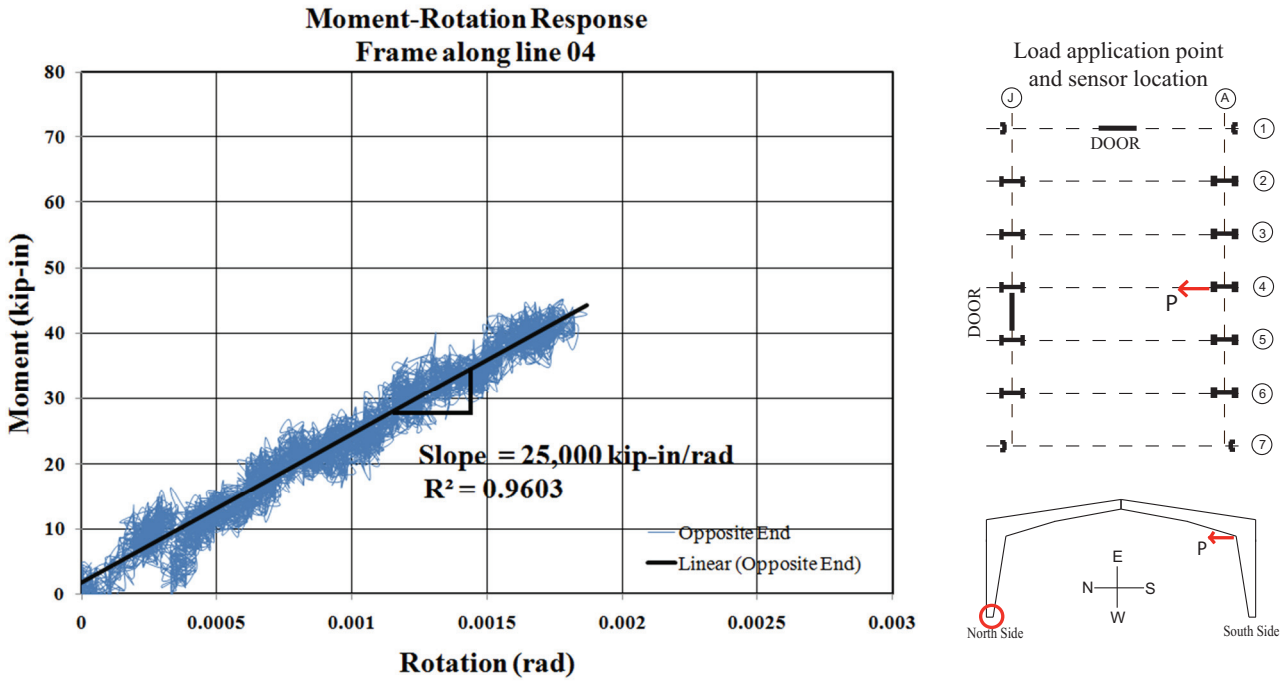

Figure E-6: Opposite End, Frame along line 04

E.4 Frame along line 05

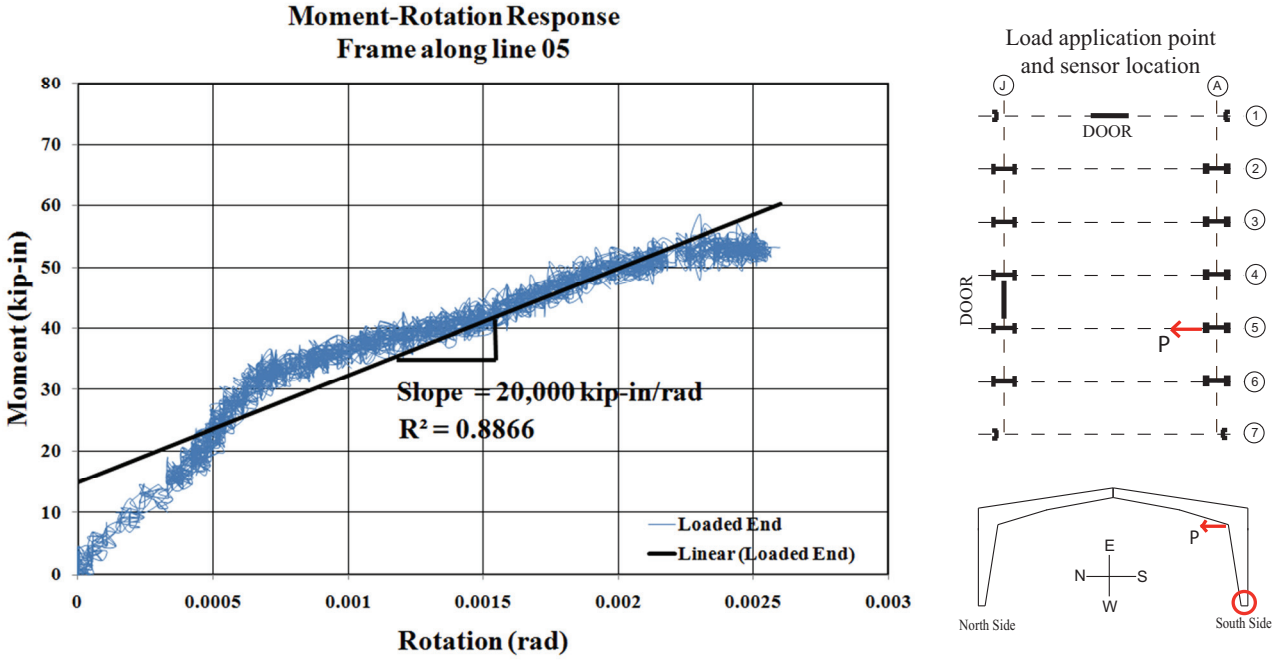

Figure E-7: Loaded End, Frame along line 05

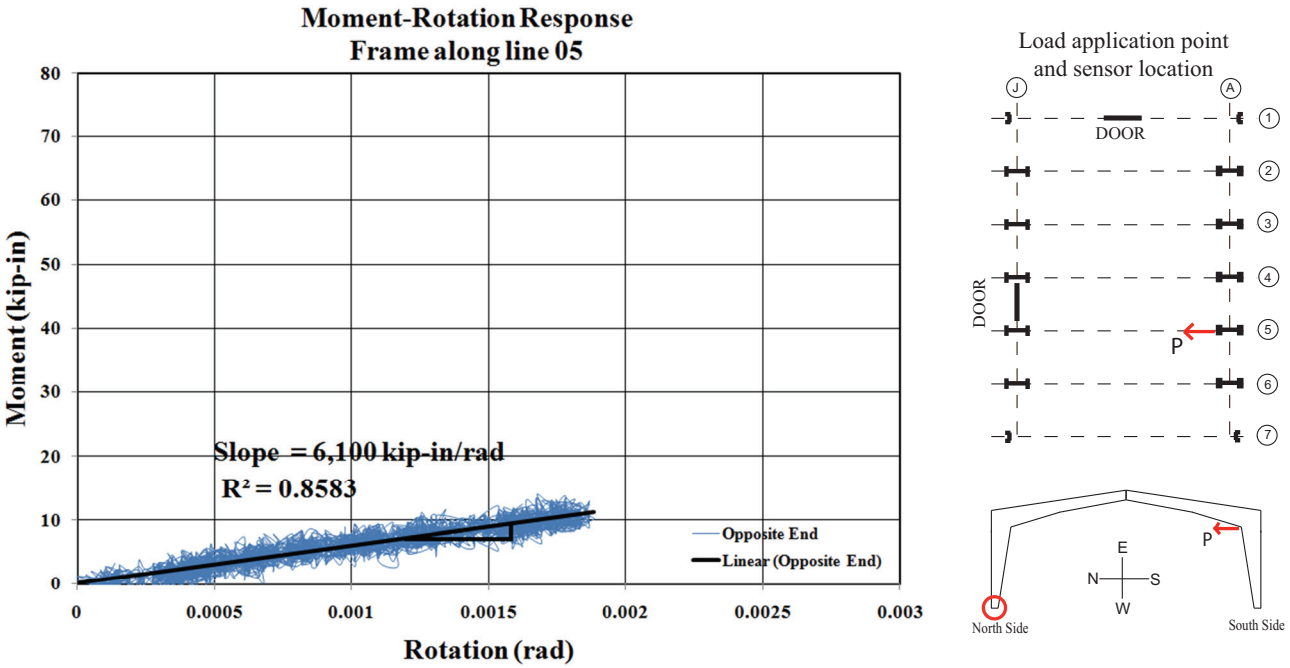

Figure E-8: Opposite End, Frame along line 05

E.5 Frame along line 06

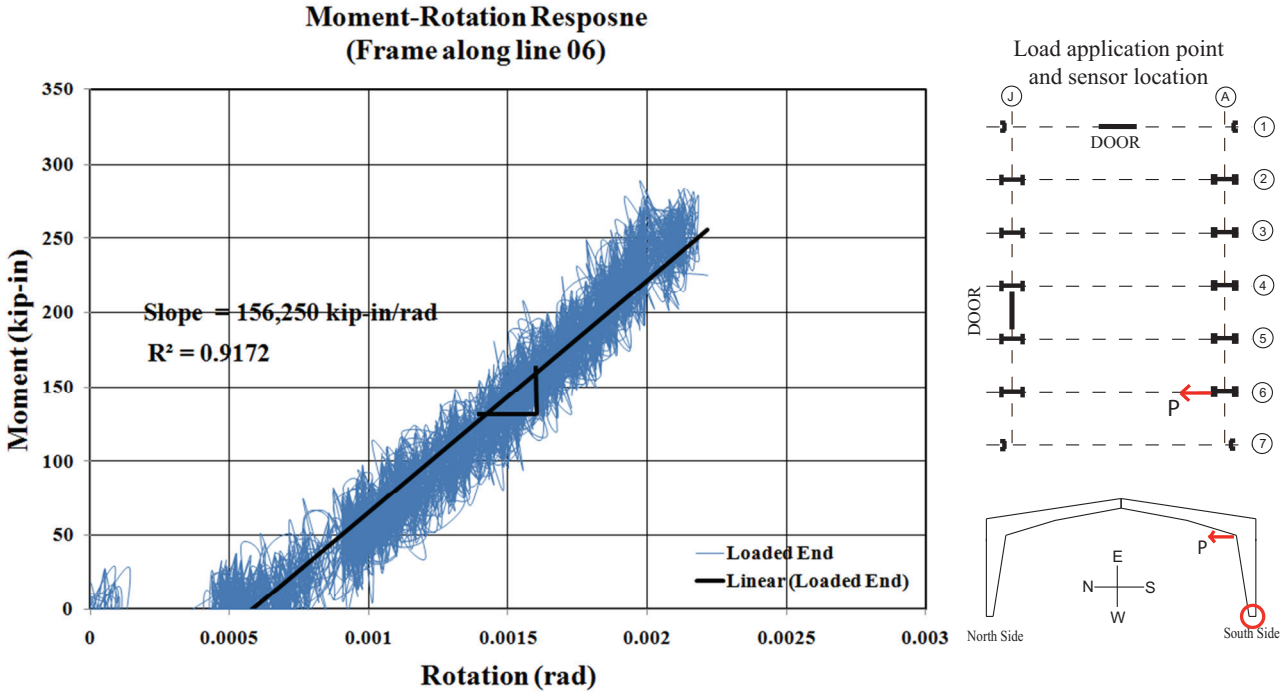

Figure E-9: Loaded End, Frame along line 06